COMPUTATIONAL ANALYSIS OF CARBON NANOTUBE NETWORKS IN MULTIFUNCTIONAL POLYMER NANOCOMPOSITES

A Dissertation

by

KEVIN S. MAXWELL

Submitted to the Office of Graduate and Professional Studies of
Texas A&M University
in partial fulfillment of the requirements for the degree of

DOCTOR OF PHILOSOPHY

Chair of Committee,	John Whitcomb
Committee Members,	Dimitris Lagoudas
	Mohammad Naraghi
	Hung-Jue Sue
Head of Department,	Ibrahim Karaman

December 2013

Major Subject: Materials Science and Engineering

Copyright 2013 Kevin S. Maxwell

ABSTRACT

Carbon nanotubes (CNTs) have attracted much attention as reinforcements in polymer composite materials because of their unique mechanical, electrical, and thermal properties. The high electrical conductivity of CNTs is especially promising for use in multifunctional materials. Dispersing a small amount of CNTs in electrically insulating polymers has been shown to increase the conductivity of the material by many orders of magnitude because the high aspect ratio CNTs form percolating networks at very low volume fractions. Additionally, it has been shown that the application of mechanical strain to these nanocomposites results in a change in material resistivity, or piezoresistivity. Many experimental research efforts have focused on optimizing this effect for strain and damage sensing applications, but much is still unknown about the dominant mechanisms affecting piezoresistivity. The objective of this work was to develop a computational model that can predict and investigate the electrical and piezoresistive properties of CNT/polymer composites.

The nanocomposites were modeled as random networks of resistors in 2D and 3D in order to understand the mechanisms that affect the percolative, electrical, and piezoresistive performance of different material systems. The model was used extensively to analyze and predict the electrical conductivity of 2D single-walled carbon nanotube thin films and 3D multi-walled carbon nanotube (MWCNT)/polymer nanocomposites. It was found that the contact resistance between individual nanotubes greatly affects the conductivity of 2D films as well as 3D MWCNT/polymer materials. Additionally, it was shown that the electrical conductivity model could

be calibrated to experimental results by adjusting the contact resistance alone.

The 3D random resistor network model was also used to predict the piezoresistive properties for MWCNT/polymer nanocomposites. The dominant mechanisms that cause the piezoresistive effect in these material systems were investigated, and the Poisson's ratio of the composite was found to greatly impact the piezoresistive performance. The predictions indicated that decreasing the Poisson's ratio of the composite leads to higher strain sensitivity, which could have implications for choosing material systems for strain sensor applications.

To Gemma.

ACKNOWLEDGEMENTS

I would like to express my sincerest gratitude to my advisor, Dr. John Whitcomb, for supporting me throughout my graduate career. His experience, patience, and drive for excellence have made me a better researcher.

I would like to thank Dr. H-J Sue for serving on my committee, as well as providing access to much of the experimental data used for comparison in this work. I also thank his PhD student, Kevin White, for his insightful discussions related to this work.

I would also like to thank Dr. Dimitris Lagoudas and Dr. Mohammad Naraghi for taking time out of their busy schedules to serve on my advisory committee.

I thank my fellow graduate students, Brian Owens, Ross McLendon, Brian Lester, and Keith Ballard, for their help and support in my endeavors and for their valuable input in our discussions.

I would like to thank Ms. Jan Gerston in the Materials Science and Engineering Department for always going out of her way to help me during the most stressful times of my PhD.

Finally, I am exceedingly grateful to all my friends and family for their support during this long journey. My wife Gemma deserves an award for her encouragement, love, and generally putting up with me while I finished this work. Mom and Dad, I could not have made it this far without you. Brandon, Paul, Tom, Schick, Forrest, and everyone else: You filled this time in my life with experiences I will never forget.

This work was supported by the Clarkson Aerospace Minority Leaders Pro-

gram: Materials and Manufacturing Nanotechnology Research (Grant # FA8650-05-D-1912-TO 18). Additional support was provided by the National Science Foundation IGERT Fellowship program (Grant # 0549487).

TABLE OF CONTENTS

Page

CHAPTER Page

LIST OF FIGURES

FIGURE Page

FIGURE Page

FIGURE Page

FIGURE Page

FIGURE Page

FIGURE Page

FIGURE Page

LIST OF TABLES

NOMENCLATURE

CNT:	Carbon nanotube
SWCNT:	Single-walled carbon nanotube
MWCNT:	Multi-walled carbon nanotube
PP:	Polypropylene
RVE:	Representative volume element
Vf:	Volume fraction
FEA:	Finite element analysis
FET:	Field effect transistor
TFT:	Thin film transistor
GF:	Gauge factor
MEMS:	Microelectromechanical system
NEMS:	Nanoelectromechanical system
R:	Electrical resistance
Ω:	Ohm; Unit of electrical resistance
ρ:	Electrical resistivity
g:	Electrical conductance
σ:	Electrical conductivity
S_{ijkl}:	Interior point Eshelby tensor
G_{ijkl}:	Exterior point Eshelby tensor
ν:	Poisson's ratio
u_i:	Displacement vector

ε_{ij}:	Elastic infinitesimal strain tensor
σ_{ij}:	Elastic stress tensor
C_{ijkl}:	Elastic stiffness tensor

CHAPTER I

INTRODUCTION AND LITERATURE REVIEW

I.A. Introduction to carbon nanotube nanocomposites

Carbon nanotubes have received much attention in the materials science community since their discovery by Iijima in 1991. [1] The mechanical, electrical, and thermal properties of carbon nanotubes make them ideal candidates for reinforcements in lightweight, multifunctional composite materials. One of the more promising research avenues in this field is the idea of electrically conducting polymer nanocomposites. There have been numerous experimental studies that have shown that the addition of a low weight percentage of carbon nanotubes to a polymer matrix results in an electrically conducting material with many potential commercial applications such as electromagnetic shielding, structural health monitoring in aircraft, and flexible electronic circuit boards [2, 3, 3–5]. Another potential application involves the piezoresistive properties that have been observed experimentally in these types of nanocomposites. Piezoresistance is defined as the change in the electrical resistivity (or conductivity) of a material due to applied stress. [6,7] The resistance of a homogeneous structure is a function of both its resistivity and geometrical dimensions. Conventional wire or foil strain gauges primarily make use of the geometrical effect. For a CNT/polymer nanocomposite, however, the microscale deformation of CNT networks can significantly change the macroscopic resistivity of the material. This piezoresistive effect could enable a new class of high-strain and/or flexible strain

sensors to be developed. It is also feasible that carbon nanotubes added to traditional carbon fiber reinforced composites could be used to create self-sensing, multifunctional materials for use in aircraft and other high performance structures. [8] However, because of the small size of the nanotubes, many of the mechanisms that govern the electrical and piezoresistive response of these nanocomposites are still not completely understood.

Computational materials science aims to enhance the knowledge of these nanoscale mechanisms such that better material systems and their applications can be devised. As Gibson [9] points out, most of the publications regarding multifunctional nanocomposite materials have so far been experimental.There is a great need for more computational modeling work to interpret experimental results as well as to design and/or optimize multifunctional materials for specific applications. This is not an easy task because the nanoscale size of fillers such as carbon nanotubes sometimes necessitates large, multiscale modeling approaches in order to make the problem computationally tractable. Additionally, the effects seen at the nanoscale are not always explained by continuum modeling methods, and the size of the macroscale for relevant applications is too large to be modeled only by atomistic methods. Hence, there has been considerable interest in modeling that either bridges the gap between atomistic and continuum methods [10, 11] or is able to capture the relevant mechanisms at the nanoscale. [12, 13]

The goal of this research is to develop a framework of computational models that can predict the electrical and piezoresistive properties of carbon nanotube/polymer composites. The composites will be modeled as random networks of resistors in 2D

and 3D in order to understand the mechanisms that affect the percolative, electrical, and piezoresistive performance of different nanocomposite systems. The numerical predictions will be compared to computational and experimental results from the literature when available. Additionally, the model will be used extensively to predict the properties of 2D single-walled carbon nanotube (SWCNT) thin films and 3D multi-walled carbon nanotube (MWCNT)/polymer materials.

I.B. Literature review

In order to introduce the main topics that relate to this work, the following literature review is split into four sections. The first describes experimental and computational work from the literature that involves electrically conducting SWCNT thin films and their applications. The second section presents work from the literature dealing with electrically conducting carbon nanotube/polymer nanocomposites and their applications. The third section details work done to investigate piezoresistive effects in CNT/polymer nanocomposites. Finally, the fourth section describes work done to characterize the piezoresistive effects seen in individual SWCNTs and MWCNTs

Many of the studies detailed below reference some form of percolation theory. Percolation theory is a fairly mature subject that focuses on the probability theory of connecting clusters of objects. [14, 15] Percolation theory can be used to model critical processes that are as diverse as forest fires, oil fields, and diffusion in disordered media. Accordingly, it has been adapted to help explain why CNT networks and CNT/polymer composites exhibit sharp increases in material properties at certain

concentrations. The percolation threshold is defined herein as the nanotube concentration at which the nanotube network first becomes connected, and the associated network conductivity starts to increase drastically. Similarly, the network is said to be percolated if the nanotube concentration is greater than the percolation threshold.

I.B.1. Electrically conducting carbon nanotube thin films

Carbon nanotube thin films have received much research and commercial interest because of their unique characteristics and diverse applications. There is some ambiguity in the literature because many of the 3D nanocomposites detailed in the next section are sometimes also referred to as thin films. However, it should be understood that the thicknesses of those thin films are still much greater than the lengths of the CNTs dispersed within them. This means that the resulting nanotube networks exhibit 3D behavior. Conversely, the thin films detailed in this section are thin enough that there is essentially a single layer of CNTs lying relatively flat in the plane of the film. Therefore, herein, the distinction will be made between thin films that are thin enough to exhibit 2D network behavior and thicker nanocomposite films that exhibit 3D behavior. The following outlines work done in the literature involving 2D thin films.

One promising application for thin film carbon nanotube networks is their use as flexible field effect transistors. Snow et al. [16] investigated SWCNT networks fabricated into thin film transistors. They found that the networks behave like p-type semiconductors, and promising transistor performance was achieved without precision assembly of the nanotube networks. The authors concluded that reduction

or elimination of metallic chirality nanotubes would greatly enhance performance. Topinka et al. [17] also investigated SWCNT network field effect transistors using a combination of electric force microscopy and computer simulations. The authors identified the ratio of semiconducting and metallic chirality nanotubes as an important factor that governs the overall behavior of the CNT network. This is because when a semiconducting nanotube is in electrical contact with a metallic nanotube, a so-called Schottky barrier forms that effectively blocks current through the junction. The authors observed large variations in transistor properties for devices with identical nanotube densities and lengths. They used a 2D random resistor network model to simulate the effects of different semiconducting to metallic ratios and found that increasing the relative amount of semiconducting nanotubes decreases the variability in the device properties.

Simien et al. [18] experimentally investigated the optical and electrical properties of transparent SWCNT thin films. They found that nanotubes longer than 200 nm lead to networks with 2D percolation behavior, and shorter tubes lead to 3D percolation behavior. Networks with mixtures of long and short tubes lead to even greater 3D behavior. This comparison was based on the calculation of critical exponents based on the generalized effective medium theory put forward by McLachlan et al. [19] The authors also measured sheet conductivities that increased by six orders of magnitude through the percolation threshold.

White et al. [20] prepared single wall carbon nanotube thin films using a nanoplatelet dispersion method to precisely control nanotube dispersion. The thin films were prepared using either fully exfoliated single nanotubes or partially exfoliated

bundles of nanotubes. Transmission electron microscopy was used to confirm that the fully exfoliated thin films consisted of networks of individual nanotubes and that the partially exfoliated films consisted of bundles of 3-4 nanotubes. The electrical sheet conductivity of the thin films was measured for different concentrations of nanotubes, and the conductivity data was used to fit a power law-type percolation model. The authors found that the effect of nanotube bundling was to shift the percolation threshold to higher CNT concentrations. This was attributed to the fact that for a given CNT concentration, there are fewer conductive paths in the bundled networks. Additionally, the partially exfoliated networks exhibited higher conductivities at higher CNT concentrations because the bundles are more efficient at carrying current than individual nanotubes.

Kumar et al. [21] modeled SWCNT thin film transistors using a 2D random network and solving the associated 2D Poisson equation for electrical potential. Note that this is technically equivalent to solving a 2D random resistor network. The authors investigated the on/off current ratios of networks with various ratios of metallic/semiconducting CNTs and showed good agreement between their predictions and experimental results from the literature. The authors concluded that this type of analysis is an invaluable tool in the understanding and design of TFT devices.

Ishida and Nihey [22] used numerical simulations to investigate the device characteristics of CNT field effect transistors (FETs). They used a 2D random resistor network taking into account the ratio of semiconducting to metallic chirality nanotubes. The simulations indicated that the FET performance could be increased by either using short nanotubes or increasing the ratio of semiconducting to metallic

tubes. Li et al. [23] used similar simulations to study SWCNT thin film transistors. They also found that decreasing the number of metallic CNTs results in better transistor performance.

Kocabas et al. [24] studied SWCNT thin film FETs experimentally and computationally. The authors prepared SWCNT thin film transistors with varying degrees of alignment and concentration. The transistors were then characterized for current-voltage response and on/off current ratios. The numerical model used was a 2D stick-type percolation model similar to the work of Topinka et al. [17], but the parameters used to generate the 2D networks were based on their experimental samples. The authors found that the amount of nanotube misalignment dramatically influenced transistor performance. The also concluded that for a FET device, a slightly misaligned system is more optimal than a perfectly aligned system.

Another interesting application for SWCNT thin films is their use as electrodes in electroluminescent devices. The transparency and flexibility inherent to SWCNT thin films make them ideal candidates for this application. Wang et al. [25] experimentally optimized SWCNT thin films for use in organic light emitting diodes (OLEDs). They used a filtration process to fabricate the films and optimized the sheet conductance of the films by improving this process. The films were found to have increasing resistance with increasing transparency. This makes sense because more transparent films have less nanotubes which leads to lower conductivity. The authors also experimented with creating 3D sandwich-type structures by depositing multiple SWCNT layers on top of each other which generally increases the conductivity of the structure. They ultimately used 2- and 3-layer SWCNT films as electrodes

in OLED devices they fabricated, and the OLEDs showed promising performance. However, it is clear from their work that much more research needs to be done involving the mechanisms that affect the transport behavior of SWCNT films.

Hu et al. [26] fabricated SWCNT thin films and measured their sheet conductances and light transmittances. The films were found to show 2D percolation behavior and were 85% transparent when the sheet resistance was 1000 Ω/sq. The authors concluded that decreasing the resistance of individual nanotubes is the best way to increase device performance, but they also acknowledged that the intertube contact resistance was actually the limiting factor with respect to performance. Scardaci et al. [27] also investigated SWCNT thin films for use in electroluminescent components where the transmittance and conductance of the films are important. They found that sheet resistance increases with higher transmittance as expected. They also investigated the effect of film thickness on conductivity values and determined that conductivity degrades for films less than approximately 20 nm thick. This was attributed to the change in percolation behavior from 3D to 2D as the films became thinner. However, the thinner films understandably had the highest transmittance values.

I.B.2. Electrically conducting carbon nanotube/polymer composites

There are many studies in the literature that show that dispersing a small weight percentage of carbon nanotubes in a polymer matrix can yield a composite material with an electrical conductivity that is many orders of magnitude greater than that of the neat polymer. Ounaies et al. prepared nanocomposite films consisting of single

wall carbon nanotubes and CP2 polyimide. [2] The authors investigated the direct current (DC) and alternating current (AC) electrical properties of the films at different concentrations of nanotubes. They found a percolation-type behavior for the DC and AC electrical conductivity, and both types of conductivity increased by approximately ten orders of magnitude at the highest CNT concentration. Additionally, the AC conductivity was found to be highly dependent on frequency at low nanotube concentrations and almost independent of frequency at high concentrations. The authors also attempted to use an analytical percolation model from Balberg [28] to predict the critical volume concentration of nanotubes at percolation. However, the percolation model was only able to predict reasonable critical concentrations when the effect of nanotube bundling was taken into account. Even so, the percolation model only provides a rough approximation of the percolation behavior. The authors therefore used numerical simulations to model the percolation behavior of the composites. Cylinders representing the nanotubes were placed randomly within a cubic representative volume element (RVE) one at a time until a connecting network was formed between two opposite faces of the RVE. The cylinders were assumed to be "soft core," which means they were allowed to overlap each other. The authors claim the soft core cylinders are one reason why the predicted critical volume concentrations were higher for the numerical simulations than for the analytical predictions or experimental results. Another possible reason for the higher predicted percolation thresholds is the fact that the nanotubes were assumed to be straight instead of curved.

Potschke et al. [3] used dielectric spectroscopy to characterize MWCNT/poly-

carbonate nanocomposites. They found that the DC conductivity increased by more than ten orders of magnitude above the percolation threshold. The authors also found that increasing the mixing time of the MWCNT/PC melt could transform non-percolated systems into percolated systems if the MWCNT concentration was near the percolation threshold. They concluded that both the percolation threshold and DC conductivity were sensitive to nanotube dispersion. Similarly, Potschke et al. [29] mixed MWCNT/PC melt and blended it with polyethylene (PE) at various concentrations. They found that when the MWCNT/PC component of the blend was able to form a connecting network through the PE, composite conductivity was greatly enhanced. In this way, much smaller amounts of MWCNTs could be used to create conductive composites.

Ramasubramaniam et al. [30] fabricated SWNCT/polymer composites using a novel process to functionalize the nanotubes. The nanotubes were dispersed into polystyrene and polycarbonate matrices, and the authors claimed that the functinoalization/dispersion process could be used with a variety of commercial polymers. Additionally, electrical conductivities as high as 6.89 S/m and 481 S/m were measured for the SWCNT/PS and SWCNT/PC, respectively.

Sandler et al. [4] prepared aligned MWCNT/epoxy specimens and investigated their electrical properties using AC impedance spectroscopy. The nanotube alignment was achieved using preformed substrates with an injection CVD method. The authors measured conductivities sufficient for anti-static applications with nanotube loadings as low as 0.005 weight percent. The authors concluded that the aligned MWCNTs lead to a lower percolation threshold than nonaligned systems.

Skakalova et al. [5] measured the electrical conductivity of pristine and doped SWCNTs in a polymethylmethacrylate (PMMA) matrix. They observed that the percolation thresholds for composites with pristine SWCNTs or SWCNTs doped with $SOCl_2$ were both as low as 0.17 weight percent. However, the maximum (saturation) conductivity for the pristine SWCNT composites was approximately 17 S/cm while the doped SWCNT composites exhibited a maximum conductivity of approximately 100 S/cm. This indicates that doping carbon nanotubes can lead to higher nanotube conductivities.

Gojny et al. [31] experimentally investigated the electrical and thermal conductivities of polymer matrix composites containing different types of carbon nanotubes. Epoxy specimens with SWCNTs, MWCNTs, double-wall CNTs, or carbon black were fabricated and characterized. The authors concluded that MWCNTs provide the greatest enhancement of both electrical and thermal conductivities, although the thermal enhancement was minimal. The better performance of the MWCNTs was attributed to relatively low CNT surface area as well as high aspect ratio.

Hu et al. fabricated nanocomposites using MWCNTs dispersed in an epoxy matrix. [32] They investigated the effects of several fabrication parameters such as mixing speed, curing process, etc. on the electrical properties of the nanocomposites. The effects of these parameters were found to be very complex and dependent upon the geometry of the specimens. However, the nanocomposites still showed an improvement of nearly eight orders of magnitude in the electrical conductivity. The study presented convincing evidence that while sensitive to processing conditions, there is a large design space available for tailoring the electrical properties of

nanotube reinforced epoxies to specific applications.

Via et al. [33] prepared carbon black/polycarbonate, MWCNT/polycarbonate, and graphite nanoplatelet/polycarbonate specimens and measured their electrical conductivities. They used several analytical models, including McLachlan's GEM model [19, 34], and compared their effectiveness in describing the composite conductivity below, at, and above the percolation threshold. They concluded that the GEM model had the best agreement with experiment over the 16 orders of magnitude in electrical conductivity.

There are many numerical and analytical models in the literature that attempt to analyze and predict the percolation threshold or electrical properties of carbon nanotube/polymer composites. Many approaches were actually developed long before the discovery of carbon nanotubes. In particular, the use of a power law to fit conductivity data as a function of nanotube concentration has been used extensively by researchers in this field. [2, 3, 15, 20] The general idea is to fit the data to a power law and then deduce properties of the material from the resulting fitting parameters. Balberg and coworkers [28, 35] developed one of the earliest percolation models that was based on an excluded volume approach and could predict the percolation threshold of random systems with various kinds of inclusions. The model attempted to distill the percolation behavior of a Balberg and Binenbaum [36] also investigated the cluster structure and conductivity exponent in 3D continuum systems. Balberg [37] reviewed progress made in applying continuum percolation theory to real systems such as porous media, doped semiconductors, and composite materials. In light of much experimental data that seemed to contradict percolation

theory, Balberg [38] showed that the exponent used to fit percolation power laws was not as universal as many researchers previously thought. McLachlan extended and re-interpreted the power law form for the percolation conductivity, and his work has been cited extensively as well. [19, 34] McLachlan et al. later used a modified form of this model to explain the AC and DC electrical conductivity behavior in SWCNT/polymer composites. [39]

Many researchers have sought to explain the effects of electron tunneling between filler particles. Rubin et al. [40] used a tunneling-percolation model to investigate the electrical conductivity of carbon black/polymer composites. The critical percolation exponents for the samples were measured experimentally and compared them to predictions from the model. The authors concluded that the experimental results for the CB/polymer specimens confirmed the validity of the tunneling-percolation model. Later, Toker et al. [41] used conductance atomic force microscopy measurements to explain why percolation theory is able to explain behavior in composites with electron tunneling. They concluded that the tunneling is limited to nearest neighbor interactions which gives rise to standard percolation behavior.

Pike and Seager were among the first researchers to use a numerical Monte Carlo model to predict the percolation threshold of random-lattices. [42] They defined the percolation threshold as the filler concentration at which filler clusters first form an infinite connecting network. Networks of 2D "sticks" were one type of lattice geometry they considered, and many researchers have since used similar approaches to predict percolation thresholds of 2D and 3D networks of sticks. Balberg and others also used numerical Monte Carlo methods to simulate the percolation behavior of

2D and 3D "stick" networks. [43,44] The numerical predictions were used to validate the excluded volume approach. Balberg et al. [45] used a computational model to investigate the effects of aspect ratio and macroscopic anisotropy on the percolation threshold of a randomly oriented 3D stick system. They concluded that the excluded volume of the sticks determines the dependence of the percolation threshold, and the orientational randomness has a stronger effect in 3D than in 2D.

Kirkpatrick developed one of the first random resistor network models. [46] Resistors were placed randomly within 2D and 3D RVEs, and the resulting network was solved for resistor voltages using the Kirchoff current law. This allowed the effective electrical conductances of the networks to be calculated. While the resistor placement was limited to sites on square and cubic lattices, this work has proven fundamental to many investigations into the electrical conductivity of carbon nanotube networks and carbon nanotube/polymer composites.

Hu et al. predicted the percolation threshold and electrical conductivity of carbon nanotube/polymer nanocomposites using a 3D random resistor model. [13] Both single wall and multi-wall nanotubes were considered. The model consisted of soft core nanotubes, which again means that the tubes were allowed to penetrate each other. The authors point out that this does introduce some error in their predictions, but they claim the error is negligible due to the high aspect ratio and low volume content of the nanotubes. The percolation threshold was predicted by adding nanotubes randomly to the 3D RVE until a connective pathway between assumed electrodes was achieved. Once the network reached percolation, the electrical conductivity of the network was calculated by solving the associated network of resistors. Note that

the conductivity could not be solved for before the network has reached percolation because an open circuit exists between the electrodes in that case. The authors used this model to investigate the effects of nanotube aspect ratio, conductivity, agglomeration, and curvature on the predicted percolation threshold and effective composite conductivity. They found that curved nanotubes cause higher percolation thresholds and lower conductivities. Also, aggregates were found to increase the percolation threshold and reduce the composite conductivity.

Ward and Spanos et al. used a thorough Monte Carlo method in conjunction with a quasi 3D resistor network model to predict the electrical conductivity of nanocomposites. [47, 48] The model used features of the Monte Carlo method that Spanos and Kontsos [49] developed to determine the mechanical properties of CNT/polymer composites. The model was also very similar to the work of Hu et al. [13, 32] except that the resistor network was actually modeled in 2D, and a thickness was assumed for the network in order to calculate an effective conductivity. A distinguishing feature of this work is that probability density functions were used to model the variation in nanotube lengths and diameters. A Weibull distribution was used for the nanotube lengths and a log-normal distribution was used for the diameters. This allowed a more realistic representation of the nanocomposites than simply using average values. The results obtained compared well to experiment, but it was unclear if the same techniques applied to a fully 3D model would yield even better predictions.

Seidel and Lagoudas [50] developed a micromechanics model to investigate the effect of electron hopping on the electrical conductivity of CNT/polymer nanocomposites. They used a composite cylinders model with a continuum interphase layer

that approximated the electron tunneling that occurs between nanotubes. A Mori-Tanaka averaging scheme was used to obtain effective conductivities of nanocomposites with randomly distributed and oriented nanotubes. Both single-wall and multi-wall carbon nanotubes were modeled and the predicted nanocomposite conductivities were compared to experimental results from the literature. The model was able to qualitatively predict a percolation threshold that was influenced by electron hopping, but the quantitative predictions did not match well with experiment. Their results indicate that simple micromechanics averaging techniques alone may not be sufficient for quantitatively predicting the effective conductivity of CNT/polymer nanocomposites.

Rahatekar et al. [51] used a dissipative particle dynamics (DPD) method to investigate the percolation thresholds of mixtures of fibers and spheres. Mixtures of long and short fibers were also studied, and the results were discussed in terms of optimizing the transport properties of carbon nanotube networks. The authors concluded that if long fibers are aligned to some degree, then shorter fibers or spherical particles can enhance the transport properties of the system.

I.B.3. Piezoresistance of polymer nanocomposites

As electrically conducting nanotube/polymer composites have drawn more research activity, there has been increased interest in the piezoresistive properties observed in these materials. As defined previously, piezoresistance is the change in the electrical resistivity of a material due to applied stress. [6, 7] Wichmann et al. investigated electrically conductive MWCNT/epoxy and carbon black/epoxy nan-

ocomposites for potential use in strain sensing applications. [52] They found that both types of nanocomposites demonstrated distinct piezoresistive behavior when subject to an applied strain field. The MWCNT/epoxy composite was found to exhibit a nearly linear relationship between electrical conductivity and strain in the elastic regime. Conversely, the carbon black/epoxy nanocomposites were found to have a more exponential relationship between conductivity and strain. The authors explained the different behaviors of the composites in terms of the different particle geometries. Additionally, the authors attempted to use a simple analytical model to gain quantitative information about the morphology of the conducting networks, but it was apparent that the networks were too complex for this approach to be accurate. Computational modeling is probably required to represent the network structures accurately.

Rizvi et al. studied the compressive piezoresistive behavior of composites consisting of polydimethyl-siloxane (PDMS) or polyethylene (PE) filled with MWCNTs. [53] They found that the MWCNT/PDMS composites exhibited higher conductivity than the PE composites, even though large aggregates of MWCNTs were observed throughout the PDMS composites. However, when the compressive piezoresistances of the nanocomposites were measured, the better dispersed PE composites were found to be more sensitive to stress. The authors also performed viscoelastic stress relaxation experiments on the two types of nanocomposites. Using a three element Maxwell model, they were able to capture the stress relaxation behavior and compare it to the resistance signal. It was found that the PDMS composites exhibited a resistance decay that was three times higher than the stress relaxation,

while the resistance decay in the PE composites was in proportion with the stress relaxation. It was hypothesized that the difference in resistance decay was due to the more compliant PDMS matrix, which allows the CNT network to be more easily disrupted by the rearrangement of polymer chains due to stress. However, more experimental and computational studies would need to be conducted in order to validate this claim.

Kang et al. investigated the piezoresistive sensitivity of SWCNT/polyimide nanocomposites for a wide range of SWCNT weight fractions. [54] They measured the piezoresistive strain coefficients (also known as the gauge factor) and the piezoresistive stress coefficients of nanocomposites at various CNT weight fractions using both surface sensing and through-thickness modes. The surface measurements were conducted in tension, and the through-thickness tests were in compression. Both tests were done using cyclic loading. It was found that a CNT weight fraction (0.05 weight %) just above the percolation threshold produced the highest piezoresistive coefficients. The highest piezoresistive gauge factor observed was 4.21, which is twice as high as that of most metal strain gauges but still much lower than other experimental studies with this type of material system. The piezoresistive sensitivity was attributed to the change in intertube tunneling distances because the data was able to be fit by an exponential function. This study was significant because it showed that measuring the piezoresistive coefficient in surface sensing and through-thickness modes can achieve similar results.

Park et al. experimentally studied the piezoresistive response of MWCNT/polyethylene oxide composite films. [55] They observed a unique and repeatable piezore-

sistive effect for the nanocomposite at different volume fractions of MWCNT. The change in resistance as a function of applied strain was found to be linear at small strains and nonlinear beyond some critical value of strain (usually around 0.1% strain). The authors hypothesized that in the linear region, the nanotubes maintained overlapping contact during loading, and they were able to fit the response with an analytical percolation-based theory. The nonlinear region was assumed to be caused by the tunneling resistance between nanotubes once the high levels of strain caused the overlapping nanotube contacts to be lost. A piecewise resistance change model was put forth that captured the linear and nonlinear regions reasonably well for strain levels up to approximately 7% strain.

Hu et al. used a 3D random resistor network model to predict the electrical and piezoresistive properties of MWCNT/polymer composites. [56,57] They incorporated the effect of electron tunneling between nanotubes through the use of an exponential cutoff function originally derived by Simmons. [58] This means that nanotubes do not have to be in physical contact in order to form an electrical connection. If the shortest distance between the nanotubes was less than the cutoff distance, a tunneling resistor was created to connect the nanotubes, and the exponential cutoff function was used to calculate the resistance of this resistor. They also used the fiber re-orientation model from Taya et al. [59] to model the reorientation of the nanotubes under an applied strain field. This allowed the effective resistance of the resistor network to be calculated as a function of applied strain. It should be noted that the individual nanotubes were assumed to be perfectly rigid. The authors also noted that simply allowing the nanotube network to break up and

reorient did not result in a statistically significant change in resistance. However, when the tunneling effect was included, a definite nonlinear response was predicted. The authors also fabricated and tested a MWCNT/epoxy strain sensor to validate the numerical predictions, and good qualitative agreement between the experimental sensor and numerical predictions were observed.

Building on the work of Hu et al., Yin et al. fabricated MWCNT/epoxy strain sensors using a different type of MWCNT that had a much smaller diameter than the MWCNTs used in Hu et al. [60] The change in resistance vs. strain for this new MWCNT/epoxy sensor was found to be surprisingly linear. The sensors were tested both statically and dynamically, and the gauge factors were calculated to be approximately 4-5 for all MWCNT concentrations and both tensile and compressive loading. This is a smaller gauge factor than that seen with the larger MWCNTs in Hu et al, but because the response was linear and non-hysteretic, the authors claimed that this material system was more suited to strain sensing applications. The authors also claimed that the different piezoresistive behavior was due to the piezoresistance of the nanotubes themselves, rather than the change in intertube tunneling distances. However, more experimental and computational studies are needed to verify this claim.

Oliva-Aviles et al. [61] prepared MWCNT/polysulfone films. Polysulfone (PSF) is a thermoplastic polymer with high thermal stability and low moisture absorption properties. The authors used an alternating electric current to align the nanotubes while the polymer crystallized. Thin films with non-aligned, random MWCNTs were also prepared for comparison. The authors found that the electrical conductivity of

the aligned films (in the longitudinal direction of the aligned CNTs) was 3-5 orders of magnitude higher than that of the randomly oriented nanocomposites. This was attributed to the increase in electron flux that occurs in the alignment direction at the expense of conductivity in the other directions. The authors also investigated the piezoresistive behavior of the thin films. They found that the aligned MWCNT networks resulted in higher gauge factors than the randomly oriented networks. Additionally, the piezoresistive response was found to be linear and could be repeated over several loading-unloading cycles.

Kang et al. prepared conducting rubber composites consisting of MWCNTs and organo-clay particles embedded in ethylene propylene diene M-class rubber (EPDM). [62] Very high weight fractions of up to 50% MWCNTs were used. These flexible composites showed increased tensile strength, stiffness, and electrical conductivity with increasing amounts of MWCNTs. Upon application of an applied load, the authors claimed the composites exhibited a non-symmetric linear piezoresistive effect. However, the results shown in the paper do not seem to show a linear relationship between resistance change and applied strain. Additionally, the "non-symmetric" qualifier seems to be referring to the fact that resistance was seen to increase with both tensile and compressive strains. This is the exact opposite terminology used by Yin et al. [60], and it is an indication that there is still some confusion over correct terminology in the field.

Srivastava et al. experimentally investigated the strain sensing behavior of well dispersed MWCNT/polystyrene composite films with MWCNT weight fractions between 1%-10%. [63] They observed a linear response between applied load and mea-

sured resistance at small and high levels of applied strain. The highest gauge factor of 3.28 was observed for the 6 wt.% composite, and the gauge factors decreased with further increases in MWCNT concentration. The results appeared to be very similar to the results obtained by Yin et al. [60]

Theodosiou and Saravanos used multiscale numerical models to investigate the mechanisms affecting the piezoresistive properties of nanotube/polymer composites. [64] They first used a nanoscale model consisting of the tight binding approximation the Landauer formula, and either the Wentzel-Kramers-Brillouin or Miller-Good approximations. This model allowed the calculation of the electronic band structure and electrical resistance of nanotubes of varying chirality at varying levels of applied load. Moving up to the microscale, the authors used a shear-lag model to predict the load transfer from the polymer matrix to a single carbon nanotube. This was then used to predict the change in resistance of the nanotube as a function of its orientation angle with respect to the far-field applied strain. Finally, 2D and 3D networks of randomly placed nanotubes were used to model the percolation behavior of the nanocomposites when subjected to an applied strain field. Interestingly, the authors did not use the random 2D and 3D networks to calculate the effective conductivity of the nanocomposites. Instead, only the probability of percolation and number of conducting paths were predicted as functions of nanotube volume fraction and applied strain level. All of this information was used to predict a linear piezoresistive effect that is dominated by nanotube resistance and the tunneling effect between nanotubes. Additionally, the authors predicted that nanocomposites with nanotubes oriented in the direction of the applied load would be more sensitive

than nanocomposites with randomly dispersed nanotubes.

Lu et al. [65] fabricated MWCNT/PDMS nanocomposite specimens and characterized their piezoresistive performance for use in microelectromechanical system (MEMS) devices. They found that the specimens exhibited piezoresistive gauge factors ranging from 1.38 to 12.4, depending on CNT weight fraction. The CNT weight fraction ranged from 4% to 25%, and the highest gauge factors were achieved at 18%. The authors concluded that despite the high cost of carbon nanotubes, the material system could be used to produce inexpensive MEMS pressure sensors.

Dang et al. [66] prepared MWCNT/silicone rubber disks and measured the piezoresistive response when compressive stress was applied to the disk faces. Surprisingly, the authors observed a positive piezoresistive pressure coefficient when the disks were loaded under compression. This means that the resistance of the disk actually increased when a compressive load was applied. The authors attributed this unusual behavior to break up of the CNT network and an increase in inter-tube distance when the load was applied. Note that this is the same reasoning used by many other researchers to explain the increase in resistance when a specimen is loaded in tension. The authors did not calculate a gauge factor, so the sensitivity of the specimens could not be compared to other experimental data from the literature.

Thostenson and Chou [67] were able to use MWCNTs embedded in traditional glass fiber/epoxy composites for in situ damage progression and health monitoring. Similarly, Gao et al. [68] demonstrated the sensing of impact damage evolution using carbon nanotube networks dispersed in a glass fiber/epoxy composite. The authors were able to establish correlations between the composite resistance change, absorbed

energy, accumulated acoustic emissions, and damage area. Li et al. [8] highlighted the promising performance characteristics of these types of in situ sensing materials, but they also pointed out that much more experimental and analytical research is needed to fully realize the benefits of these materials.

Loh et al. [69] fabricated piezoresistive strain sensors using a layer-by-layer method. Thin films consisting of layers of SWCNT/polyelectrolyte were created with varying combinations of SWCNT concentration, polyelectrolyte concentration, and film thickness. The sensors were able to be tailored to achieve desired sensing characteristics, but the associated gauge factors were were only between 0.1-1.8. In addition to piezoresistive sensors, the authors also used the composites as capacitive strain sensors which resulted in linear strain sensors that could be coupled to RFID chips.

Pham et al. [70] fabricated MWCNT/PMMA composite thin films and measured the piezoresistive response to the specimens under applied tensile load. The authors found that surface resistivity increased proportionally with increasing applied strain, which was attributed to an increase in inter-tube tunneling distances. They also found that higher concentrations of nanotubes resulted in lower sensitivity sensors. Near the percolation threshold, however, gauge factors as high as 15 were measured.

I.B.4. Piezoresistance of individual carbon nanotubes

In addition to the piezoresistive response that occurs due to the changing carbon nanotube network structure, the nanotubes themselves have been shown to exhibit piezoresistive properties. Stampfer et al. [71–73] showed this experimentally with

single wall carbon nanotubes. They were able to achieve gauge factors of up to approximately 2900 using a doubly clamped nanotube subjected to bending from an atomic force microscopy (AFM) probe. Additionally, they predicted the piezoresistive response of a SWNT using a strain dependent band gap model in conjunction with a thermal activated transport model. They found that the piezoresistive response of the nanotubes depends greatly on the chiral angle and nanotube family. A direct comparison was not made between their experimental and computational results because the exact type of nanotubes used in the experiments was unknown. Hierold et al. [74] discussed ways that these highly sensitive SWCNTs could be integrated into nanoelectrocmechanical systems (NEMS), but they point out that improvements in the control and reproducibility of CNT growth is needed to make NEMS sensor devices a reality.

Grow et al. investigated the piezoresistance of SWCNTs by fabricating two-terminal nanotube devices on silicon nitride membranes. [75] Single semiconducting nanotubes were deposited between palladium electrodes and the conductances of the nanotubes were measured while the pressure applied to the membrane was varied from 0-15 psi. Additionally, finite element analysis was used to calculate the strain distribution in the membranes, and atomic force microscopy was used to measure the nanotube diameter and orientation with respect to the electrodes. The strains applied were found to range from 0-0.2%. From this data, the authors were able to calculate the gauge factors of the devices to be up to 400 for plain semiconducting nanotubes and up to 850 for short-gap semiconducting nanotubes. This is clearly better performance than the maximum gauge factor of 200 for silicon based

strain sensors. This study illustrates that individual carbon nanotubes can exhibit a piezoresistive effect even under small strains.

Similar to the studies already presented, Cao et al. investigated the electrical conductances of metallic, quasimetallic, and semiconducting SWCNTs as functions of applied axial strain. [76] They found that for small strains the quasimetallic nanotubes exhibited a gauge factor of 600-1000. This is again much higher than the gauge factor for silicon strain gauges. Conversely, the metallic nanotubes were the least sensitive with gauge factors ranging from 40-60. While there are currently few experimental studies such as this, the results obtained thus far show potential for utilizing the inherent piezoresistive effect in nanotubes. However, in order to take advantage of this effect in nanotube/polymer composites, the interface between nanotube and polymer must be strong enough to transfer the applied load from polymer to nanotube. It is unclear from the literature if this is yet possible.

I.C. Objectives

As stated previously, the overarching goal of this work is to develop a framework of computational models that can predict the electrical and piezoresistive properties of carbon nanotube/polymer nanocomposites. A random resistor network approach will be used to develop several models in 2D and 3D, and parametric studies will be performed to investigate the effects of various assumptions on model predictions. There are three main objectives that will be considered, and each objective will attempt to improve the fundamental understanding of a material system behavior beyond what is currently found in the literature. A summary for each objective is

given below.

1. **Predict the electrical properties of SWCNT thin films.** Implementing a random resistor network in two dimensions is much easier than beginning with a fully 3D model. Thus, the first objective is to implement a 2D random resistor network to predict the electrical conductivities of SWCNT thin films. Thin films made up of highly exfoliated single nanotubes (no bundles) and networks of partially exfoliated bundles of nanotubes will be investigated. A Monte Carlo approach will be used to statistically analyze the properties of hundreds of random networks at varying SWCNT volume fractions. The chirality of individual nanotubes, as well as contact resistances between nanotubes will be taken into account. Additionally, the results will be compared to experimental results from the literature. The effects of nanotube exfoliation, chirality, and intertube tunneling on thin film conductivity will be explored. The model predictions can then be used to advance the understanding of dominant mechanisms that affect applications such as field effect transistors and optoelectronic components.

2. **Predict the electrical properties of CNT/polymer nanocomposites.** After implementing a 2D nanotube network model, a fully 3D random resistor model will be developed using lessons learned from the 2D model. The 3D model will be used to predict the electrical conductivity of MWCNT/epoxy and MWCNT/polypropylene nanocomposites that have been experimentally investigated in the literature. With the explosion of interest in electrically conducting polymers, it is useful to have a computational model that can illuminate and verify experimental results. The effects of nanotube resistivity, electron tunneling between CNTs, con-

tact resistance, and CNT size on composite conductivity will be investigated, and dominant mechanisms influencing conductivity will be identified.

3. **Predict piezoresistive properties of CNT/polymer nanocomposites.** The 3D resistor network model will be modified to include the effects of nanocomposite piezoresistivity. The elastic deformation of the network at different levels of applied strain will be predicted, and the effective conductivity of the deformed network will be calculated. To predict elastic deformation of the networks, a uniform strain model used in the literature will be implemented and compared to a new hybrid FEA/Eshelby model that incorporates elastic interaction between nanotubes. The models will be used to predict piezoresistive properties for the MWCNT/epoxy and MWCNT/PP nanocomposites, which could prove to be useful materials in strain sensing applications. The predictions will be compared to experimental results in the literature. The dominant mechanisms that cause the piezoresistive effect in these material systems will be investigated, and the potential for using the nanocomposites in strain sensing applications will also be evaluated.

CHAPTER II

THEORY

The purpose of this chapter is to present the theoretical details of the various models that were developed to investigate carbon nanotube networks. The modeling was done in both 2D and 3D. Models to predict the percolation threshold, electrical conductivity, and piezoresistive response were developed. Note that some of the more specific implementation details for various algorithms used or developed in this work are given in Chapter III.

II.A. 2D nanotube network model

A random resistor network approach was used to model the SWCNT thin films. In the model developed, nanotubes are added one at a time to a 2D square RVE at random positions and orientations as shown in Figure II.1a. The positions and orientations are sampled from a uniform distribution using a Mersenne Twister random number generator. [77] The Mersenne Twister number generator was chosen for its speed and efficiency in generating high quality pseudorandom numbers. In addition, the random number generator is used to assign each nanotube a chirality of metallic or semiconducting as it is added to the RVE. The ratio of metallic to semiconducting SWCNTs is taken from the literature to be 1:3. [17] When each SWCNT is generated, a random number on the interval [0,1.0] is sampled from a uniform distribution. The CNT is flagged as metallic if the number is less than 0.33 or semiconducting if the number is greater than or equal than 0.33. This results in a uniformly random

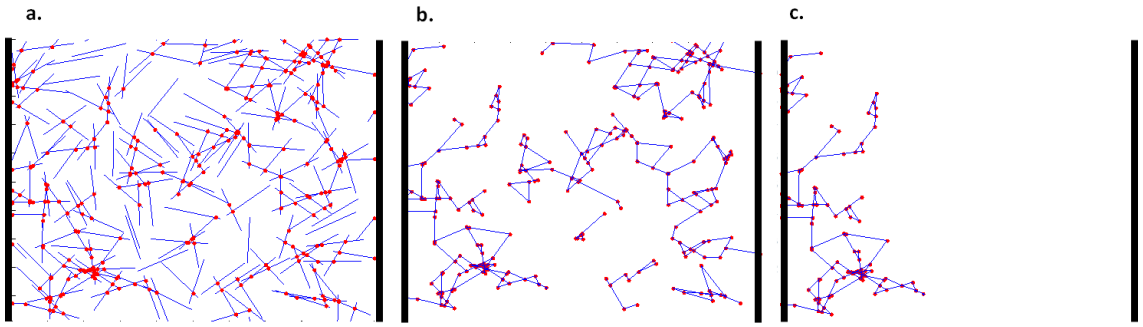

Figure II.1. Nanotube network creation process. Black bars represent electrodes.

distribution of SWCNTs that are approximately 1/3 metallic.

When enough nanotubes are added for a specific concentration, the intersections between nanotubes (shown as red dots in Figure II.1) are searched for and mapped using an efficient kd-tree searching algorithm (see Chapter III). Clusters of disconnected nanotubes are removed (Figure II.1b) from the network. Note that removal of the disconnected clusters is necessary because of the finite element method used to solve the resistor network. The resulting system of equations is singular if there are any nanotubes that are not connected to either the electrodes or the network backbone. After removing disconnected nanotubes, the remaining nanotubes are checked to see if they create a a spanning network that connects the left and right electrodes of the RVE (Figure II.1c). This is done by starting at the left electrode and looping through all connected nanotubes until either the right electrode is reached or the list of connected nanotubes is exhausted. If the nanotubes form a spanning network, the network is said to be at or beyond the percolation threshold. Note that the network shown in Figure II.1c does not form a spanning network, so it can be concluded that the network volume fraction is below the percolation threshold.

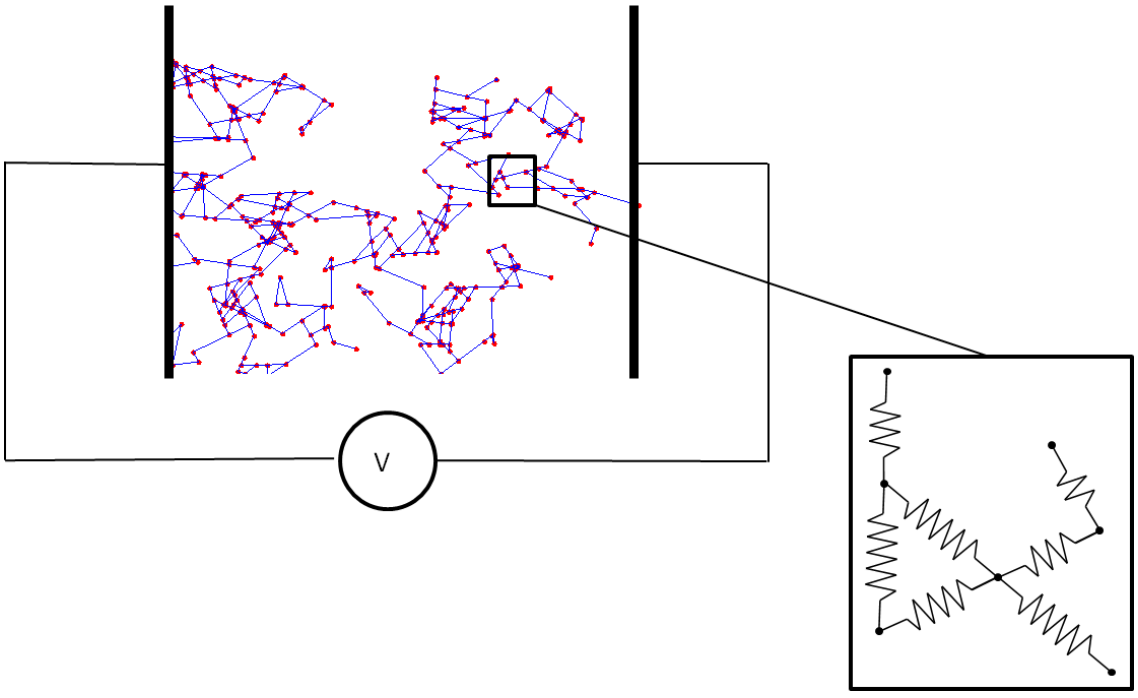

Figure II.2. Reduction to equivalent resistor network.

If a spanning, percolated network is found, the network is then reduced to an equivalent resistor network. Each nanotube segment between two intersection points is assumed to be an Ohmic resistor as shown schematically in Figure II.2. Additionally, at each junction between nanotubes, a resistor is inserted to simulate the contact resistance between nanotubes. The junction resistance for the 2D model (seen in Figure II.3) can be thought of as a point resistor with zero length.

Once an equivalent network of resistors has been mapped, a finite element framework is used to analyze the resistor network. As shown in Reddy [78], finite element equations can be derived for an electrical resistor using Ohm's law and Kirchoff's voltage rule. Ohm's law for an ideal resistor like the one in Figure II.4 is given as

$$\Delta V = IR, \tag{2.1}$$

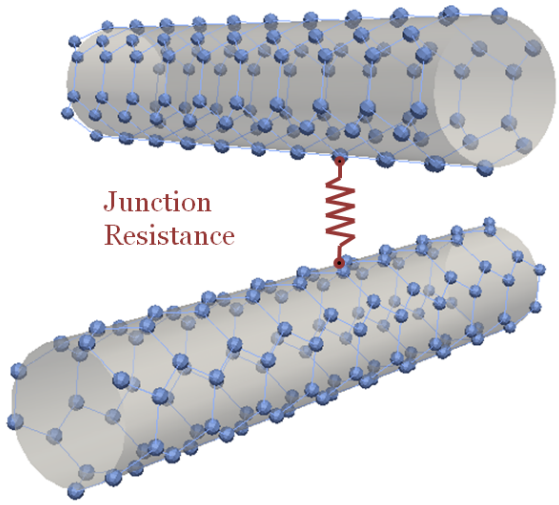

Figure II.3. Diagram of junction resistance inserted between nanotubes at junction points.

where ΔV is the voltage drop (in volts) between ends of the resistor, I is the current through the resistor (in amperes), and R is the electrical resistance (in ohms) of the resistor.

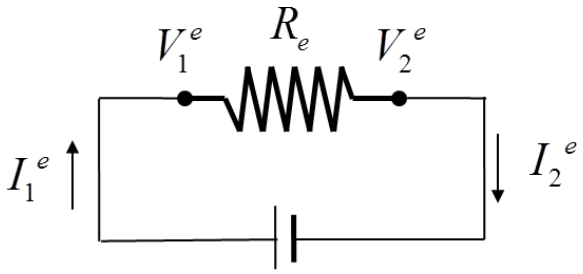

Figure II.4. Finite element formulation for an electrical resistor.

Kirchoff's voltage rule states that the sum of voltage drops along any circuit

loop must be zero. Applying this rule to the resistor in Figure II.4 gives

$$
\begin{aligned}
{I_1}^e R_e + {V_2}^e - {V_1}^e &= 0 \\
{I_2}^e R_e + {V_1}^e - {V_2}^e &= 0.
\end{aligned} \tag{2.2}
$$

Equation 2.2 can be further expressed in matrix form as

$$
\frac{1}{R_e}\begin{bmatrix} 1 & -1 \\ -1 & 1 \end{bmatrix}\begin{Bmatrix} {V_1}^e \\ {V_2}^e \end{Bmatrix} = \begin{Bmatrix} {I_1}^e \\ {I_2}^e \end{Bmatrix}. \tag{2.3}
$$

Note that the element equations for a resistor are analagous to the element equations for a spring. Once the element equations in Equation 2.3 are calculated for each resistor in the network, the resistor equations are assembled into a global system of equations using a standard finite element assembly algorithm. The assembly process for resistors can also be thought of as applying Kirchoff's current rule to all nodes or junctions in the network. Kirchoff's current rule states that the sum of all currents entering and exiting a node is equal to zero.

Once the global system of equations is assembled, boundary conditions are applied. The boundary conditions can be either applied currents or applied voltages. For the resistor network model, the boundary conditions are a zero V potential applied to the left electrode and a 10 V potential applied to the right electrode. The voltages at all nodes in the network are then solved for using an Intel®MKL conjugate gradient solver with Jacobi preconditioning. Knudsen and Fazekas [79] discussed other methods for solving random resistor networks, but they found that a conjugate gradient solver usually performs as well as other, more specialized resistor network methods.

Some post-processing must be done to calculate the element currents and effective resistance of the network. The element currents are calculated by substituting the two nodal voltages for each resistor into the element equations in Equation 2.3. The current through the resistor element can then be solved for, and this is repeated for all of the resistors in the network. After calculating the element currents, an effective resistance (or inversely, conductance) is calculated for the network. The calculation of the effective network resistance is based on the idea that the total network current passes through each electrode. Therefore, for the total number of nodes n that are on an electrode, the nodal currents (I_i) are summed via

$$I_{total} = \sum_{i=1}^{n} I_i \ , \tag{2.4}$$

where I_{total} is equal to the total current passing through the electrode. Since this current also represents the total network current, the effective network resistance (R_{eff}) can be found using Ohm's law

$$R_{eff} = \frac{V_{total}}{I_{total}}, \tag{2.5}$$

where V_{total} is the applied potential difference between the electrodes. It should be noted that it makes no difference which electrode is chosen to sum the currents on. The total currents on each electrode should be equal and opposite in sign. This is actually a good computational check for the model. If the total currents are calculated on both electrodes and they are not equal and opposite, there is clearly something wrong with the model. It should be noted that the software used to create the nanotube networks, reduce to equivalent resistor networks, create finite element meshes from the resistor networks, and solve the system of equations is written

in parallel to take advantage of multi-processor computer systems. The parallel programming was done using the OpenMP API. [80]

The material properties used to model carbon nanotube networks play a critical role in the model's efficacy. Unfortunately, the properties associated with carbon nanotubes and their composites vary greatly in the literature. The electrical conductivity of SWCNTs and MWCNTs has been measured experimentally [17, 81, 82], but there is still much uncertainty in the data. Much of the variability is due to the variability of carbon nanotubes themselves. Different CNT growth procedures and conditions results in a wide variety of nanotube sizes and properties. It should also be noted that electrical conductivity is a continuum material property that is being used to describe an atomistic structure, which may not always be valid. The conductivity σ for a material specimen with uniform cross section can be defined as

$$\sigma = g\frac{L}{A} = \frac{L}{RA}, \tag{2.6}$$

where g is the conductance of the material specimen, L is the specimen length, R is the specimen resistance, and A is the cross sectional area of the specimen. The units of conductivity are Siemens per meter (S/m). Also note that for Ohmic materials, the resistance R and conductance g are defined as

$$R = \frac{1}{g} = \frac{\Delta V}{I}. \tag{2.7}$$

The units of resistance are Ohms (Ω), and the units of conductance are Siemens (S). Similarly, the resistivity, ρ, of a material is the inverse of conductivity, or

$$\rho = R\frac{A}{L}. \tag{2.8}$$

The units of resistivity are Ohm-meters ($\Omega - m$). It should be noted that the terms conductivity/resistivity and resistance/conductance are frequently used interchangeably in the literature. However, it should be repeated that conductivity and resistivity are material properties that do not depend on the size or shape of a given block of material. Conversely, resistance and conductance are measures of a given specimen's ability to carry current, and they depend on the size and shape of the specimen.

The conductivity of a single carbon nanotube is determined experimentally by measuring its resistance, length, and cross sectional area. The conductivity is then calculated using Equation 2.6. However, while the length of the nanotube is easily measured, the cross sectional area is not so easily determined. Figure II.5 shows that the cross section of a carbon nanotube is actually an atomistic structure with no clear definition of a cross sectional area. An assumption for the cross sectional area must be made in order to calculate a conductivity, but as Figure II.5 shows, there are several assumptions that can be made. Many researchers choose to assume the area of a solid cylinder [56], but it may actually be more appropriate to assume a hollow cylinder that has some given thickness. Of course, the latter assumption means that a cylinder thickness must also be assumed which is not easy given that the actual nanotube is made up of individual atoms that do not touch each other. Additionally, the conductivity assuming a solid cylinder will be less than that assuming a hollow cylinder. Thus, when looking at measured CNT conductivities in the literature, it is necessary to understand the assumptions made to calculate these values.

One way to avoid the problems associated with measuring nanotube conductivity is to simply not calculate it. Because the nanotube is an atomistic structure, it can

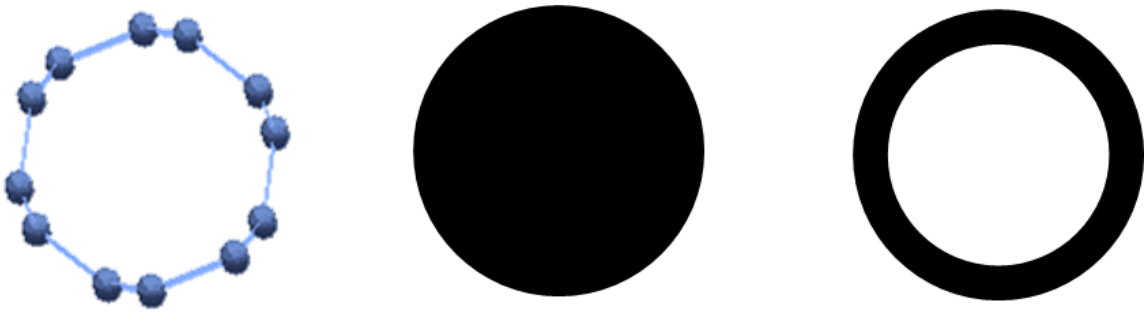

Figure II.5. Different approximations of CNT cross sections.

be argued that only the CNT resistance per unit length needs to be measured. For the purposes of investigating the electrical behavior of nanotube networks, this is the only parameter that is needed to model the nanotubes. Each resistor element has an associated resistance that is a function of the element length. However, because CNT conductivity is used so frequently in the literature, the conductivities are calculated herein assuming a solid cylinder cross sectional area.

It should be noted that there is a large variation of CNT conductivities and resistivities reported in the literature. The resistivities of various sized MWCNTs were measured by Hobara et al. [81] to be 1.0×10^{-3} to 2.0×10^{-2} $\Omega \cdot cm$. Topinka [17] measured the resistance per unit length for SWCNTs to be 13 $k\Omega/\mu m$. Kaneto et al. [82] also measured MWCNT conductivities to be 1000-2000 S/cm which results in a resistance per length of 2-30 $k\Omega/\mu m$. The associated resistance per unit length used in the this work is 1.3×10^{10} Ω/m for both semiconducting and metallic SWCNTs.

In addition to the nanotube resistivity, the contact resistance at junctions between individual CNTs was modeled. The chirality of each nanotube was taken into account by assigning appropriate contact resistances at junctions between different

combinations of nanotubes. The different junction resistances are taken from experimental values in the literature. Fuhrer et al. [83] measured the contact resistance between two metallic SWCNTs to be 2.0×10^5 Ω. The contact resistance at junctions between two semiconducting SWCNTs was measured to be approximately 2.36×10^6 Ω. Fuhrer also showed that Schottky barriers form at the junctions between semiconducting and metallic SWCNTs. A Schottky barrier is a quantum mechanical effect that causes a high contact resistance at the junction between a semiconducting and metallic material. Thus, when a Schottky barrier forms between semiconducting and metallic SWCNTs, the resulting contact resistance between the two SWCNTs is several orders of magnitude greater than the metallic-metallic or semiconducting-semiconducting contact resistances, and very little current flows through this type of junction. The contact resistance used for metallic-semiconducting junctions in the model is 1.0×10^{10} Ω. Additionally, the Schottky barrier between a metallic and semiconducting SWCNT has been shown to modulate current flow throughout the entire semiconducting SWCNT. Therefore, for every metallic-semiconducting junction in the model, the resistance of the semiconducting tube is set to 1.0×10^{10} Ω in order to inhibit current flow. This is very similar to the approach used by Topinka [17].

One of the main objectives of the 2D network investigation is to understand the relationship between nanotube exfoliation and network percolation behavior. Note that herein, nanotube exfoliation refers to the level of dispersion of CNTs, where a network of fully exfoliated CNTs does not exhibit any agglomeration or bundling. Thus, the model has to be capable of representing single nanotubes as well as partially exfoliated bundles. The single nanotubes are simply represented by individual

resistor elements. Similarly, each nanotube bundle is represented by a single resistor element, but the bundle is assumed to contain one metallic and two semiconducting SWCNTs. In this way, the only differences between the highly exfoliated and partially exfoliated networks are the material properties used to describe the resistors and the number of resistors needed to describe the networks at a specific concentration. It is assumed that the resistance per unit length of the bundle is 1.3×10^{10} Ω/m. Note, however, that the junction resistance between bundles of partially exfoliated nanotubes was initially chosen somewhat arbitrarily to be 2.0×10^{5} Ω because there are currently no experimental measurements for this value in the literature. The junction resistance was chosen to be the same as the resistance between metallic nanotubes. This is assumed to be the lowest possible resistance between bundles of nanotubes, and the actual resistance is probably higher. Parametric studies were performed to investigate the validity of this assumption, and the results are given in Chapter IV.

Because the nanotube networks are created randomly, there is inherent statistical fluctuation between different realizations of the same RVE with the same nanotube concentration. Therefore, many unique realizations must be generated and solved in order to find some statistical average of the effective resistance. This Monte Carlo type of approach has been proven to work well when dealing with randomly oriented microstructures. [17, 47–49].

II.B. 3D nanotube network model

In order to predict the electrical conductivity of carbon nanotube/polymer nanocomposites, the 2D random resistor network model was extended to a 3D network model. While many of the same methods are used, the computational requirements for the 3D model are much greater than the 2D model. Individual nanotubes are idealized as straight cylinders and placed randomly in a 3D cubic RVE as seen in Figure II.6. The CNT positions are sampled from a uniform distribution using a Mersenne Twister random number generator. However, unlike the 2D model, the orientation angles cannot simply be sampled from a uniform distribution. In order to obtain a truly uniform distribution of orientations, a specialized method utilizing the statistical properties of normal deviates was used. [84] Details of this method and how it is applied to the carbon nanotube orientations are given in Chapter III.

After filling the 3D RVE with the required number of CNTs for a given volume fraction, the junctions between nanotubes are then searched for and mapped such that the state of contact between nanotubes can be ascertained. The procedure to search for contact and tunneling junctions between nanotubes uses an efficient kd-tree algorithm that is an extension of the algorithm used for the 2D model. Details of this algorithm are given in Chapter III. The nanotubes are assumed to be in contact if the cylinders are touching, but non-contacting nanotubes within a specified cutoff distance of each other are assumed to have a tunneling junction resistance. The CNTs are considered "soft-core," which means that the cylinders are allowed to overlap. This does introduce some error into the model, but other researchers [13, 56] have shown that this error can be small. Additionally, developing a model

that incorporates non-overlapping, "hard-core" nanotubes is quite complex. The computational requirements increase drastically because finding voids in the RVE to place cylinders without touching other cylinders already in place is extremely difficult at meaningful volume fractions. Much of the difficulty is due to the high aspect ratio of the CNTs and the fact that they cannot bend. Also, even if a completely non-overlapping network is achieved, the resulting microstructure is highly dependent on the algorithm used to generate the network and may not be representative of the actual microstructure. Thus, while hard-core CNT networks should definitely be investigated in future works, they will not be pursued further herein.

In addition to mapping all junctions between nanotubes, the network backbone must be mapped so that a valid system of FEA equations can be obtained. Two opposing faces of the RVE are assumed to be electrodes, and all nanotubes connected to one electrode are flagged during CNT generation. The nanotubes attached to these initial connected nanotubes are then searched for, and the process is repeated until all connected nanotubes between the electrodes are found. Figure II.6 illustrates a percolated network with a backbone of connected nanotubes that span the gap between the electrodes. The two electrodes are the positive and negative X-faces of the RVE, and all connected nanotubes are highlighted in yellow.

Once all of the contact and tunneling junctions are mapped, the network is approximated as an equivalent network of resistors as shown in Figure II.7. Interestingly, the equations used to model the 2D resistor networks (Equation 2.3) can be used for the 3D resistor network. All CNTs that are not connected to the network backbone are discarded so that a non-singular system of equations can be assembled.

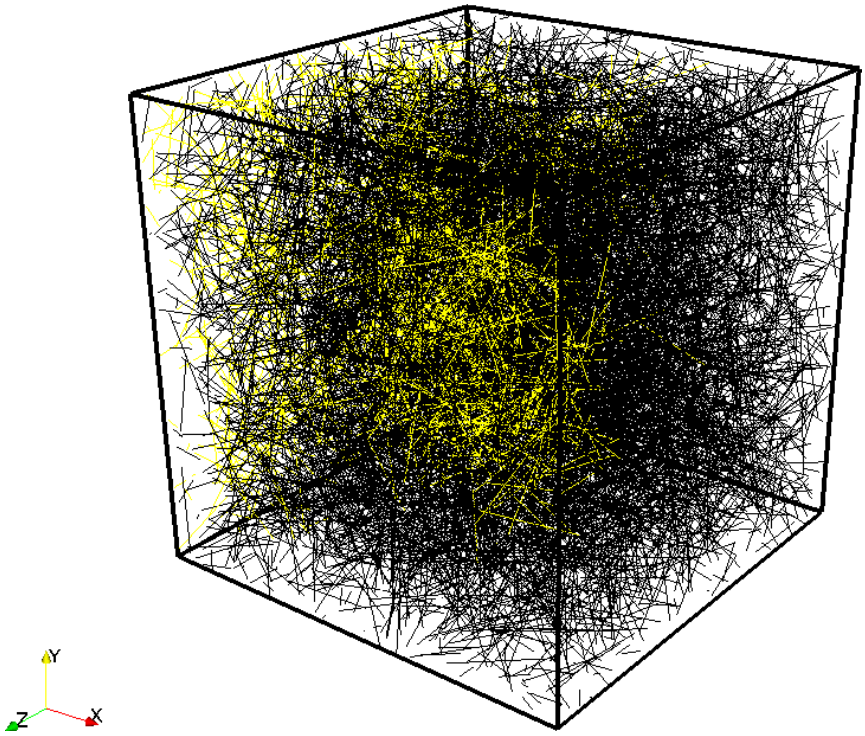

Figure II.6. Representative volume element for 3D nanotube network.

The boundary conditions consist of zero potential on the negative X-face electrode and 10.0 volts on the positive X-face electrode. All other faces are assumed to be insulating. The nodal voltages, element currents, and effective resistance of the resistor network can then be solved for using the same finite element approach used for the 2D network model. Refer to Section II.A for details relating to the solution and postprocessing procedures. Figure II.7 shows the results of a network analysis. Electrical currents are highlighted in color, and it is clear from this that the network forms a conductive path between the two electrodes.

Just like the 2D model, the material properties of CNTs greatly affect the validity of the 3D model. Unlike the 2D network model, the chirality of CNTs is not taken

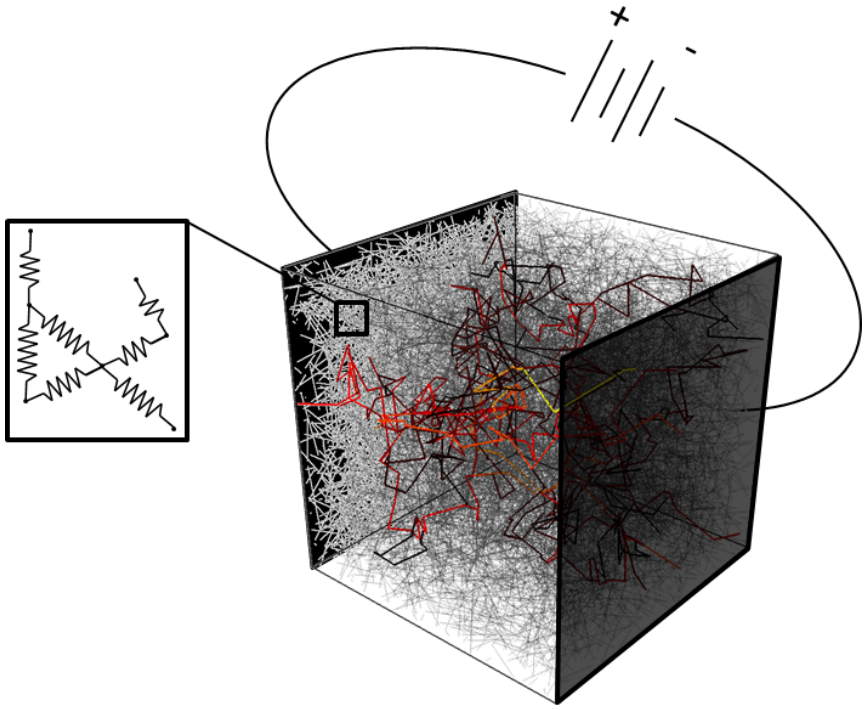

Figure II.7. Representative volume element approximated as resistor network with potential gradient applied to electrodes. Resistor currents are highlighted in color.

into account for the 3D model. This is because the material systems investigated contain MWCNTs instead of SWCNTs. The chirality of MWCNTs is ambiguous because of their multiple layers of carbon. However, the model could easily be extended in the future to model SWCNT/polymer composites. The conductivity of the MWCNTs used is assumed to be the same as the SWCNTs in the 2D model. The MWCNT resistance per unit length is thus $1.3 \times 10^{10}\ \Omega/m$.

If two cylinders are in contact, a contact resistance is assumed between the cylinders, which is similar to the junction resistances used in the 2D network model. The contact resistance is initially assumed to be 200 $k\Omega$ which is the contact resistance measured between two metallic SWCNTs by Fuhrer et al. [83]. Even though MWC-

NTs are modeled here, it can be reasonably assumed that this contact resistance is the lowest possible resistance between MWCNTs.

Recall that with the soft-core cylinder assumption, CNTs considered in contact include any CNTs that overlap each other by any amount. However, if the two cylinders are not in contact but are within a specified tunneling distance of each other, an electron tunneling resistance is inserted between the cylinders. The tunneling junction resistances are calculated using an exponential function similar to the ones used in Hu et al. [56] and Ward. [47] This function was first derived by Simmons [58] and is given in Equation 2.9. Equation 2.9 is a solution to the Schroedinger equation using the Wentzel-Kramers-Brillouin (WKB) approximation. The WKB approximation is a method commonly used in quantum mechanics to find approximate solutions to linear partial differential equations. The resistance R in Equation 2.9 is the tunneling resistance between two similar electrodes separated by a thin insulating film. Additionally, V is the voltage potential between the electrodes, A is the cross sectional area of the tunnel, J is the current density through the tunnel, h is Planck's constant, d is the distance between the electrodes, e is the quantum of electricity, m is the mass of an electron, and λ is the height of the potential barrier. The cross sectional area of the tunneling current is generally not known, but it is approximated in the model as the solid cross sectional area of the CNT. This is a reasonable assumption that yields the correct order of magnitude for the tunneling resistance, and this assumption can also be found in the literature. [13, 56] Another assumption made throughout this work is the value for λ. Hu et al. claim the range for the tunneling barrier height of epoxy is 0.5-2.5 eV, so $\lambda = 2.0$ is used herein for both epoxy and polypropylene.

The barrier height for polypropylene is expected to be similar, and the model was not found to be very sensitive to the barrier height in the given range.

$$R = \frac{V}{AJ} = \frac{h^2 d}{Ae^2\sqrt{2m\lambda}} \exp\left(\frac{4\pi d}{h}\sqrt{2m\lambda}\right) \tag{2.9}$$

Figure II.8 schematically illustrates how Equation 2.9 is used within the nanotube network model. The matrix resistance is plotted as a red line, and the variation of tunneling resistance with distance between CNTs is in blue. For clarity, the figure does not show the actual plot of Equation 2.9. For any pair of CNTs that are in contact with each other, the junction resistor between them is assigned the contact resistance value. For any pair of CNTs that are not in contact but are closer than the tunnel cutoff distance, the junction resistor between them is assigned a resistance that is calculated from Equation 2.9. Any pairs of CNTs that are further apart than the tunneling cutoff distance are not connected.

Because many of the material properties for CNTs are uncertain and vary greatly in the literature, it is generally expected that the model must be calibrated to each material system using experimental data. The assumed CNT properties provide a good baseline, but values for contact resistance, CNT resistivity, and CNT size can be adjusted to obtain effective conductivities that match experiment. This approach is valid because the many different CNT/polymer material systems in the literature all have unique characteristics that relate to these calibration parameters. Contact resistance is affected by the type of CNT used as well as the wettability of that particular nanotube in each polymer. Nanotube resistivity is obviously related to the type or "brand" of CNTs used, and the distribution of lengths in any given

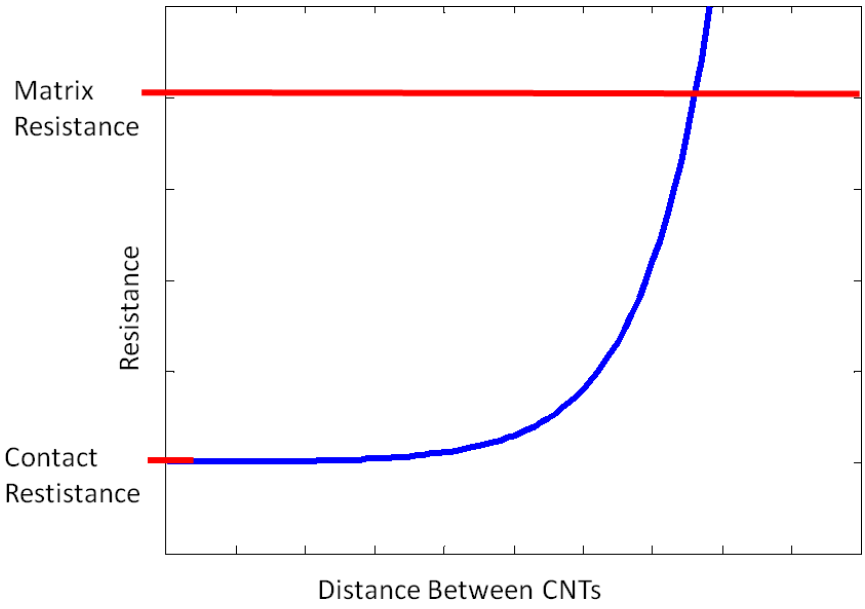

Figure II.8. Plot of exponential relationship of tunneling junction resistance as a function of distance between nanotubes.

batch of CNTs is usually not known to a high level of precision. Additionally, by calibrating the model to each material system, these uncertain characteristics of the experimental material specimens can be inferred.

II.C. Piezoresistance of 3D networks

This section outlines the models that were used to investigate the piezoresistive properties of 3D carbon nanotube/polymer nanocomposites. The general modeling approach involves using the 3D model from Section II.B to predict the electrical conductivity of a mechanically unloaded nanocomposite as a function of nanotube concentration. The deformation of the nanotube network is then modeled at incremental levels of applied strain, and the conductivity at each strain increment is calculated. Before each strain increment, all junctions between CNTs are discarded

because network deformation alters the distances between all CNTs. After each strain increment, the junctions between CNTs are again searched for and mapped using the methods described in Section II.B, and the resulting finite element equations are solved. The effective conductivity at each strain increment is then calculated and used to calculate the piezoresistive properties of the material.

The piezoresistive perfomance of a material can be expressed in several different ways. Many recent studies of piezoresistive CNT/polymer materials use a normalized change in resistance to describe the piezoresistvity. [54–56,61] The normalized change in resistance is defined as the change in resistance ΔR normalized by the resistance of the specimen at zero strain R_0. This can be expressed as

$$\frac{\Delta R}{R_0}. \tag{2.10}$$

In addition to the change in resistance, the piezoresistive gauge factor (GF) is commonly used to describe the strain sensing performance of a specimen. [85, 86] The gauge factor is defined in terms of the normalized change in resistance as

$$GF = \frac{\Delta R}{R_0 \varepsilon}, \tag{2.11}$$

where ε is the applied strain. Another important definition of the gauge factor can be derived by starting with the resistance R of a wire of constant cross section which is expressed as

$$R = \frac{\rho L}{A}. \tag{2.12}$$

Taking the natural logarithm of both sides of the equation yields

$$\ln R = \ln \rho + \ln L - \ln A. \tag{2.13}$$

Taking the derivative with respect to the applied strain ε gives

$$\frac{1}{R}\frac{\partial R}{\partial \varepsilon} = \frac{1}{\rho}\frac{\partial \rho}{\partial \varepsilon} + \frac{1}{L}\frac{\partial L}{\partial \varepsilon} - \frac{1}{A}\frac{\partial A}{\partial \varepsilon}. \tag{2.14}$$

Replacing the differentials with small, finite increments yields

$$\frac{\Delta R}{R_0} = \frac{\Delta \rho}{\rho_0} + \frac{\Delta L}{L_0} - \frac{\Delta A}{A_0}. \tag{2.15}$$

As noted in Yarnell [87], for a homogeneous, isotropic material, the area and length terms can be approximately related via

$$\frac{\Delta A}{A_0} \approx -2\nu\frac{\Delta L}{L_0}, \tag{2.16}$$

where ν is the Poisson ratio of the material. Thus, Equation 2.15 can be rewritten as

$$\frac{\Delta R}{R_0} \approx \frac{\Delta \rho}{\rho_0} + \frac{\Delta L}{L_0}(1 + 2\nu). \tag{2.17}$$

Rearranging terms and substituting $\varepsilon = \frac{\Delta L}{L_0}$ (and noting that most authors drop the approximation sign for small strains) yields the alternate expression for the gauge factor

$$GF = \frac{\Delta \rho}{\rho_0 \varepsilon} + 1 + 2\nu, \tag{2.18}$$

where $\Delta\rho$ is the change in the material's resistivity, ρ_0 is the resistivity under zero strain, and ν is the Poisson ratio of the material. It should be noted that a conventional metallic foil strain gauge has a GF of approximately two, but this type of strain gauge does not make use of the piezoresistive effect. The metals used in most metallic strain gauges do not exhibit a significant change in resistivity as they deform. Rather, the change in geometry of the metallic gauge under applied load is the sole cause of the gauge's change in resistance. These geometric effects are also

present in the CNT/polymer materials, but the resistivity of material changes under applied load as well. Hence, it is easy to imagine that these combined effects can yield higher gauge factors than metallic strain gauges.

The crux of the piezoresistivity model outlined thus far is the way in which the CNT network deformation under applied load is predicted. The deformation must be modeled accurately in order to predict accurate piezoresistive performance. Note that network deformation does not necessarily mean deformation of individual CNTs. The purely rigid body motion and reorientation of nanotubes can cause network deformation and result in piezoresistance. Two types of models are used in this work to predict the CNT network deformation when a load is applied to the composite RVE. The first is similar to the model used in Hu et al. [56], and it assumes a uniform strain distribution throughout the entire RVE. Additionally, the CNTs are assumed to be completely rigid bodies. This model is easy to implement, but it neglects the local elastic perturbations in the matrix due to the presence of the individual nanotubes. These local perturbations might be extremely important in predicting accurate piezoresistive properties because the piezoresistive effect in these material systems is thought to be mainly due to the small changes in tunneling distance between individual pairs of nanotubes. Thus, the second piezoresistivity model attempts to take some of these local, elastic effects into account using a hybrid FEA/Eshelby micromechanics framework. Details of the two models are given in the following sections.

II.C.1. Uniform strain piezoresistivity model

The first piezoresistivity model assumes a uniform strain field in the nanocomposite. Additionally, the individual CNTs are assumed to be rigid bodies that only undergo rigid body translation and rotation. A schematic representing how the CNT network deforms using the uniform strain model with an applied strain field is given in Figure II.9, where ε is the applied strain and ν is the assumed Poisson's ratio of the nanocomposite.

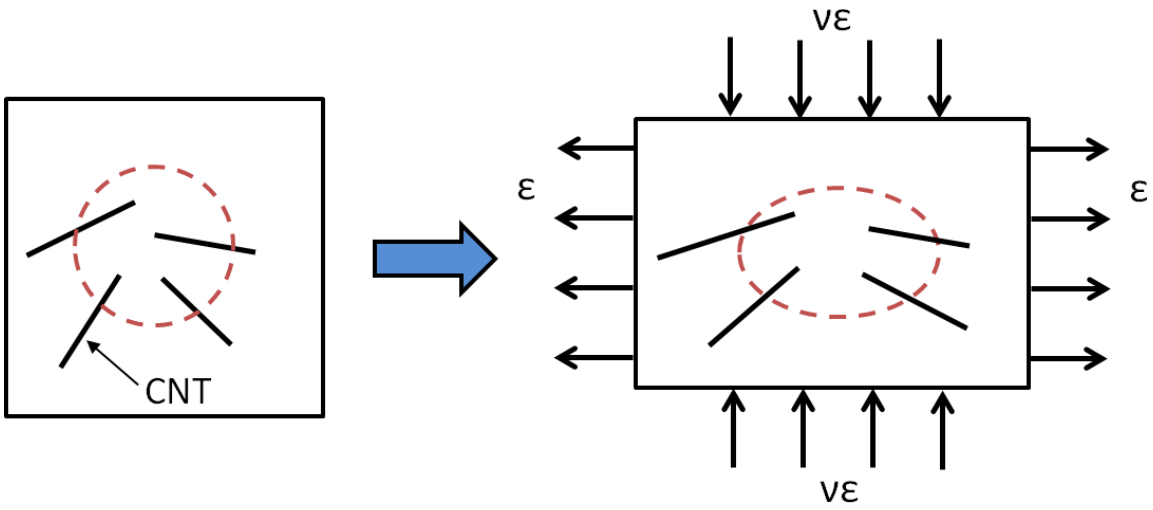

Figure II.9. Schematic showing uniform strain piezoresitive model.

Rigid body motion is a reasonable assumption because the nanotubes are much stiffer than the polymer matrix that surrounds them. The uniform strain assumption means that for a given applied strain state, the displacements at all points in the nanocomposite can easily be calculated directly from

$$u_i = u_i^0 + \varepsilon_{ij} x_j, \tag{2.19}$$

where ε_{ij} is the applied uniform strain field and u_i^0 is the initial displacement. However, note that applying Equation 2.19 directly to the end points of a given nanotube results in stretching of the nanotube. It has been shown in the literature that for most current material systems, the mechanical interface between CNTs and polymer matrix is not strong enough to allow for this type of induced stretching. Therefore, the displacements calculated above must be modified such that the CNTs only exhibit rigid body motion. This is done by using Equation 2.19 to calculate the new coordinates of the endpoints and center of each CNT. The center point is then fixed, and the endpoints are rescaled along the cylinder's axis until the CNT is back to its original prestretched length. Including the scaling step makes the uniform strain model equivalent to the piezoresistivity models in Taya et al. [59] and Hu et al. [56] that use an affine transformation to reorient the nanotubes. An affine transformation is simply a translation of a rigid body followed by a linear transformation. It should be noted that omitting the scaling step results in significant differences in network percolation and conductivity. This has interesting implications for material systems with strong CNT/polymer interfaces that facilitate good load transfer to the nanotubes.

II.C.2. Hybrid FEA/Eshelby piezoresistivity model

In order to incorporate the local elastic effects due to CNTs in the polymer matrix, a novel piezoresistivity method was formulated based on the well known Eshelby equivalent inclusion method for ellipsoidal inhomogeneities. [88] This method and its derivatives have been used extensively in the field of micromechanics to

develop models like the Mori-Tanaka model [89] that predict effective properties of composite materials. However, most of these micromechanics models do not make use of the equivalent inclusion method's ability to determine the elastic fields outside of an ellipsoidal inclusion. There has been work extending the Eshelby problem to nano-inhomogneities [90], and that approach does calculate the exterior elastic fields. The piezoresistivity model introduced in this work uses a hybrid FEA/Eshelby equivalent inclusion framework to calculate the elastic fields outside each nanotube in a 3D network subject to an applied strain state. The elastic fields can then be used to calculate the positions of the nanotubes in the reoriented network. While this framework was developed specifically for the piezoresistivity model used in this work, it is likely that the framework could be used to solve other problems of interest in micromechanics.

II.C.2.a. Eshelby equivalent inclusion method

A summary of the equivalent inclusion method will now be presented in order to set up the theoretical background for the hybrid framework. Consider an ellipsoidal domain Ω embedded in an infinite domain D as shown in Figure II.10. The elastic material properties in Ω are denoted by C^*_{ijkl}, and the properties in $D-\Omega$ are denoted by C_{ijkl}. Both C_{ijkl} and C^*_{ijkl} can be anisotropic.

Using the definitions from Eshelby [88, 91] and Mura [92], the domain Ω is referred to as an inclusion if $C^*_{ijkl} = C_{ijkl}$ or an inhomogeneity if $C^*_{ijkl} \neq C_{ijkl}$. Eshelby derived the solution for the elastic fields in and around an ellipsoidal inclusion, but the fields for an ellipsoidal inhomogeneity are more difficult to obtain. Thus, the

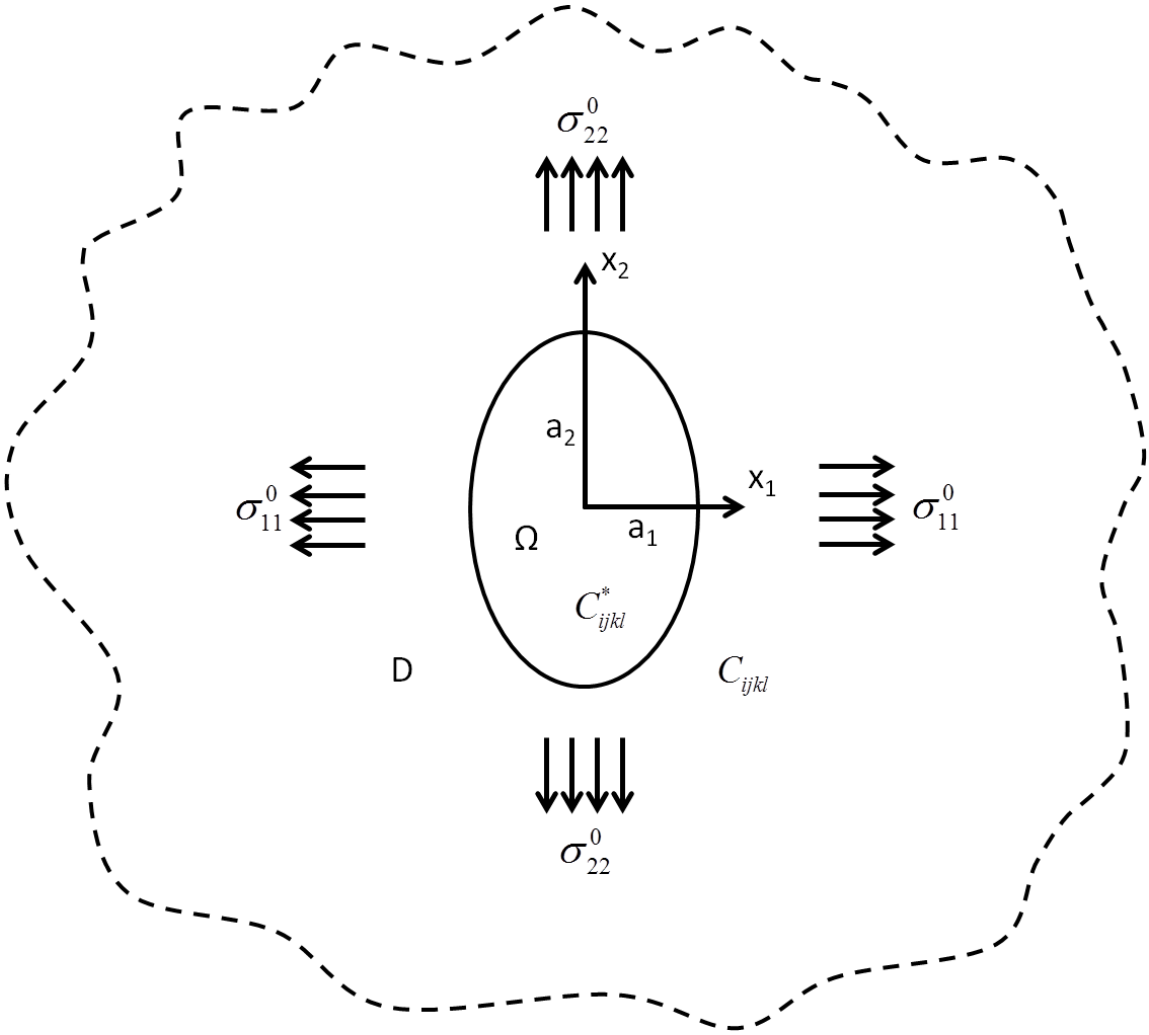

Figure II.10. Ellipsoidal domain with stress field applied at infinity.

equivalent inclusion method accounts for the elastic disturbance of an inhomogeneity by using the eigenstrain that results from an equivalent inclusion in Ω. An eigenstrain is defined by Mura as "a generic name given to such nonelastic strains as thermal expansion, phase transformation, initial strains, plastic strains, and misfit strains." It should be noted that Eshelby referred to eigenstrains as stress-free transformation strains. An ellipsoidal inhomogeneity and its equivalent inclusion are shown in Figure II.11.

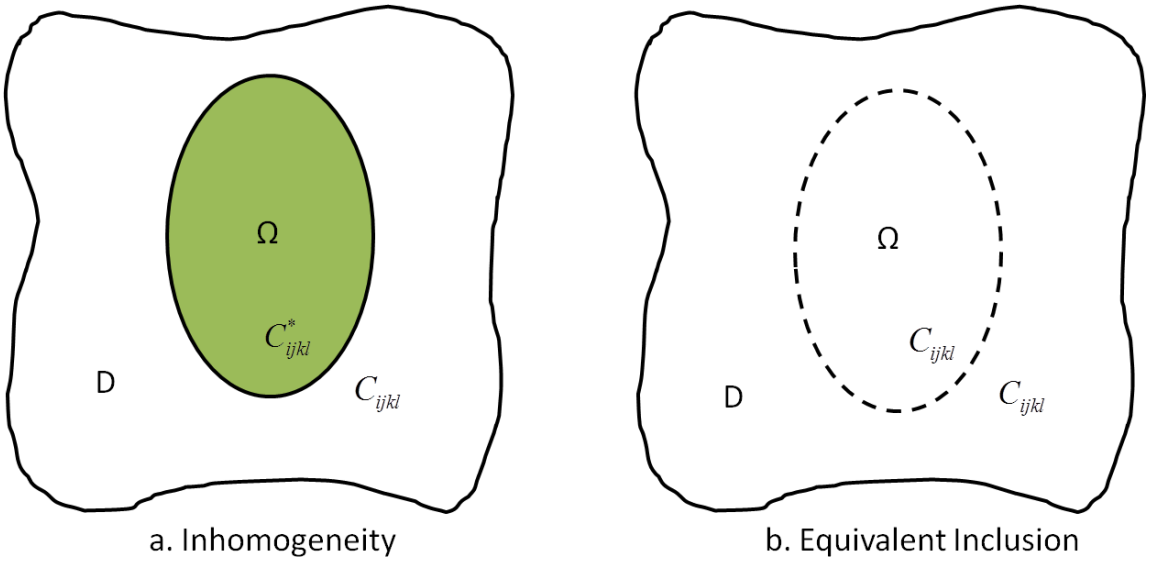

Figure II.11. Schematic of an ellipsoidal inhomogeneity and its equivalent inclusion.

For the inhomogeneity in Figure II.11a, assume the domain is subject to a far-field applied stress σ^0_{ij} and corresponding strain ε^0_{ij}. The stress and strain disturbances due to the presence of the inhomogeneity are denoted by σ_{ij} and ε_{ij},

respectively. The stress σ_{ij}^t and strain ε_{ij}^t are

$$\begin{aligned}\sigma_{ij}^t &= \sigma_{ij}^0 + \sigma_{ij} \\ \varepsilon_{ij}^t &= \varepsilon_{ij}^0 + \varepsilon_{ij}.\end{aligned} \tag{2.20}$$

Herein, σ_{ij}^t and ε_{ij}^t are referred to as the total stress and total strain, respectively. The stresses are in equilibrium in the body, and there are no body forces. This is expressed as

$$\sigma_{ij,j}^t = 0. \tag{2.21}$$

The kinematic equations are given by

$$\varepsilon_{ij}^t = \frac{1}{2}\left(u_{i,j} + u_{j,i}\right). \tag{2.22}$$

Hooke's law for the inhomogeneity problem can be written piecewise as

$$\begin{aligned}\sigma_{ij}^0 + \sigma_{ij} &= C_{ijkl}^*(\varepsilon_{kl}^0 + \varepsilon_{kl}) \text{ in } \Omega \\ \sigma_{ij}^0 + \sigma_{ij} &= C_{ijkl}(\varepsilon_{kl}^0 + \varepsilon_{kl}) \text{ in } D - \Omega.\end{aligned} \tag{2.23}$$

Now, consider the inclusion problem that is equivalent to the above inhomogeneity problem. An inclusion is embedded in an infinite body as shown in Figure II.11b, and σ_{ij}^0 is applied at infinity. The inclusion has the same geometry as the inhomogeneity, but the material properties are the same as the infinite body ($C_{ijkl}^* = C_{ijkl}$). Unlike the inhomogeneity problem, assume there is an eigenstrain ε_{ij}^* in Ω. This fictitious eigenstrain, called an equivalent eigenstrain, is used to simulate the inhomogeneity via the inclusion problem. The total strain, $\varepsilon_{ij}^t = \varepsilon_{ij}^0 + \varepsilon_{ij}$, is represented in Ω by the sum of the elastic strain ε_{ij}^e and the (nonelastic) eigenstrain ε_{ij}^*, or

$$\varepsilon^0_{ij} + \varepsilon_{ij} = \varepsilon^e_{ij} + \varepsilon^*_{ij} \text{ in } \Omega. \tag{2.24}$$

The elastic strain in the inclusion is then given by

$$\varepsilon^e_{ij} = \varepsilon^0_{ij} + \varepsilon_{ij} - \varepsilon^*_{ij} \text{ in } \Omega, \tag{2.25}$$

and Hooke's law for the inclusion problem can then be written as

$$\begin{aligned} \sigma^0_{ij} + \sigma_{ij} &= C_{ijkl}(\varepsilon^0_{kl} + \varepsilon_{kl} - \varepsilon^*_{kl}) \text{ in } \Omega \\ \sigma^0_{ij} + \sigma_{ij} &= C_{ijkl}(\varepsilon^0_{kl} + \varepsilon_{kl}) \text{ in } D - \Omega. \end{aligned} \tag{2.26}$$

In order to guarantee the mathematical equivalence of the inhomogeneity and inclusion problems, assume that the two problems are subject to the same total strain $\varepsilon^t_{ij} = \varepsilon^0_{ij} + \varepsilon_{ij}$ and equate Equation 2.23 and Equation 2.26 to obtain the so-called equivalency relation in Equation 2.27. This relation guarantees the equivalence of the total stresses inside the inhomogeneity and its equivalent inclusion. Thus, the solution for the inhomogeneity problem can be obtained from the solution for the equivalent inclusion. Recall that the terms in parentheses on the left and right hand sides of Equation 2.27 represent the elastic strains in the inhomogeneity and inclusion, respectively. The equivalency relation does not guarantee the equivalence between the elastic strains in the inhomogeneity and inclusion, and in general, they are not equivalent.

$$C^*_{ijkl}(\varepsilon^0_{kl} + \varepsilon_{kl}) = C_{ijkl}(\varepsilon^0_{kl} + \varepsilon_{kl} - \varepsilon^*_{kl}) \text{ in } \Omega \tag{2.27}$$

It should be pointed out that all terms in Equation 2.27 are known except ε_{ij}, the strain in Ω due to the presence of the inhomogeneity, and ε^*_{ij}, the equivalent

eigenstrain. In order to be able to solve the equation for ε_{ij}^*, ε_{ij} must be found. Fortunately, ε_{ij} can be expressed as

$$\varepsilon_{ij} = S_{ijkl}\varepsilon_{kl}^*, \tag{2.28}$$

where S_{ijkl} is the so-called interior point Eshelby tensor. The Eshelby tensor can be derived for any ellipsoidal domain, but the components are functions of elliptic integrals that do not reduce to closed form solutions for general ellipsoids with anisotropic material properties. However, if isotropic material properties are assumed, the elliptic integrals do reduce to simple closed form functions for certain ellipsoidal shapes such as spheres, spheroids, and elliptic cylinders. Additionally, Eshelby [88] proved that for an isotropic, ellipsoidal inhomogeneity with a uniform applied stress σ_{ij}^0, the equivalent eigenstrains, and therefore the interior stress and strain fields, are always uniform.

In this work, infinite, circular cylinders are used to approximate the geometry of carbon nanotubes, so the Eshelby solution for these shapes are utilized. However, the Eshelby solution for a sphere is also used in order to illustrate the capabilities of the FEA/micromechanics framework. The components of the interior point Eshelby tensor for a sphere with isotropic material properties is given in Equation 2.29, where ν is the Poisson's ratio of the matrix.

$$\begin{aligned} S_{1111} &= S_{2222} = S_{3333} = \frac{7-5\nu}{15(1-\nu)} \\ S_{1212} &= S_{2323} = S_{3131} = \frac{4-5\nu}{15(1-\nu)} \\ S_{1122} &= S_{2211} = S_{3311} = S_{1133} = S_{2233} = S_{3322} = \frac{5\nu-1}{15(1-\nu)} \end{aligned} \tag{2.29}$$

All other components of $S_{ijkl} = 0$. Equation 2.30 shows Equation 2.28 in contracted,

matrix notation for clarity. Note especially the factors of two in the vector representing ε^*_{ij} and the lack thereof in the vector representing ε_{ij}. This is not a typographical error; it is a result of the derivation of S_{ijkl}. These factors can be a source of confusion because there is significant variation in the literature on how S_{ijkl} is derived. Some texts include the two on the shear terms in ε_{ij} while others "bury" the two inside the components of S_{ijkl}.

$$\begin{bmatrix} \varepsilon_{11} \\ \varepsilon_{22} \\ \varepsilon_{33} \\ \varepsilon_{12} \\ \varepsilon_{31} \\ \varepsilon_{23} \end{bmatrix} = \begin{bmatrix} S_{1111} & S_{1122} & S_{1133} & 0 & 0 & 0 \\ S_{2211} & S_{2222} & S_{2233} & 0 & 0 & 0 \\ S_{3311} & S_{3322} & S_{3333} & 0 & 0 & 0 \\ 0 & 0 & 0 & S_{1212} & 0 & 0 \\ 0 & 0 & 0 & 0 & S_{3131} & 0 \\ 0 & 0 & 0 & 0 & 0 & S_{2323} \end{bmatrix} \begin{bmatrix} \varepsilon^*_{11} \\ \varepsilon^*_{22} \\ \varepsilon^*_{33} \\ 2\varepsilon^*_{12} \\ 2\varepsilon^*_{31} \\ 2\varepsilon^*_{23} \end{bmatrix} \tag{2.30}$$

Substitution of Equation 2.28 into the equivalency relation in Equation 2.27 results in

$$C^*_{ijkl}(\varepsilon^0_{kl} + S_{klmn}\varepsilon^*_{mn}) = C_{ijkl}(\varepsilon^0_{kl} + S_{klmn}\varepsilon^*_{mn} - \varepsilon^*_{kl}), \tag{2.31}$$

which is used to calculate the equivalent eigenstrain ε^*_{ij}. Note that Equation 2.31 is actually a linear system of six equations and six unknowns. The equations can be solved algebraically to obtain the six components of the equivalent eigenstrain.

Infinitely extended, circular cylinders will be used herein to approximate the shape of carbon nanotubes, so the interior point Eshelby tensor for this shape must also be considered. Mura gives the Eshelby tensor for an elliptic cylinder with semi-axes $a_1 \neq a_2$ and $a_3 \to \infty$. Remarkably, setting $a_1 = a_2$ leads to the following simple

expressions for the componenents of S_{ijkl}

$$\begin{aligned} S_{1111} &= S_{2222} = \frac{4\nu - 5}{8(\nu - 1)} \\ S_{1122} &= S_{2211} = \frac{1 - 4\nu}{8(1 - \nu)} \\ S_{1212} &= \frac{4\nu - 3}{8(\nu - 1)} \\ S_{2323} &= S_{3131} = \frac{1}{4} \\ S_{1133} &= S_{2233} = \frac{-\nu}{2(\nu - 1)}, \end{aligned} \tag{2.32}$$

where ν is again the Poisson's ratio of the matrix, and all other components of $S_{ijkl} = 0$. The total strain in the inclusion can then be expressed in contracted, matrix notation as

$$\begin{bmatrix} \varepsilon_{11} \\ \varepsilon_{22} \\ \varepsilon_{33} \\ \varepsilon_{12} \\ \varepsilon_{31} \\ \varepsilon_{23} \end{bmatrix} = \begin{bmatrix} S_{1111} & S_{1122} & S_{1133} & 0 & 0 & 0 \\ S_{2211} & S_{2222} & S_{2233} & 0 & 0 & 0 \\ 0 & 0 & 0 & 0 & 0 & 0 \\ 0 & 0 & 0 & S_{1212} & 0 & 0 \\ 0 & 0 & 0 & 0 & S_{3131} & 0 \\ 0 & 0 & 0 & 0 & 0 & S_{2323} \end{bmatrix} \begin{bmatrix} \varepsilon^*_{11} \\ \varepsilon^*_{22} \\ \varepsilon^*_{33} \\ 2\varepsilon^*_{12} \\ 2\varepsilon^*_{31} \\ 2\varepsilon^*_{23} \end{bmatrix}. \tag{2.33}$$

Once ε^*_{ij} is calculated from Equation 2.31, the displacements, stresses, and strains inside the inhomogeneity can be calculated. The equations thus far have been used by many researchers to calculate the volume averaged elastic moduli of composite materials via the Eshelby, self-consistent, and Mori-Tanaka methods [89]. However, for the piezoresistive model, we desire the local exterior elastic fields due to cylindrical inclusions. Specifically, we need the displacement field outside each inclusion (i.e., nanotube).

Eshelby [91] first derived the elastic field outside an ellipsoidal inhomogeneity, but this solution is difficult to use in practice. Mura [92] improved on the exterior solution, but the formulation was still unwieldy. Fortunately, Ju and Sun [93] expanded Mura's exterior point Eshelby solution into a novel, easier to implement formulation. Furthermore, Jin, Keer, and Wang [94] used this formulation to derive a closed-form solution for the elastic field outside an elliptic cylinder. It should be noted that Kim and Lee [95] also derived an exterior point Eshelby tensor for elliptic cylinders, but Jin, Keer, and Wang point out that this solution contains fundamental errors. The solutions for the exterior point Eshelby tensors for spheres and infinite cylinders are summarized herein. See the aforementioned references for complete derivations.

Consider again a single ellipsoidal inhomogeneity in an infinite medium. The exterior point Eshelby tensor, $G_{ijkl}(x_\alpha)$, can be defined as

$$\varepsilon_{ij} = G_{ijkl}(x_\alpha)\varepsilon^*_{kl} \text{ in } D - \Omega, \tag{2.34}$$

where ε^*_{ij} is the equivalent inclusion eigenstrain for the inhomogeneity, and ε_{ij} is the elastic strain in the infinite medium due to the presence of the inhomogeneity. This relation is similar to the relation that defines the interior point Eshelby tensor S_{ijkl} (Equation 2.28). However, $G_{ijkl}(x_\alpha)$ is a function of the position vector x_α.

The exterior point Eshelby tensor for a sphere was derived by Ju and Chen [96] and is given in Equation 2.35.

$$\begin{aligned} G_{ijkl}(x_\alpha) = \frac{\rho^3}{30(1-\nu_0)}&((3\rho^2 - 10\nu_0 + 5)(\delta_{ik}\delta_{jl} + \delta_{il}\delta_{jk}) + (3\rho^2 + 10\nu_0 - 5)\delta_{ij}\delta_{kl} \\ &+ 15(1-\rho^2)\delta_{ij}n_k n_l + 15(1 - 2\nu_0 - \rho^2)\delta_{kl}n_i n_j + 15(7\rho^2 - 5)n_i n_j n_k n_l \\ &+ 15(\nu_0 - \rho^2)(\delta_{ik}n_j n_l + \delta_{il}n_j n_k + \delta_{jk}n_i n_l + \delta_{jl}n_i n_k)). \end{aligned} \tag{2.35}$$

The strains outside the inclusion can then be expressed in contracted, matrix notation as

$$\begin{bmatrix} \varepsilon_{11} \\ \varepsilon_{22} \\ \varepsilon_{33} \\ \varepsilon_{12} \\ \varepsilon_{31} \\ \varepsilon_{23} \end{bmatrix} = \begin{bmatrix} G_{1111} & G_{1122} & G_{1133} & 0 & 0 & 0 \\ G_{2211} & G_{2222} & G_{2233} & 0 & 0 & 0 \\ G_{3311} & G_{3322} & G_{3333} & 0 & 0 & 0 \\ 0 & 0 & 0 & G_{1212} & 0 & 0 \\ 0 & 0 & 0 & 0 & G_{3131} & 0 \\ 0 & 0 & 0 & 0 & 0 & G_{2323} \end{bmatrix} \begin{bmatrix} \varepsilon_{11}^* \\ \varepsilon_{22}^* \\ \varepsilon_{33}^* \\ 2\varepsilon_{12}^* \\ 2\varepsilon_{31}^* \\ 2\varepsilon_{23}^* \end{bmatrix}. \tag{2.36}$$

The individual components of $G_{ijkl}(x_\alpha)$ that were derived by Jin, Keer, and Wang [94] for an infinite elliptic cylinder are given below.

$$\begin{aligned} G_{1111} &= \frac{(1-2\nu)J_1(\lambda) + 3a_1^2 J_{11}(\lambda)}{2(1-\nu)} + \frac{\rho_1\rho_2 n_1^2}{2(1-\nu)} \\ &\quad \left(2 + 2\nu - 6\rho_1^2 + (8\rho_1^2 + T_6)n_1^2\right) \\ G_{2222} &= \frac{(1-2\nu)J_2(\lambda) + 3a_2^2 J_{22}(\lambda)}{2(1-\nu)} + \frac{\rho_1\rho_2 n_2^2}{2(1-\nu)} \\ &\quad \left(2 + 2\nu - 6\rho_2^2 + (8\rho_2^2 + T_6)n_2^2\right) \end{aligned} \tag{2.37}$$

$$\begin{aligned} G_{2211} &= \frac{(2\nu-1)J_2(\lambda) + a_1^2 J_{12}(\lambda)}{2(1-\nu)} \\ &\quad + \frac{\rho_1\rho_2}{2(1-\nu)}\left((1-\rho_2^2)n_1^2 + (1-2\nu-\rho_1^2)n_2^2 + (4\rho_1^2 + 4\rho_2^2 + T_6)n_1^2 n_2^2\right) \\ G_{1122} &= \frac{(2\nu-1)J_1(\lambda) + a_2^2 J_{12}(\lambda)}{2(1-\nu)} \\ &\quad + \frac{\rho_1\rho_2}{2(1-\nu)}\left((1-\rho_1^2)n_2^2 + (1-2\nu-\rho_2^2)n_1^2 + (4\rho_1^2 + 4\rho_2^2 + T_6)n_1^2 n_2^2\right) \\ G_{1133} &= \frac{\nu}{1-\nu}\left(J_1(\lambda) - \rho_1\rho_2 n_1^2\right) \\ G_{2233} &= \frac{\nu}{1-\nu}\left(J_2(\lambda) - \rho_1\rho_2 n_2^2\right) \end{aligned} \tag{2.38}$$

$$
\begin{aligned}
G_{1212} &= \frac{(1-2\nu)\left(J_1(\lambda)+J_2(\lambda)\right)+(a_1^2+a_2^2)J_{12}(\lambda)}{4(1-\nu)} \\
&\quad + \frac{\rho_1\rho_2}{2(1-\nu)}\left((\nu-\rho_2^2)n_1^2+(\nu-\rho_1^2)n_2^2+(4\rho_1^2+4\rho_2^2+T_6)n_1^2n_2^2\right) \\
G_{2323} &= \frac{1}{2}\left(J_2(\lambda)-\rho_1\rho_2 n_2^2\right) \\
G_{3131} &= \frac{1}{2}\left(J_1(\lambda)-\rho_1\rho_2 n_1^2\right) \\
G_{1233} &= -\frac{\nu}{1-\nu}\rho_1\rho_2 n_1 n_2 \\
G_{3123} &= G_{2331}(\mathbf{x}) = -\frac{\rho_1\rho_2 n_1 n_2}{2} \\
G_{1112} &= \frac{\rho_1\rho_2 n_1 n_2}{2(1-\nu)}\left(1+2\nu-3\rho_1^2+(6\rho_1^2+2\rho_2^2+T_6)n_1^2\right) \\
G_{2212} &= \frac{\rho_1\rho_2 n_1 n_2}{2(1-\nu)}\left(1+2\nu-3\rho_2^2+(6\rho_2^2+2\rho_1^2+T_6)n_2^2\right) \\
G_{1211} &= \frac{\rho_1\rho_2 n_1 n_2}{2(1-\nu)}\left(1-3\rho_1^2+(6\rho_1^2+2\rho_2^2+T_6)n_1^2\right) \\
G_{1222} &= \frac{\rho_1\rho_2 n_1 n_2}{2(1-\nu)}\left(1-3\rho_2^2+(6\rho_2^2+2\rho_1^2+T_6)n_2^2\right)
\end{aligned}
\tag{2.39}
$$

The term λ is given by

$$
\lambda = \frac{1}{2}\left(x_1^2+x_2^2-a_1^2-a_2^2+\sqrt{(x_1^2+x_2^2-a_1^2+s_2^2)^2+4(a_1^2-a_2^2)x_2^2}\right), \tag{2.40}
$$

and

$$
\begin{aligned}
\rho_1 &= \frac{a_1}{\sqrt{a_1^2+\lambda}} \\
\rho_2 &= \frac{a_2}{\sqrt{a_2^2+\lambda}} \\
n_1 &= \frac{m_1}{\sqrt{m_1^2+m_2^2}} \\
n_2 &= \frac{m_2}{\sqrt{m_1^2+m_2^2}} \\
m_1 &= \frac{x_1}{a_1^2+\lambda} \\
m_2 &= \frac{x_2}{a_2^2+\lambda} \\
J_1(\lambda) &= \frac{\rho_1^2\rho_2 a_2}{a_1\rho_2+a_2\rho_1} \\
J_2(\lambda) &= \frac{\rho_2^2\rho_1 a_1}{a_1\rho_2+a_2\rho_1} \\
J_{12}(\lambda) &= J_{21}(\lambda) = \frac{\rho_1^3\rho_2^3}{(a_1\rho_2+a_2\rho_1)^2} \\
J_{11}(\lambda) &= \frac{\rho_1^4\rho_2 a_2}{3a_1^2}\frac{2a_1\rho_2+a_2\rho_1}{(a_1\rho_2+a_2\rho_1)^2} \\
J_{22}(\lambda) &= \frac{\rho_2^4\rho_1 a_1}{3a_2^2}\frac{2a_2\rho_1+a_1\rho_2}{(a_1\rho_2+a_2\rho_1)^2} \\
J_3(\lambda) &= J_{33}(\lambda) = J_{13}(\lambda) = \\
J_{31}(\lambda) &= J_{23}(\lambda) = J_{32}(\lambda) = 0 \\
T_6 &= \rho_1^2+\rho_2^2-4\rho_1^2n_1^2-4\rho_2^2n_2^2-4.
\end{aligned}
\tag{2.41}
$$

The strains outside the inclusion, ε_{ij}, can then be expressed in contracted, matrix notation as

$$\begin{bmatrix} \varepsilon_{11} \\ \varepsilon_{22} \\ \varepsilon_{33} \\ \varepsilon_{12} \\ \varepsilon_{31} \\ \varepsilon_{23} \end{bmatrix} = \begin{bmatrix} G_{1111} & G_{1122} & G_{1133} & G_{1112} & 0 & 0 \\ G_{2211} & G_{2222} & G_{2233} & G_{2212} & 0 & 0 \\ 0 & 0 & 0 & 0 & 0 & 0 \\ G_{1211} & G_{1222} & G_{1233} & G_{1212} & 0 & 0 \\ 0 & 0 & 0 & 0 & G_{3131} & G_{3123} \\ 0 & 0 & 0 & 0 & G_{2331} & G_{2323} \end{bmatrix} \begin{bmatrix} \varepsilon^*_{11} \\ \varepsilon^*_{22} \\ \varepsilon^*_{33} \\ 2\varepsilon^*_{12} \\ 2\varepsilon^*_{31} \\ 2\varepsilon^*_{23} \end{bmatrix}. \tag{2.42}$$

Up to this point, it has been shown how to obtain the stress and strain fields for interior and exterior points of an ellipsoidal inhomogeneity using the equivalent inclusion method. The calculation of the displacement field, which is the end goal for the novel piezoresistivity model, requires some further calculations which will now be presented. In order to calculate the displacement field, the equivalent inclusion eigenstrain ε^*_{ij} must first be calculated for the inhomogeneity. This eigenstrain can then be used to calculate both the interior and exterior displacement fields, which is given by Mura for a single ellipsoidal inhomogeneity as

$$u_i(x) = \frac{1}{8\pi(1-\nu)} \left(\Psi_{,jli} \varepsilon^*_{jl} - 2\nu \varepsilon^*_{mm} \Phi_{,i} - 4(1-\nu)\varepsilon^*_{il} \Phi_{,l} \right), \tag{2.43}$$

where

$$\begin{aligned} \Phi(x) &= \int_\Omega |x - x\prime| \, \mathrm{d}x\prime \\ \Psi(x) &= \int_\Omega \frac{1}{|x - x\prime|} \, \mathrm{d}x\prime. \end{aligned} \tag{2.44}$$

Herein, the index notation from Mura will be adopted. All upper case indices take on the values of their corresponding lower case indices, but repeated upper case indices are not summed. All lower case indices follow the usual summation convention. Using relationships in Meng et al. [97], Mura [92], Ferrers [98], and

Dyson [99], the derivatives of $\Phi(x)$ and $\Psi(x)$ can be expressed as

$$\begin{aligned}
\Phi_{,i} &= -x_i I_I(\lambda) \\
\Psi_{,ijl} &= -\delta_{ij}x_l(I_L(\lambda) - a_I^2 I_{IL}(\lambda)) - x_i x_j (I_J(\lambda) - a_I^2 I_{IJ}(\lambda))_{,l} \\
&\quad - (\delta_{il}x_j + \delta_{jl}x_i)(I_J(\lambda) - a_I^2 I_{IJ}(\lambda)),
\end{aligned} \tag{2.45}$$

where λ is the largest positive root of

$$\frac{x_1^2}{a_1^2+\lambda} + \frac{x_2^2}{a_2^2+\lambda} + \frac{x_3^2}{a_3^2+\lambda} = 1, \tag{2.46}$$

and

$$\begin{aligned}
I_1(\lambda) &= \frac{4\pi a_1 a_2 a_3}{(a_1^2-a_2^2)(a_1^2-a_3^2)^{1/2}}(F(\theta(\lambda),k) - E(\theta(\lambda),k)) \\
I_2(\lambda) &= 4\pi a_1 a_2 a_3 \left(\frac{(a_1^2-a_3^2)^{1/2}}{(a_1^2-a_2^2)(a_2^2-a_3^2)} E(\theta(\lambda),k) - \frac{(F(\theta(\lambda),k)}{(a_1^2-a_2^2)(a_1^2-a_3^2)^{1/2}} \right. \\
&\quad \left. - \frac{(a_3^2+\lambda)^{1/2}}{(a_2^2-a_3^2)(a_1^2+\lambda)^{1/2}(a_2^2+\lambda)^{1/2}} \right) \\
I_3(\lambda) &= \frac{4\pi a_1 a_2 a_3}{(a_2^2-a_3^2)(a_1^2-a_3^2)^{1/2}} \left(\frac{(a_2^2+\lambda)^{1/2}(a_1^2-a_3^2)^{1/2}}{(a_3^2+\lambda)^{1/2}(a_1^2+\lambda)^{1/2}} - E(\theta(\lambda),k) \right) \\
I_{ij}(\lambda) &= \frac{I_i(\lambda) - I_j(\lambda)}{a_i^2 - a_j^2} \\
I_{i,j} &= \frac{-2\pi a_1 a_2 a_3}{(a_i^2+\lambda)(a_1^2+\lambda)^{1/2}(a_2^2+\lambda)^{1/2}(a_3^2+\lambda)^{1/2}} \lambda_{,j} \\
I_{ij,k} &= \frac{-2\pi a_1 a_2 a_3}{(a_i^2+\lambda)(a_j^2+\lambda)(a_1^2+\lambda)^{1/2}(a_2^2+\lambda)^{1/2}(a_3^2+\lambda)^{1/2}} \lambda_{,k} \\
\lambda_{,i} &= \frac{2x_i(a_J^2+\lambda)^2}{x_j x_j (a_I^2+\lambda)}.
\end{aligned} \tag{2.47}$$

The elliptic integrals $F(\theta,k)$ and $E(\theta,k)$ are given by the following equations.

$$F(\theta,k) = \int_0^\theta \frac{\mathrm{d}w}{(1-k^2 sin^2 w)^{1/2}} \tag{2.48}$$

$$E(\theta,k) = \int_0^\theta (1-k^2 sin^2 w)^{1/2} \mathrm{d}w \tag{2.49}$$

$$\theta = sin^{-1}(1 - a_3^2/a_1^2)^{1/2} \tag{2.50}$$

$$k = \left(\frac{a_1^2 - a_2^2}{a_1^2 - a_3^2}\right)^{1/2} \tag{2.51}$$

Fortunately, the preceding equations can be reduced significantly for certain shapes. The I-integrals for a sphere ($a_1 = a_2 = a_3 = a$) are given in Mura as

$$I_1(\lambda) = I_2(\lambda) = I_3(\lambda) = \frac{4\pi a^3}{3(a^2 + \lambda)^{3/2}}$$
$$I_{ij} = \frac{4\pi a^3}{5(a^2 + \lambda)^{5/2}}. \tag{2.52}$$

In order to get the I-integrals for an infinite, circular cylinder, Equations 2.47 were simplified using the assumptions $a_1 = a_2$ and $a_3 \to \infty$. Thus, the I-integrals for an infinite, circular cylinder were found to be

$$
\begin{aligned}
I_1(\lambda) = I_2(\lambda) &= \frac{2\pi a^2}{(a^2+\lambda)} \\
I_3(\lambda) &= 0 \\
I_{11} = I_{22} = I_{12} &= \frac{\pi a^2}{(a^2+\lambda)^2} \\
I_{1,1} = I_{2,1} &= -\frac{4\pi a^2 x_1}{(a^2+\lambda)(x_1^2+x_2^2)} \\
I_{2,2} = I_{1,2} &= -\frac{4\pi a^2 x_2}{(a^2+\lambda)(x_1^2+x_2^2)} \\
I_{1,3} = I_{2,3} &= -\frac{4\pi a^2 x_3}{(a^2+\lambda)(x_1^2+x_2^2)} \\
I_{3,3} = I_{3,1} = I_{3,2} &= 0 \\
I_{11,1} = I_{22,1} = I_{12,1} = I_{21,1} &= -\frac{4\pi a^2 x_1}{(a^4+2a^2\lambda+\lambda^2)(x_1^2+x_2^2)} \\
I_{11,2} = I_{22,2} = I_{12,2} = I_{21,2} &= -\frac{4\pi a^2 x_2}{(a^4+2a^2\lambda+\lambda^2)(x_1^2+x_2^2)} \\
I_{11,3} = I_{22,3} = I_{12,3} = I_{21,3} &= -\frac{4\pi a^2 x_3}{(a^4+2a^2\lambda+\lambda^2)(x_1^2+x_2^2)} \\
I_{33,3} = I_{13,1} = I_{31,1} = I_{23,1} = I_{32,1} = I_{13,2} = I_{31,2} &= I_{23,2} \\
= I_{32,2} = I_{13,3} = I_{31,3} = I_{23,3} = I_{32,3} &= 0.
\end{aligned}
\tag{2.53}
$$

These I-integrals were numerically verified by comparing their values to calculations from the Eshelby solver software distributed freely by Meng et al. [97]. For a given point x_i, which can be interior or exterior to the ellipsoid, the I-integrals given above can be easily calculated and substituted into Equation 2.45 to obtain the required derivatives of $\Phi(x)$ and $\Psi(x)$. The derivatives and equivalent inclusion eigenstrains are then substituted into Equation 2.43 to obtain the displacement field at the point x_i.

II.C.2.b. Decomposition of the boundary value problem

We now have everything to calculate the stress, strain, and displacement field inside and outside an ellipsoidal inclusion. The specific solutions for spheres and infinite, circular cylinders have been presented, but the solutions for other ellipsoidal shapes could be easily obtained. However, it should be stressed that the elastic fields are valid only for a single inhomogeneity embedded in an infinite body. In order to obtain the displacement field for a nanotube network comprised of thousands of carbon nanotubes embedded in a finite matrix, a superposition method was implemented to approximately correct for the presence of boundaries in the finite body. The method is similar to parts of the discrete dislocation plasticity model developed in several works by Lubarda, Blume, Cleveringa, Van der Giessen, and Needleman [100–103]. Needleman et al. decomposed the problem for a body with dislocations into a superposition of interacting dislocations in an infinite solid and a complementary solution for a finite body without dislocations.

Similarly, the FEA/micromechanics framework in this work decomposes a CNT/polymer nanocomposite into the superposition of the analytic elastic fields (interior and exterior) of nanotubes in an infinite medium and the complementary solution for a finite body without nanotubes. The complementary solution corrects for the presence of the actual boundaries. This decomposition is shown in Figure II.12 for a boundary value problem with mixed boundary conditions. Note that while carbon nanotubes are shown in the figure, any shape inhomogeneity with an analytical solution could be used in this framework.

The ($\tilde{}$) fields are obtained by superposing the elastic fields obtained from the

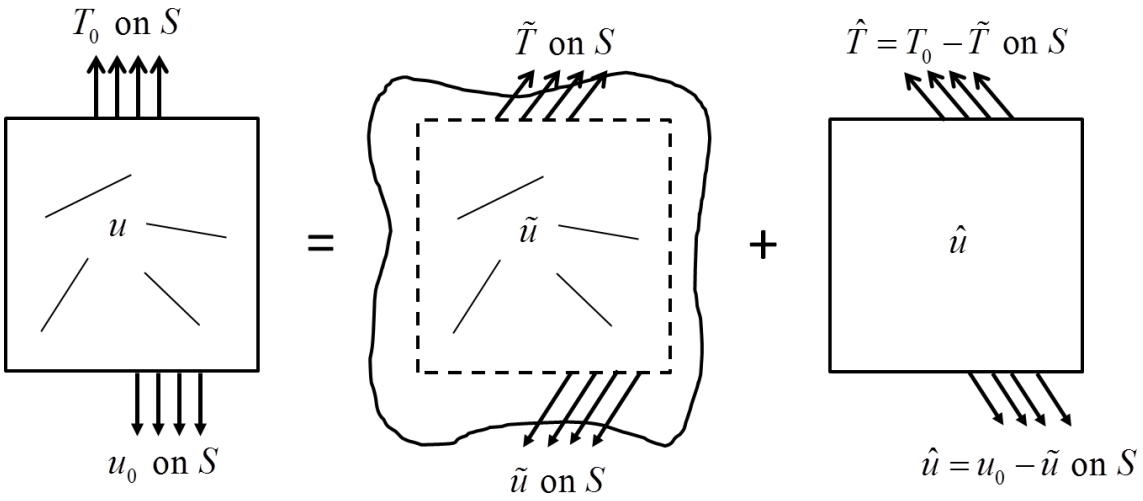

Figure II.12. Decomposition of nanocomposite boundary value problem.

Eshelby equivalent inclusion method for each nanotube. The tractions and displacements are summed on the imaginary boundary S, given by the dashed line in the figure, which corresponds to where the RVE boundary would be located inside the infinite medium. The ($\hat{}$) fields of the complementary problem are obtained by solving a finite element model of the RVE without nanotubes. The ($\tilde{}$) and ($_0$) fields are used to calculate the boundary conditions on S of the complementary FEA model as shown. Finally, the ($\tilde{}$) and ($\hat{}$) fields are superposed to obtain the final elastic solution for the nanocomposite. Note that the boundary conditions on the complementary problem perfectly cancel the tractions on S due to the nanotubes in the infinite problem.

At this point it should be noted that there are two important sources of error in the above problem decomposition. First, the Eshelby solution for an ellipsoidal inhomogeneity assumes that there are no other inhomogeneities acting on it. Therefore, the superposition of solutions to obtain the ($\tilde{}$) fields is not exact. Consider the case

where two inhomogeneities are embedded in an infinite medium. It is easy to imagine that the stress field from the first inhomogeneity acts on the second inhomogeneity and vice versa. Unlike Eshelby's important result for a single inhomogeneity, this results in nonuniform stress and strain fields inside the inhomogeneities. Also, the equivalent eigenstrains are not uniform. The second source of error is due to the lack of nanotubes in the complementary problem. In order for the superposition to be exact, the nanotubes represented in the infinite body would have to be present in the complementary FEA problem. Of course, if this FEA problem were readily solvable, there would be no need to use the Eshelby method in the first place. It has already been mentioned, however, that the direct solution of a large network of carbon nanotubes is not easily obtained using finite elements. Thus, the decomposition in Figure II.12 is used as an approximation of the elastic solution. The errors due to this approximation are explored in several benchmark problems in Appendix A. Additionally, a strategy to incorporate the interaction effects between inhomogeneities was developed and is presented in the next section.

II.C.2.c. Accounting for elastic interaction between nanotubes

In order to obtain accurate piezoresistivity predictions, the relative displacements between individual nanotubes must be accurately calculated when the entire CNT/polymer composite is subjected to an applied deformation. The novel piezoresistivity method outlined in the previous section attempts to accomplish this, but its biggest source of error is in the superposition of analytical solutions for each CNT. The superposition is technically invalid because it does not account for the

elastic interaction between neighboring CNTs. The purpose of this section is to derive a method that can account for at least some of the elastic interaction between individual nanotubes in a CNT network.

Consider the case of two ellipsoidal inhomogeneities that are positioned an arbitrarily close distance away from each other in an infinite medium, as shown in Figure II.13.

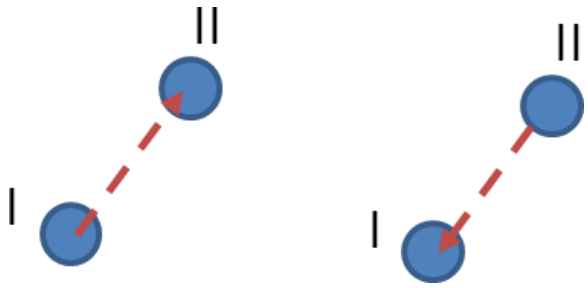

Figure II.13. Interaction between two ellipsoidal inhomogeneities in an infinite medium.

The strain ε_{ij} in each inhomogeneity is no longer given by

$$\varepsilon_{ij} = S_{ijkl}\varepsilon^*_{kl} \text{ in } \Omega \tag{2.54}$$

because the elastic field of each inhomogeneity acts upon the other. Ju and Yanase [104], as well as Mura, have shown that the strain in inhomogeneity I and II are given by

$$\begin{aligned} \varepsilon^I_{ij}(x_\alpha) &= S^I_{ijkl}\varepsilon^{I*}_{kl} + G^{II}_{ijkl}(x_\alpha)\varepsilon^{II*}_{kl} \text{ in } \Omega^I \\ \varepsilon^{II}_{ij}(x_\alpha) &= G^I_{ijkl}(x_\alpha)\varepsilon^{I*}_{kl} + S^{II}_{ijkl}\varepsilon^{II*}_{kl} \text{ in } \Omega^{II}. \end{aligned} \tag{2.55}$$

For inhomogeneity I, the strain is a function of the interior point Eshelby tensor S^I_{ijkl} for that inhomogeneity, the exterior point Eshelby tensor G^{II}_{ijkl} for the other

inhomogeneity, and two eigenstrains that serve to simulate each inhomogeneity as equivalent inclusions. Note that, unlike the case of a single inhomogeneity, the equivalent eigenstrains, and therefore the total strains in each inhomogeneity, are not uniform. Using the Eshelby equivalency condition for each inhomogeneity,

$$C^0_{ijkl}\left(\varepsilon^0_{kl}+\varepsilon^I_{kl}-\varepsilon^{I*}_{kl}\right)=C^I_{ijkl}\left(\varepsilon^0_{kl}+\varepsilon^I_{kl}\right)\ \text{in}\ \Omega^I \tag{2.56}$$

$$C^0_{ijkl}\left(\varepsilon^0_{kl}+\varepsilon^{II}_{kl}-\varepsilon^{II*}_{kl}\right)=C^{II}_{ijkl}\left(\varepsilon^0_{kl}+\varepsilon^{II}_{kl}\right)\ \text{in}\ \Omega^{II} \tag{2.57}$$

and Equation 2.55 for the strain in each inhomogeneity, the following system of equivalency equations can be obtained.

$$\begin{aligned}
&C^0_{ijkl}\left(\varepsilon^0_{kl}+S^I_{klmn}\varepsilon^{I*}_{mn}+G^{II}_{klmn}(x_\alpha)\varepsilon^{II*}_{mn}-\varepsilon^{I*}_{kl}\right)\\
&\quad=C^I_{ijkl}\left(\varepsilon^0_{kl}+S^I_{klmn}\varepsilon^{I*}_{kl}+G^{II}_{klmn}(x_\alpha)\varepsilon^{II*}_{mn}\right)\ \text{in}\ \Omega^I\\
&C^0_{ijkl}\left(\varepsilon^0_{kl}+S^{II}_{klmn}\varepsilon^{II*}_{mn}+G^I_{klmn}(x_\alpha)\varepsilon^{I*}_{mn}-\varepsilon^{II*}_{kl}\right)\\
&\quad=C^{II}_{ijkl}\left(\varepsilon^0_{kl}+S^{II}_{klmn}\varepsilon^{II*}_{mn}+G^I_{klmn}(x_\alpha)\varepsilon^{I*}_{mn}\right)\ \text{in}\ \Omega^{II}
\end{aligned} \tag{2.58}$$

Rearranging Equation 2.58 and switching to matrix notation for clarity, the system of equations can be represented in matrix form as

$$\begin{bmatrix}\Delta\mathbf{C}^I\mathbf{S}^I+\mathbf{C}^0 & \Delta\mathbf{C}^I\mathbf{G}^{II}(x)\\ \Delta\mathbf{C}^{II}\mathbf{G}^I(x) & \Delta\mathbf{C}^{II}\mathbf{S}^{II}+\mathbf{C}^0\end{bmatrix}\begin{bmatrix}\varepsilon^{I*}\\ \varepsilon^{II*}\end{bmatrix}=\begin{bmatrix}-\Delta\mathbf{C}^I\varepsilon^0\\ -\Delta\mathbf{C}^{II}\varepsilon^0\end{bmatrix}, \tag{2.59}$$

where

$$\Delta\mathbf{C}^N=\mathbf{C}^N-\mathbf{C}^0, \tag{2.60}$$

and $N=I,II$.

The set of 12 equations can be solved to obtain the equivalent eigenstrains for each inhomogeneity. However, it is important to note that there is a unique set of equivalency equations for every point x_α. Once the equivalent eigenstrains at each

point are known, the standard equivalent inclusion method can be used to evaluate the elastic field inside and outside each inhomogeneity.

This method can be extended to the case of N inhomogeneities in an infinite medium. Figure II.14 shows how the inclusion I acts elastically on inclusions $II - N$ and inclusions $II - N$ act elastically on inclusion I. The strain in each of the N inhomogeneities is given in Equations 2.61.

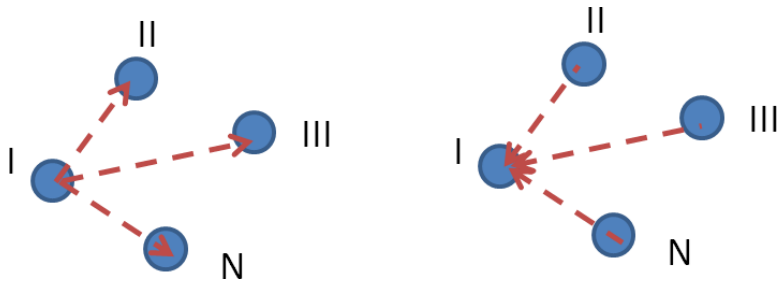

Figure II.14. Interaction between N ellipsoidal inhomogeneities in an infinite medium.

$$\begin{aligned}
\varepsilon_{ij}^{I}(x_\alpha) &= S_{ijkl}^{I}\varepsilon_{kl}^{I*} + G_{ijkl}^{II}(x_\alpha)\varepsilon_{kl}^{II*} + \ldots + G_{ijkl}^{N}(x_\alpha)\varepsilon_{kl}^{N*} \\
\varepsilon_{ij}^{II}(x_\alpha) &= S_{ijkl}^{II}\varepsilon_{kl}^{II*} + G_{ijkl}^{I}(x_\alpha)\varepsilon_{kl}^{I*} + \ldots + G_{ijkl}^{N}(x_\alpha)\varepsilon_{kl}^{N*} \\
&\vdots \\
\varepsilon_{ij}^{N}(x_\alpha) &= S_{ijkl}^{N}\varepsilon_{kl}^{N*} + G_{ijkl}^{I}(x_\alpha)\varepsilon_{kl}^{I*} + \ldots + G_{ijkl}^{N-1}(x_\alpha)\varepsilon_{kl}^{N-1*}
\end{aligned} \tag{2.61}$$

Using the equivalency conditions, the following system of equations can be solved for the interacting eigenstrains.

$$\begin{bmatrix} \Delta\mathbf{C}^I\mathbf{S}^I + \mathbf{C}^0 & \Delta\mathbf{C}^I\mathbf{G}^{II}(x) & \cdots & \Delta\mathbf{C}^I\mathbf{G}^N(x) \\ \Delta\mathbf{C}^{II}\mathbf{G}^I(x) & \Delta\mathbf{C}^{II}\mathbf{S}^{II} + \mathbf{C}^0 & \cdots & \Delta\mathbf{C}^{II}\mathbf{G}^N(x) \\ \vdots & & \ddots & \vdots \\ \Delta\mathbf{C}^N\mathbf{G}^I(x) & \Delta\mathbf{C}^N\mathbf{G}^{II}(x) & \cdots & \Delta\mathbf{C}^N\mathbf{S}^N + \mathbf{C}^0 \end{bmatrix} \begin{bmatrix} \varepsilon^{I*} \\ \varepsilon^{II*} \\ \vdots \\ \varepsilon^{N*} \end{bmatrix} = \begin{bmatrix} -\Delta\mathbf{C}^I\varepsilon^0 \\ -\Delta\mathbf{C}^{II}\varepsilon^0 \\ \vdots \\ -\Delta\mathbf{C}^N\varepsilon^0 \end{bmatrix} \tag{2.62}$$

The efficacy of this interacting eigenstrain method is explored in several benchmark problems in Appendix A.

Several important modifications are made to the multiple inhomogeneity equivalent inclusion method given above so that a computationally tractable form can be implemented in the novel piezoresistivity method. First, because the carbon nanotubes are so much stiffer than the polymer matrix, the equivalent inclusion eigenstrains for each CNT are assumed to be uniform. Careful inspection of Equation 2.62 reveals that this cuts down drastically the number of equations that must be solved for a given CNT network. Second, note that extending the interaction method in Equation 2.62 to a network of thousands of interacting inhomogeneities (nanotubes) requires solving an n-body problem because each CNT is interacting with all of the others. In order to avoid this computationally intensive problem, an interaction cutoff distance was introduced into the model. Only nanotubes within this cutoff distance from each other are assumed to interact. This substantially reduces the number of equations to be solved in Equation 2.62. Details of how the interaction cutoff distance was implemented are given in Chapter III. Finally, the equivalent eigenstrains in Equation 2.62 are only calculated at the centers of the nanotubes.

Using this modified multiple inhomogeneity equivalent inclusion method allows the calculation of all relative displacements between nanotubes in the network. The displacements are calculated at incremental levels of applied load, and the corresponding resistor networks at each load are generated and solved to obtain the effective electrical conductivity of the CNT/polymer. The piezoelectric predictions calculated in this manner should be more accurate than simply assuming a uniform strain field in the composite material.

II.D. Summary

This chapter described the theory behind the different types of nanotube network models used in this work. The methods and equations needed to generate networks in 2D and 3D were presented. Additionally, the process of reducing CNT networks to equivalent networks of electrical resistors, utilizing a finite element framework to obtain the solution for these resistor networks, and calculating an effective electrical conductivity for the composite was discussed in detail. Finally, the models used to predict and evaluate the piezoelectric performance of 3D CNT/polymer nanocomposites were described. This included a simple uniform strain piezoresitivity model that has been used in the literature, as well as a new model that uses a hybrid FEA/Eshelby micromechanics framework to include local elastic effects.

CHAPTER III

IMPLEMENTATION

The purpose of this chapter is to provide details for some of the important algorithms used in the nanotube network models. Some of the algorithms were developed specifically for this work, and others were taken from other sources in the literature or on the Internet. Well known algorithms used in fields like computer graphics are extremely helpful in modeling CNT networks. These algorithms are generally more efficient and robust because they have been tested and optimized extensively by others.

III.A. Generating a uniform distribution of CNT orientations

Care must be taken in order to generate a truly uniform distribution of CNT orientations in 3D space. This is because naive approaches to this problem actually produce nonuniform distributions that can affect the predictions in the resistor network model. The method of normal deviates from Marsaglia [84] was used to generate uniform distributions of orientations. This method can be used for any number of dimensions, but the algorithm will be specialized here for 3D. First, a 3D vector, $\mathbf{u} = (u1, u2, u3)$, of normal deviates is generated. A normal deviate is defined as a random variable with a Gaussian (normal) distribution. The normal deviates in this case are the u_1, u_2, and u_3 components of $\mathbf{u}$, and their distributions are generated with limits of $[-1, 1]$ and a mean of zero. Then, the magnitude r of this vector is

calculated using

$$r = \sqrt{u_1^2 + u_2^2 + u_3^2}, \tag{3.1}$$

and the original vector $\mathbf{u}$ is normalized using

$$\mathbf{x} = \frac{1}{r}\mathbf{u}, \tag{3.2}$$

where $\mathbf{x}$ is a vector that is uniformly distributed over the surface of the 3D sphere. This vector can then be used as an orientation for a specific nanotube. It is interesting to note that this method begins with Gaussian distributions of points but ends with uniform distributions of points. This is due to the special properties of normal distributions. This method extends easily to n-dimensions, but Marsaglia [84] notes that it may not be the most efficient method in 3D. Indeed, the speed of the method depends heavily on the functions used to generate a normal distribution, but the algorithm's efficiency was more than adequate for the problems considered in this work.

Figure III.1 shows that the algorithm does indeed produce a uniform distribution of orientations. In the figure, a unit sphere is plotted along with unit vectors that all begin at the center of the sphere (located at the origin). The tips of each vector are plotted as dots on the sphere's surface. Three unit spheres are shown with 100, 1,000, and 10,000 orientations sampled. If the distribution of orientations was nonuniform, there would be distinct, nonuniform clusters of points on the spheres.

For a more detailed example of how the algorithm is applied to CNT orientations, consider a single nanotube to be placed randomly into the RVE. The two endpoints of the nanotube are described by (x_1, y_1, z_1) and (x_2, y_2, z_2). The coordinates (x_1, y_1, z_1) are sampled from a uniform distribution generated using a Mersenne

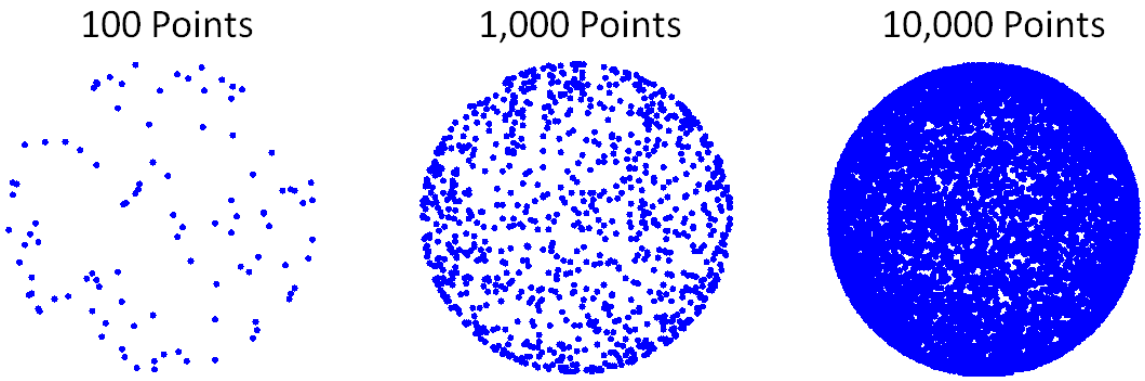

Figure III.1. Uniform sampling on unit sphere with 100, 1,000, and 10,000 sample points.

Twister random number generator. [77] The Mersenne Twister number generator was chosen for its speed and efficiency in generating high quality pseudorandom numbers. The coordinates are then scaled so that they are located within the dimensions of the RVE. The coordinates (x_1, y_1, z_1) now represent a point that is located randomly within the RVE.

To get the second endpoint (x_2, y_2, z_2), the coordinates of the vector $\mathbf{u} = (u_1, u_2, u_3)$ are sampled from a normal distribution as described above. Note that a Mersenne Twister random number generator is again used to generate the normal distribution. The radius of $\mathbf{u}$ is calculated using Equation 3.1, and the endpoint (x_2, y_2, z_2) is then calculated using Equation 3.2. The entire algorithm is then repeated for each CNT to be generated in the network.

III.B. Determining if two nanotubes are in contact with each other

In order to take a network of randomly distributed and oriented nanotubes and map it into a finite element mesh, the individual connections between nanotubes

must be determined. Specifically, it is necessary to determine all junctions where nanotubes are either in physical contact with each other or are close enough to each other for electrons to tunnel between them. If the nanotubes are idealized as straight line segments, then several algorithms used in computational geometry can be used to determine all of the junctions in the network. For efficiency reasons, there are differences in the algorithms used for 2D nanotubes and 3D nanotubes, and the algorithms for each are given in the following subsections.

III.B.1. Determining contact in 2D

In two dimensions, determining contact between two nanotubes can be calculated by representing the nanotubes as infinite lines and solving the corresponding set of two line equations to determine the point at which they intersect. Assume that we have two line segments $P(s)$ and $Q(t)$ parametrically expressed as

$$\begin{aligned} P(s) &= P_1 + s(P_2 - P_1) \\ Q(t) &= Q_1 + t(Q_2 - Q_1), \end{aligned} \tag{3.3}$$

where P_1, P_2, Q_1, and Q_2 are the end points of the line segments and

$$\begin{aligned} 0.0 \leq s \leq 1.0 \\ 0.0 \leq t \leq 1.0. \end{aligned} \tag{3.4}$$

The two lines intersect if there are unique values of s and t such that

$$\begin{aligned} P_c &= P_1 + s(P_2 - P_1) \\ P_c &= Q_1 + t(Q_2 - Q_1), \end{aligned} \tag{3.5}$$

where P_c is the point at which the lines intersect. The parameters s and t can be solved explicitly using Cramer's rule for a system of two equations and two unknowns. Cramer's rule is used because it results in explicit equations that can be calculated using only add/subtract and multiply/divide functions. This is much faster than implementations that rely on using square root functions.

There are four cases that can occur after solving for the intersecting point, and these are illustrated in Figure III.2. The first case occurs when the intersecting point falls within the finite line segments that represent each nanotube. In this case the nanotubes are in contact at that point. If the intersecting point occurs outside the finite line segment of one of the nanotubes, then the nanotubes do not intersect. Additionally, the end point of the segment closest to the intersecting point is the closest point between the nanotubes. The third case occurs when the intersecting point is located outside of the finite line segments for both nanotubes. Again, the nanotubes are not in contact. The shortest distance between the nanotubes is the distance between the two endpoints that are closest to the intersecting point. The final case occurs when the two nanotubes are perfectly parallel to each other. In this case, Equation 3.3 does not have a valid solution because it is impossible for the line segments representing the nanotubes to intersect. However, it is possible for two parallel nanotubes to be in contact if the distance between their representative line segments is less than the diameter of the nanotubes. Thus, if Equation 3.3 returns a singular result for a pair of nanotubes, the distance between them has to be calculated another way.

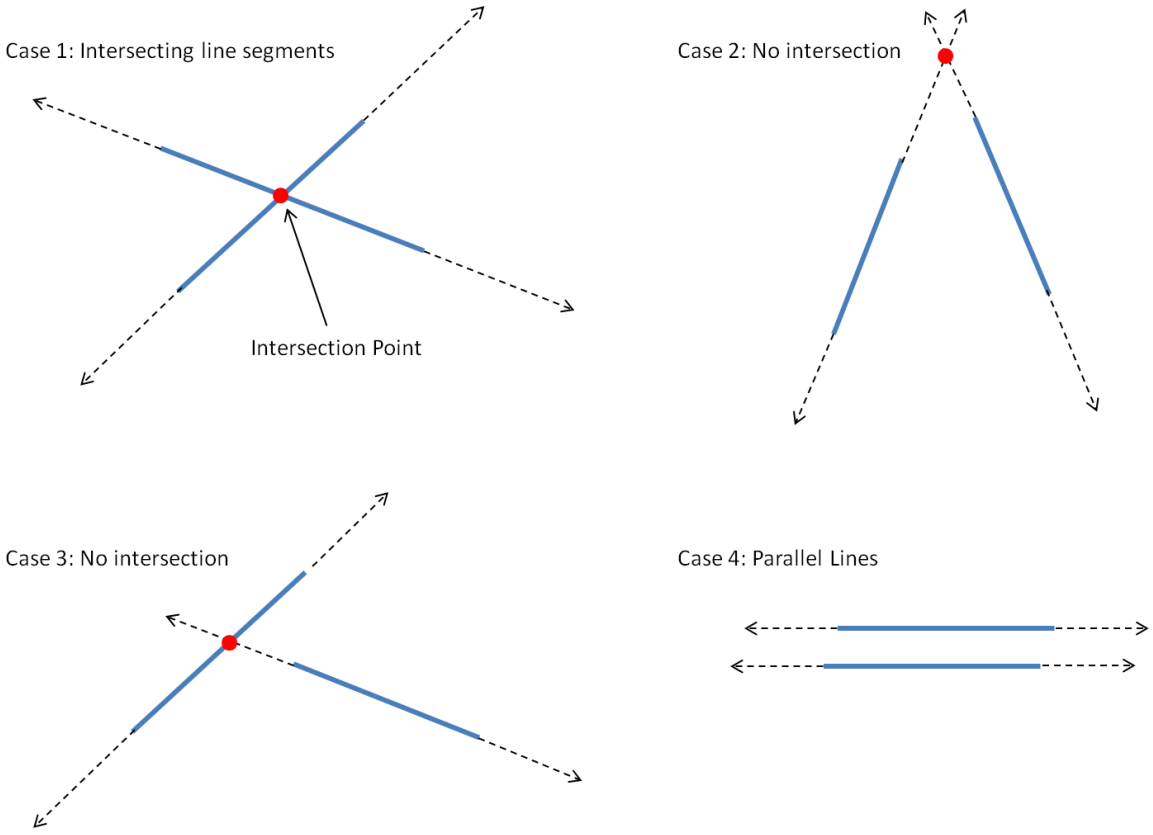

Figure III.2. Schematic of four cases that can occur with 2D line segments.

III.B.2. Determining contact in 3D

Determining if two straight nanotubes are in contact with each other in 3D space requires a more general form of the technique for determining contact in 2D. Moreover, simply determining if the CNTs are touching each other is not sufficient because it is also necessary to determine if the CNTs are close enough for electron tunneling to occur. Thus, the problem can be reduced to finding the shortest distance between two 3D line segments. The algorithm and C++ code used to calculate this distance are taken from Dan Sunday's geometric algorithms website. [105] According to Sunday, the shortest distance between two non-parallel, infinite lines is always the length of the line segment that connects the two segments and is uniquely perpendicular to both of them. The following derivation is a brief summary from Sunday's website.

Consider again the line segments $P(s)$ and $Q(t)$

$$\begin{aligned} P(s) &= P_1 + s(P_2 - P_1) = P_1 + s\mathbf{u} \\ Q(t) &= Q_1 + t(Q_2 - Q_1) = Q_1 + t\mathbf{v}, \end{aligned} \tag{3.6}$$

where P_1, P_2, Q_1, and Q_2 are the end points of the line segments, $\mathbf{u}$ and $\mathbf{v}$ are direction vectors describing the lines, and

$$\begin{aligned} 0.0 \leq s \leq 1.0 \\ 0.0 \leq t \leq 1.0. \end{aligned} \tag{3.7}$$

Now consider the vector $\mathbf{w}_c = \mathbf{w}(s_c, t_c)$, which corresponds to the minimum distance between the two line segments and is uniquely perpendicular to $\mathbf{u}$ and $\mathbf{v}$. Thus, the equations $\mathbf{u} \cdot \mathbf{w}_c = 0$ and $\mathbf{v} \cdot \mathbf{w}_c = 0$ must be satisfied. These equations can be solved

by substituting $\mathbf{w}_c = P(s_c) - Q(t_c) = \mathbf{w}_0 = s_c\mathbf{u} - t_c\mathbf{v}$ into each equation, where $P(s_c)$ and $Q(t_c)$ are the closest unique points and $\mathbf{w}_0 = P_1 - Q_1$. Then, s_c and t_c can be solved for by using

$$s_c = \frac{be - cd}{ac - b^2}$$
$$t_c = \frac{ae - bd}{ac - b^2}, \tag{3.8}$$

where $a = \mathbf{u} \cdot \mathbf{u}$, $b = \mathbf{u} \cdot \mathbf{v}$, $c = \mathbf{v} \cdot \mathbf{v}$, $d = \mathbf{u} \cdot \mathbf{w}_0$, and $e = \mathbf{v} \cdot \mathbf{w}_0$. If s_c and t_c are inside the range for the given line segments, then they represent the closest points. However, if s_c and t_c are outside the range for either line segment, then a series of cases must be checked to determine if the closest points are on the endpoints of the segments or a combination of an endpoint and a point on the interior of a segment.

III.C. KD-Trees for CNT network sorting

Because of the large computational burden involved with running hundreds or thousands of simulations with tens of thousands of nanotubes each, every effort was made to make the computational code more efficient. One of the biggest computational costs associated with generating CNT networks is the mapping of the nanotubes into a connected graph. Searching for each connection that exists between individual nanotubes can become quite inefficient if the algorithm in Section III.B is used for each pair of nanotubes in the network. Indeed, this would result an an N-body problem which is very computationally expensive. Even implementing a truncation distance so that only nanotubes within a specific region are searched can be inefficient. This is because looping through all nanotubes to determine if they fall in the current region is quite costly for large networks. An efficient algorithm for

performing this search was developed using a data construct called a KD-tree. KD-trees were first proposed by Bentley [106] in 1975, and they can be used for efficient range search and nearest neighbor algorithms in multiple dimensions. The purpose of this section is to outline the algorithm that was developed to utilize KD-trees in an efficient search for nanotube junctions.

A sorted binary tree is a data structure that is often used in computer science to efficiently store and search for data. [106] It consists of a tree of nodes that are connected by leaves. An example binary tree is given in Figure III.3. Each circular node represents a piece of data that has a numeric label used to sort the data. The arrows represent the leaves that connect parent nodes to child noes. Each parent node can have a maximum of two child nodes. Additionally, the tree is sorted such that each child node is greater than or less than it's parent. There are many standard algorithms that can be used to balance the tree, search for nodes, and insert/delete nodes.

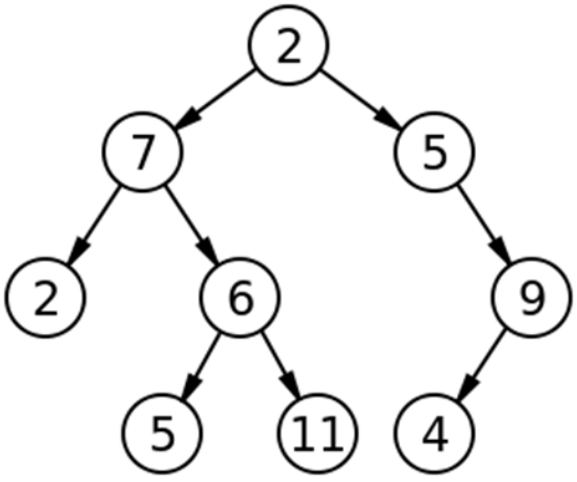

Figure III.3. Example binary tree.

A KD-tree is simply a type of binary tree that is able to handle multidimensional data. It is a binary tree in k-dimensions, and each node represents a point in k-dimensional space. An example 2D KD-tree is shown in Figure III.4. Each circular node represents a point in 2D space given by the coordinates shown. Each level of the tree corresponds to an alternating dimension as shown by the X and Y levels. Each node again has a maximum of two child nodes. For each parent node, its dimension level determines which dimension its child nodes will be sorted on. For example, the root node (7,2) is on the x-dimension level, so its children are sorted by their x-coordinates. Thus, the (5,4) node is less than the root, and the (9,6) node is greater than the root. There are again many standard algorithms to perform common functions (balance, search, insert, delete, etc...) on this type of tree.

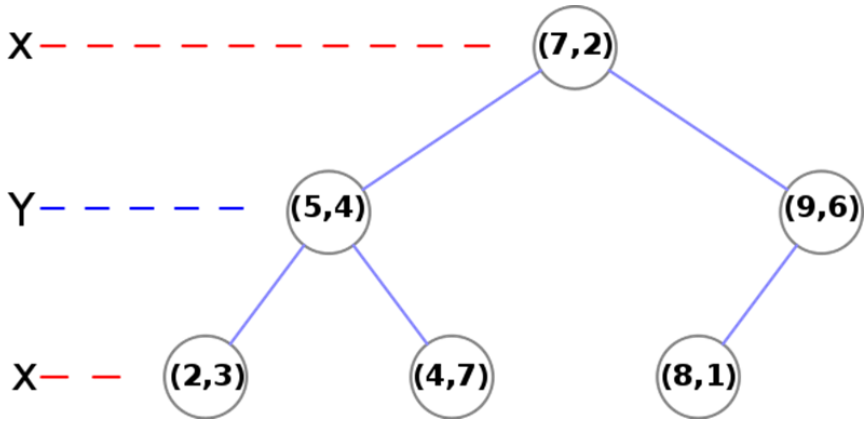

Figure III.4. Example KD-tree.

One way to visualize a KD-tree is to think of it in terms of partitioning a k-dimensional space of interest. Each parent node can be represented as a splitting hyperplane that divides the space in half. The subtree to the left of (less than) the

parent node includes points that are to the left hyperplane, and the right subtree includes all the points to the right (greater than the parent node). The normal direction of the hyperplane is determined by the dimension level of the parent node. If the parent node is on the x-dimension level, then the hyperplane is perpendicular to the x-axis. This partitioning continues recursively through all of the points in the tree.

An example of this space partitioning is given in Figure III.5 for the KD-tree in Figure III.4. All of the nodes in the tree are represented as 2D points in the figure, and the hyperplanes are 1D lines. Starting at the root node (7,2), the space is partitioned by a hyperplane at $x = 7$. All of the points with x-coordinates that are less than the root node are to the left of this plane, and all points with greater x-coordinates are to the right. Following the tree down to the left, the next node is (5,4), and it is on a y-dimension level. A hyperplane at $y = 4$ then partitions the remaining space. Note that each hyperplane only partitions space that is below it in the tree structure. The partitioning continues recursively for the remaining points. This partitioning scheme is useful for range-type search procedures because it is very quick to traverse the tree and find all of the points that are within a given subspace.

The space partitioning for a 3D KD-tree is similar to the 2D case. However, nodes in the tree are now represented by points in 3D space. The hyperplanes are now 2D planes that split the space into subvolumes. The procedures for generating, balancing, and searching a 3D tree are the same as the 2D case except for the obvious addition of a third dimension to the tree. It is easy to see how this approach could be extended to a tree of N-dimensions, even if it is hard or impossible to visualize

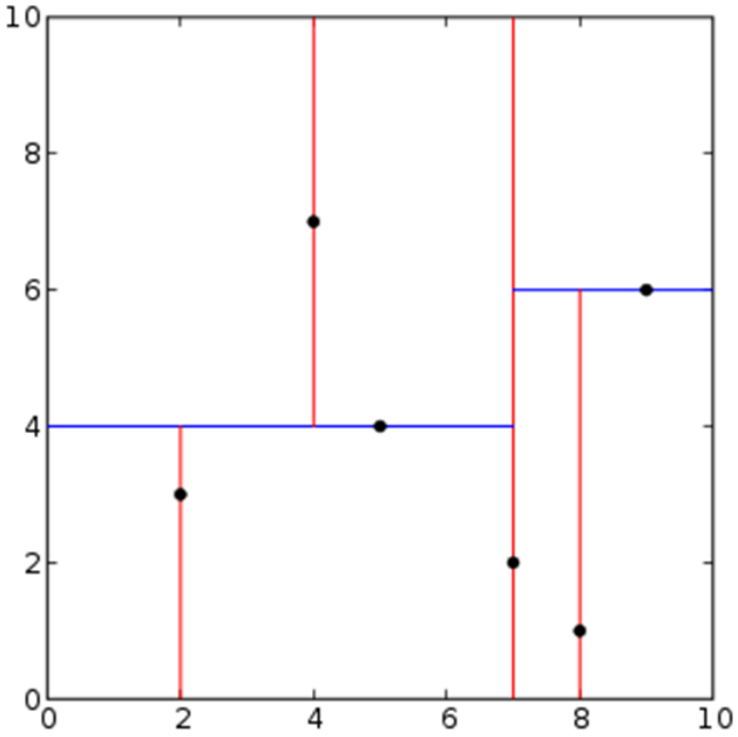

Figure III.5. Example KD-tree partition.

the resulting space partitioning.

Rather than implement a KD-tree library from scratch, an open source library written by Tagliasacchi [107] was used for the KD-trees in this work. The library is written in C++ and was originally intended to be used as an add-on package for Matlab. However, the library also works very well when compiled with a native C++ code, and that is how it is used in this work. The library is capable of generating a KD-tree based on user-supplied input data, and functions such as rectangular range search, ball (circular) range search, and k-nearest neighbor search are supported. Figure III.6 shows examples of these functions. The blue dots are randomly generated

points in 2D space that have been used to construct a 2D KD-tree. The blue rectangle shows the results of a rectangular range search where all points inside the specified rectangular region are found using the KD-tree and circled in red. The green circle indicates all points found within a specified radius using the ball (circular) search function. Finally, the figure shows the results of a k-nearest neighbor query using the KD-tree library. The point (0.8, 0.2) is chosen as an example point, and the seven nearest neighbors of this point are found using the KD-tree and circled in green. These search functions are efficiently performed by traversing the KD-tree to find the data subset that corresponds to the desired search region. More details can be found in Bentley and Tagliasacchi. [106, 107]

In order to use the KD-tree structure in the 2D nanotube search algorithm, each CNT is given a rectangular bounding box whose size is determined by the minimum and maximum coordinates of the CNT. This bounding box is defined in Figure III.7. The nanotube is represented by the blue cylinder, and the bounding box is in black. The bounding box can be defined by four parameters: x_{min}, x_{max}, y_{min}, and y_{max}. These four parameters can be thought of as coordinates for a point in 4D space. Thus, we can sort all of the nanotubes in a network into a 4D KD-tree by using their bounding boxes as coordinates.

The problem of interest is quickly finding all of the nanotubes within a certain distance of a specific nanotube. If we use a 4D KD-tree containing all of the nanotubes, we can perform a rectangular range search on the tree to get all of the nodes within a certain distance of the node that corresponds to the specific nanotube. Even though this problem is in 4D space, it can be visualized as the search for intersecting

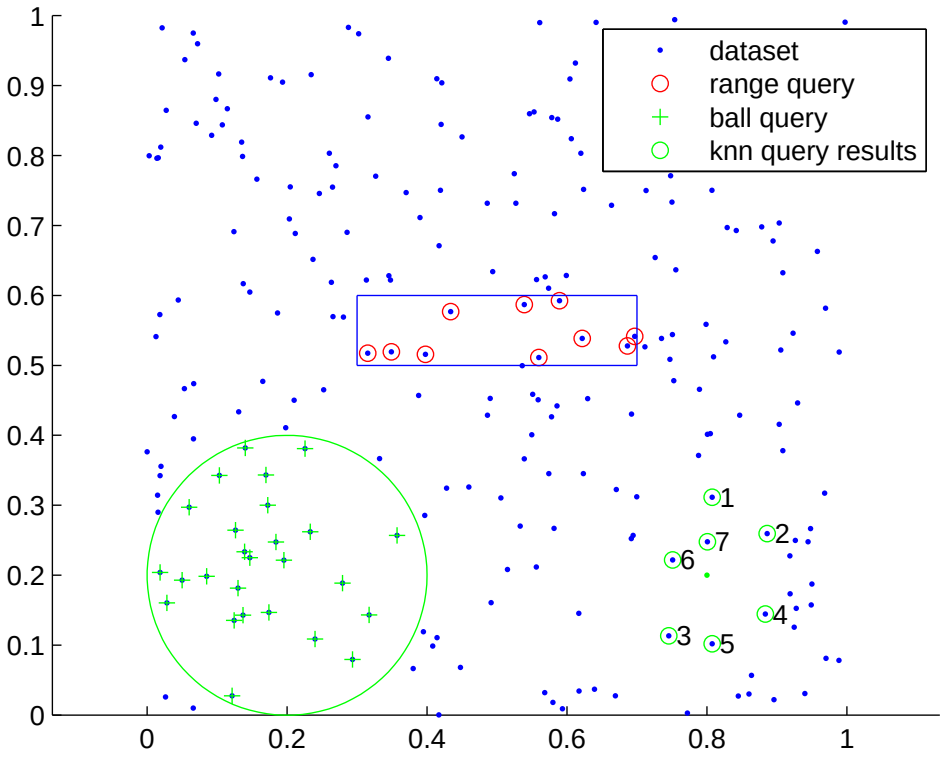

Figure III.6. Capabilities of KD-Tree library used in this work.

rectangles in 2D space as shown in Figure III.8. Note that if two rectangles (representing nanotubes) do not intersect, there is no possible way for their corresponding nanotubes to intersect. If two rectangles do intersect, their corresponding nanotubes might intersect, but it is not guaranteed. Therefore, if we use the KD-tree rectangular search function to find all nanotubes whose bounding boxes intersect, we can then use more expensive calculations to determine if the nanotubes actually intersect.

In order to use the KD-tree rectangular search function, a rectangular search region must be defined. For the 4D KD-tree used for the 2D nanotube model, the "'rectangular"' region is actually a 4D rectangular prism that has minimum and

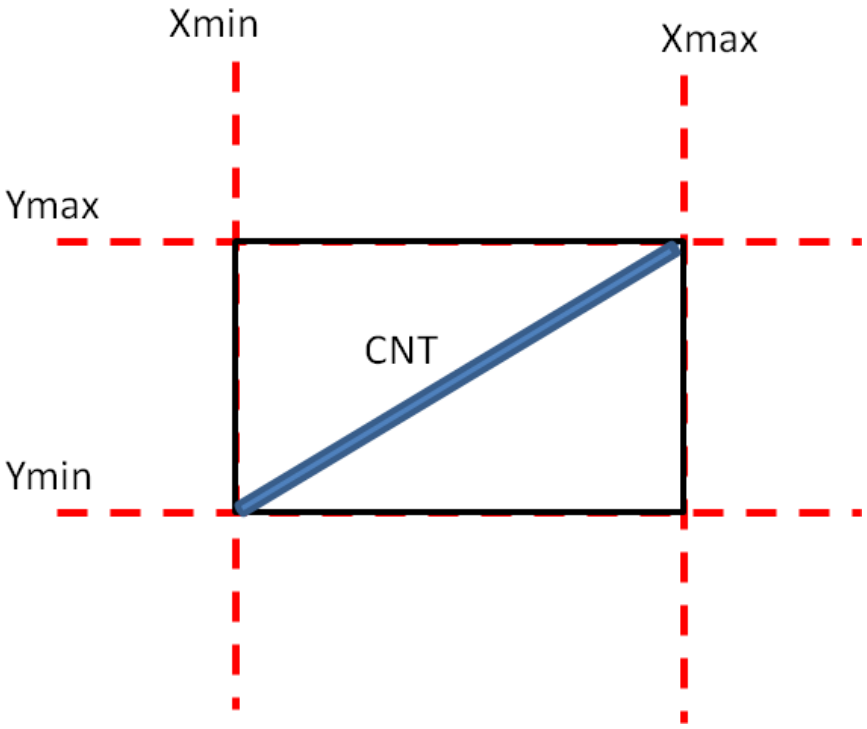

Figure III.7. Rectangular bounding box around nanotube.

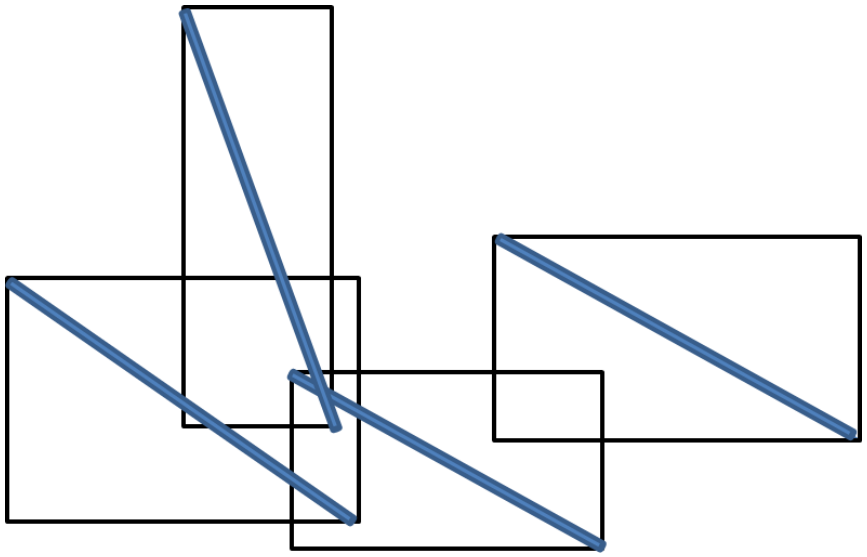

Figure III.8. Searching for intersecting rectangles.

maximum values for each of the four dimensions. It is convenient to label the four dimensions of the KD-tree as x_{min}, x_{max}, y_{min}, and y_{max}. While it is impossible to directly visualize the 4D search region, four of the eight parameters used to define the region are illustrated in Figure III.9. The CNT in the center of the figure is the reference CNT, and the algorithm finds all other CNTs whose bounding rectangles intersect the reference CNT's bounding rectangle. The search region parameters are based on the x-coordinates of the reference CNT as well as the length of the CNTs in the network. The search region is described by minimum and maximum values for the x_{min} dimension which are given in the figure as $x_{min-min}$ and $x_{min-max}$. Likewise, the search region is also described by minimum and maximum values for the x_{max} dimension. These are shown as $x_{max-min}$ and $x_{max-max}$. Parameters for $y_{min-min}$, $y_{min-max}$, $y_{max-min}$, and $y_{max-max}$ are not shown but are similarly defined. These eight parameters define a complete hyper-rectangular search region in 4D space. The KD-tree library uses this search region to efficiently determine all CNTs whose bounding rectangles intersect the reference CNT's bounding rectangle. This list of possible intersecting CNTs is then looped through, and the contact algorithm described in Section III.B is used to determine if the CNTs actually intersect. This entire procedure is repeated for each nanotube in the network. It should be noted that dividing the network region into separate bins that each have their own KD-tree could result in an even more efficient implementation, but this was not tested.

It is easy to extend the nanotube searching algorithm to three dimensions. Instead of each nanotube having a 2D bounding rectangle, a 3D bounding box is used to define each CNT. Each bounding box is defined by six parameters, x_{min}, x_{max},

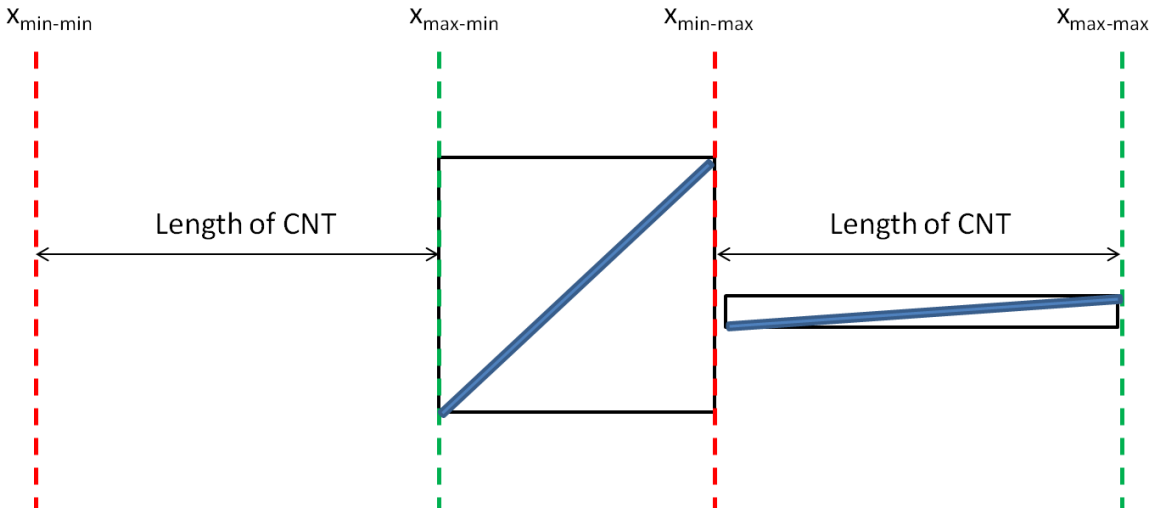

Figure III.9. Bounding coordinates for range search.

y_{min}, y_{max}, z_{min}, and z_{max}. The boxes can then be represented as points in 6D space, and they can be sorted using a 6D KD-tree. The problem of finding nanotubes that might intersect can then be visualized by finding all of the 3D bounding boxes that intersect, as shown in Figure III.10. The nanotubes are represented by the blue cylinders, and their bounding boxes are in black. Again, if the boxes do not intersect, there is no way for their corresponding nanotubes to intersect. If the boxes do intersect, their corresponding nanotubes might intersect. The more expensive contact calculation from Section III.B can then be performed to determine if they do intersect.

Similar to the 4D KD-tree, a hyper-rectangular search region must be defined in 6D space to determine if the boxes intersect. The 12 parameters that define this region are $x_{min-min}$, $x_{min-max}$, $x_{max-min}$, $x_{max-max}$, $y_{min-min}$, $y_{min-max}$, $y_{max-min}$, $y_{max-max}$, $z_{min-min}$, $z_{min-max}$, $z_{max-min}$, and $z_{max-max}$. Refer to Figure III.9 for how these parameters are defined.

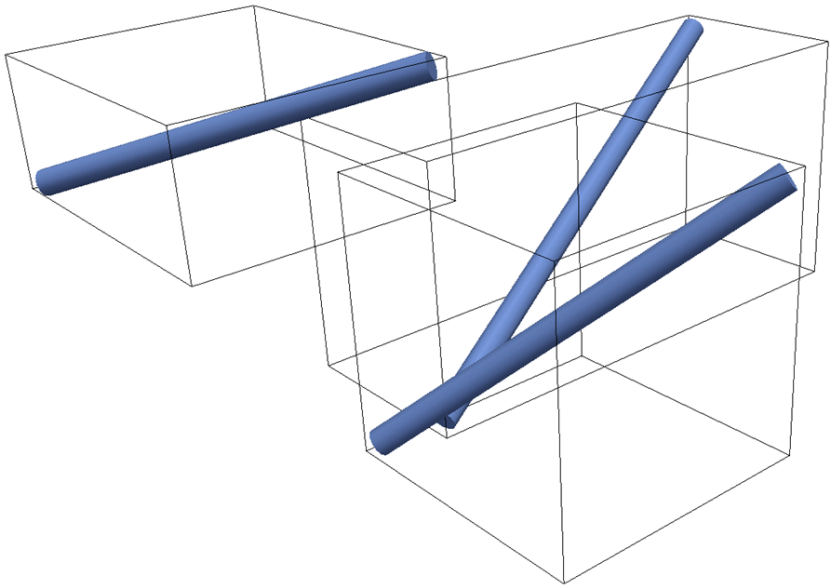

Figure III.10. Searching for intersecting boxes.

III.D. Efficient algorithm for calculating interacting eigenstrains

The method for calculating interacting eigenstrains presented in Section II.C.2 is essential for predicting more accurate elastic fields when many equivalent inclusions interact with each other. However, the method outlined can become computationally expensive when large numbers of inhomogeneities are modeled. For N inclusions, there is a $6N \times 6N$ system of equations that must be solved. In order to reduce the computational cost of the interacting eigenstrains, an algorithm was developed to truncate the interaction distance between individual inhomogeneities. A schematic representing this algorithm is given in Figure III.11.

The algorithm works by assuming that only inhomogeneities that are within a

specified distance from each other elastically interact. Referring to the schematic, a single inhomogeneity is chosen as the in-focus inclusion (shown in red). The specified interaction region around this inclusion is shown as the red dashed box. The KD-tree structure for the CNT network is used to find all of the inclusions within this interaction region (shown in blue). Any inclusion that crosses the boundary of the interaction region is included in the list of interacting inclusions. The interaction matrix described in Section II.C.2 is then constructed for the in-focus inclusion and the list of interacting inclusions around it. Finally, the interaction matrix is used to calculate the interacting eigenstrains for this collection of inclusions. However, only the interacting eigenstrain for the in-focus inclusion is extracted from the solution because the interacting eigenstrains for the out-of-focus inclusions may not be as accurate. For example, an inclusion that is just inside the interaction region boundary is most likely interacting strongly with inclusions outside the current region. Therefore, after saving the interacting eigenstrain for the in-focus inclusion, another inclusion is chosen as the in-focus inclusion, and the interaction region is moved accordingly. The interacting eigenstrains are calculated for this new interaction region, and the in-focus interacting eigenstrain is saved. This process is iterated until the interacting eigenstrain for each inclusion in the network is calculated.

III.E. Summary

This chapter provided details for specific algorithms that were implemented in the various nanotube network models. It is intended to be a supplement to the theory presented in Chapter II. The algorithms included methods to generate uniform

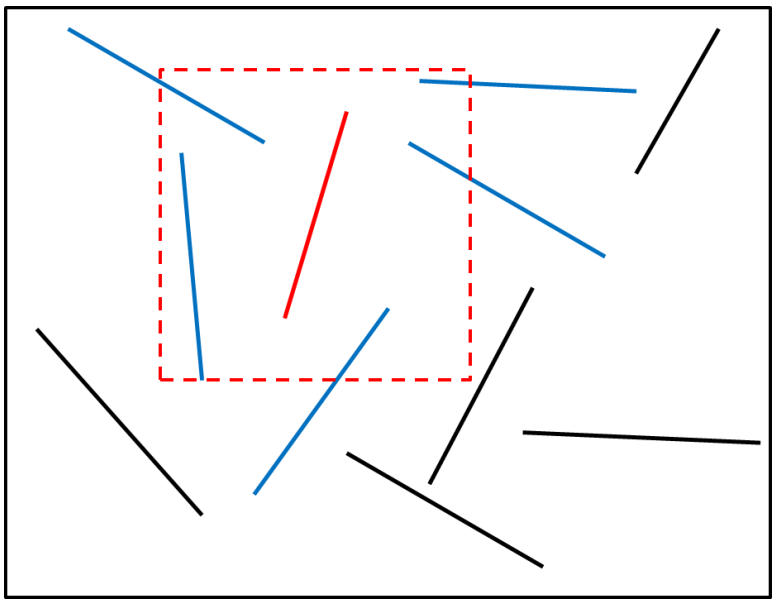

Figure III.11. Schematic of interacting eigenstrains algorithm.

distributions of CNTs, determine CNT contact in 2D and 3D, and more efficiently implement the FEA/Eshelby micromechanics framework for piezoresistivity modeling. It was also shown how many of the algorithms developed for this work utilize well known principles from computer graphics and computer science to facilitate the efficient modeling of carbon nanotube networks.

CHAPTER IV

ELECTRICAL CONDUCTIVITY OF 2D SWCNT THIN FILMS

White et al. [20] experimentally investigated the electrical conductivity of SWCNT thin films that were prepared using a method that carefully controls the amount of nanotube bundling. The authors observed percolation behavior that closely matched the ideal 2D network behavior predicted by an analytical percolation scaling law. They also observed a difference in percolation behavior between the thin films with highly exfoliated networks consisting of single nanotubes and partially exfoliated networks consisting of bundles of approximately 3-4 nanotubes. In order to explore possible explanations for this behavior, the 2D random resistor network model presented in Chapter II was used to investigate the electrical behavior of SWCNT thin films at various nanotube concentrations and exfoliation states. A summary of results from this investigation are given in this section.

The predicted sheet conductance as a function of CNT concentration is shown in Figure IV.1 for both highly exfoliated and partially exfoliated thin films. Note that the units for sheet conductance are Siemens $\cdot$ square ($S \cdot Sq$), where a square is a unitless measure of how many square regions of area the thin film has. The number of squares in a rectangular thin film will be equal to the aspect ratio of the rectangle (length/width). Each predicted data point represents the average of 10 unique realizations. The experimental results from White et al. are also shown for comparison. It is clear that neither the highly exfoliated nor partially exfoliated film predictions completely agree with experiment. However, the predicted partially

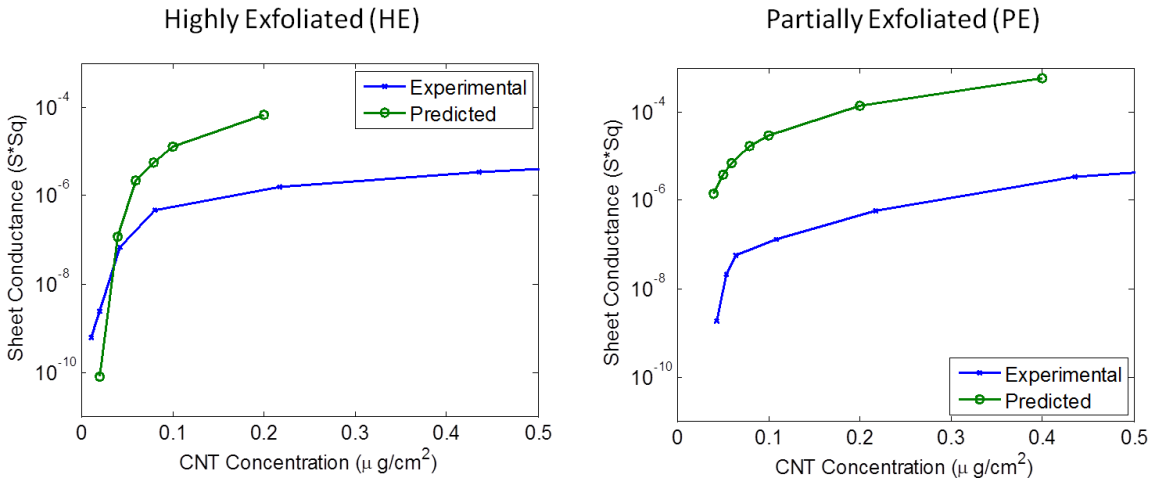

Figure IV.1. Predicted sheet conductance vs. CNT concentration for highly exfoliated and partially exfoliated networks. Experimental data from White et al. [20]

exfoliated percolation curve has the same shape as the experimental curve. From percolation theory, this indicates that the model is representative of the material's percolation behavior but is off by some scaling factor. Several parametric studies were performed to investigate what could account for this difference, and the results are presented in Section IV.B.

Contour plots of the electrical current flowing through two different nanotube networks are given in Figure IV.2. The networks are two realizations of the same nanotube concentration ($0.04\mu g/cm^2$). However, it is obvious that the current flowing through the network in Figure IV.2b is much higher than the current in Figure IV.2a. Because of this, the sheet conductance for the network in Figure IV.2a is $4.4 \times 10^{10}\ S \cdot \square$ and the sheet conductance in Figure IV.2b is $1.25 \times 10^{7}\ S \cdot \square$. There is a difference in conductance of three orders of magnitude between networks with the same CNT concentration. This illustrates the fact that randomness can play

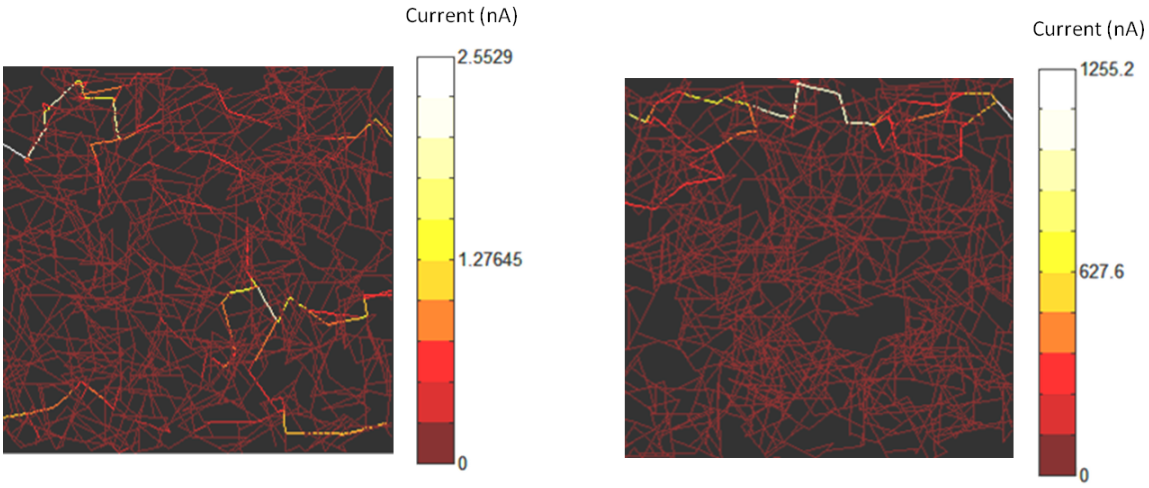

Figure IV.2. Electrical current distribution in nanotube network.

a large role in determining electrical properties, especially around the percolation threshold.

The effect of randomness is also tied to the effect of the chosen RVE size. Figure IV.3 shows the predicted conductances vs. nanotube concentration for three different sizes of RVE. For each concentration, 100 realizations were generated, and the predicted conductance for each realization is plotted as a separate point in the figures. The scatter in predictions is quite evident for the $1\mu m \times 1\mu m$ RVE. As the RVE size is increased, the scatter decreases as expected. This means that the effects of randomness can be negated somewhat by simply using a large RVE. However, the computational cost of generating and solving for the resistor networks goes up exponentially with increasing RVE size. It is therefore a good idea to understand how to use the smallest RVE size possible without losing too much accuracy in the results. One final thought on RVE size is that the use of SWCNT thin films in NEMS and MEMS devices could necessitate the total size of the device being small

enough for randomness to play a dominant role in device performance. For example, if a MEMS device used a SWCNT thin film that was the size of the $1\mu m \times 1\mu m$ RVE in Figure IV.3, there is a possibility that the conductance could vary by several orders of magnitude at some concentrations. This is obviously undesirable for many applications.

IV.A. Highly exfoliated networks

In order to understand how different network parameters affect the performance of the SWCNT thin film, a series of parametric studies was performed. The easiest parameters to study are the material properties used to describe the nanotubes and network connections. Recall that the nanotube resistivities and contact junction resistances were taken from experimental values in the literature. However, due to the great variability in nanotube and thin film processing, it is quite feasible that the experimental samples compared to in this study contain nanotubes with different material properties than originally assumed. For example, the contact resistance between metallic nanotubes was assumed to be 2.0×10^5 Ω, which was measured by Fuhrer et al. [83] This corresponds to the baseline curve in Figure IV.4, which shows the sheet conductance of highly exfoliated networks as functions of CNT concentration. The Metal-Metal 1 curve corresponds to a junction resistance of 1.0×10^6 Ω, the Metal-Metal 2 curve corresponds to 1.0×10^7 Ω, and the Metal-Metal 3 curve corresponds to 1.0×10^8 Ω. It is clear that varying this junction resistance causes orders of magnitude change in the sheet conductance of the networks.

Figure IV.5 presents the effect of varying the resistance of junctions between

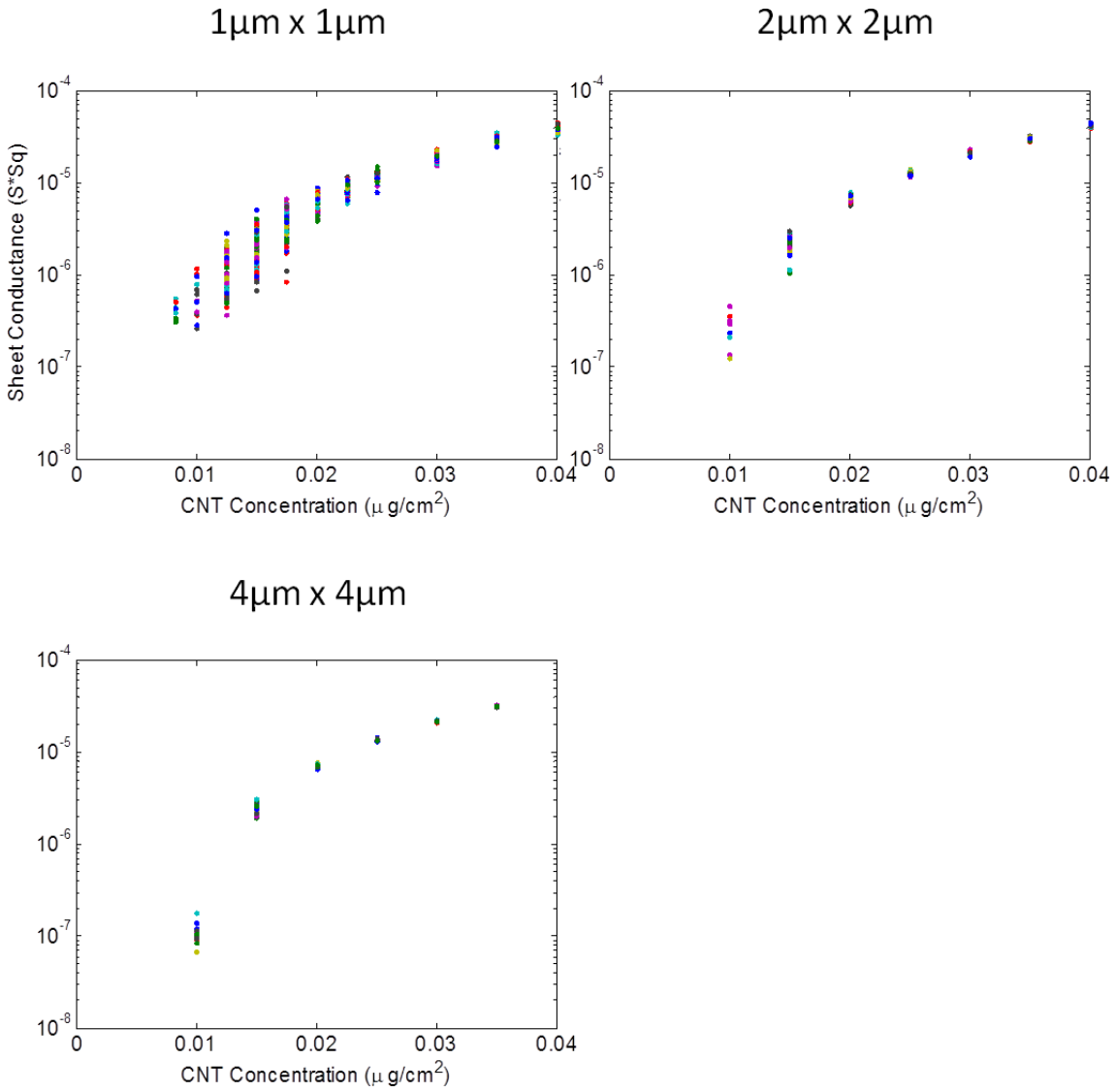

Figure IV.3. Predicted sheet conductances for different RVE sizes. Note that 100 realizations were computed for each CNT concentration.

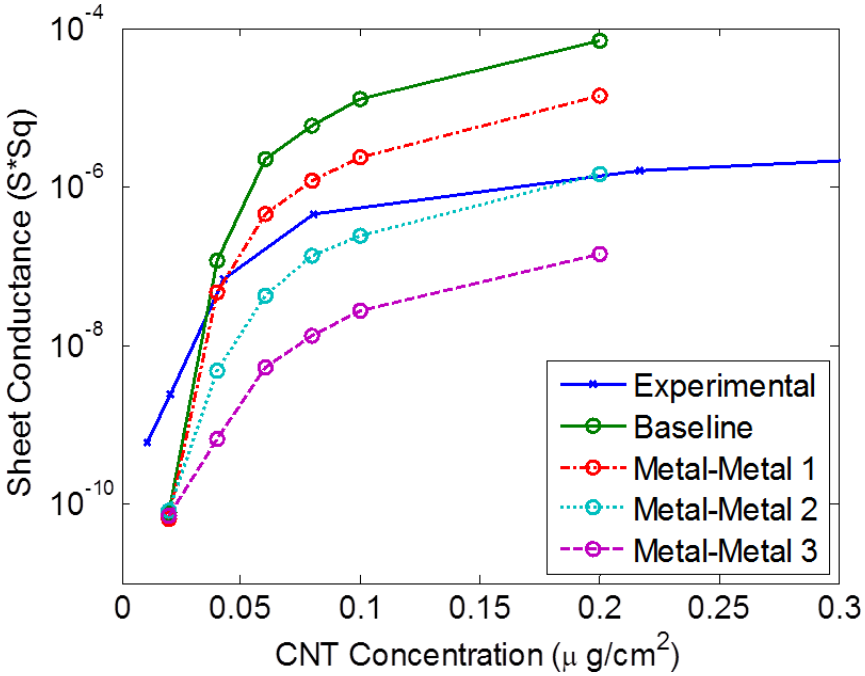

Figure IV.4. Highly exfoliated network conductance vs. CNT concentration for different values of metallic-metallic nanotube junctions. Experimental data from White et al. [20]

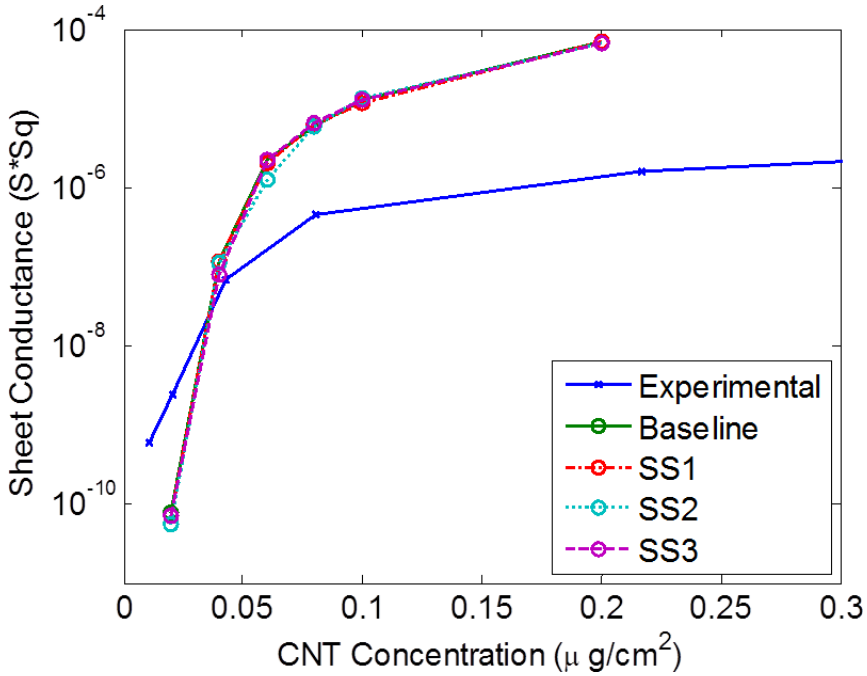

Figure IV.5. Highly exfoliated network conductance vs. CNT concentration for different values of semiconducting-semiconducting nanotube junctions. Experimental data from White et al. [20]

two semiconducting nanotubes. The baseline semiconducting-semiconducting (SS) junction resistance taken from the literature was 2.36×10^6 Ω. The SS1 curve corresponds to a junction resistance of 1.0×10^7 Ω, SS2 corresponds to 1.0×10^8 Ω, and SS3 corresponds to 1.0×10^9 Ω. Unlike varying the metallic-metallic junction resistance, varying the semiconducting-semiconducting resistance does not seem to change the overall conductance or percolation behavior of the networks.

The final parametric study performed on the highly exfoliated networks is given in Figure IV.6. The network sheet conductances vs. CNT concentration is plotted for different values of nanotube resistivities. The baseline resistivity taken from the literature was 13.0×10^3 $\Omega/\mu m$. The Tube Resistance 1 curve corresponds to a

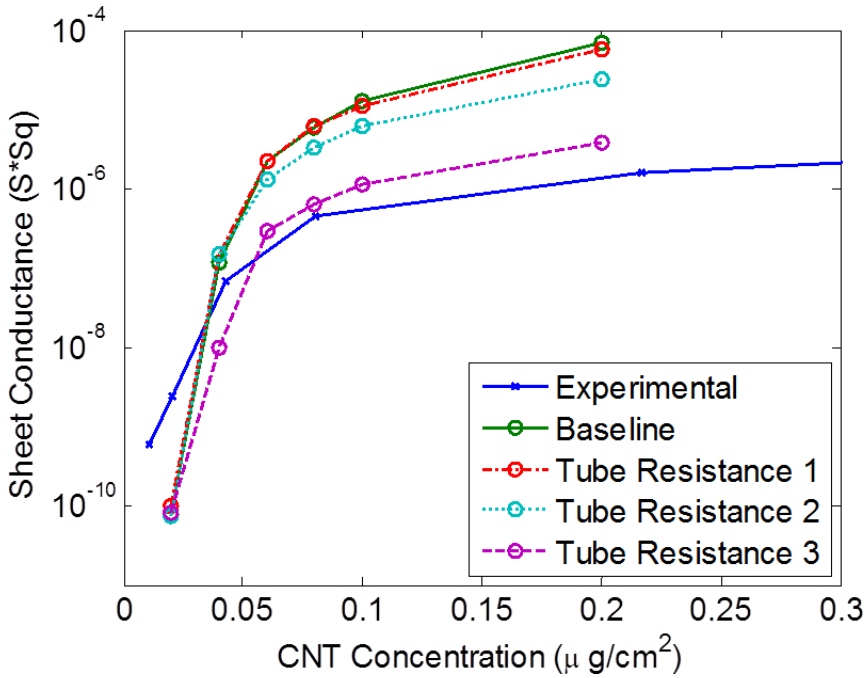

Figure IV.6. Highly exfoliated network conductance vs. CNT concentration for different values of nanotube resistivity. Experimental data from White et al. [20]

nanotube resistivity of $13.0 \times 10^4\ \Omega/\mu m$, Tube Resistance 2 corresponds to 13.0×10^5 $\Omega/\mu m$, and Tube Resistance 3 corresponds to $13.0 \times 10^6\ \Omega/\mu m$. It is clear from the figure that the nanotube resistivity can make a difference in the overall sheet conductance but only at very high values of nanotube resistivity. It is unlikely that the nanotube resistances would be this high in the experimental samples because that would indicate severe structural defects in the nanotubes. Therefore, it can be concluded that the dominant factor in predicting the network conductance is the junction resistance between metallic nanotubes.

IV.B. Partially exfoliated networks

Figure IV.7 presents the partially exfoliated network conductance as a function of CNT concentration for different values of junction resistances between bundles. Recall that the baseline value for the bundle-bundle resistance was assumed to be the value for metallic-metallic junctions (2.0×10^5 Ω), and this is probably the lowest possible resistance between bundles. Therefore, higher values of bundle-bundle junction resistances were investigated. The Bundle-Bundle 1 curve in Figure IV.7 corresponds to a junction resistance of 1.0×10^6 Ω, Bundle-Bundle 2 corresponds to 1.0×10^7 Ω, and Bundle-Bundle 3 corresponds to 1.0×10^8 Ω. The plot clearly shows that network conductance depends strongly on the bundle-bundle contact resistance. Additionally, it can be seen that increasing the contact resistance decreases the network conductance by several orders of magnitude.

The parametric studies for both the highly exfoliated and partially exfoliated networks were used to help calibrate the numerical model. The results of this calibration are given in Figure IV.8 below. The best predictions of network conductance obtained from varying the parameters given above are shown as functions of nanotube concentration for the two types of networks. The metallic-metallic junction resistance for the highly exfoliated network was assumed to be 3.0×10^6 Ω, and the semiconducting-semiconducting junction to be 1.0×10^7 Ω. The predicted conductances using these material properties are somewhat better than the initial predictions from Figure IV.1. However, the shape of the predicted percolation curve does not quite match the experimental curve. This means that the inaccuracy is due to some phenomenon or mechanism that is not currently modeled. The inclusion

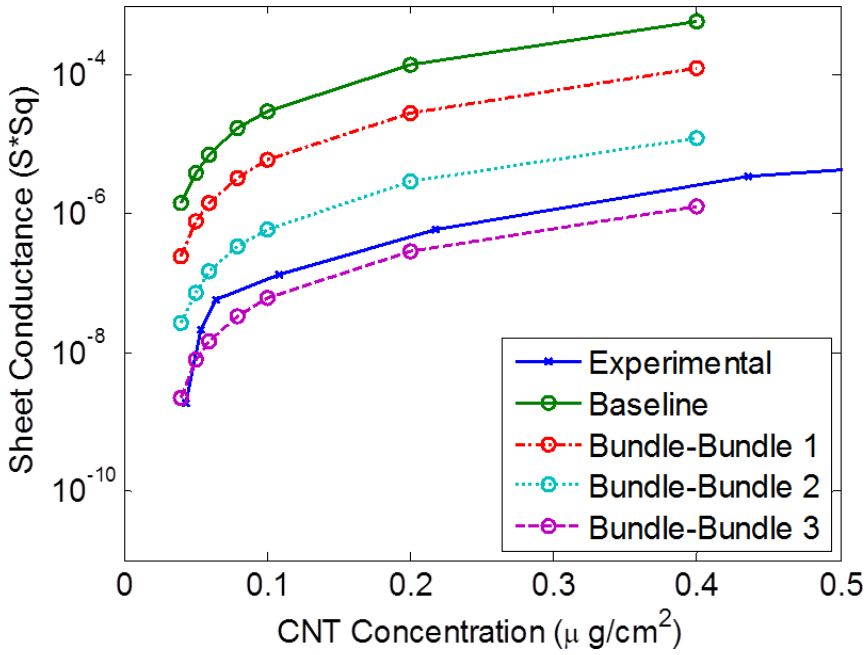

Figure IV.7. Partially exfoliated network conductance vs. CNT concentration for different values of junction resistance between nanotube bundles. Experimental data from White et al. [20]

of electron tunneling between nanotubes might correct this. Another possibility is that the complex interactions due to Schottky barriers at metallic-semiconducting junctions were not modeled accurately enough. On the other hand, the figure shows that the partially exfoliated network predictions can be made quite accurate simply by adjusting the junction resistance between nanotube bundles. The bundle-bundle junction resistance was assumed to be $5.0 \times 10^7\ \Omega$, which is quite reasonable considering the bundles are made up of a mix of semiconducting and metallic nanotubes.

IV.C. Summary

The 2D nanotube network model was used to investigate the electrical properties of SWCNT thin films. Networks consisting of highly exfoliated SWCNTs and

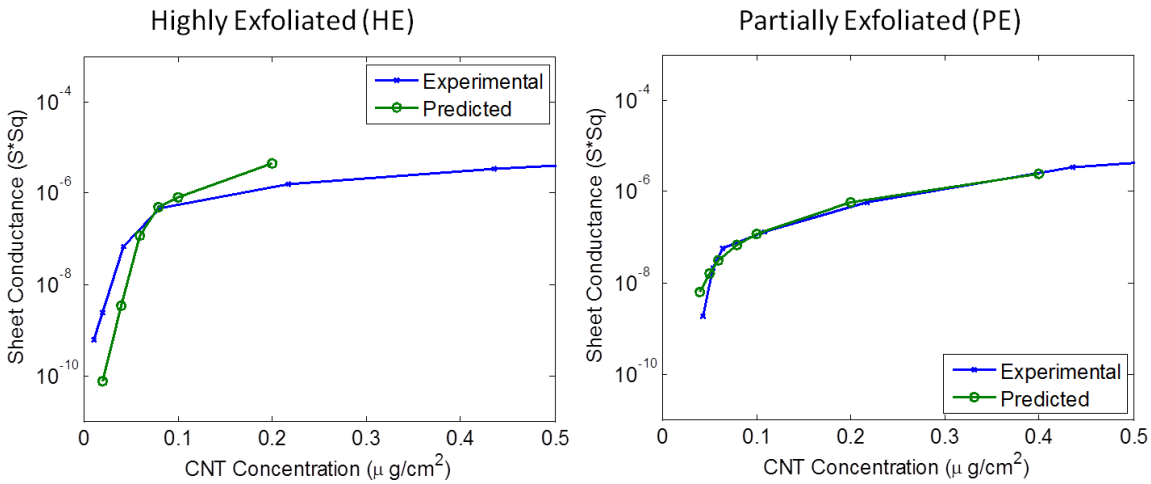

Figure IV.8. Best predictions from numerical simulations after calibrating model. Experimental data from White et al. [20]

partially exfoliated SWCNT bundles were considered and predictions were compared to experimental results in White et al. [20]. The effects of nanotube chirality were also considered. Parametric studies investigating the effects of RVE size, nanotube resistivity, and contact resistances between the SWCNTs of various chiralities were investigated. For the partially exfoliated networks, it was found that the model could be made to match experimental results if the contact resistance between nanotubes was calibrated to experiment. However, even after calibration, the highly exfoliated network model predicted a percolation curve with a different shape than the experimental results. This could indicate that it might be necessary to include the effects of electron tunneling between nanotubes in the model, or the effects of Schottky barriers at metallic-semiconducting junctions might need to be modeled differently to match experimental conditions. Additionally, it was found that the contact resistance between individual CNTs and bundles of CNTs greatly affects the conductivity of the film.

CHAPTER V

ELECTRICAL CONDUCTIVITY OF 3D CNT/POLYMER COMPOSITES

V.A. Predicted conductivity of MWCNT/epoxy

The MWCNT/epoxy material system from Hu et al. [13, 56] was investigated using the 3D nanotube network model. This material was chosen because of the experimental and numerical results available in the literature, which included electrical conductivity and piezoresistivity data. The system consisted of MWCNTs of length 5 μm and diameter 50 nm embedded in an epoxy matrix. The material system was also ideal for numerical studies because the aspect ratio of 100 allows much smaller models to be used than what would have been necessary for higher aspect ratio nanotubes. In comparison, SWCNTs with aspect ratios up to 10,000 are much more computationally expensive to investigate. Table V.1 gives the assumptions used to model the material system. The MWCNT resistance per unit length [17] and contact resistance between nanotubes [83] were taken from experimental results in the literature. As mentioned in the literature review in Chapter I, Hu et al. predicted the effective conductivity of the nanocomposites using a 3D random resistor network model similar to the model used in this work. However, it should be noted that the model of Hu et al. does not include the effect of a contact resistance between nanotubes that are touching.

As explained in Chapter II, part of the CNT network generation process includes

MWCNT length	5 μm
MWCNT diameter	50 nm
MWCNT resistance per unit length	13.0×10^9 Ω/m
Contact resistance	2.0×10^5 Ω
RVE length	25 μm

Table V.1. Network parameters for MWCNT/epoxy nanocomposite.

an algorithm that removes all nanotubes that are not connected to the network backbone between electrodes. It is easy to imagine that lower volume fraction networks will be less connected, and therefore more nanotubes will be discarded. Conversely, higher volume fractions have a higher percentage of nanotubes connected to the backbone, so fewer nanotubes will be discarded. This idea is clearly demonstrated in Figure V.1. The percentage of discarded CNTs is plotted as a function of nanotube volume fraction, and each data point represents an average of 50 unique network realizations. At lower volume fractions, almost all of the CNTs in the original network are discarded because there are too few nanotubes to connect the network between the electrodes. However, as volume fraction increases, the percentage of discarded CNTs decreases drastically because the connectedness of the network increases exponentially. These results are expected from basic percolation theory, but it is important to verify that the model is able to capture this behavior.

Figure V.2 depicts a 3D network that represents the MWCNT/epoxy system with a volume fraction of 0.006. This volume fraction was found to be right at the percolation threshold for the nanocomposite. For comparison, Hu et al. found

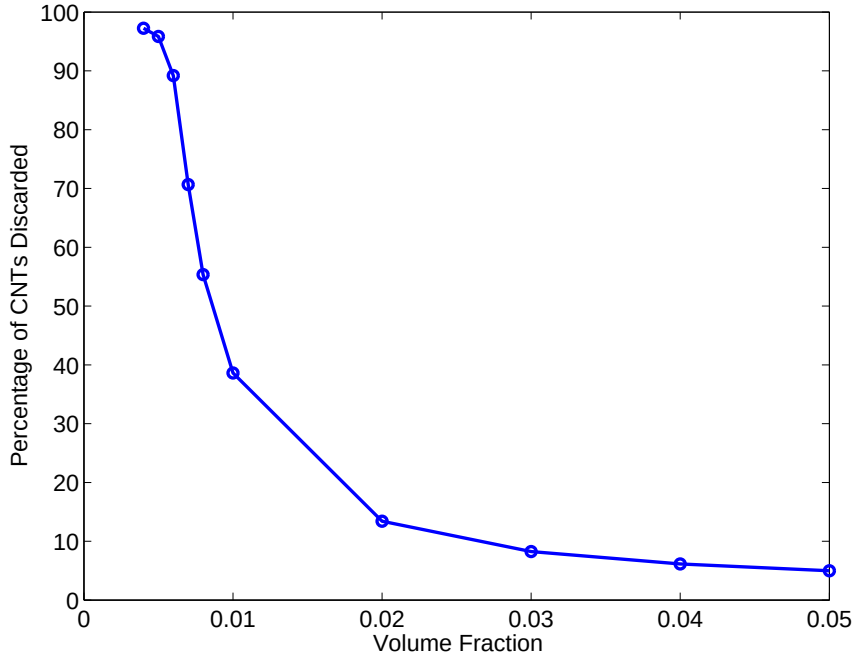

Figure V.1. Average percentage of CNTs discarded for the MWCNT/epoxy network.

the percolation threshold to be 0.006165. [56] Figure V.2a shows the entire CNT network before any nanotubes were discarded, and it is clear that even at this low volume fraction, the 9,549 nanotubes result in an indecipherable ink blot. Thus, Figure V.2b shows the connected network backbone of 1,676 CNTs that results after all non-connected CNTs were discarded. Even this sub-figure obscures the current carrying capacity of the network, so Figure V.2c shows only the connected CNTs that carry a current greater than 1.0×10^{-12} A. Additionally, the currents in each CNT are plotted as color contour values. Only 11.3% of the elements that make up the connected network backbone carry a current greater than 1.0×10^{-12} A. It is clear from the figure that there are only a small number of nanotubes that form a connected path that is able to bridge the two "electrode" sides of the RVE. Note

that the electrodes for this simulation are located on the +X/-X faces of the RVE. Furthermore, it can be seen in the figure that along this connected path, there are only a small number of nanotubes that carry most of the current in the network. This is similar to the results seen for the 2D networks in Chapter IV. The effective conductivity of the network is 0.0193 S/m.

In order to better understand the distribution of nanotubes that carry current in the 0.006 volume fraction network in Figure V.2, a histogram for the number of CNT elements in the network is plotted in Figure V.3. The x-axis is divided into 5 bins that represent ranges of current values. The median value of each bin is labeled. The y-axis gives the number of elements in each bin. It should be stressed that the y-axis does not represent the number of individual CNTs: it represents the number of finite elements associated with each bin. Recall from Chapter II that each CNT is divided up into a number of elements during the RVE generation process. However, because all of the CNTs in a given network have a similar number of elements, the figure still provides a measure of the number of CNTs associated with each bin. This type of plot is useful because it shows the distribution of current in the network. For this particular network, the largest bin represents the smallest amount of current, and there are very few elements that have more than about $1.0 \times 10^{-}7$ A. This is further evidence that only a a small number of CNTs carry most of the current in the network. Additionally, it is evident that the distribution of current in the network is highly non-Gaussian.

A network with a volume fraction of 0.007 is shown in Figure V.4. Only the nanotubes that carry a current of 1.0×10^{-12} A or greater are shown, and they are

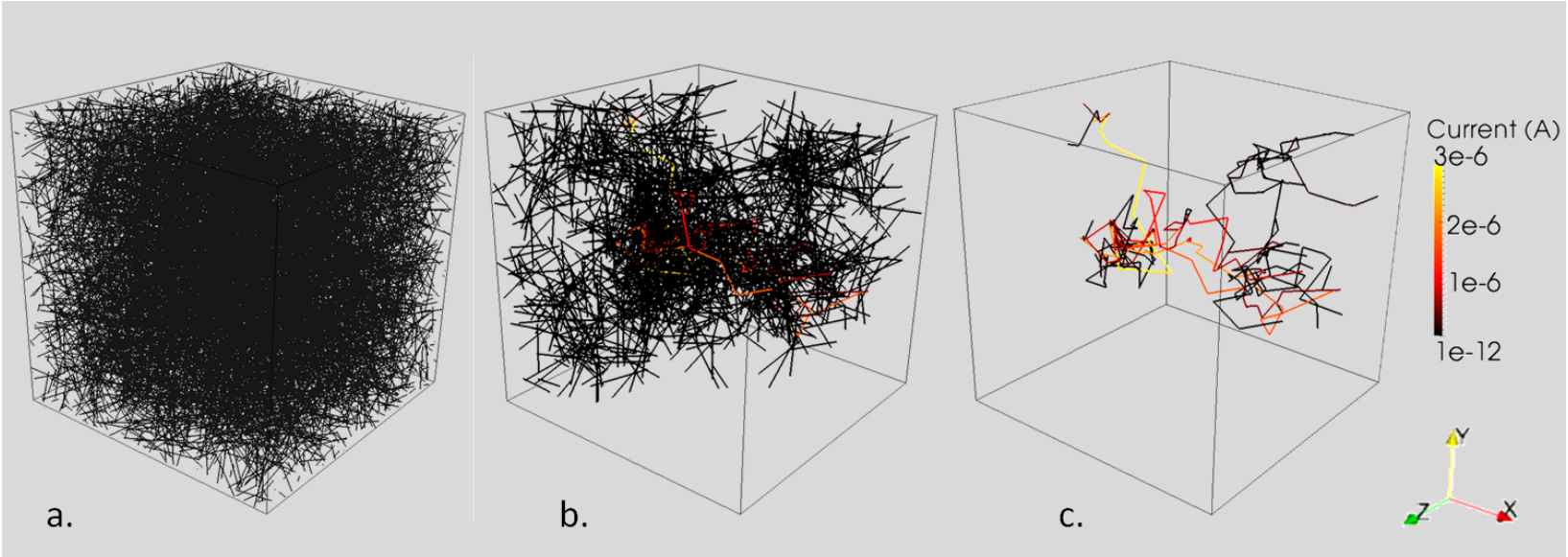

Figure V.2. MWCNT/epoxy network with Vf=0.006. Contour values for electrical current are only plotted on CNTs that carry more than 1.0×10^{-12} A.

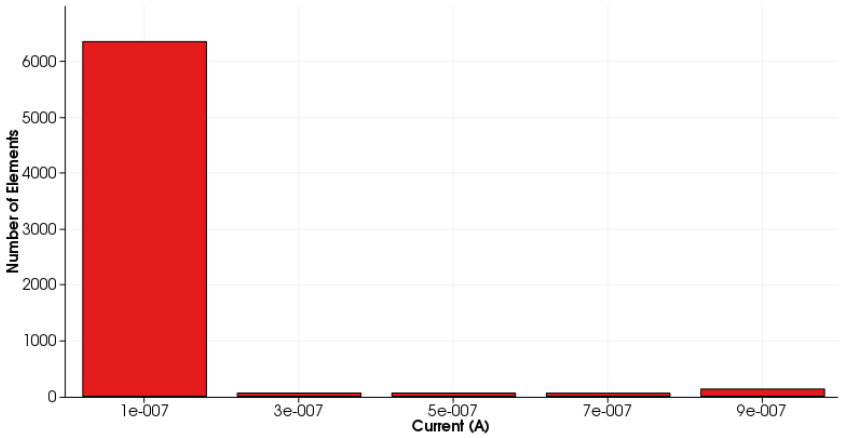

Figure V.3. Distribution of CNT elements that carry current. MWCNT/epoxy network with Vf=0.006.

colored according to the electrical current in each nanotube. Compared to the 0.006 volume fraction network, the 0.007 volume fraction network has a few more conductive paths that carry current through the percolated network. However, compared to the total number of nanotubes in the network (11,140), only 3,166 CNTs are actually connected to the network backbone. Moreover, only 17.7% of the elements that make up the connected backbone carry a current greater than 1.0×10^{-12} A. Also note that the contour legend indicates the maximum current in the network is higher than the maximum current in the 0.006 volume fraction network. The effective conductivity of the network is 0.0366 S/m, which is higher than the Vf=0.006 network as expected.

A network with a volume fraction of 0.01 is shown in Figure V.5. It is clear from the figure that the network is well past the percolation threshold, as a very large percentage of the nanotubes carry current. Of the 15,915 CNTs that make up the entire network, 9,799 CNTs are connected to the network backbone, and 39.2%

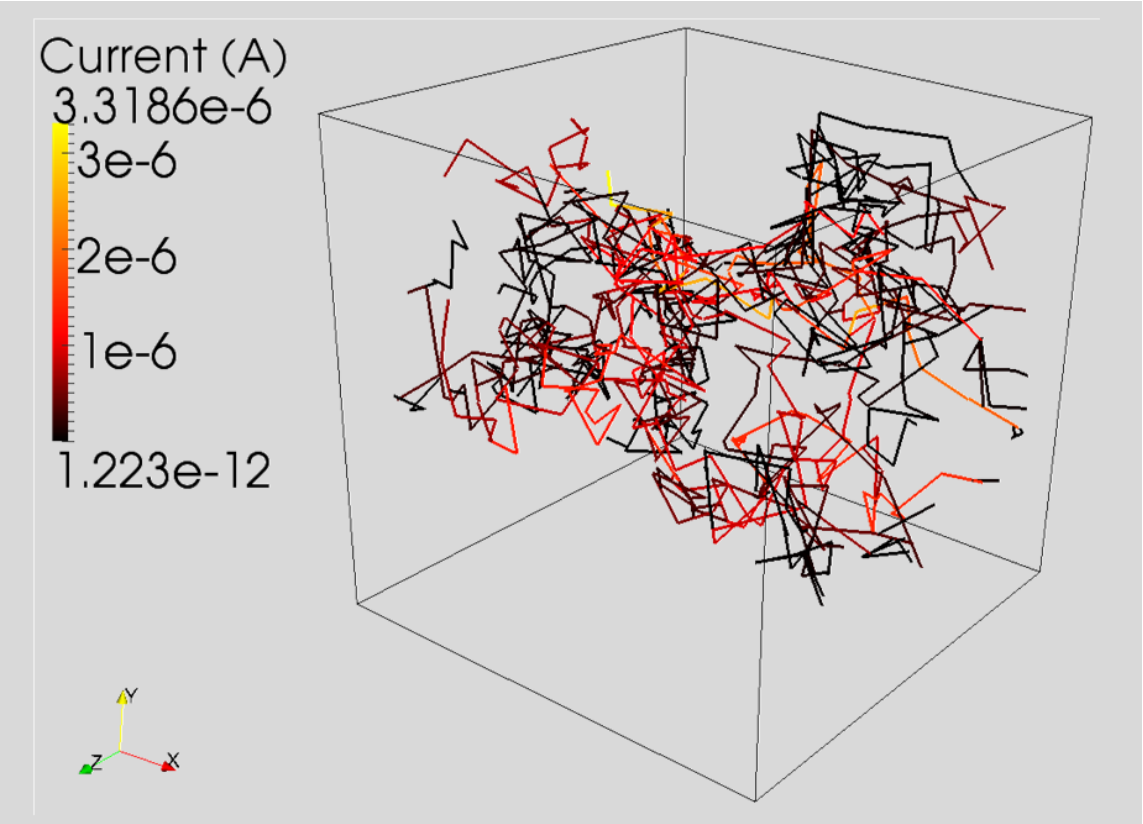

Figure V.4. MWCNT/epoxy network with Vf=0.007. Contour values for electrical current are only plotted on CNTs that carry more than 1.0×10^{-12} A**.**

of the elements in the connected backbone carry a current greater than 1.0×10^{-12} A. The maximum current is also higher than the maximum currents in Figures V.2-V.4, which is expected. The effective conductivity of the network is 0.739 S/m.

A network with a volume fraction of 0.05 is shown in Figure V.6. There are 79,577 CNTs in the network, and 75,562 of those are connected to the network backbone. Additionally, 86.3% of the elements in the connected backbone carry current greater than 1.0×10^{-12} A. The maximum network current is also larger than the networks with lower volume fraction shown previously. The effective conductivity of

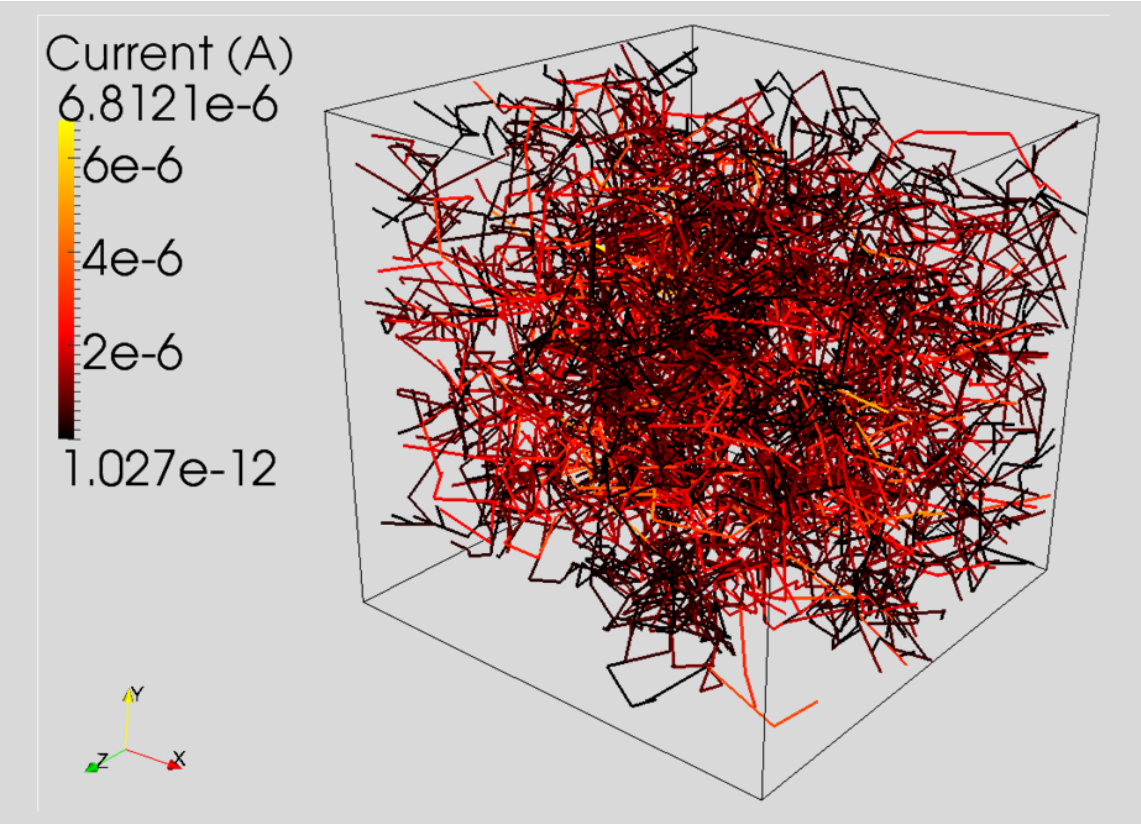

Figure V.5. MWCNT/epoxy network with Vf=0.01. Contour values for electrical current are only plotted on CNTs that carry more than 1.0×10^{-12} A**.**

the network (82.8 S/m) is the highest conductivity predicted for this material, which is expected. It is clear from Figures V.2-V.6 that higher volume fractions yield more current-carrying CNTs which in turn yield greater conductivities. Furthermore, instead of only a few CNTs forming pathways for the current, there are many CNTs that form pathways between the electrodes. Thus, the current distribution throughout the network is more homogeneous for higher volume fraction networks.

The current distribution for the network in Figure V.6 is plotted as a histogram in Figure V.7. The histogram for the 0.05 volume fraction network is very different

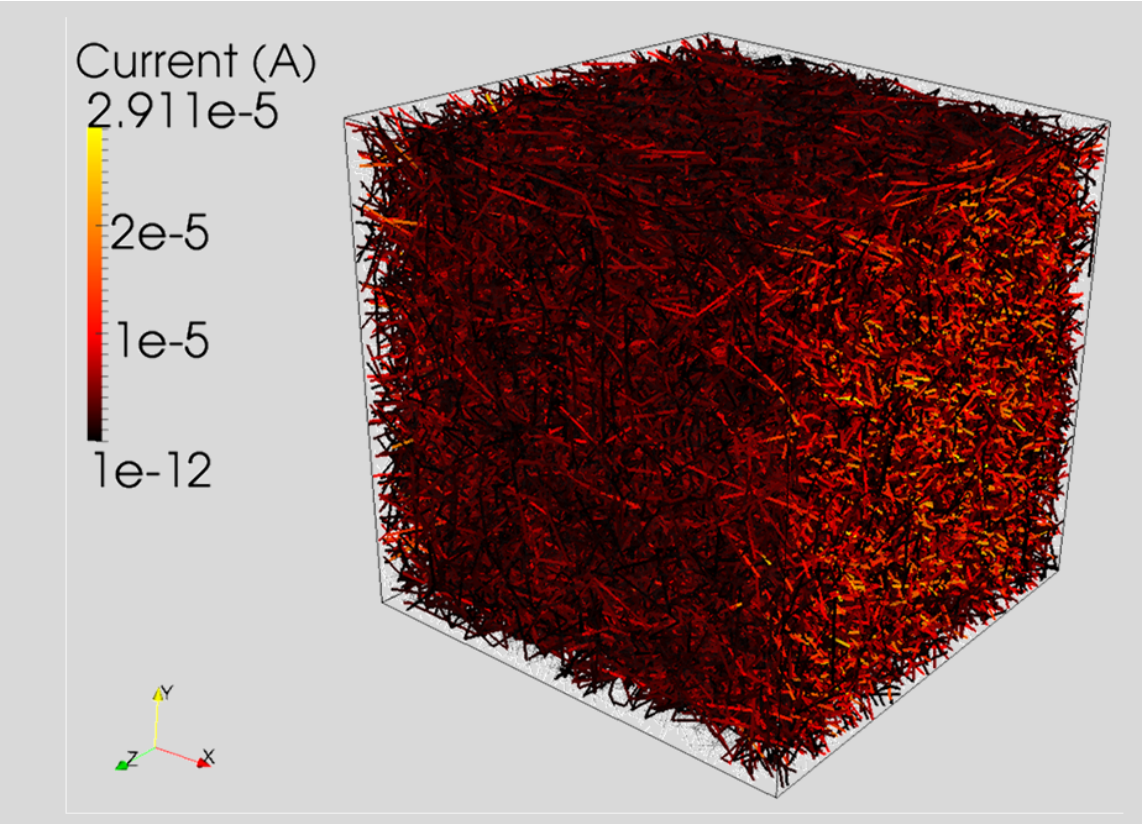

Figure V.6. MWCNT/epoxy network with Vf=0.05. Contour values for electrical current are only plotted on CNTs that carry more than 1.0×10^{-12} A**.**

from the histogram fro the 0.006 volume fraction network (Figure V.3). For the Vf=0.05 network, the majority of the CNT elements are located in the highest-current bin. This is expected because almost all of the nanotubes in this network carry current.

The variation of effective conductivity as a function of nanotube volume fraction is given in Figure V.8 along with the experimental and numerical results from Hu et al. The results from Hu et al. were digitized from their published figures in [56]. For each data point from the current model, 50 unique realizations were analyzed,

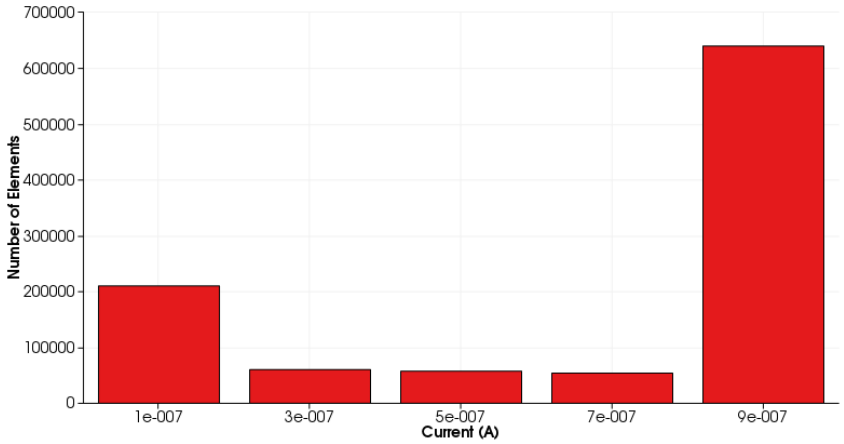

Figure V.7. Distribution of CNT elements that carry current. MWCNT/epoxy network with Vf=0.05.

and the average conductivity for each volume fraction is plotted in the figure. It is apparent in the plotted data that the numerical model in this work actually does a better job predicting the network conductivity than the numerical model from Hu et al. This is most likely due to the fact that the Hu et al. model neglects contact resistance between nanotubes.

Figure V.9 gives the effect of assuming different RVE sizes in the model. Up to this point, the model for the MWCNT/epoxy system has assumed a cubic RVE with sides of length 25 μm. This is the RVE size used by Hu et al., and they claimed that this RVE size was sufficiently large to capture the representative electrical conductivity of the material. However, this assumption was verified in this work by assuming RVE lengths of 12.5 μm and 50 μm and analyzing the resulting predictions. The results are plotted in Figure V.9 with each predicted data point again representing the average of 50 unique network realizations. Surprisingly, the size of the RVE does not seem to have much of an effect on the average predicted conductivity. However,

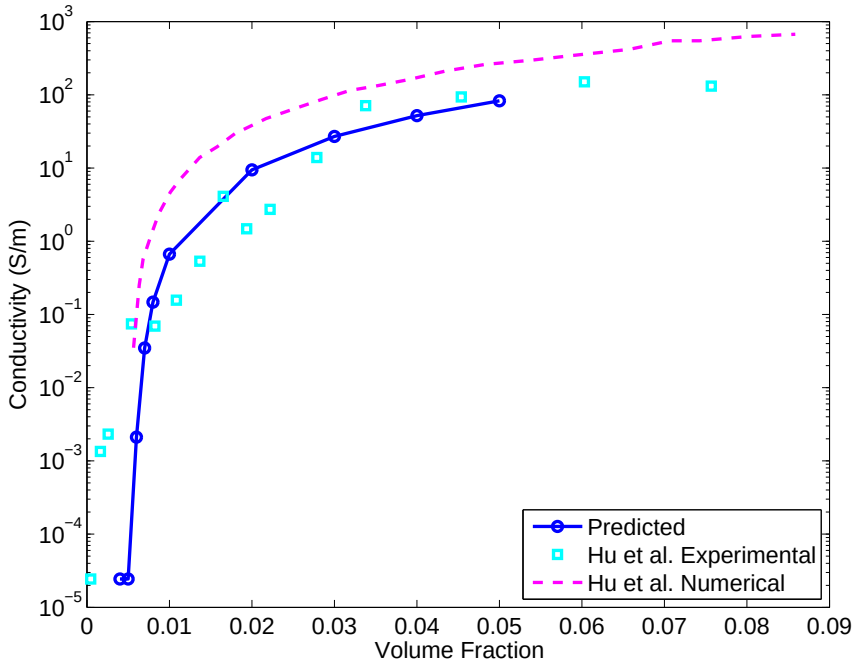

Figure V.8. Predicted MWCNT/epoxy conductivity as a function of volume fraction compared to experimental and numerical results from Hu et al. [13, 56]

the figure is not able to show that there is more scatter in the data for the smaller RVE sizes, as seen in the 2D network results in Chapter IV.

This scatter is depicted in Figure V.10 which gives the coefficient of variation of the distribution of network conductivities for each RVE size. The coefficient of variation is defined as the standard deviation of the distribution divided by the mean of the distribution. It is used here in lieu of standard deviation because the network conductivity values vary exponentially over the range of volume fractions considered. The standard deviation is not a good measure of scatter for this type of data set because it is too heavily biased by values that are orders of magnitude larger than the minimum distribution value. However, since the coefficient of variation is

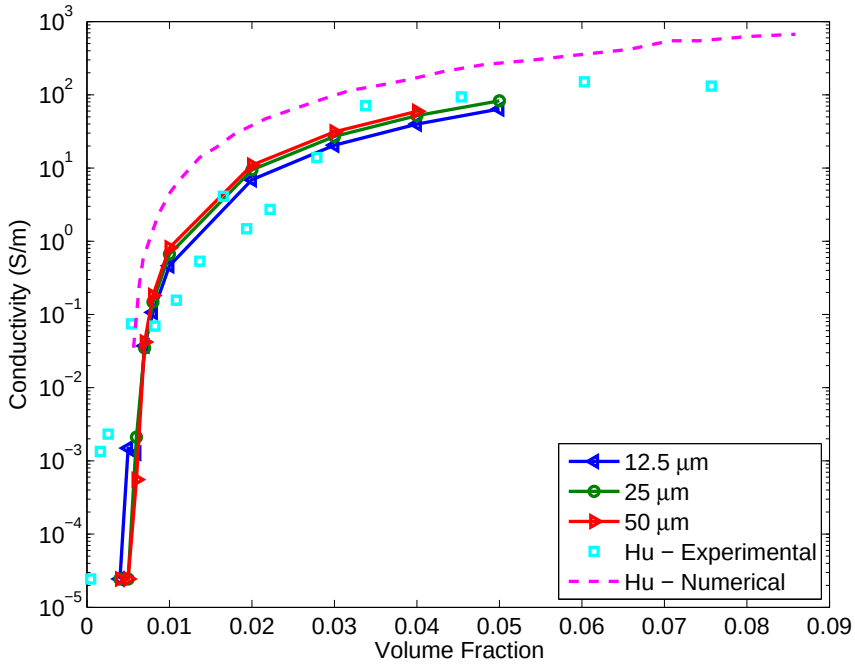

Figure V.9. Effect of RVE size on predicted MWCNT/epoxy conductivity.

normalized by the distribution mean, the coefficients of variation for the network conductivities can be readily compared to each other. The coefficients of variation in Figure V.10 show that the scatter decreases with increasing RVE size and increasing volume fraction, as expected. Additionally, it can be deduced from the figure that using the larger 50 μm RVE size does not decrease the variation much as compared to the 25 μm size. Therefore, the 25 μm size will be used henceforth for this material system in order to decrease computational costs while maintaining accuracy.

Another consideration in this analysis was the number of unique RVEs needed to get accurate average properties. Several analyses were run using identical network parameters, but the number of RVEs used to calculate the average conductivities was varied. The results of this study are given in Figure V.11. The average network

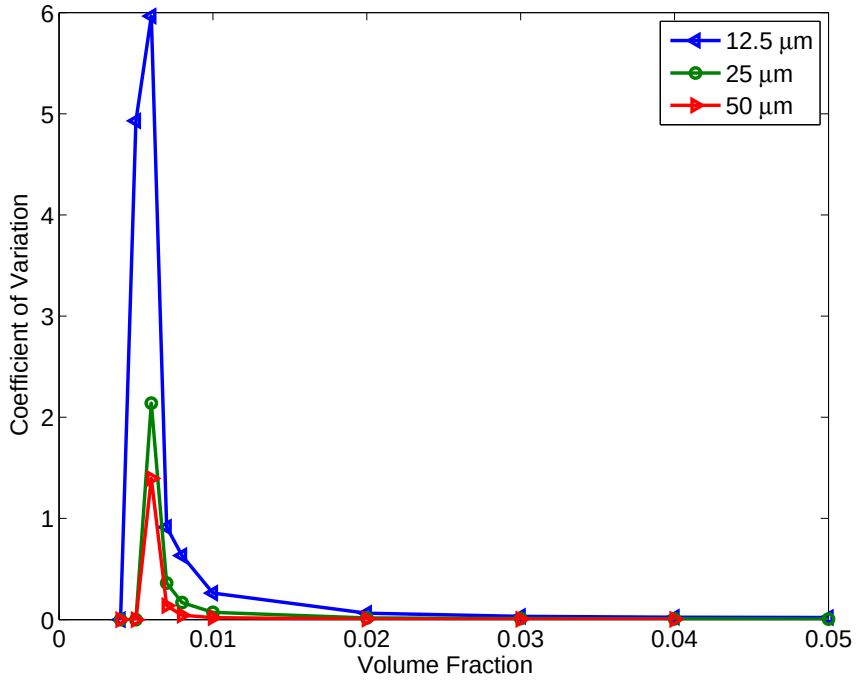

Figure V.10. Effect of RVE size on conductivity coefficient of variation for MWCNT/epoxy.

conductivities are plotted for sets of 10, 25, 50, 75, and 100 RVEs. The average conductivity values are again surprisingly similar for the different numbers of RVEs considered. Except for some noticeable scatter in the data points at a volume fraction of 0.006, the plots are nearly indistinguishable.

The coefficient of variation is again used to investigate the amount of scatter in Figure V.12. The coefficients of variation for the network conductivities at each volume fraction are plotted for sets of 10, 25, 50, 75, and 100 RVEs. The data shows that the most variation in conductivity values occurs close to the percolation threshold and decreases as volume fraction increases. It should be noted that the variation in conductivities at the percolation threshold are skewed because there

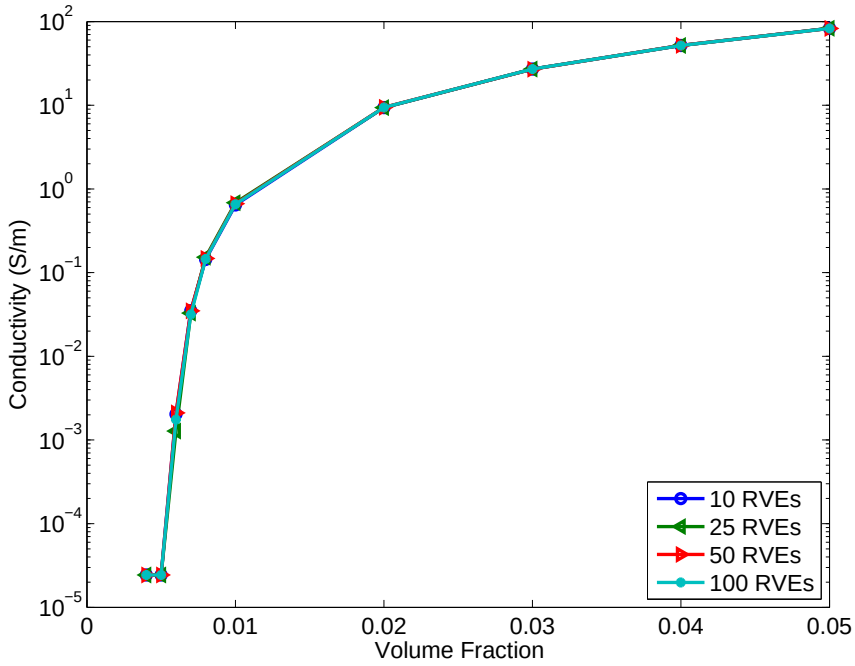

Figure V.11. Effect of number of RVEs on predicted MWCNT/epoxy conductivity.

is some percentage of networks at this volume fraction that do not form complete spanning networks. The resistor network model is unable to calculate an effective conductivity for these cases, so the conductivity is assumed to be that of the polymer matrix. Thus, the scatter in conductivities is higher. The results in Figure V.12 give reasonable justification to use sets of 50 RVEs to calculate average properties for this material system because the coefficient of variation does not decrease noticeably with greater numbers of RVEs. Therefore, sets of 50 RVEs with dimensions of 25 μm will be used henceforth for this material system.

Based on the 2D network results in Chapter IV, the contact resistance between nanotubes was expected to have a significant effect on electrical conductivity. Thus, a parametric study with varying contact resistances was performed, and the predicted

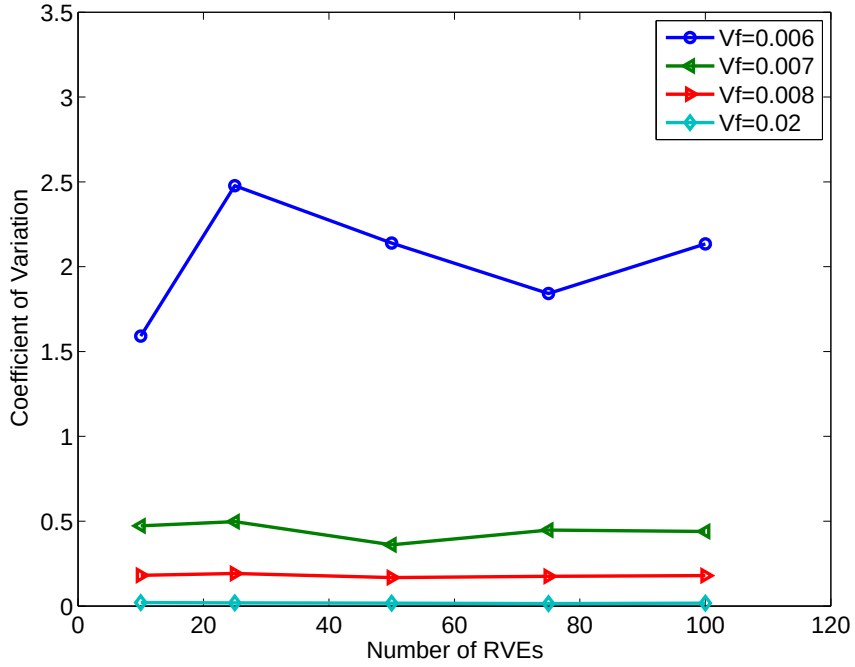

Figure V.12. Effect of number of RVEs on conductivity coefficient of variation for MWCNT/epoxy.

conductivities from this study are plotted in Figure V.13. Contact resistances of 2.0×10^5 Ω and 2.0×10^6 Ω were assumed. It should be noted that 2.0×10^5 Ω is the contact resistance measured experimentally by Fuhrer et al. [83] Additionally, an extremely small contact resistance of 0.01 Ω was chosen to approximate the effect of having zero contact resistance. The approximately zero contact resistance case provides a more fair comparison to the numerical model of Hu et al. because they did not assume any contact resistance in their model. Note that a contact resistance of exactly zero could not be used because this would cause the system of finite element equations to be singular. The figure shows that assuming this small contact resistance value results in predictions that are almost identical to the model of Hu et al. It is clear from the figure that using this value for the contact resistance yields very good predictions for

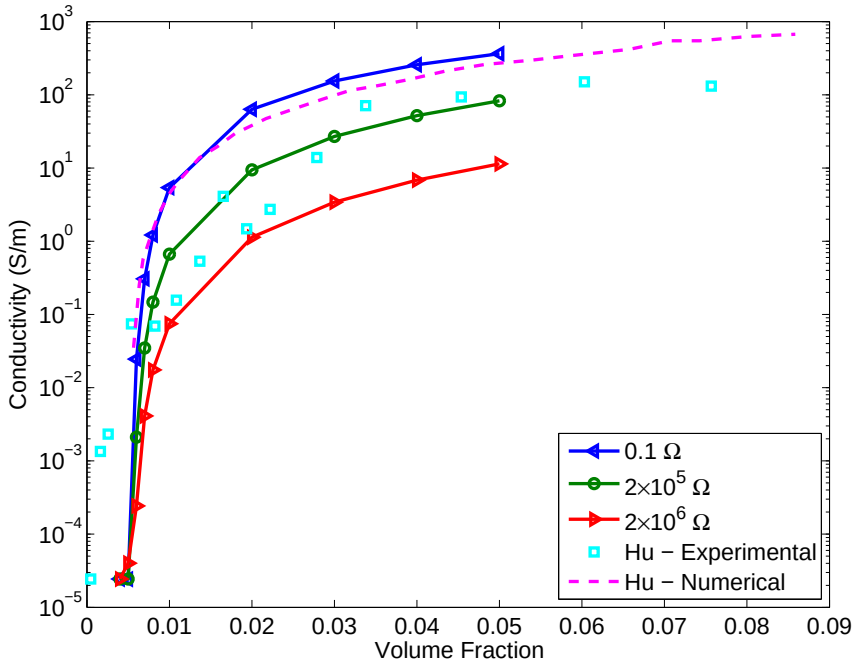

Figure V.13. Effect of assumed contact resistance on predicted MWCNT/epoxy conductivity.

the effective conductivity. Increasing the assumed contact resistance to 2.0×10^6 Ω results in lower predicted conductivity values, which effectively shifts the predicted conductivity curve downward. This makes good qualitative sense because the extra resistance in the network should decrease network conductivity.

Because the exact lengths of carbon nanotubes are difficult to identify experimentally, it is important to investigate the effect different nanotube lengths have on the effective conductivity of the nanocomposite. Figure V.14 presents the effective conductivity of the MWCNT/epoxy system as a function of CNT volume fraction for several different assumed CNT lengths. The predicted data points are again the average values from 50 unique network realizations. In addition to the 5 μm length already analyzed, CNT lengths of 2.5 μm and 10 μm were also analyzed. The results

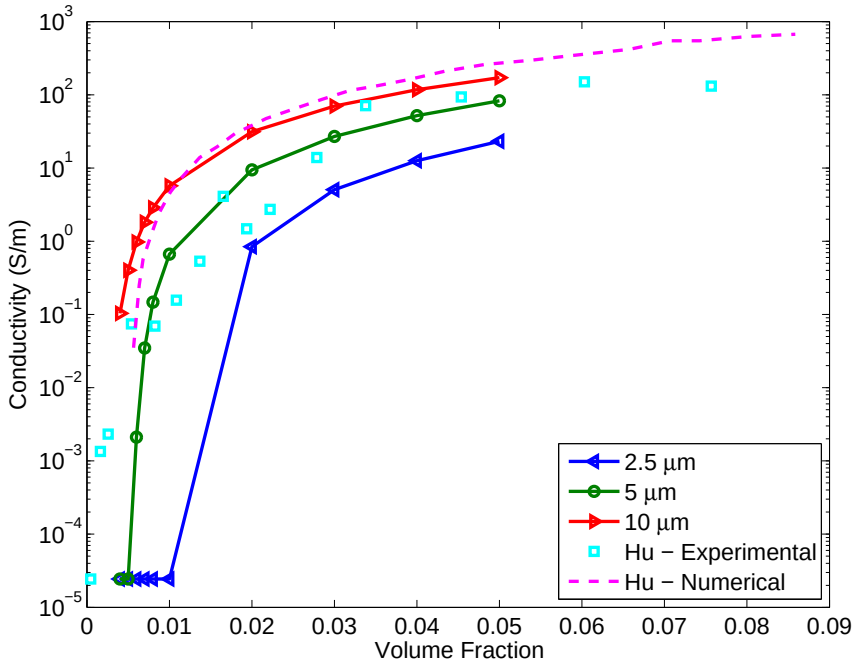

Figure V.14. Effect of CNT length on predicted MWCNT/epoxy conductivity.

indicate that increasing the length of the nanotubes shifts the predicted conductivity curve toward lower volume fractions. This makes qualitative sense because longer nanotubes result in a higher probability that a percolating network can form at lower volume fractions. Furthermore, this effect has been observed in the literature for various CNT/polymer materials. [13, 32, 47]

The electrical properties of the individual nanotubes could also affect the network conductivity of the composite. Therefore, the resistance per unit length of the nanotubes was varied in order to investigate how sensitive the network conductivity is to this effect. Figure V.15 gives the effective network conductivity as a function of nanotube volume fraction for CNT resistances of $13 \times 10^8\ \Omega/m$, $13 \times 10^9\ \Omega/m$, $13 \times 10^{10}\ \Omega/m$. These resistances per unit length correspond to conductivities of

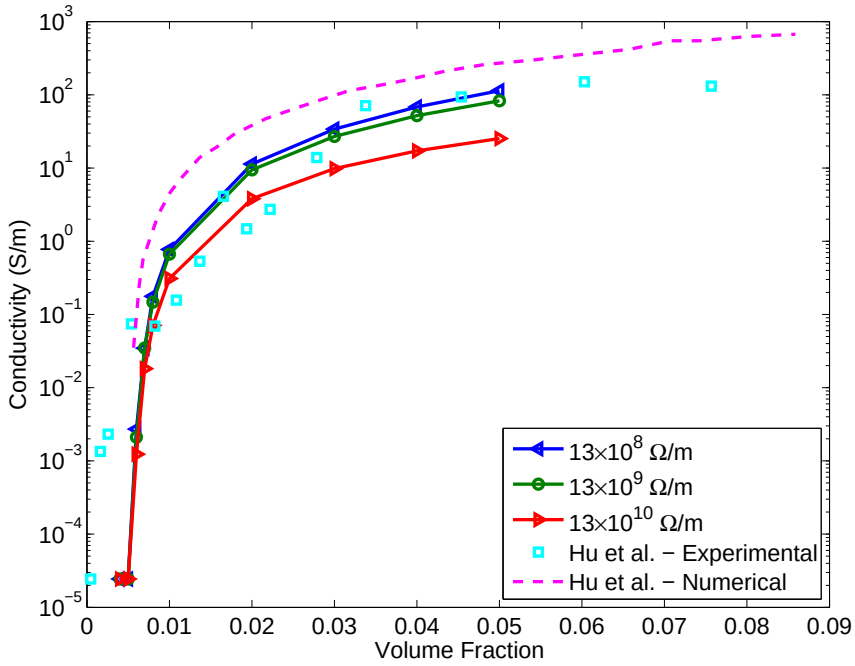

Figure V.15. Effect of CNT resistance on predicted MWCNT/epoxy conductivity.

3.9×10^5 S/m, 3.9×10^4 S/m, and 3.9×10^3 S/m, respectively. Recall that 13×10^9 Ω/m is the material property used in the previous parametric studies for this material system, and it was measured experimentally in the literature. [17] The results show that increasing the nanotube resistance causes a decrease in network conductivity, as expected. This is because increasing nanotube resistance effectively increases the average resistance value for each resistor in the resistor network. It has been shown that defects in the CNT atomic structure can increase CNT resistance. Thus, assuming higher resistance CNTs in the computational model could provide a way to approximate material systems with nanotubes damaged from processing conditions.

V.B. Predicted conductivity of MWCNT/polypropylene

Chu et al. [108] investigated the conductivity of MWCNT/polypropylene (PP) nanocomposites that had been processed using a unique nanotube disentanglement process. The disentangled nanotubes result in nanocomposites with a high level of nanotube dispersion, which leads to lower percolation thresholds than what can be achieved with pristine, entangled MWCNTs. This is an ideal experimental system with which to compare the proposed 3D network model because the well dispersed nanocomposite allows the effects of nanotube agglomeration to be neglected. The assumptions used to model the material are given in Table V.2. The MWCNT length and diameter represent average values from Chu et al., but it should be noted that the MWCNTs used in that work had a large distribution in lengths that could not be measured accurately. The MWCNT resistance per unit length was again assumed to be $13.0 \times 10^9\ \Omega/m$, which was taken from experimental measurements in Topinka et al. [17].

MWCNT length	$3\ \mu m$
MWCNT diameter	$10\ nm$
MWCNT resistance per unit length	$13.0 \times 10^9\ \Omega/m$
Contact resistance	$2.0 \times 10^5\ \Omega$
RVE length	$15\ \mu m$

Table V.2. Network parameters for MWCNT/PP nanocomposite.

Predicted conductivity values for the MWCNT/PP system are shown in Figure V.16, along with the experimental results from Chu et al. The model assumes the nanotubes are 3 μm long and 10 nm in diameter. It is clear from the results that the predicted conductivity values are much higher than the experimental results. This is an unexpected result since the model was reasonably accurate for the MWCNT/epoxy system. Determining the cause of this discrepancy is important to understanding the validity of the model.

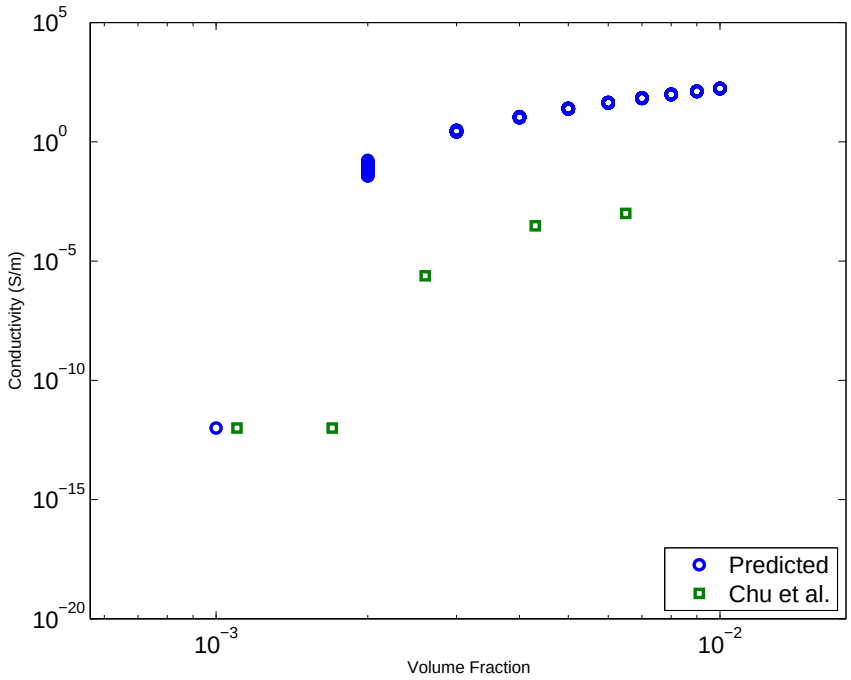

Figure V.16. Predicted conductivity for MWCNT/PP compared to experiment. [108]

Figure V.17 shows a 3D network that represents the MWCNT/PP system with a volume fraction of 0.002, which was found to be near the percolation threshold for

the nanocomposite. For reference, Chu et al. [108] reported a percolation threshold at a volume fraction of 0.0024. The entire network, including the nanotubes that are not connected to the spanning network, are shown in Figure V.17a. All of the CNTs that are connected to the network backbone between electrodes are shown in Figure V.17b. Finally, the nanotubes that carry a current of at least 1.0×10^{-12} A are shown in Figure V.17c, and they are colored according to the electrical current in each nanotube.

The figure shows that the nanotubes form several connected paths that are able to bridge the two electrode sides of the RVE. Note that the electrodes for this simulation are located on the +X/-X faces of the RVE. Furthermore, it can be seen in the figure that along the connected paths, there are only a small number of nanotubes that carry most of the current in the network, which is similar to the results for the MWCNT/epoxy system. The effective conductivity for this network is 0.0958 S/m.

A network with a volume fraction of 0.003 is depicted in Figure V.18. Only the CNTs that carry current greater than 1.0×10^{-12} A are shown for clarity. It is clear from the figure that the nanotubes form a much more homogeneous connected network backbone between the electrodes than the 0.002 volume fraction network. The effective conductivity for this network is 2.93 S/m, which is higher than the the conductivity for the 0.002 volume fraction network. Note that the maximum current in the network is also higher than that for the 0.002 volume fraction network. These trends are again seen in Figure V.19, where a network with a volume fraction of 0.01 is shown. The effective conductivity for this network is 169 S/m. Note that most of the nanotubes in this network appear to carry some current, which leads to the

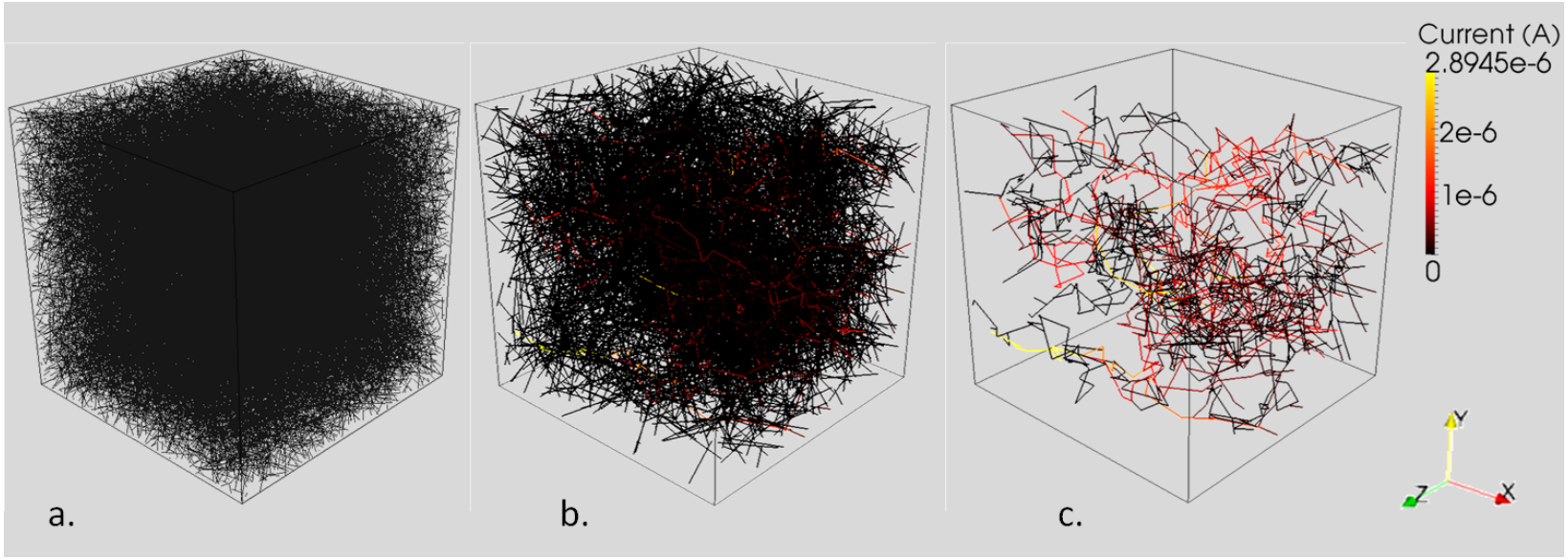

Figure V.17. MWCNT/PP network with Vf=0.002 with color contour values for electrical current.

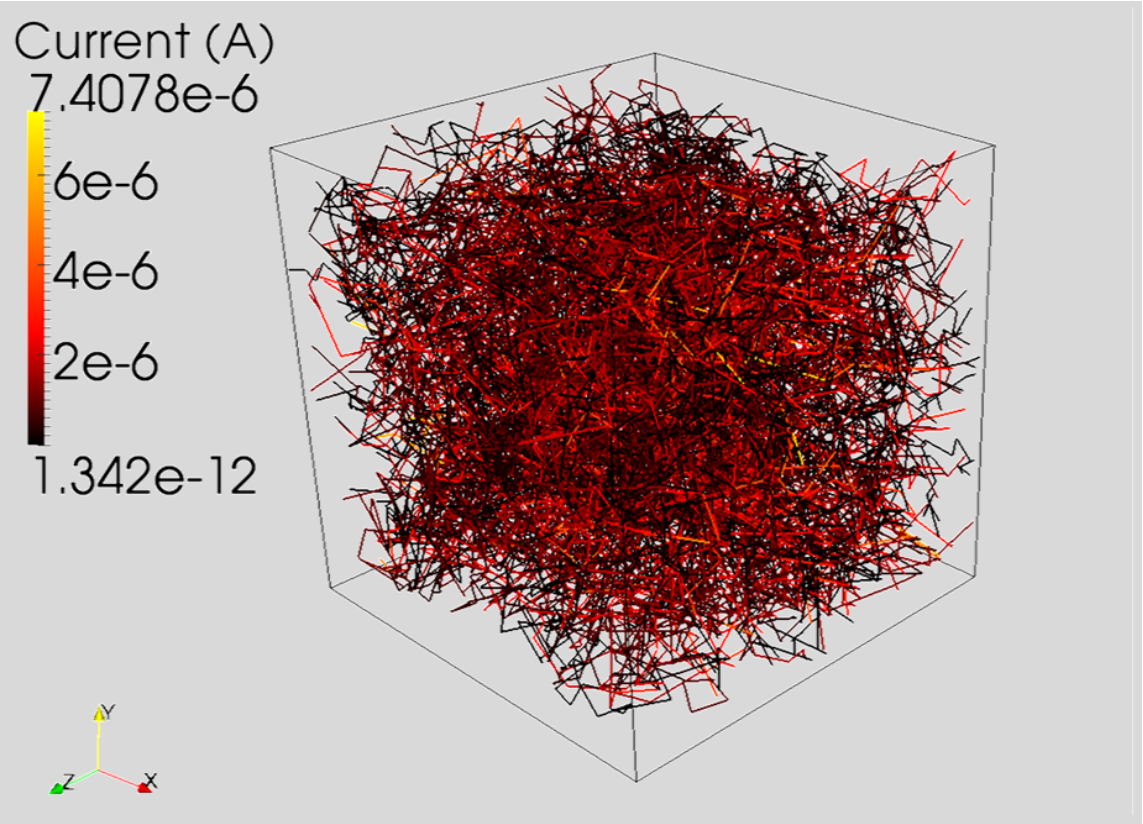

Figure V.18. MWCNT/PP network with Vf=0.003 with color contour values for electrical current.

higher current and conductivity values.

The RVE size of 15 μm was initially chosen based on the length of the MWCNTs used in this material system. However, to ensure that this RVE size is large enough to be representative of the microstructure, several different RVE sizes were investigated. Figure V.20 shows the average network conductivity as a function of volume fraction for RVE sizes of 10 μm, 15 μm, and 20 μm. It is evident in the figure that the results for the 15 μm and 20 μm RVEs are almost identical. There is a small but noticeable difference between these and the 10 μm RVE.

In order to investigate the different RVE sizes further, the coefficients of variation

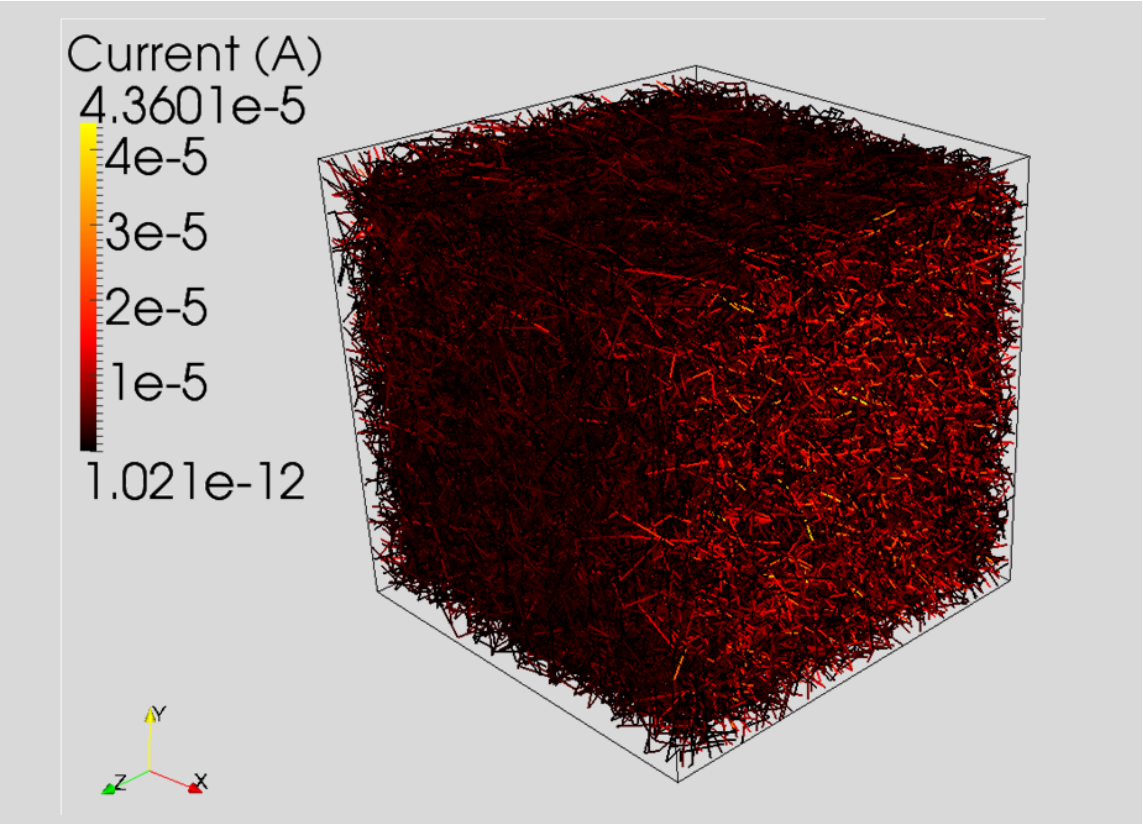

Figure V.19. MWCNT/PP network with Vf=0.01 with color contour values for electrical current.

for the network conductivities at each volume fraction are given in Figure V.21 for the 10 μm, 15 μm, and 20 μm RVE sizes. It is clear from the figure that the 10 μm RVE size has much greater variation than the 15 μm and 20 μm RVE sizes, especially for the lower volume fractions. Additionally, the variations for the 15 μm and 20 μm RVE sizes are very similar which indicates there is no benefit to using the larger RVE size. Therefore, the 15 μm RVE was deemed the most efficient of the three to use for this material system.

The experimental samples from Chu et al. were prepared using MWCNTs with a large distribution of lengths. The nanotube vendor, Sigma-Aldrich, specifies a range

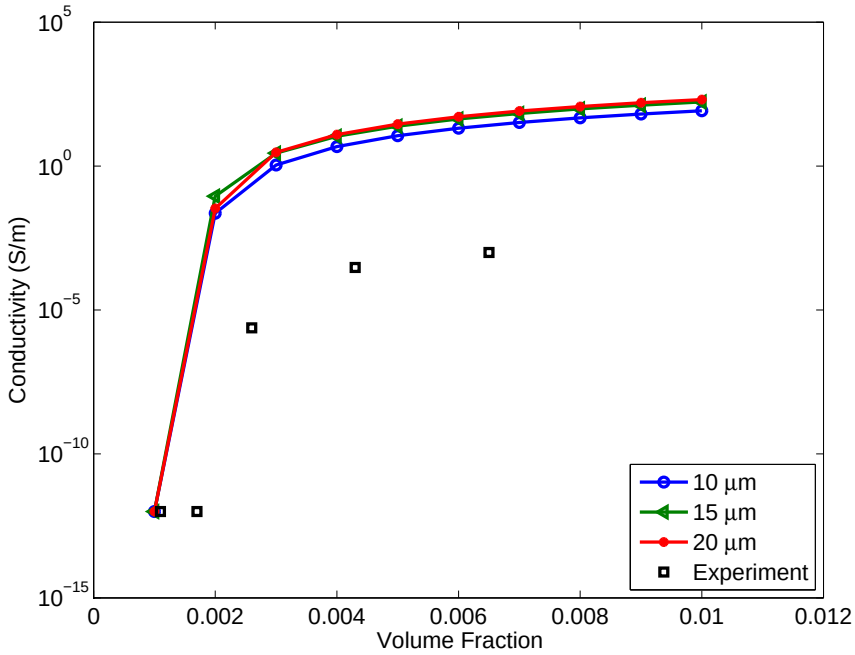

Figure V.20. Effect of RVE size on predicted MWCNT/PP conductivity.

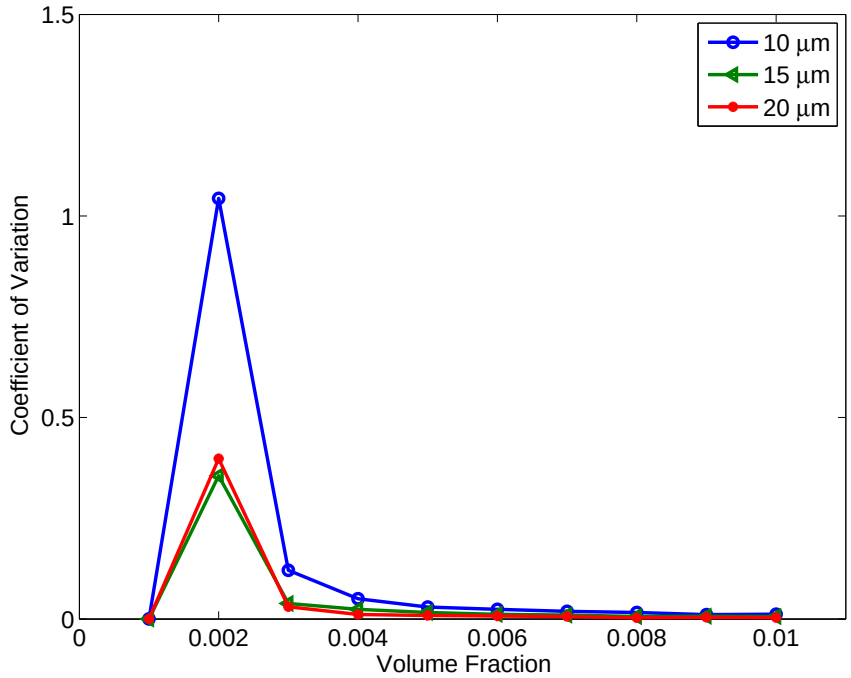

Figure V.21. Effect of RVE size on conductivity coefficient of variation for MWCNT/PP.

of 0.1-10 μm. A MWCNT length of $3\mu m$ was chosen for the initial computations, but the effect of this parameter was studied more carefully because of the uncertainty in the experimental data. Figure V.22 gives the average network conductivity values as a function of volume fraction for several different nanotube lengths. As expected, shorter nanotubes shift the percolation curve toward higher volume fractions because fewer conductive paths develop between individual CNTs. Conversely, longer CNTs have a higher probability of coming into contact with other CNTs, so the percolation threshold happens at lower volume fractions. Additionally, the higher number of electrical contacts with the longer CNTs leads to slightly higher effective conductivity values. It can be concluded from these results that being able to experimentally determine the average lengths of carbon nanotubes in a given material system is vitally important to being able to predict the percolation threshold and effective conductivity using computational modeling. An experimentally determined statistical distribution of nanotube lengths coupled with a computational model that allows different lengths of CNTs in the same network would be even more accurate. Ward [47] implemented this feature for a 2D network model, and although it would be much more computationally expensive to implement for the 3D model, it would still be a good feature to add in future work.

Because MWCNT conductivities can vary greatly depending on the batch and manufacturer, a parametric study investigating the effect of nanotube resistance per unit length was performed. Figure V.23 shows the network conductivity as a function of volume fraction for different values of MWCNT resistance. Recall that the model initially assumed a resistance per unit length of $13 \times 10^9\ \Omega/m$. For reference, Kaneto

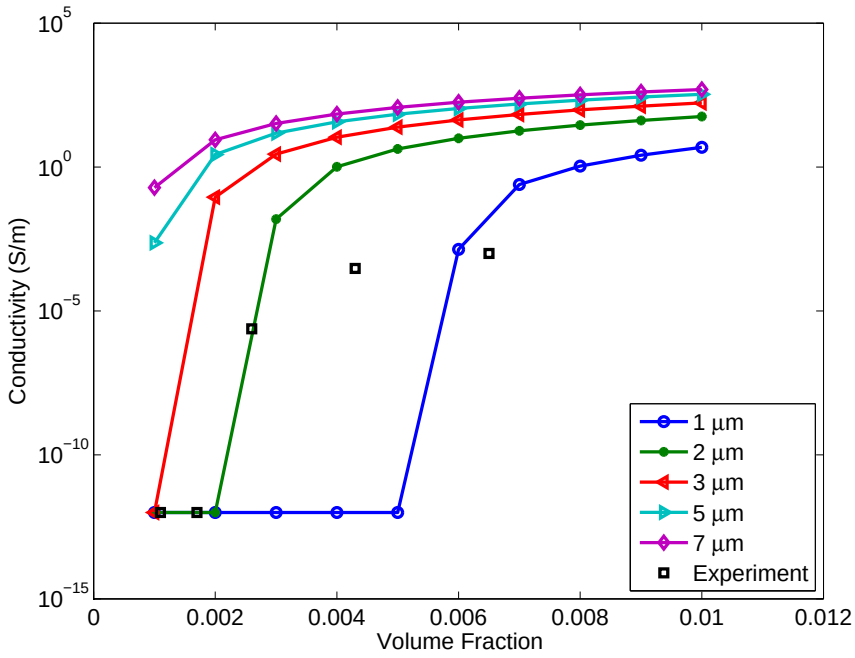

Figure V.22. Effect of MWCNT length on predicted MWCNT/PP conductivity.

et al. [82] measured the resistance per unit length of various MWCNTs to be between $2.0 \times 10^9 - 30 \times 10^9\ \Omega/m$. As expected, increasing the resistance of the nanotubes results in lower effective conductivity for the network, but the percolation threshold does not change much. However, it should be stressed that the main cause of high resistance nanotubes is atomic defects along individual nanotubes. Therefore, the results in the figure indicate that either the oxidized nanotubes in this material system contain a large number of defects that cause very high CNT resistances, or some other phenomenon causes lower network conductivities. Chu et al. [108] measured the conductivity of buckypaper specimens consisting of the MWCNTs used in the MWCNT/PP material system. The conductivity of buckypaper is frequently used as an estimate for the conductivity of CNTs, but it should be stressed that this

value includes the effects of contact resistance between the individual nanotubes. Chu et al. reported a buckypaper conductivity of 1100 S/m, which corresponds to a CNT resistance per unit length of 12×10^{12} Ω/m. It is apparent from Figure V.23 that even with this value of CNT resistance, the predicted conductivities are still several orders of magnitude too high.

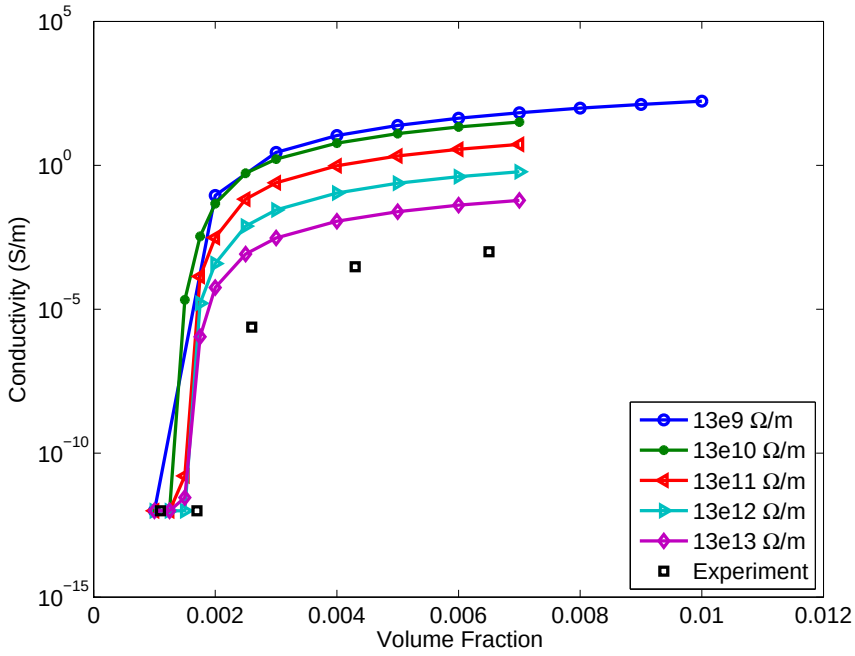

Figure V.23. Effect of MWCNT resistance on predicted MWCNT/PP conductivity.

One phenomenon that could cause the lower experimental MWCNT/PP conductivities is increased contact resistance between nanotubes. The experimentally measured contact resistance of $2.0 \times 10^5\Omega$ (200 $k\Omega$) was initially assumed in the model. However, this value was measured by Fuhrer et al. [83] for single-walled CNTs in good contact and with no matrix material between them. It is possible that the

actual contact resistances between MWCNTs in the nanocomposite are larger than the experimental value. Therefore, the contact resistance between nanotubes was investigated parametrically, and the results are given in Figure V.24.

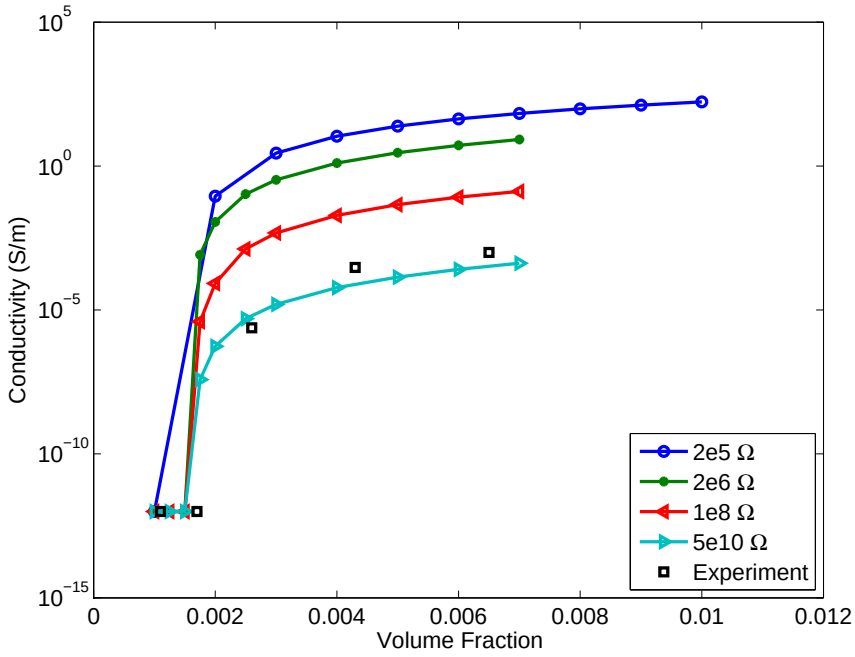

Figure V.24. Effect of contact resistance on predicted MWCNT/PP conductivity.

The results indicate that the model can be calibrated to the experimental data by adjusting the assumed value of contact resistance between nanotubes. Unfortunately, the contact resistance must be adjusted by four orders of magnitude in order for the model to predict values that match experiment. Instead of assuming 2.0×10^5 Ω (200 $k\Omega$) for each contact resistance (recall this is an experimentally measured value), a contact resistance closer to 5.0×10^{10} Ω results in a more accurate prediction. The calibrated predicted conductivity assuming a 5.0×10^9 Ω contact

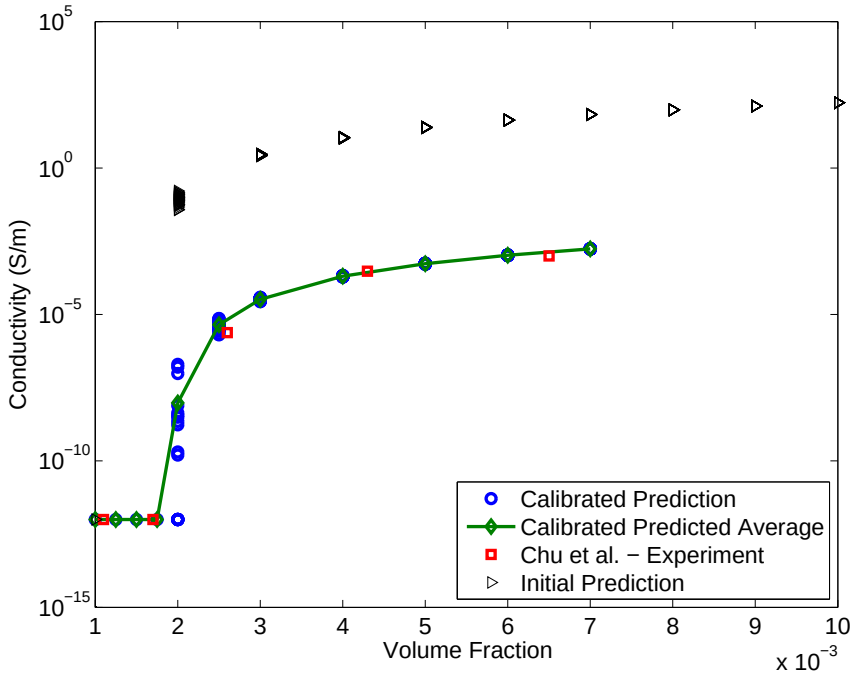

Figure V.25. Calibrated predicted conductivity for MWCNT/PP compared to experiment.

resistance and a slightly modified CNT length of 2.5 μm is shown in Figure V.25. While the calibrated predictions do predict the correct magnitude of nanocomposite conductivity, the idea of changing the assumed contact resistance by four orders of magnitude to obtain this result is troubling. One explanation for this result is that the contact resistance between two MWCNTs in this particular material system really is much larger than the contact resistance between two MWCNTs in the MWCNT/epoxy system. The fact that the MWCNTs in the polypropylene system have been functionalized and dispersed so well could be a reason why the apparent contact resistance is so high. There could be a small amount of polymer between nanotubes that the model assumes to be in contact. Due to the exponential nature of the tunneling resistance between nanotubes, even a tiny layer of polypropylene could

increase the apparent contact resistance by many orders of magnitude. Thus, it is reasonable to assume that the polypropylene more effectively coats the MWCNTs than the epoxy does for the MWCNT/epoxy system. It should also be pointed out that the calibrated network parameters chosen are only one possible set of parameters that can be used to calibrate the model to the material system. Another possibility is that the MWCNT resistance per unit length is higher than originally assumed, but more specific experimental data for the conductivity of individual MWCNTs would be needed to confirm this.

V.C. Summary

The electrical conductivities of the MWCNT/epoxy and MWCNT/polypropylene sytems were predicted using the 3D random resistor network model. The conductivities were calculated at various volume fractions and compared to experimental results from the literature. Parametric studies were performed to investigate the effects of RVE size, number of RVEs, CNT length, CNT resistance, and contact resistance between CNTs. The parametric studies were used to determine the number and size of RVEs needed to predict electrical properties that were representative of the bulk material.

It was found that the MWCNT/epoxy predictions matched experimental values well assuming a contact resistance of $2.0 \times 10^5\ \Omega$, which was obtained experimentally in the literature. The CNT length of 5.0 μm reported in the literature also seemed to provide the best predictions. The MWCNT/PP predictions did not initially compare well to experimental conductivity measurements reported in the literature. However,

it was found that adjusting the assumed contact resistance and CNT length was sufficient to calibrate the model to experimental results. The contact resistance was increased by four orders of magnitude to $5.0 \times 10^9 \Omega$, but the CNT length was only decreased slightly to 2.5 μm. It was hypothesized that the much higher contact resistance needed to calibrate the model indicated that the MWCNTs were better encapsulated in the polypropylene, which caused higher contact resistance values between CNTs. The difference in CNT length was attributed to the large distribution of lengths found in the MWCNTs used in the experimental specimens, as well as uncertainty in measuring the lengths. It should be emphasized that the calibrated network parameters are only one possible set of parameters that can be used to calibrate the model to the material system, but the parameters chosen make sense qualitatively.

CHAPTER VI

PIEZORESISTIVITY OF 3D CNT/POLYMER COMPOSITES

The purpose of this chapter is to investigate the piezoresistive response of the MWCNT/epoxy and MWCNT/polypropylene material systems. The piezoresistivity models developed in Chapter II were used to predict the change in resistance of CNT networks with incremental levels of applied strain. The piezoresistivity models were used to investigate the dominant mechanisms responsible for the piezoresistive effect in CNT/polymer nanocomposites as well as the effects of various assumptions on piezoresistive performance.

VI.A. Predicted piezoresistivity of MWCNT/epoxy using the uniform strain model

The MWCNT/epoxy material system was modeled using the same network assumptions as in Chapter V, which are given again in Table VI.1. The system was first investigated using the uniform strain piezoresistivity model so that the results could be easily compared to experimental and numerical results from the literature. Specifically, the work of Hu et al. [13, 56] was again used for comparison because their piezoresistivity model is essentially the same as the uniform strain model used herein.

The relative change in network resistance at strain levels up to 1% is given in Figure VI.1, where each data point is the average value for 50 unique realizations. The change in resistance ΔR is normalized by the initial resistance R_0 of the unde-

MWCNT length	5 μm
MWCNT diameter	50 nm
MWCNT resistance per unit length	13.0×10^9 Ω/m
Contact resistance	2.0×10^5 Ω
RVE length	25 μm

Table VI.1. Material properties used for MWCNT/epoxy in piezoresistivity models.

formed network. The relative resistance change for a conventional strain gauge with a gauge factor of two is plotted in the figure for reference. The nanocomposite was assumed to have an effective Poisson's ratio of 0.3, and volume fractions from 0.007 to 0.02 were investigated. While the predicted piezoresistive responses for the 0.008 and higher volume fraction networks seem reasonable, the figure indicates an inconsistent response for the 0.007 and 0.0075 volume fraction networks. Indeed, the 0.007 Vf network actually has a negative change in resistance at lower levels of applied strain, and there are large spikes and dips in the network resistance at increasing levels of applied strain. In other words, the material initially became less resistive as the RVE was stretched, and then resistivity increased rapidly at higher strain levels. This behavior is unexpected and not seen experimentally in the literature. The decrease in average resistance could be explained by the Poisson contraction of the RVE in individual network realizations. The contraction could cause clusters of nanotubes to be pushed into contact or within tunneling range of each other, thereby increasing the current flow and decreasing the overall resistance of the network re-

alization. It was found that having just a few of these lower resistance realizations could skew the average resistance change drastically. Upon further investigation, it was also discovered that this effect happens much more frequently for smaller RVE sizes, which indicates a larger RVE may be needed to adequately capture the piezoresistive response. However, the networks with higher volume fractions in Figure VI.1 do show increases in resistance with applied strain as expected. Additionally, the positive change in network resistance appears to be approximately linear for volume fractions greater than 0.008.

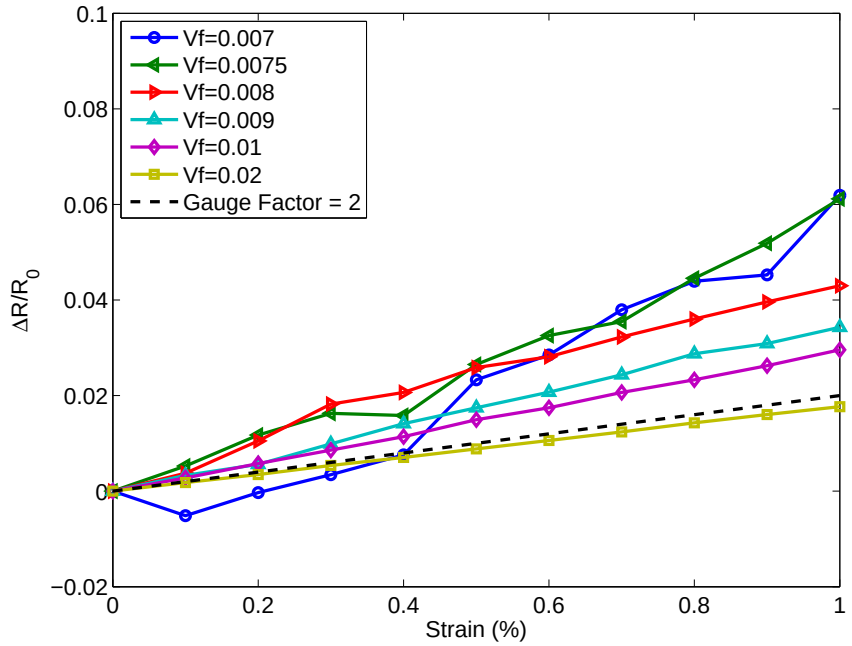

Figure VI.1. Predicted normalized change in resistance for MWCNT/epoxy with Poisson's ratio of 0.3.

The gauge factors for the CNT networks represented in Figure VI.1 are plotted in Figure VI.2 as a function of nanotube volume fraction. Each data point is again

the average of 50 unique network realizations. It is clear from the figure that the 0.007 and 0.0075 volume fraction networks again vary erratically. This is not surprising because the gauge factors are actually the slopes of the curves plotted in Figure VI.1. The 0.007 volume fraction networks show average gauge factors between -5 and 5 for the shown strain levels, which would be highly undesirable in an actual strain gauge. The higher volume fraction networks do show promisingly consistent gauge factors of approximately 2-5, however. Thus, the slightly lower gauge factors indicate a tradeoff between greater sensitivity to strain and the ability to calibrate a sensor.

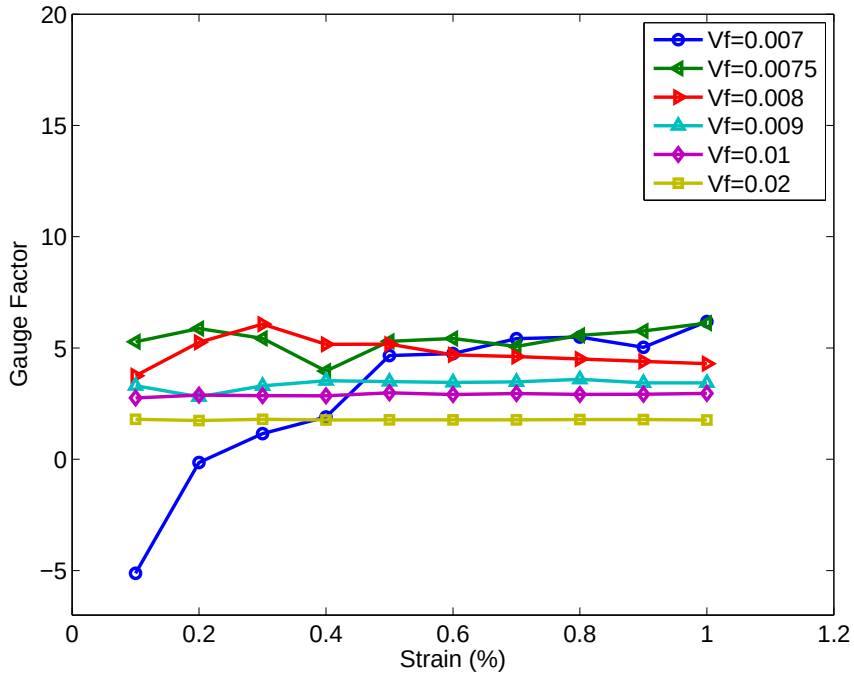

Figure VI.2. Predicted gauge factors for MWCNT/epoxy with Poisson's ratio of 0.3.

Because the lower volume fraction networks seemed to have erratic predictions

using the 25 μm RVE size, the 0.007 and 0.0075 volume fraction networks were re-analyzed using an RVE size of 50 μm. This size was chosen based on the electrical conductivity results for different RVE sizes in Chapter V (see Figures V.9-V.10). Note that in addition to using a larger RVE, it was found that using a different method to average the predictions was required. The randomness of the CNT networks tended to produce outliers in the predicted piezoresistive data that heavily biased the mean values. The 10% trimmed mean was found to appropriately and systematically handle these outliers. The 10% trimmed mean is a robust estimator of location used in statistics that systematically discards the highest 5% and lowest 5% of the observations in a given distribution and calculates the mean of the remaining observations. Thus, the 10% trimmed mean of the predicted gauge factors for 50 network realizations discards the highest two and lowest two predictions and calculates the mean using the remaining 46 predictions. Unless noted otherwise, the 10% trimmed mean is used to average all of the piezoresistivity predictions for the remainder of the chapter.

The average change in resistance is plotted for these larger RVE sizes in Figure VI.3, and the corresponding gauge factors are plotted in Figure VI.4. The results for the 25 μm RVE size networks with volume fractions greater than or equal to 0.008 are also plotted in Figures VI.3-VI.4. It is clear from the figures that the larger RVE sizes give a much more consistent piezoresistive prediction. Increasing the RVE size seems to have the effect of producing a more homogenized piezoresistive response because the effect of individual clusters coming into contact with each other does not bias the average response as much. It should be noted that using a 50 μm RVE

size for the networks with volume fractions greater than 0.008 does not significantly change the response, but the computational time required is approximately 10 times larger. Thus, based on the parametric studies on RVE size presented in Chapter V, it seems reasonable to use the 50 μm RVE size for the smaller volume fraction networks while using the 25 μm size RVE for the larger volume fractions.

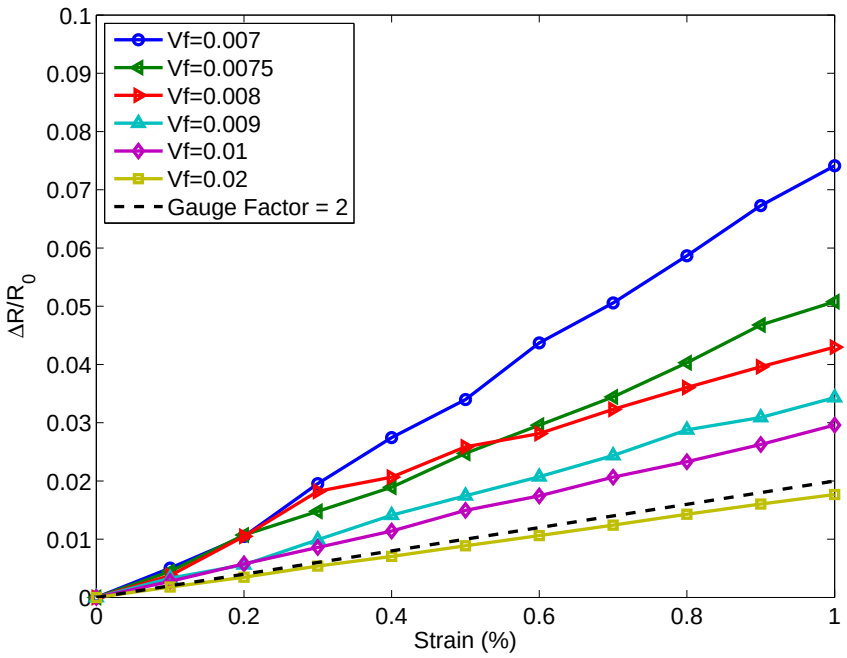

Figure VI.3. Predicted normalized change in resistance for MWCNT/epoxy with Poisson's ratio of 0.3. A 50 μm RVE was used for Vf=0.007 and Vf=0.0075.

The results in Figures VI.3-VI.4 indicate that the nanocomposite has the largest change in resistance at lower nanotube volume fractions, which has been shown by Hu et al. and others in the literature. [13,56] As mentioned previously, the predicted piezoresistive response also appears to be approximately linear. This contradicts the

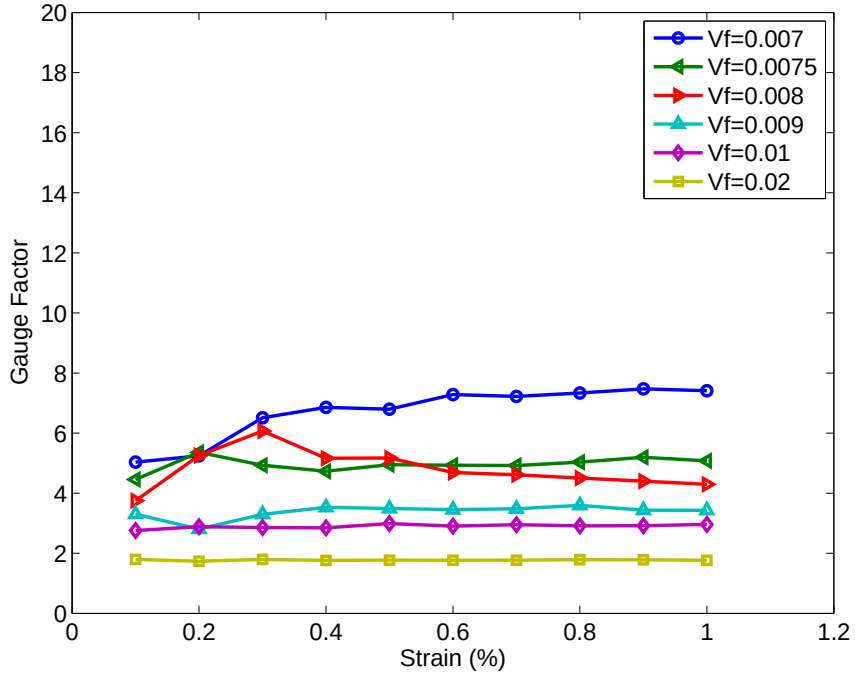

Figure VI.4. Predicted gauge factors for MWCNT/epoxy with Poisson's ratio of 0.3. A 50 μm RVE was used for Vf=0.007 and Vf=0.0075.

numerical results of Hu et al., which showed a nonlinear response that was attributed to the electron tunneling between CNTs. Because the equation that describes the tunneling resistance between CNTs is an exponential function, it is reasonable to assume that small changes in tunneling distances could result in a nonlinear response. However, the results shown here also include the electron tunneling effect, but it seems there are not enough tunneling junctions in the networks to cause a nonlinear piezoresistive response. It should be noted that other experimental and computational studies in the literature have shown a linear response similar to the results seen here. [61, 63, 64]

The predictions from Figure VI.3 were also compared to the experimental results from Hu et al. The experimental data plotted in [56] was digitized and plotted

alongside the predictions from this work in Figure VI.5. Note that the weight fractions were given for the data in [56], so they were converted to volume fractions for comparison. The densities for epoxy and MWCNTs were assumed to be 1100 kg/m^3 and 2100 kg/m^3, respectively, and these values were obtained from Hu et al. [32]. Figure VI.5 indicates that the experimentally measured piezoresistivities were greater than the predictions from this work. The predictions do qualitatively match the relative resistance behavior, but the magnitude of the resistance changes do not match between prediction and experiment. However, it should be noted that even the numerical predictions from Hu et al. [56, 57] did not match quantitatively with their experimental results. In contrast with the underpredicted piezoresistivity herein, their numerical predictions overpredicted the experimental piezoresistance.

The assumed Poisson's ratio for the nanocomposite was varied in order to determine whether this elastic material property had any impact on piezoresistive performance. Figure VI.6 shows the normalized change in resistance when Poisson's ratio is assumed to be zero. The corresponding gauge factors are also plotted in Figure VI.7. Note that larger RVE sizes were again used for the 0.007 and 0.0075 volume fraction networks due to reasons given above. While a Poisson's ratio of zero is an extreme case, it is useful for identifying the dominant mechanisms responsible for the piezoresistive effect. Thus, it is interesting to note that the resistance change and gauge factors are much higher for this case than those predicted for the 0.3 Poisson's ratio cases. The zero Possion's ratio assumption yields a greater than 20% change in relative resistance at 1% strain, but the resistance change when assuming a 0.3 Poisson's ratio is only about 7% at that strain level. This large difference could

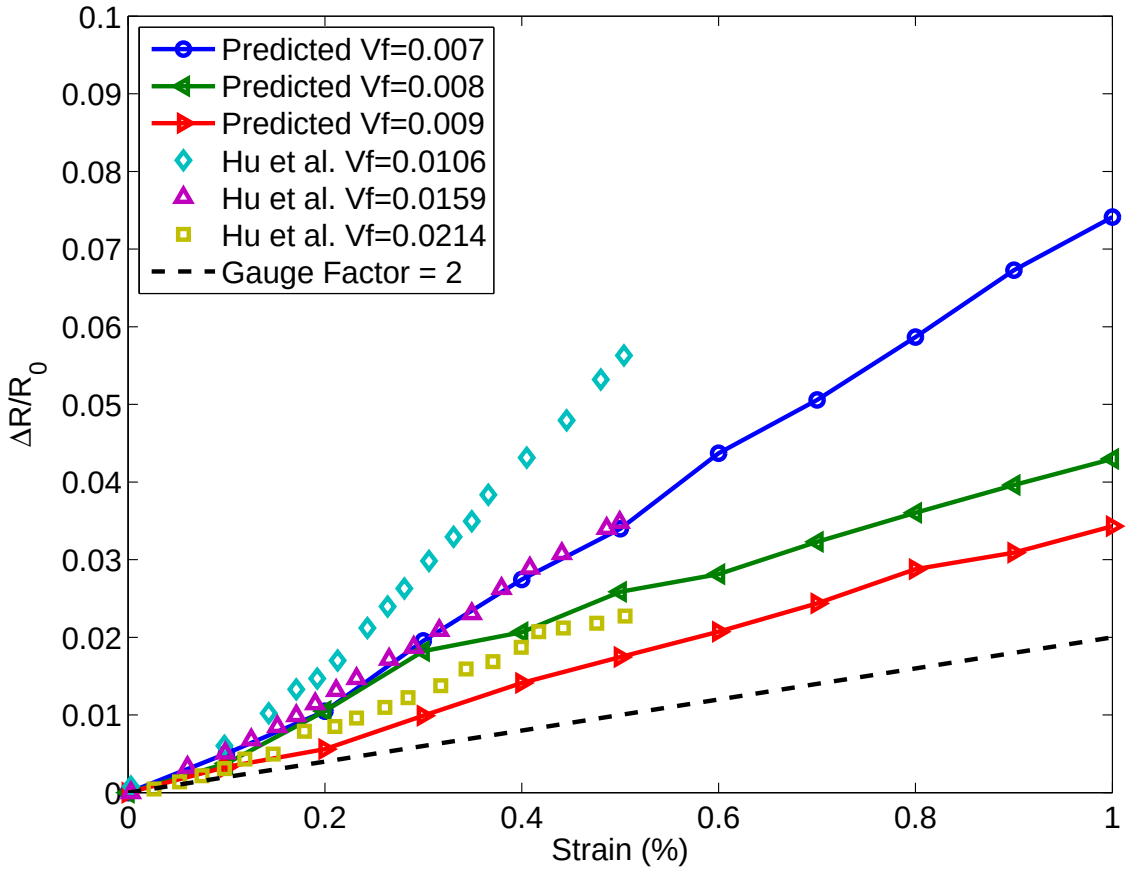

Figure VI.5. Comparison between predicted and experimental relative resistance change for MWCNT/epoxy. Experimental data digitized from [56]

be due to the Poisson contraction in the directions transverse to the applied strain. The contraction may cause clusters of nanotubes to come into contact with each other, thereby causing a decrease in network resistance. It is not expected that the nanotubes have much effect on the effective Poisson's ratio. Therefore, these results indicate that picking specific matrix materials could be used to tailor piezoresistive sensitivity. Unfortunately, there are not many materials that have extremely low Poisson's ratios. Some materials, such as natural cork and some polymer foams,

do exhibit near-zero Poisson's ratios. If a method to disperse nanotubes in a cork or foam material could be developed, the resulting sensors would theoretically be highly sensitive. However, Mott and Roland have shown that the true lower limit for Poisson's ratio in elastic materials is 0.2. [109] They argue that classical elasticity is not applicable to materials that do exhibit lower Poisson's ratios. This obviously has implications for attempting to optimize piezoresistive materials.

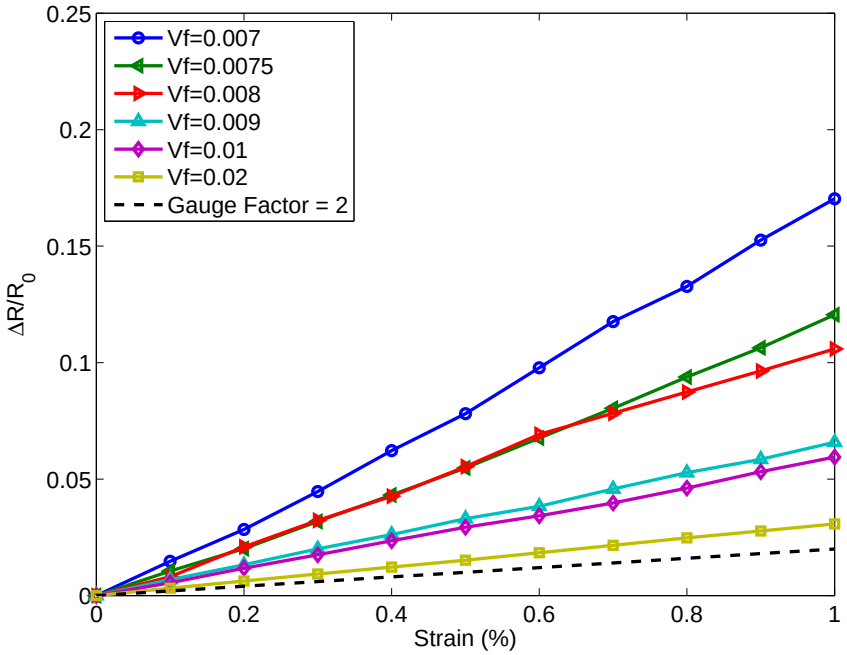

Figure VI.6. Predicted normalized change in resistance for MWCNT/epoxy with Poisson's ratio of zero. A 50 μm RVE was used for Vf=0.007 and Vf=0.0075.

The resistance change assuming a network Poisson's ratio of 0.4 is given in Figure VI.8. Additionally, the gauge factors for these cases are given in Figure VI.9. Many polymer materials have Poisson's ratios of approximately 0.4 (e.g. Nylon). Thus,

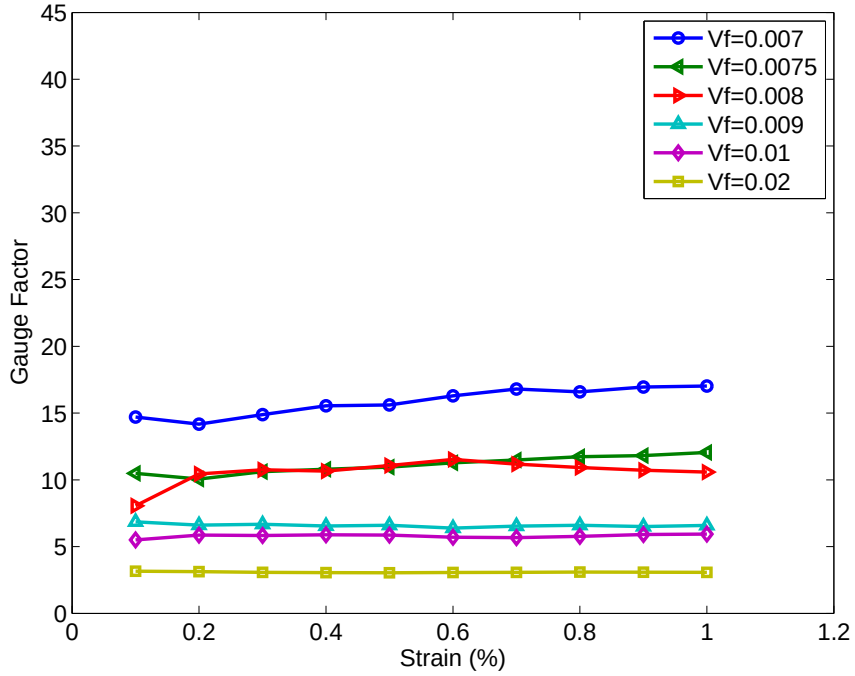

Figure VI.7. Predicted gauge factors for MWCNT/epoxy with Poisson's ratio of zero. A 50 μm RVE was used for Vf=0.007 and Vf=0.0075.

this is an important case to consider. The results in Figures VI.8-VI.9 indicate a lower piezoresistive response than the 0.3 Poisson's ratio predictions. The maximum relative resistance change was approximately 5%, and the maximum gauge factor was approximately five. The highest piezoresistive sensitivity was again found in the lowest volume fraction networks. Figures VI.8-VI.9 provide further evidence supporting the idea that the Poisson contraction can cause a decrease in resistance because of the nanotube clusters that come into contact with each other. Considering that many researchers either overlook Poisson's ratio or assume it to be 0.3, it is very interesting that the results indicate this material property has such a large effect on piezoresistive behavior.

The relative resistance change assuming a network Poisson's ratio of 0.5 is given

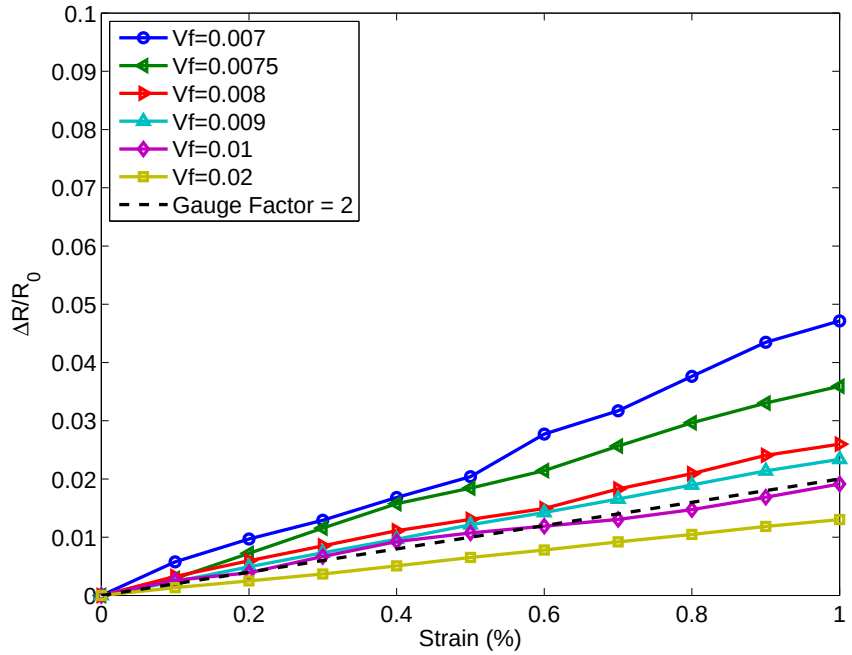

Figure VI.8. Predicted normalized change in resistance for MWCNT/epoxy with Poisson's ratio of 0.4. A 50 μm RVE was used for Vf=0.007 and Vf=0.0075.

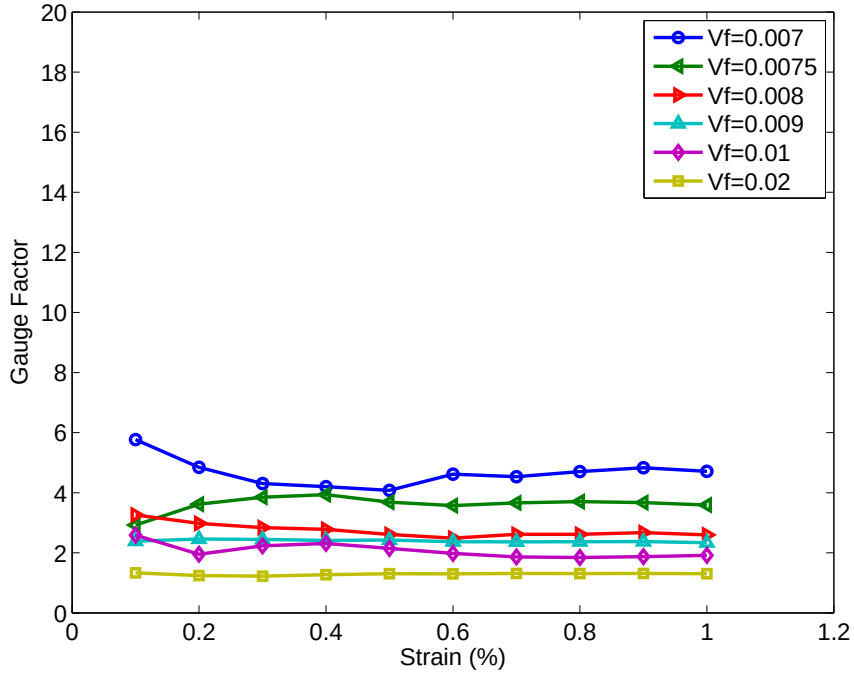

Figure VI.9. Predicted gauge factors for MWCNT/epoxy with Poisson's ratio of 0.4. A 50 μm RVE was used for Vf=0.007 and Vf=0.0075.

in Figure VI.10. Additionally, the gauge factors for these cases are given in Figure VI.11. Assuming a Poisson's ratio of 0.5 is obviously another limit case, but this analysis may be very applicable to many potential material systems because many polymers (e.g. polypropylene) can have very high Poisson's ratios approaching 0.5 under certain conditions. There has also been some interest in the literature in fabricating strain sensors from nanotubes embedded in silicone rubber. [66] As silicone rubber has a Poisson's ratio of nearly 0.5, the results herein would seem to indicate that this is not the most effective piezoresistive material system. Interestingly, the piezoresistivity model in Hu et al. assumes that the material is incompressible (Poisson's ratio of 0.5) even though most epoxies have a Poisson's ratio between 0.35-0.4.

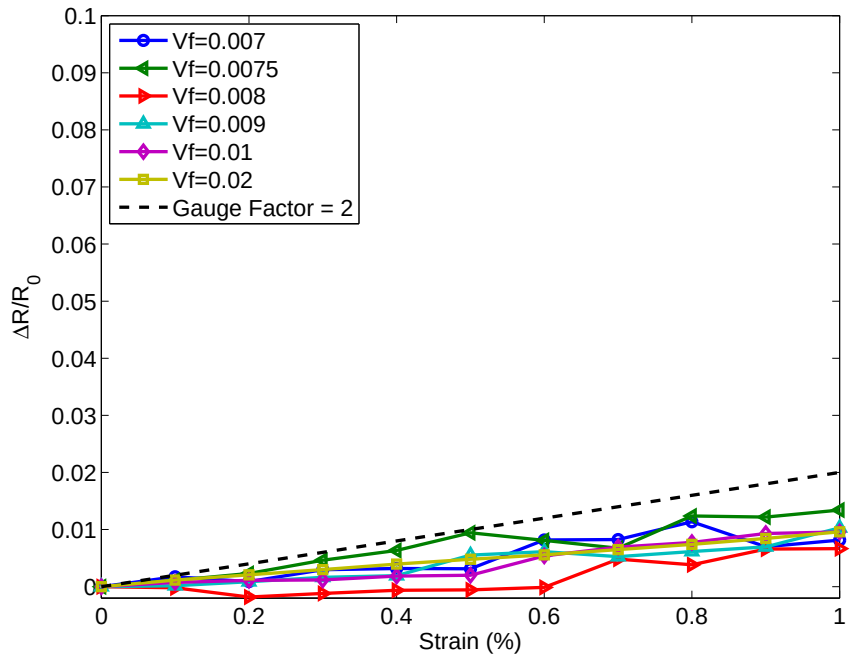

Figure VI.10. Predicted normalized change in resistance for MWCNT/epoxy with Poisson's ratio of 0.5. A 50 μm RVE was used for Vf=0.007 and Vf=0.0075.

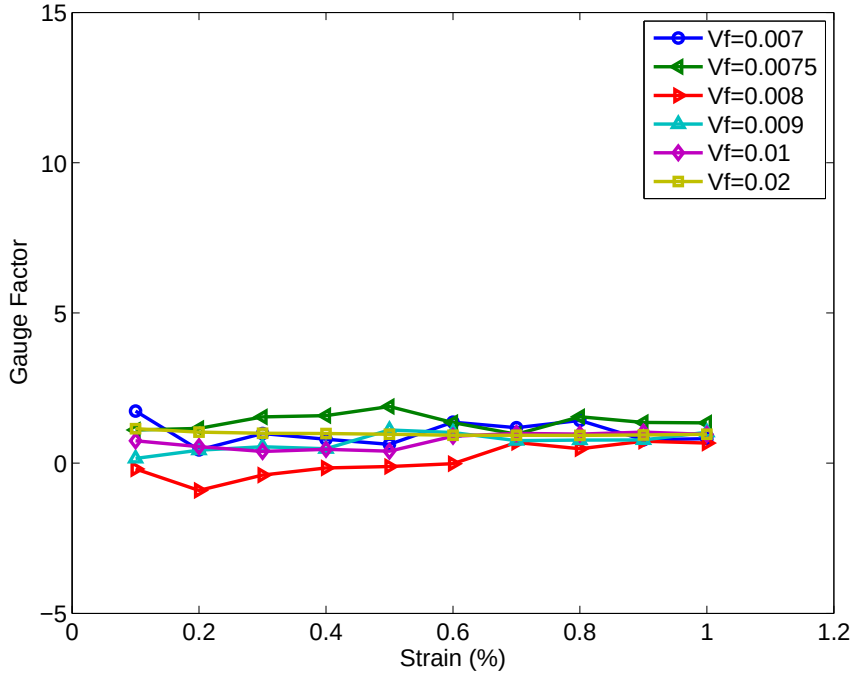

Figure VI.11. Predicted gauge factors for MWCNT/epoxy with Poisson's ratio of 0.5. A 50 μm RVE was used for Vf=0.007 and Vf=0.0075.

At this point, it is helpful to consider another measure of piezoresistive material performance. The relative resistance change and gauge factor have been used thus far to indicate a CNT/polymer nanocomposite's piezoresistance. Much of the literature reports performance in such terms, so this allows easy comparison of results. However, a truer representation of a material's piezoresistive potential might be the relative change in resistivity $\Delta\rho/\rho_0$. Recall from Chapter II that the strain sensing capability of a specific material specimen is due to contributions from a piezoresistive term $\Delta\rho/(\rho_0\varepsilon)$ and a geometrical effects term $1+2\nu$. Thus, the gauge factor can be expressed as

$$GF = \frac{\Delta R}{R_0\varepsilon} \approx \frac{\Delta\rho}{\rho_0\varepsilon} + 1 + 2\nu. \tag{6.1}$$

Many metals used in strain gauges have very small piezoresistive terms, so their response to strain is mainly due to geometrical effects related to Poisson's ratio. However, Equation 6.1 shows that the maximum gauge factor that can be achieved by geometrical effects alone is 2.0, which corresponds to an incompressible material. Any gauge factors larger than two must be due to a piezoresistive effect. By investigating $\Delta\rho/\rho_0$ and its relationship with $\Delta R/R_0$, the contributions of material piezoresistance and geometrical effects for a CNT/polymer material might be better understood.

Average values for the relative changes in resistance and resistivity are both plotted in Figure VI.12 assuming a Poisson's ratio of 0.3. The dashed lines represent relative resistivity, and the solid lines represent relative resistance. The relative resistance change for a gauge factor of two is also plotted for reference. The resistivity was calculated for each network using $\rho = RA/L$, where the RVE cross-sectional area A and RVE length L were calculated using the current length and area at each strain increment. The trends for the relative resistance and relative resistivity appear to be similar. The change in resistance and resistivity is greater for lower volume fractions, and the piezoresistive performance for all volume fractions shown is generally much better than a conventional strain gauge material. The figure also shows that the relative resistance change is always greater than the relative resistivity change. This is expected because Equation 6.1 indicates that the relative resistance change should be equal to the sum $\Delta\rho/\rho_0 + (1+2\nu)\varepsilon$. It is interesting to note that if $\Delta\rho/\rho_0 + (1+2\nu)\varepsilon$ is plotted instead of $\Delta\rho/\rho_0$, the resulting plot falls almost exactly on the plot of $\Delta R/R_0$. Thus, it can be concluded that for each volume fraction shown, the difference between the solid lines ($\Delta R/R_0$) and dashed lines ($\Delta\rho/\rho_0$) is

the geometrical effect related solely to Poisson's ratio.

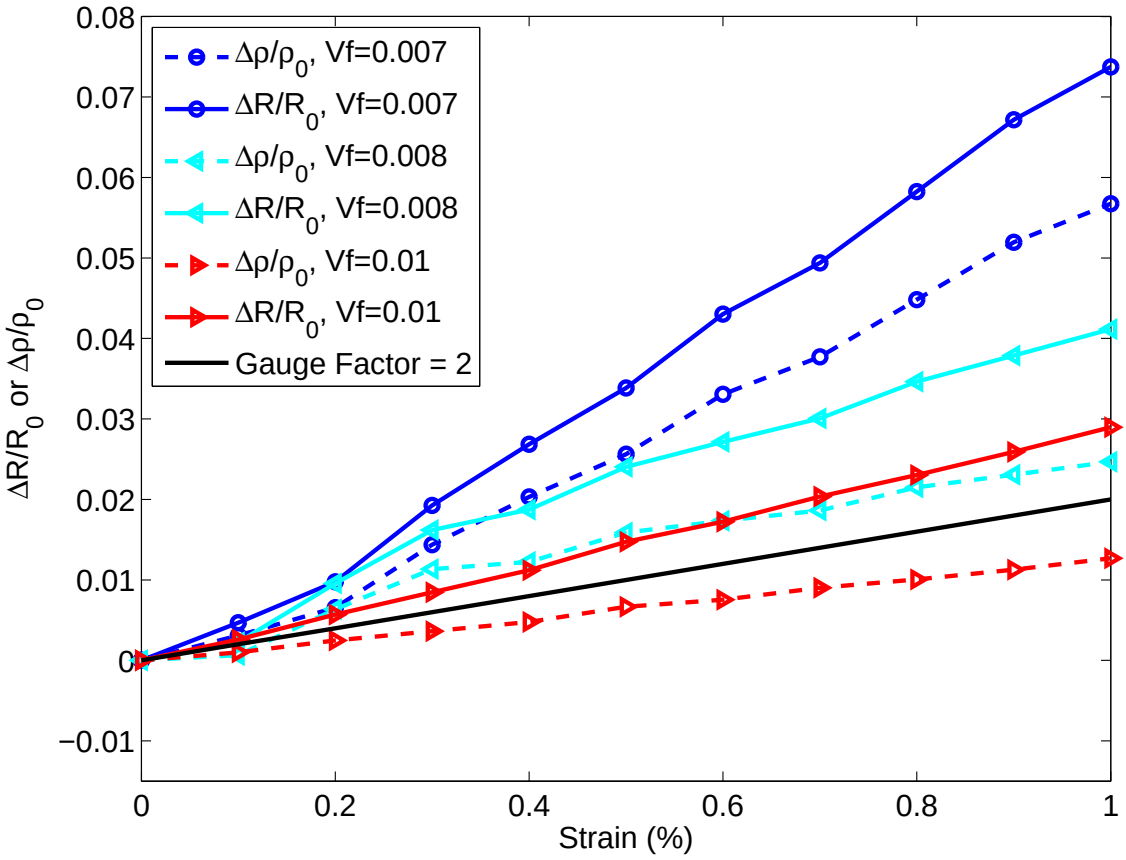

Figure VI.12. Predicted normalized change in resistance and resistivity for MWCNT/epoxy with Poisson's ratio of 0.3.

The relative changes in resistance and resistivity are both plotted in Figure VI.13 assuming a Poisson's ratio of 0.4. The relative change in resistivity is again greater for lower volume fractions, and the effect of Poisson's ratio is again apparent when comparing the predictions to Figure VI.12. The maximum resistivity change for the 0.4 Poisson's ratio case is about 3% while the maximum resistivity change for the 0.3 Poisson's ratio case is about 6%. This clearly shows that the relative

change in resistivity is highly sensitive to Poisson's ratio, and that higher Poisson's ratios yield lower piezoresistance. Interestingly, inspection of Equation 6.1 seems to indicate that higher Poisson's ratios lead to higher gauge factors. However, the results in Figure VI.13 indicate that the opposite is actually true for CNT/polymer nanocomposites. This is again explained by the fact that Poisson contraction causes clusters of CNTs to come within tunneling range of each other, thereby decreasing the resistivity of the nanocomposite. It is apparent from the results that this causes the piezoresistive term in Equation 6.1 to have a greater contribution to the strain sensitivity of a material specimen than the geometrical effects term.

The relative changes in resistance and resistivity are both plotted in Figure VI.14 assuming a Poisson's ratio of 0.5. The predictions in the figure are very interesting because the relative resistivities are all negative while the relative resistances are all positive. This means that the material resistivity actually decreased with increasing strain. However, the overall resistance of the CNT networks increased with increasing strain. This again highlights the competing piezoresistive and geometrical effects. Higher Poisson's ratios for CNT/polymer materials result in low or even negative changes in relative resistivity, and the positive change in relative resistance is due solely to the geometrical effect. The resistivity decreases with increasing strain because of the clusters of CNTs that are brought into contact by the Poisson contraction.

All of the piezoresistive predictions for MWCNT/epoxy have thus far been calculated assuming a MWCNT contact resistance of 2.0×10^5 Ω. Recall that this value for contact resistance corresponds to experimental measurements in the liter-

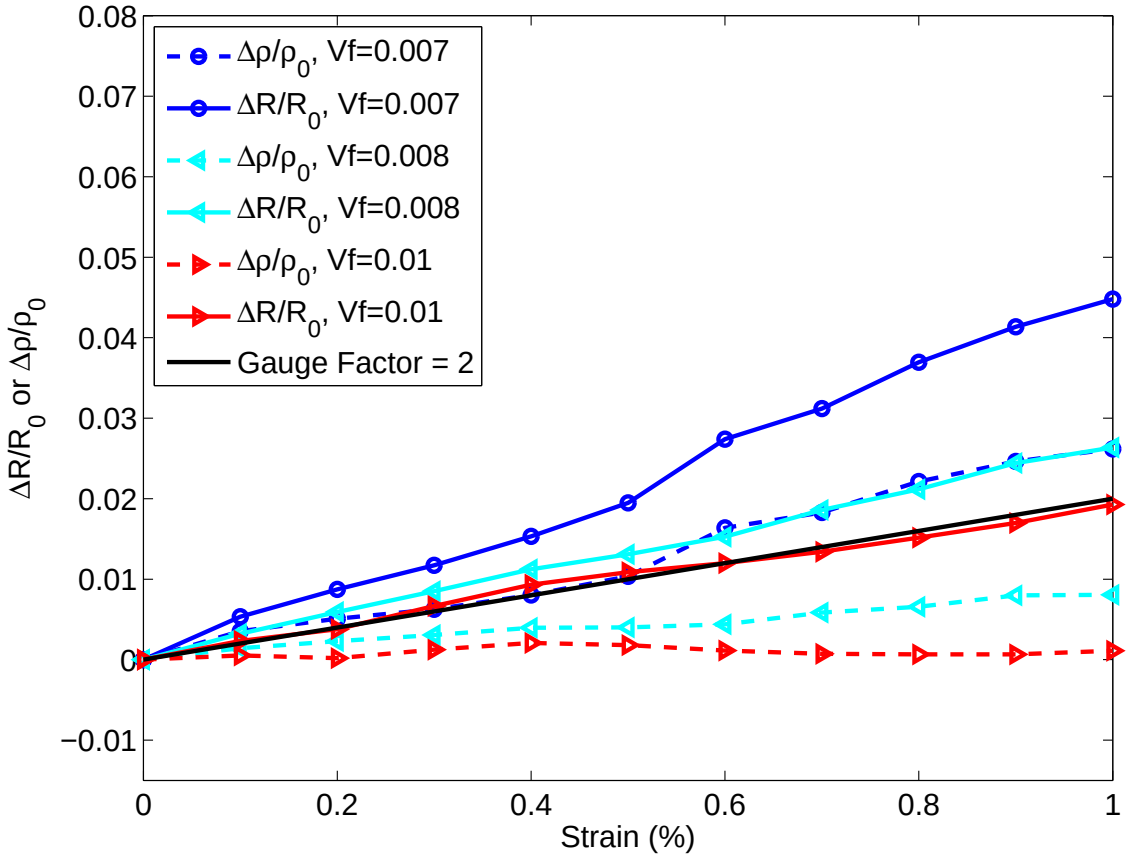

Figure VI.13. Predicted normalized change in resistance and resistivity for MWCNT/epoxy with Poisson's ratio of 0.4.

ature [83], and the parametric studies in Chapter V confirmed that this value yields accurate conductivity predictions. In order to further investigate the mechanisms responsible for network piezoresistivity, an assumed contact resistance of 0.01 Ω was used to approximate zero contact resistance between nanotubes. Note that a contact resistance of exactly zero could not be used because the finite element equations in the model would become singular. The relative resistance change assuming that Poisson's ratio and the contact resistance are both zero is given in Figure VI.15, and the gauge factors are plotted in Figure VI.16. The predictions assuming a contact re-

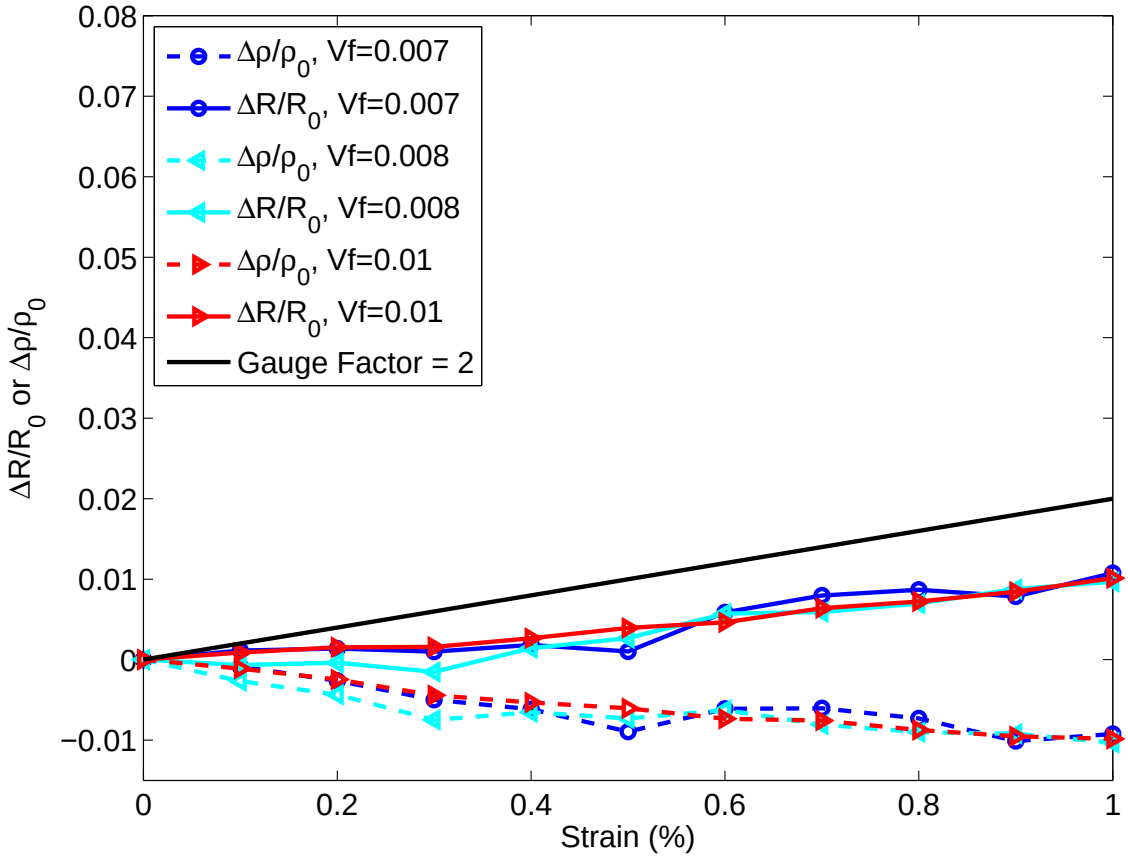

Figure VI.14. Predicted normalized change in resistance and resistivity for MWCNT/epoxy with Poisson's ratio of 0.5.

sistance of 2.0×10^5 Ω are also shown in the figures for comparison. It should again be stressed that the MWCNT/epoxy material is not expected to have a Poisson's ratio close to zero. However, assuming zero Poisson contraction is useful for determining the relationships between network resistance, contact resistance, and Poisson's ratio. It is clear from the figures that the networks with low volume fractions, close to the percolation threshold, are much more sensitive to applied strain. Gauge factors between 14-18 were calculated for the 0.007 volume fraction networks. Interestingly, even though the contact resistance was shown in Chapter V to have a large effect

on composite conductivity, the contact resistance does not appear to have much effect on the piezoresistive behavior. The Vf=0.007 and Vf=0.01 cases show nearly indistinguishable predictions between the zero and nonzero contact resistance. This is surprising considering the zero and nonzero contact resistances differ by seven orders of magnitude. The Vf=0.008 case does show a higher relative resistance change and gauge factor for the 2.0×10^5 Ω contact resistance, but the predictions are still relatively similar.

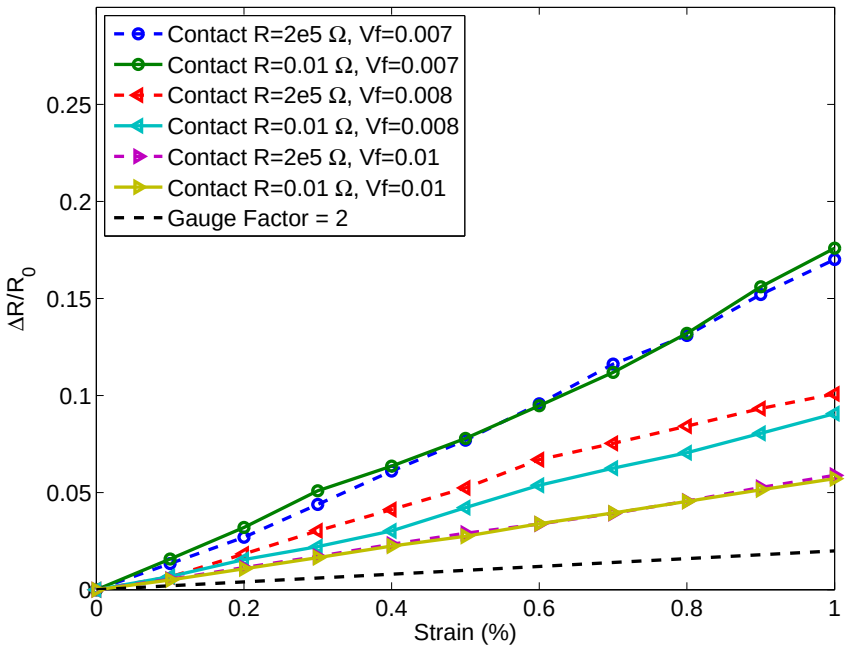

Figure VI.15. Effect of CNT contact resistance on predicted change in resistance for MWCNT/epoxy with Poisson's ratio of zero.

The relative resistance change assuming a Poisson's ratio of 0.3 and zero contact resistance between MWCNTs is given in Figure VI.17, and the gauge factors are given in Figure VI.18. The predictions assuming a contact resistance of 2.0×10^5 Ω are

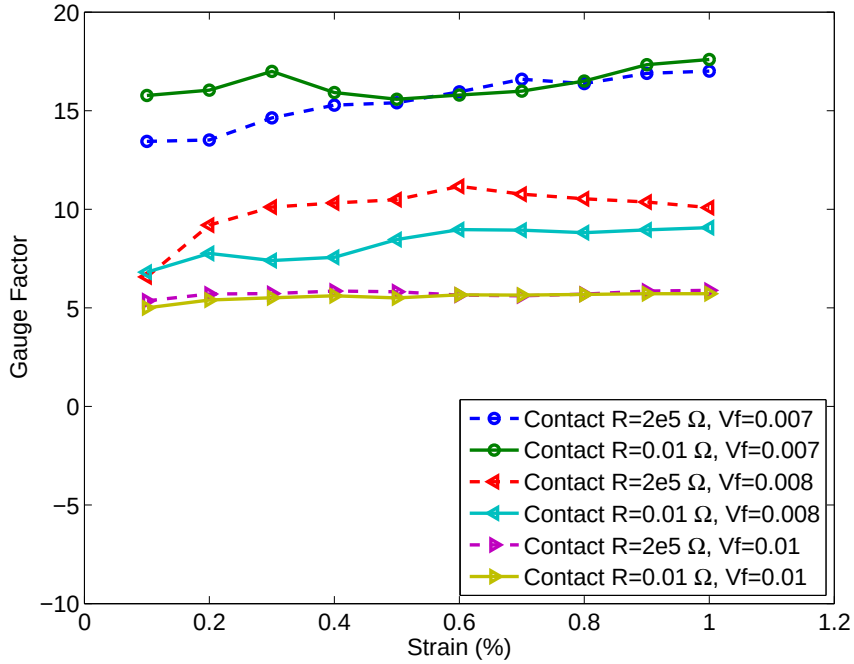

Figure VI.16. Effect of CNT contact resistance on predicted gauge factors for MWCNT/epoxy with Poisson's ratio of zero.

again shown in the figures for comparison. The Poisson's ratio of 0.3 is closer to what many CNT/polymer systems would exhibit although it is still lower than the Poisson's ratio of many polymers. Figures VI.17-VI.18 show that the higher Poisson's ratio again lowers the relative resistance change and gauge factors of the material. More importantly, the figures indicate that the contact resistance between nanotubes does not have any significant impact on piezoresistivity. The relative resistance changes and gauge factors are almost identical between the zero and nonzero contact resistance cases.

The change in resistance assuming a Poisson's ratio of 0.5 and zero contact resistance is given in Figure VI.19. Additionally, the gauge factors for these cases are given in Figure VI.20. The predictions assuming a contact resistance of 2.0×10^5 Ω

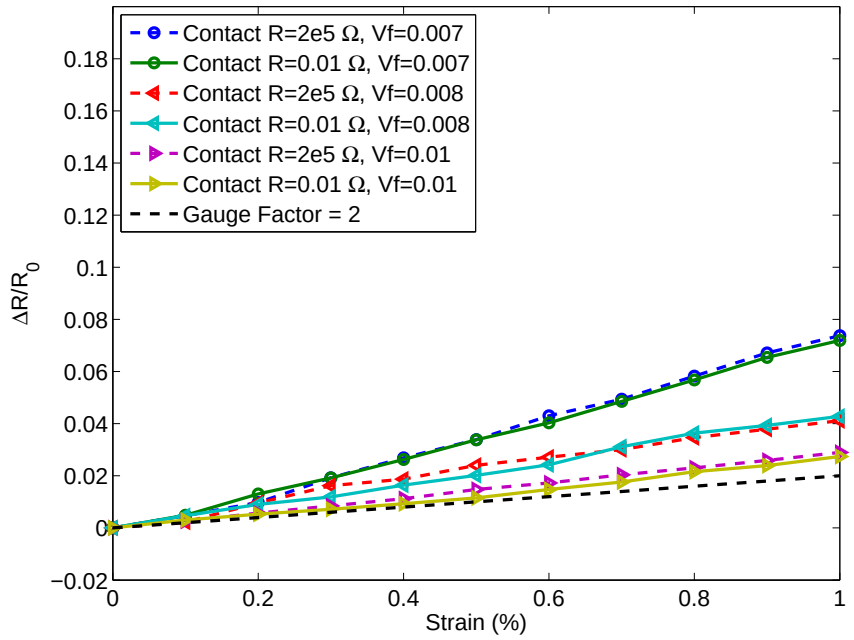

Figure VI.17. Effect of CNT contact resistance on predicted change in resistance for MWCNT/epoxy with Poisson's ratio of 0.3.

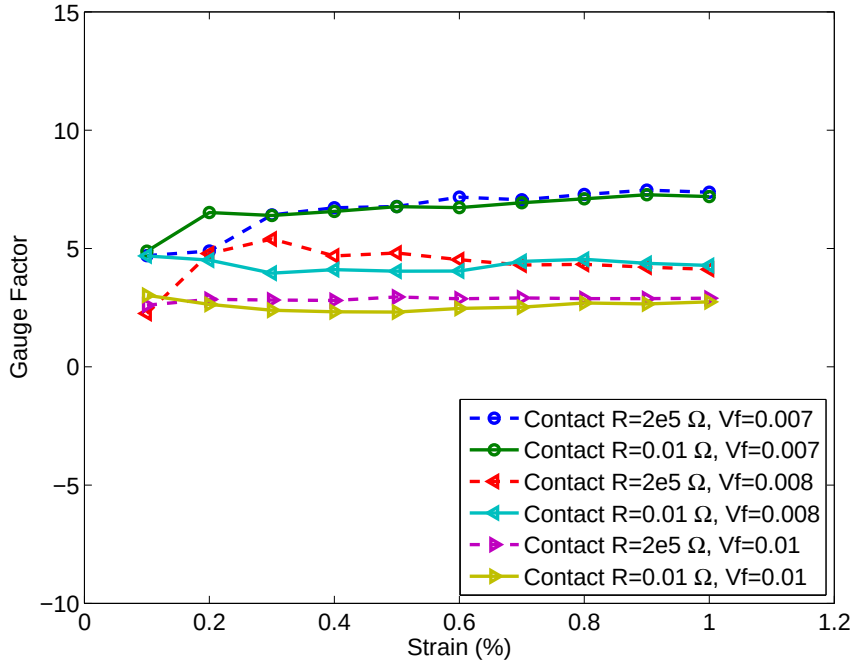

Figure VI.18. Effect of CNT contact resistance on predicted gauge factors for MWCNT/epoxy with Poisson's ratio of 0.3.

are again shown in the figures for comparison. Unlike the 0.0 and 0.3 Poisson's ratio predictions, the contact resistance appears to have a noticeable effect on piezoresistivity when the Poisson's ratio is 0.5. The nonzero contact resistance predictions do not show any appreciable difference between the three volume fractions shown in the figures. However, the zero contact resistance predictions vary for the three volume fractions. The Vf=0.007 case has a nearly constant gauge factor of approximately two, while the Vf=0.008 case has a slightly negative gauge factor. The Vf=0.01 case actually has gauge factors that are higher than the Vf=0.008 case, which is unexpected. The lack of a clear trend for the zero contact resistance predictions indicates that lower contact resistances lead to greater random variation in the predicted response. To understand why, consider two clusters of CNTs that are brought into contact due to Poisson contraction. If the contact resistance between the two clusters is relatively similar to the resistance of the CNTs, the

VI.B. Predicted piezoresistivity of MWCNT/epoxy using the FEA/Eshelby model

In addition to the predictions using the uniform strain piezoresistivity model, the MWCNT/epoxy system was also investigated using the hybrid FEA/Eshelby piezoresistivity model. The predicted change in resistance using this model with an assumed Poisson's ratio of 0.3 is given in Figure VI.21, and the associated gauge factors are shown in Figure VI.22. The predictions from the uniform strain model are also plotted for comparison. Note that the FEA/Eshelby piezoresistivity model is much more computationally expensive than the uniform strain model, so only the

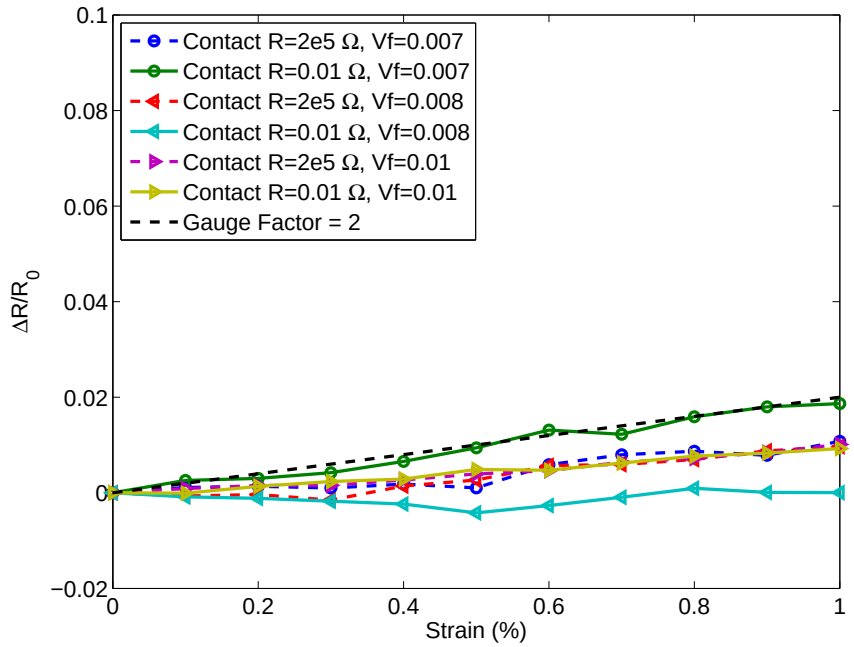

Figure VI.19. Effect of CNT contact resistance on predicted change in resistance for MWCNT/epoxy with Poisson's ratio of 0.5.

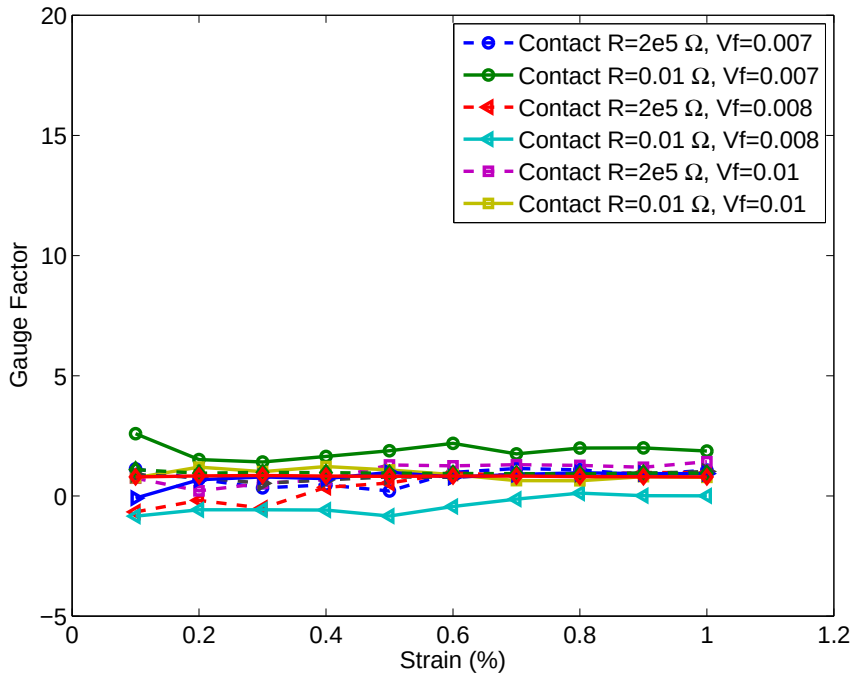

Figure VI.20. Effect of CNT contact resistance on predicted gauge factors for MWCNT/epoxy with Poisson's ratio of 0.5.

0.007 and 0.008 volume fractions are shown. However, the uniform strain results indicate that the greatest piezoresistive response occurs at these volume fractions.

Figures VI.21-VI.22 reveal that the uniform and FEA/Eshelby piezoresistivity models yield similar predictions of piezoresistive performance. However, there appears to be more variance in the FEA/Eshelby predictions than the uniform strain predictions. This is expected because the FEA/Eshelby model takes the local elastic interactions between CNTs into account. It is reasonable to assume that these interactions cause more scatter in the predictions than the uniform strain model. This could mean that many more realizations with larger sized RVEs are needed to average out the scatter, or it could be that the actual material does not behave uniformly. Even with the additional scatter, however, both piezoresistivity models predict a maximum change in resistance of approximately 7%.

Because of the large effects of Poisson's ratio seen thus far, the assumed Poisson's ratio was again varied using the FEA/Eshelby piezoresistivity model. The predicted change in resistance using this model with an assumed Poisson's ratio of 0.4 is given in Figure VI.23, and the associated gauge factors are shown in Figure VI.24. The predictions from the uniform strain model are also shown for comparison. The two models predicted comparable values of relative resistance and gauge factors at small strains up to about 0.4% strain. However, at higher strains, the FEA/Eshelby model predicted significantly higher values than the uniform strain model. It is unclear why this would be the case, but it could be due to the local interactions taken into account in the FEA/Eshelby model. It is possible that the interactions between CNTs keep the CNT clusters from being pushed as close together when the network undergoes

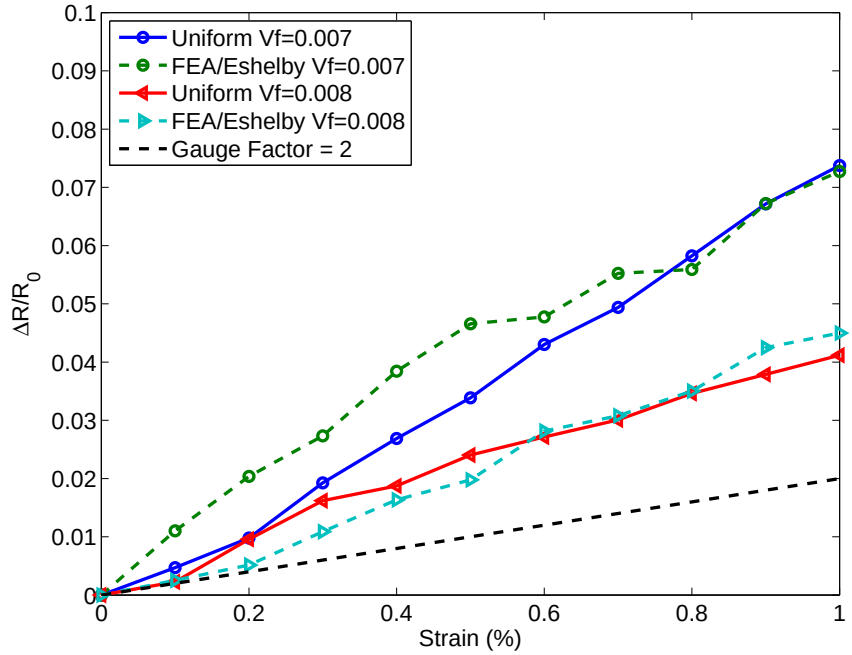

Figure VI.21. Predicted normalized change in resistance for MWCNT/epoxy with Poisson's ratio of 0.3 using the FEA/Eshelby piezoresistivity model.

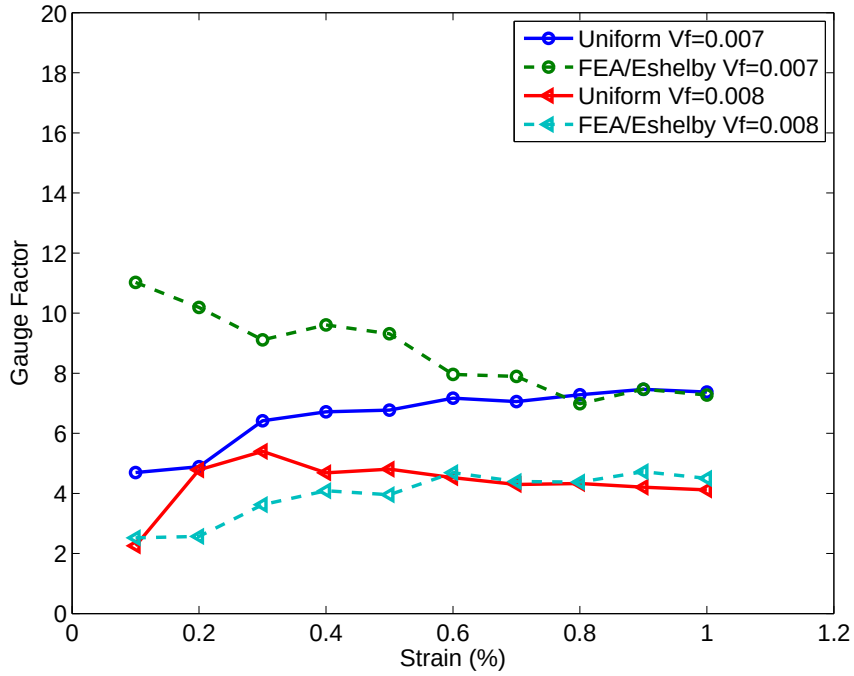

Figure VI.22. Predicted gauge factors for MWCNT/epoxy with Poisson's ratio of 0.3 using the FEA/Eshelby piezoresistivity model.

Poisson contraction, which would result in higher resistivities as well as a higher change in resistance.

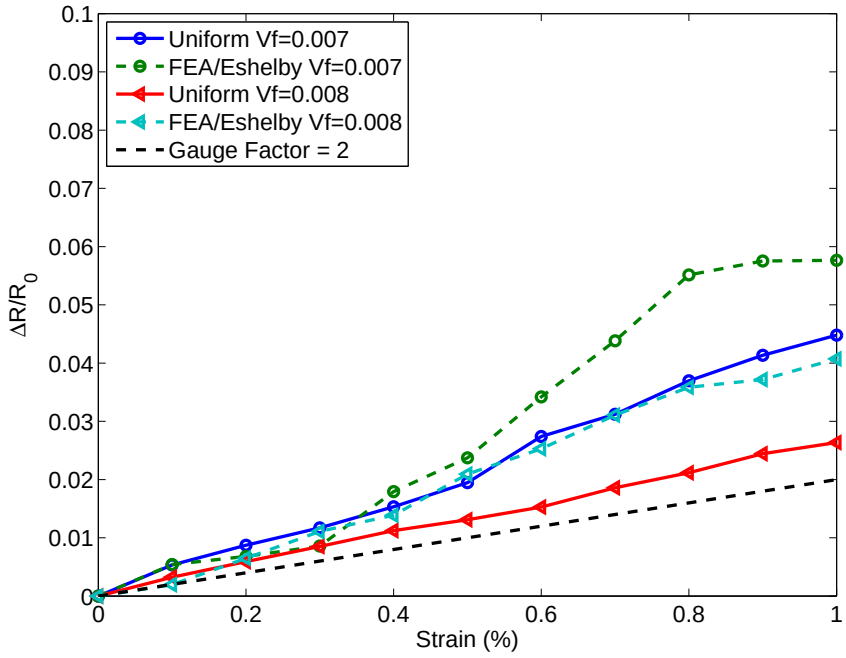

Figure VI.23. Predicted normalized change in resistance for MWCNT/epoxy with Poisson's ratio of 0.4 using the FEA/Eshelby piezoresistivity model.

The predicted change in resistance using the FEA/Eshelby model with an assumed Poisson's ratio of 0.5 is given in Figure VI.25, and the associated gauge factors are shown in Figure VI.26. Except for some erratic behavior at very low strains, the FEA/Eshelby model predicted a nearly nonexistent piezoresistive response. The figures show that the gauge factors hover close to zero for most of the levels of applied strain. The uniform strain model predicted a slightly greater piezoresistive response, but the predicted gauge factors were still less than two. The lack of a significant

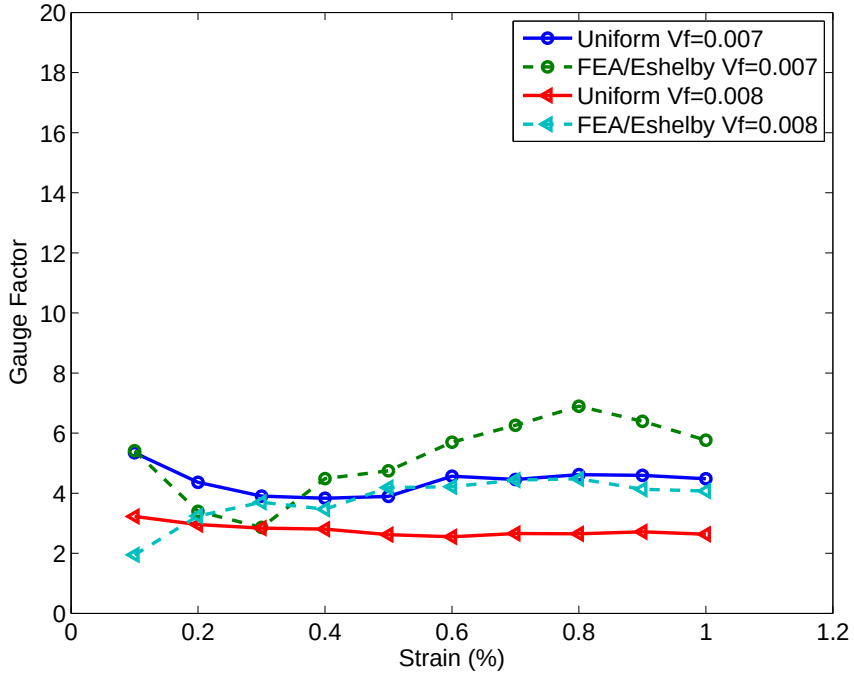

Figure VI.24. Predicted gauge factors for MWCNT/epoxy with Poisson's ratio of 0.4 using the FEA/Eshelby piezoresistivity model.

piezoresistive response predicted by both models is further evidence that the Poisson contraction of the RVE effectively cancels out any resistivity increase in the loading direction.

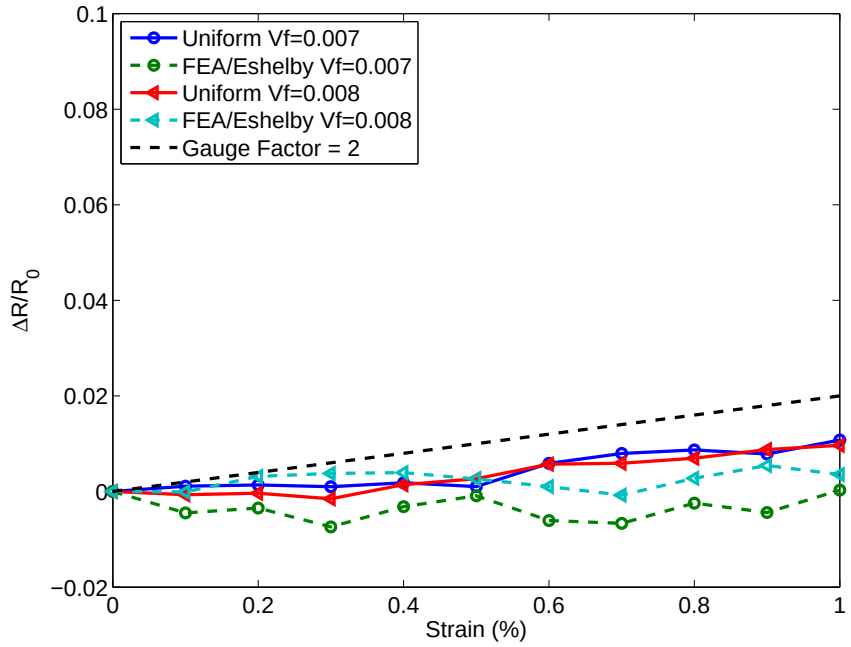

Figure VI.25. Predicted normalized change in resistance for MWCNT/epoxy with Poisson's ratio of 0.5 using the FEA/Eshelby piezoresistivity model.

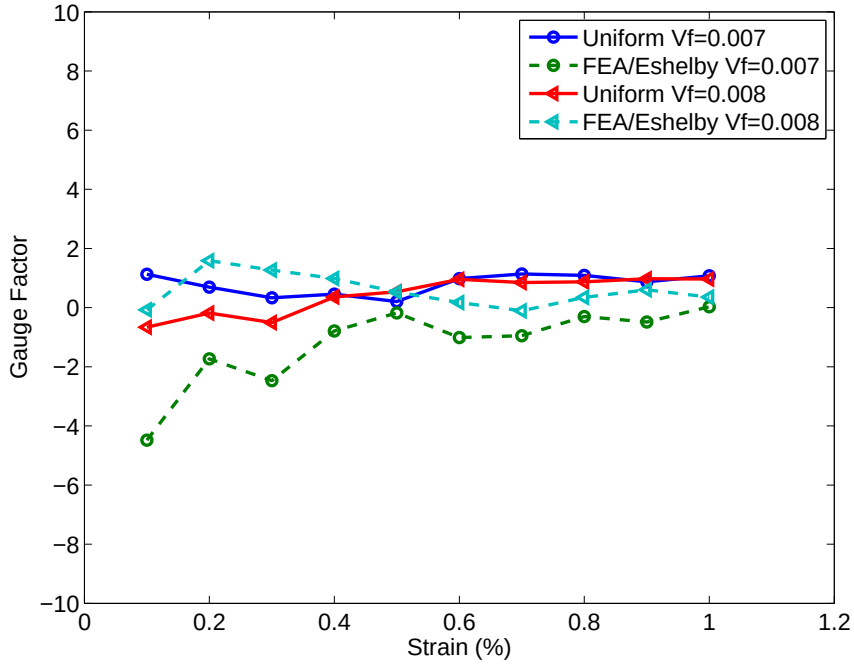

Figure VI.26. Predicted gauge factors for MWCNT/epoxy with Poisson's ratio of 0.5 using the FEA/Eshelby piezoresistivity model.

VI.C. Predicted piezoresistivity of MWCNT/polypropylene using the uniform strain model

The piezoresistive properties of the MWCNT/polypropylene (PP) material system were modeled using the calibrated network assumptions determined in Chapter V, which are given in Table VI.2. Recall from Chapter V that the predicted conductivities of this material system compared well with experimental conductivity values after calibrating the contact resistance of the model. It should be noted that the piezoresistive response of this material system has not been investigated experimentally. However, this system could have interesting sensing applications because, as Chu et al. [108] pointed out, it is suitable for high volume production techniques (e.g. injection molding).

MWCNT length	2.5 μm
MWCNT diameter	10 nm
MWCNT resistance per unit length	13.0×10^9 Ω/m
Contact resistance	5.0×10^9 Ω
RVE length	15 μm

Table VI.2. Material properties used for MWCNT/PP in piezoresistivity models.

Compared to the thermoset epoxy in the MWCNT/epoxy system, the thermoplastic polypropylene matrix has very different mechanical, thermal, and chemical properties. However, it must be stressed that many of these properties are not ex-

plicitly accounted for in the piezoresistivity models. Only the Poisson's ratio of the nanocomposite, the contact resistance between CNTs, and the electron tunneling barrier height of the polymer account for the matrix properties in the models. Additionally, the FEA/Eshelby model does assume a Young's modulus for the polymer, but the moduli of epoxy and polypropylene are similar enough to assume a modulus of 3.0 GPa for both. The Poisson's ratio for the two types of nanocomposites has not been reported, so parametric studies investigating the effect of Poisson's ratio were performed. The tunneling barrier height is approximately the same for epoxy and polypropylene, so values of 2.0 eV were assumed for both. Thus, the piezoresistivity models only account for different matrix materials via the calibrated contact resistance between CNTs.

For the purposes of the piezoresistivity models in this work, the main differences between the MWCNT/epoxy and MWCNT/PP systems are the length and diameter of the MWCNTs used in each material. As detailed in Chapter V, the MWCNTs dispersed by Chu et al. in polypropylene were shorter and of smaller diameter than the MWCNTs used by Hu et al. [56] in the epoxy system. The higher aspect ratio MWCNTs used with the polypropylene result in percolation thresholds at lower volume fractions, so it is expected that good piezoresistive performance can be achieved with MWCNT/PP at lower volume fractions than the MWCNT/epoxy system.

The changes in network resistance at strain levels up to 1% are given in Figure VI.27 where each data point is the 10% trimmed mean value for 50 unique realizations. The corresponding gauge factors are given in Figure VI.28. The uniform strain piezoresistivity model from Chapter II was used. The volume fractions consid-

ered were 0.0025, 0.003, and 0.004. These volume fractions were chosen because the electrical conductivity results from Chapter V indicated these were the lowest volume fractions that could be used that virtually always result in percolated networks. Additionally, the piezoresistive results for the MWCNT/epoxy system showed that increasing nanotube volume fraction leads to lower piezoresistive gauge factors, so volume fractions greater than 0.004 were not considered for the MWCNT/PP system.

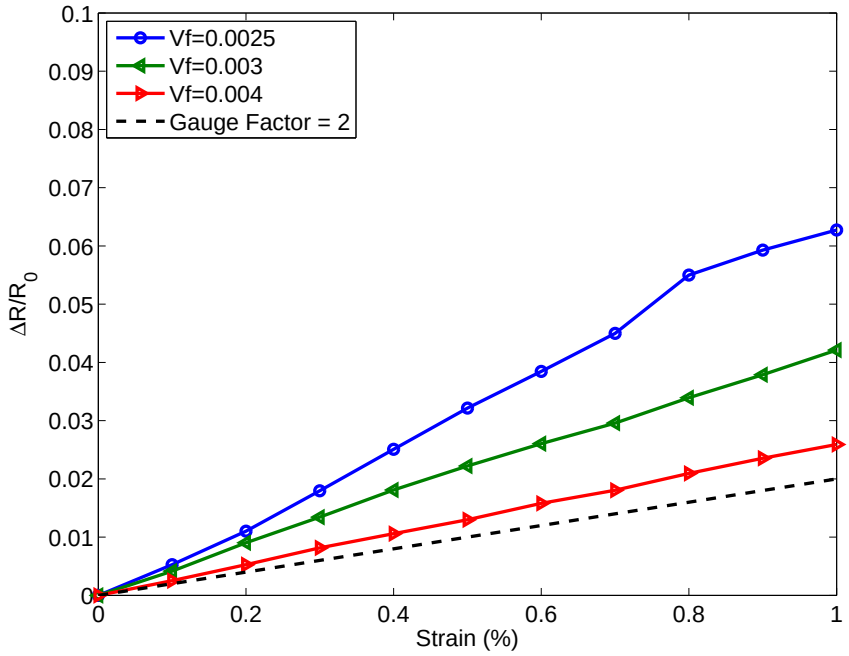

Figure VI.27. Predicted normalized change in resistance for MWCNT/PP with assumed Poisson's ratio of 0.3.

The predictions in Figures VI.27-VI.28 are very similar to the predictions for the MWCNT/epoxy system. The maximum change in resistance is approximately 6% with a maximum gauge factor just above six. Additionally, the relative resistance change is approximately linear, and the volume fraction appears to significantly af-

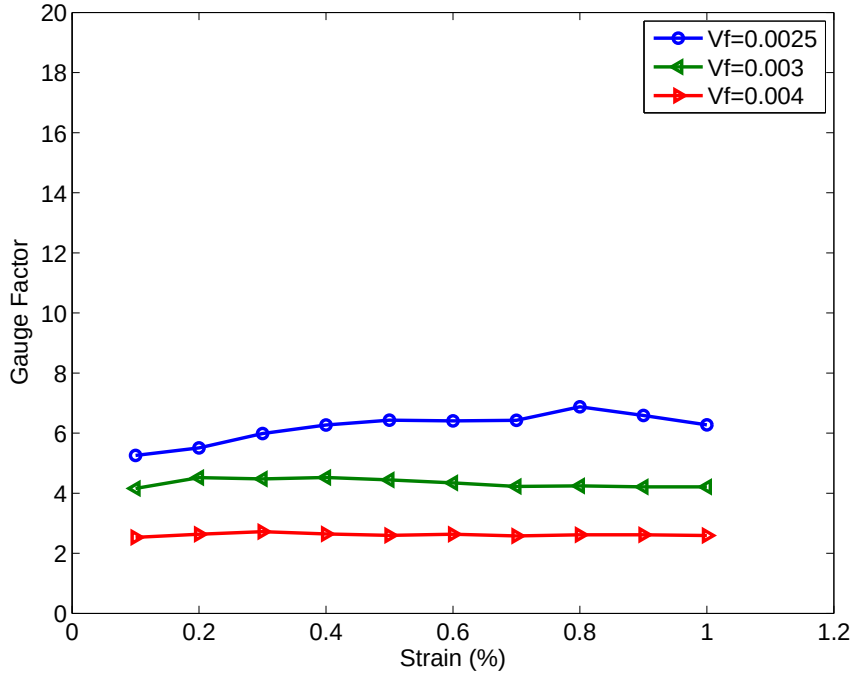

Figure VI.28. Predicted gauge factors for MWCNT/PP with assumed Poisson's ratio of 0.3.

fect the piezoresistive response. Like the MWCNT/epoxy system, the results indicate that lower volume fractions of MWCNTs in polypropylene yield greater piezoresistance. The predicted resistance changes do not appear to be erratic for any of the volume fractions, which indicates that the 15 μm RVE size is large enough to capture the representative piezoresistive behavior for the MWCNT/PP system.

Because the Poisson's ratio was found to have a large effect on the MWCNT/epoxy piezoresistivity, the assumed Poisson's ratio of the MWCNT/PP system was varied. Tscharnuter et al. showed experimentally that the viscoelastic Poisson's ratio for polypropylene varied from 0.3-0.5. [110] Thus, it is important to investigate the piezoresistive material behavior in this range. The change in resistance and gauge factors assuming a Poisson's ratio of 0.4 are given in Figures VI.29-VI.30. The pre-

dictions are again similar to the MWCNT/epoxy results. The maximum change in resistance is approximately 4% with maximum gauge factors between 4-6. The Poisson's ratio again clearly affects the piezoresistive response greatly. It is interesting that even with MWCNTs of different length and diameter, the Poisson's ratio still seems to be the dominant effect. However, it should be noted that even though the size of the MWCNTs does not appear to affect the piezoresistance, the volume fractions needed to obtain the same piezoresistive response are much lower for the MWCNT/PP system. This is due to effects presented in Chapter V. Specifically, higher CNT aspect ratios lead to lower percolation thresholds. The piezoresistive results thus far indicate the greatest piezoresistance occurs at the lowest volume fraction past the percolation threshold. Thus, the best piezoresistance for the MWCNT/epoxy system occurs at Vf=0.007 while the best piezoresistance for MWCNT/PP occurs at Vf=0.0025. However, it is still surprising that the piezoresistance at these volume fractions are so similar.

Many polymers are known to approach the incompressible limit, especially at elevated temperatures, so it is again necessary to investigate the piezoresistive performance with an assumed Poisson's ratio of 0.5. The change in resistance and gauge factors assuming a Poisson's ratio of 0.5 are given in Figures VI.31-VI.32. Inspection of the plots reveals that the relative changes in resistance are all less than 1%, and the gauge factors for all three volume fractions are between 0-1. As expected, the higher Poisson's ratio of the material leads to an insignificant piezoresistive response. This is again most likely due to the CNT clusters that come into contact with each other due to Poisson contraction.

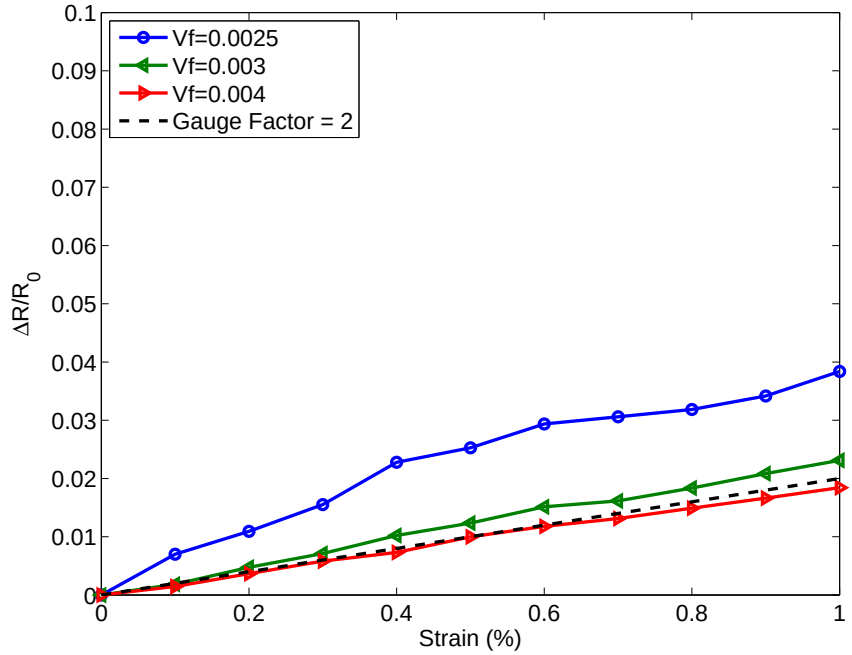

Figure VI.29. Predicted normalized change in resistance for MWCNT/PP with assumed Poisson's ratio of 0.4.

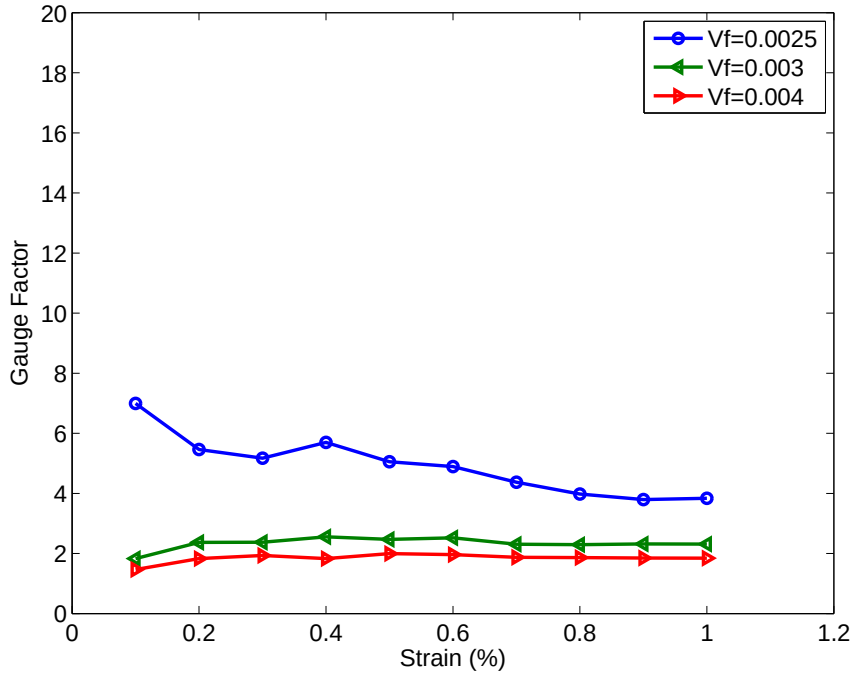

Figure VI.30. Predicted gauge factors for MWCNT/PP with assumed Poisson's ratio of 0.4.

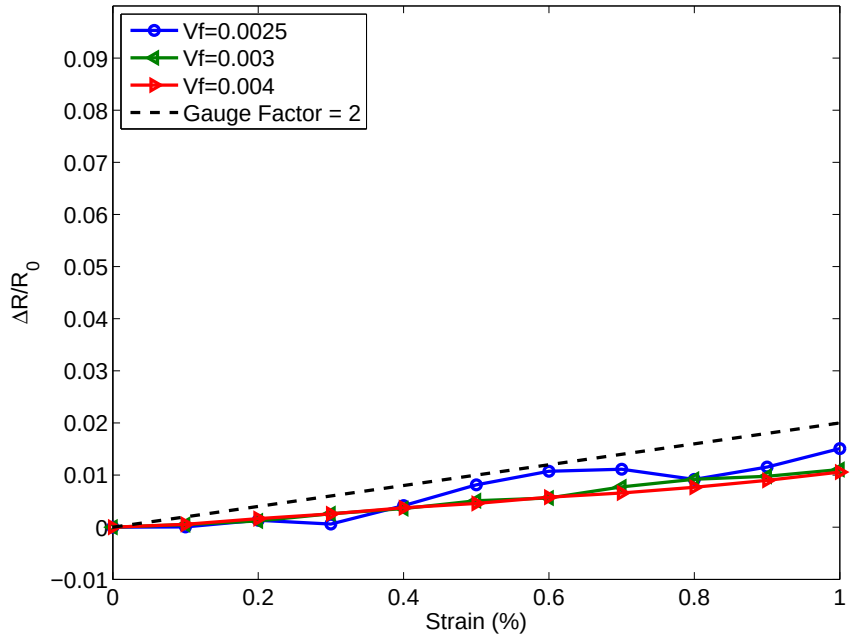

Figure VI.31. Predicted normalized change in resistance for MWCNT/PP with assumed Poisson's ratio of 0.5.

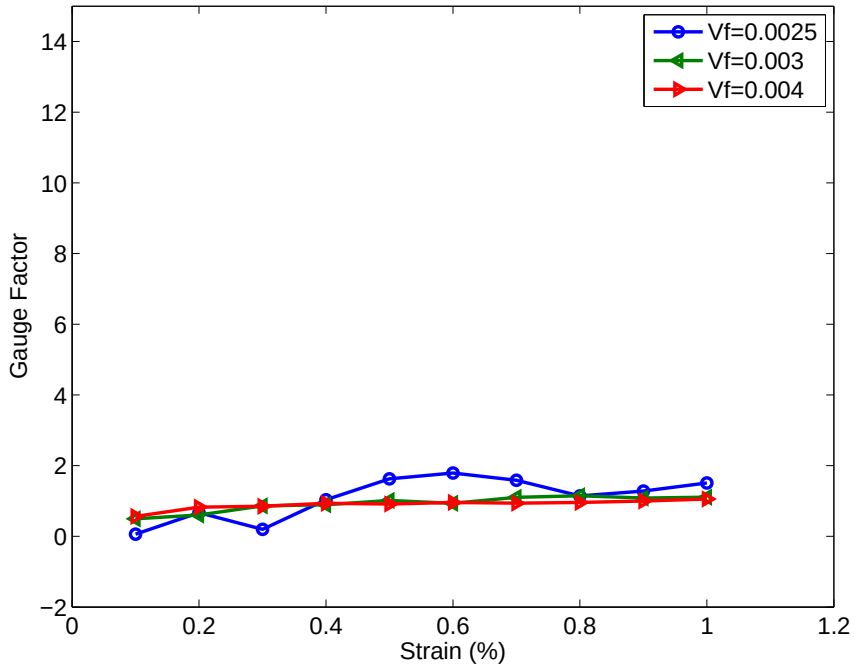

Figure VI.32. Predicted gauge factors for MWCNT/PP with assumed Poisson's ratio of 0.5.

The piezoresistance for the MWCNT/PP material system was also predicted for an assumed Poisson's ratio of zero, and the change in resistance and gauge factors from these analyses are given in Figures VI.33-VI.34. While most polymers have Poisson's ratios that range from 0.3-0.5, assuming a value of zero gives a good measure of the material's maximum possible piezoresistance. It is clear from the figures that the absence of Poisson contraction does indeed result in much higher piezoresistance for the MWCNT/PP material. The maximum gauge factors between 15-20 are not quite as high as those predicted for the MWCNT/epoxy (20-25), but they are still much higher than the gauge factors for the 0.3-0.5 Poisson's ratio predictions. This is further evidence that Poisson contraction is the dominant mechanism affecting piezoresistance.

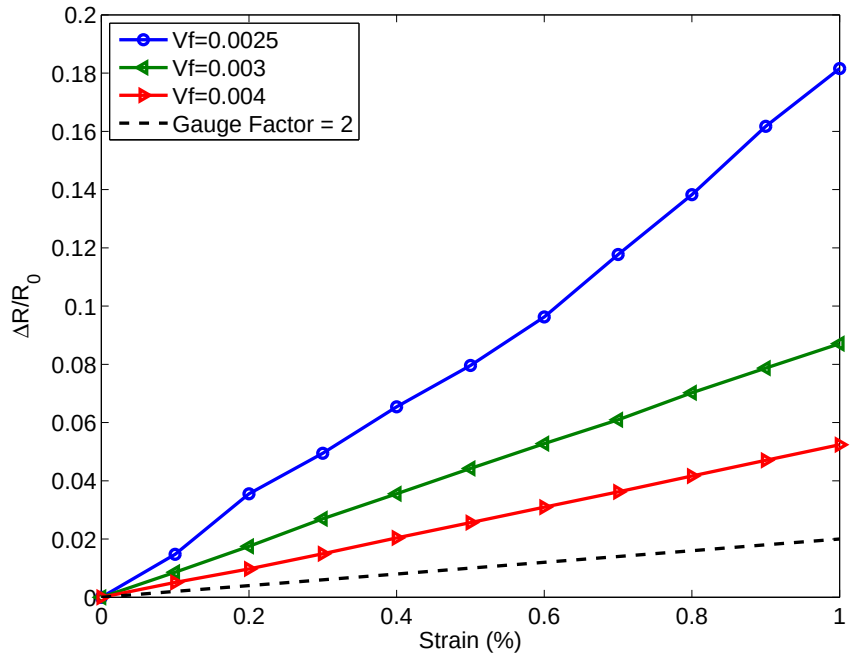

Figure VI.33. Predicted normalized change in resistance for MWCNT/PP with assumed Poisson's ratio of 0.0.

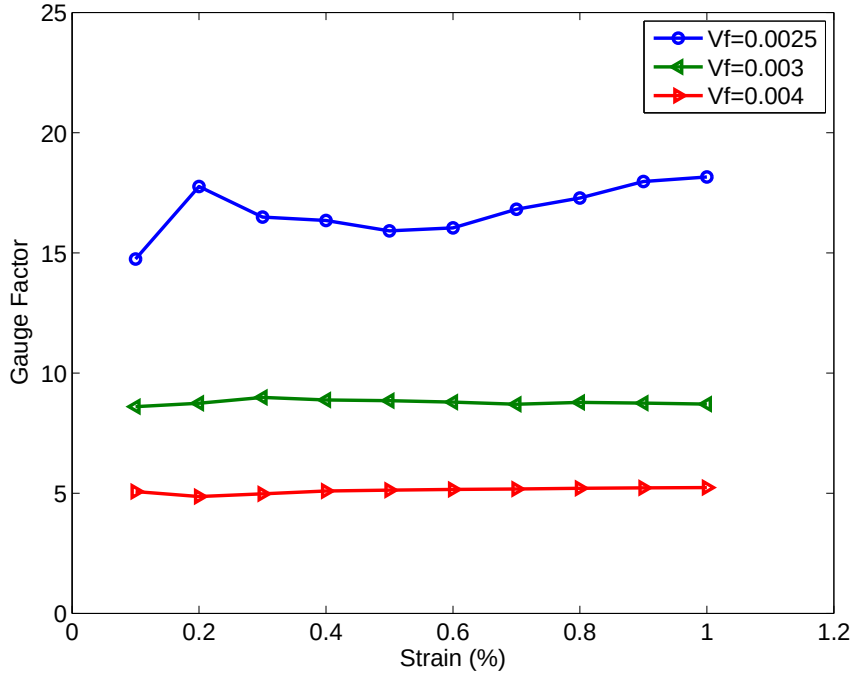

Figure VI.34. Predicted gauge factors for MWCNT/PP with assumed Poisson's ratio of 0.0.

VI.D. Predicted piezoresistivity of MWCNT/polypropylene using the FEA/Eshelby model

In addition to the predictions using the uniform strain piezoresistivity model, the MWCNT/PP system was also investigated using the FEA/Eshelby piezoresistivity model. The 10% trimmed mean of the predicted change in resistance using both models are compared in Figure VI.35, and the associated gauge factors are shown in Figure VI.36. The assumed value for Poisson's ratio was 0.3. Again, note that the FEA/Eshelby piezoresistivity model is much more computationally expensive than the uniform strain model, so only two volume fractions are shown.

However, predictions using the uniform strain piezoresistivity model indicate that the best piezoresistive response occurs at volume fractions around 0.0025-0.003. The predicted relative change in resistance is similar between the two models, but the magnitudes do not match exactly. However, this is to be expected because of the local interaction effects incorporated into the FEA/Eshelby model. Additionally, both models appear to predict relatively linear changes in resistance, which is ideal for strain sensing applications.

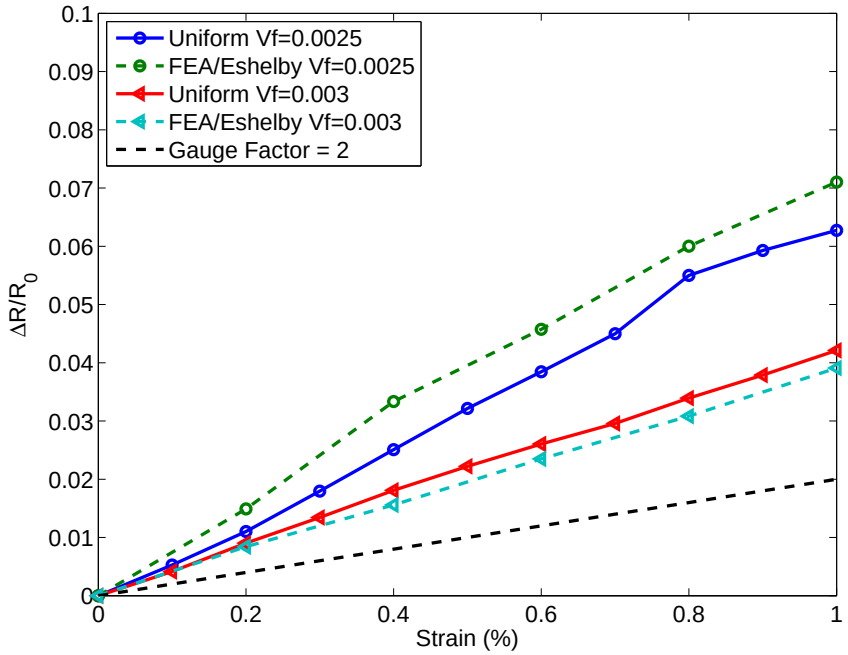

Figure VI.35. Predicted normalized change in resistance for MWCNT/PP with Poisson's ratio of 0.3 using the FEA/Eshelby piezoresistivity model.

Figures VI.37-VI.38 compare the predicted changes in resistance and gauge factors using the FEA/Eshelby and uniform strain models for a Poisson's ratio of 0.4. While the models predict similar responses, the FEA/Eshelby predictions for the

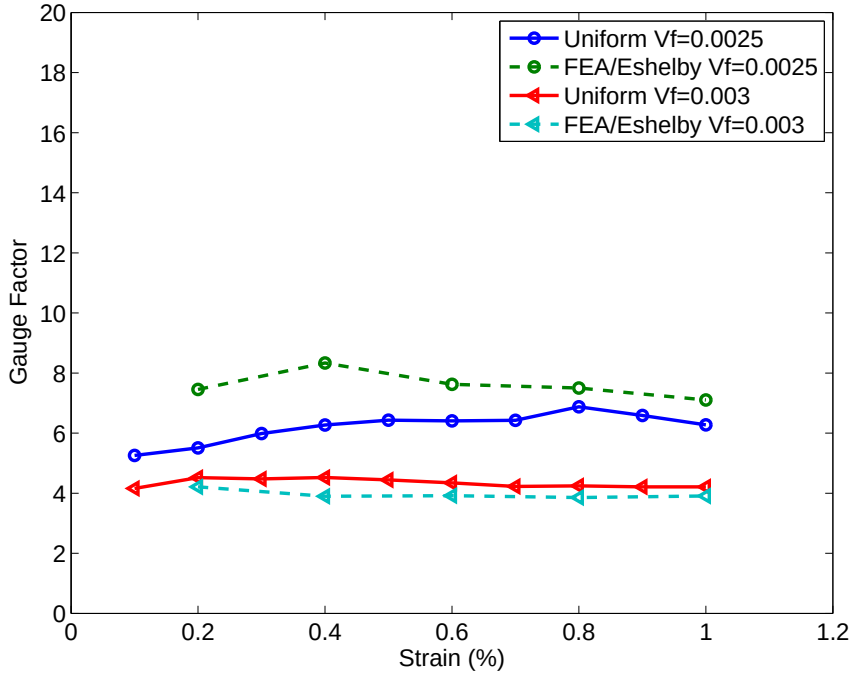

Figure VI.36. Predicted gauge factors for MWCNT/PP with Poisson's ratio of 0.3 using the FEA/Eshelby piezoresistivity model.

0.0025 and 0.003 volume fractions are both larger than the uniform strain predictions. The larger change in resistance predicted by the FEA/Eshelby model could again possibly be explained by the effects of local CNT interactions already discussed.

Finally, the predicted changes in resistance using the FEA/Eshelby and uniform strain models with an assumed Poisson's ratio of 0.5 are given in Figure VI.39, and the associated gauge factors are plotted in Figure VI.40. This incompressible limit case provides more evidence that lower Poisson's ratios are needed for any significant piezoresistance. All of the predicted resistance changes and gauge factors for both piezoresistivity models indicate that the piezoresistive performance is lower than a strain gauge with a gauge factor of two. This is again most likely due to the effect of Poisson contraction pushing CNT clusters within tunneling range of each other.

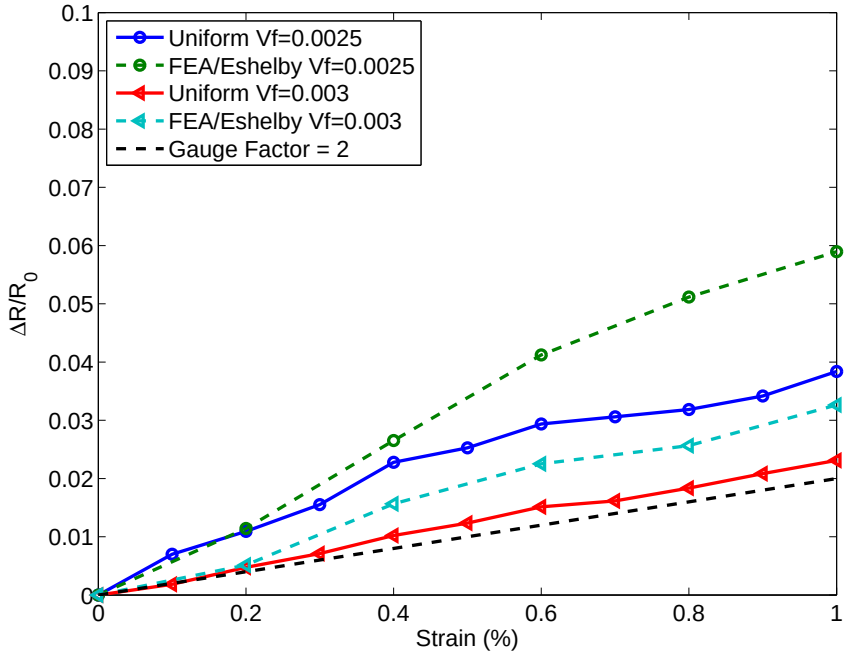

Figure VI.37. Predicted normalized change in resistance for MWCNT/PP with Poisson's ratio of 0.4 using the FEA/Eshelby piezoresistivity model.

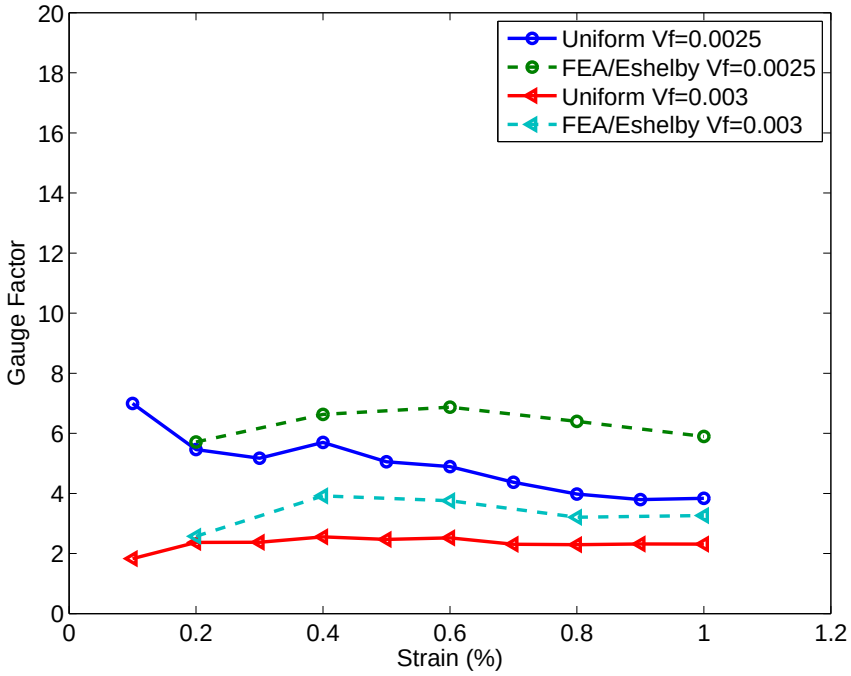

Figure VI.38. Predicted gauge factors for MWCNT/PP with Poisson's ratio of 0.4 using the FEA/Eshelby piezoresistivity model.

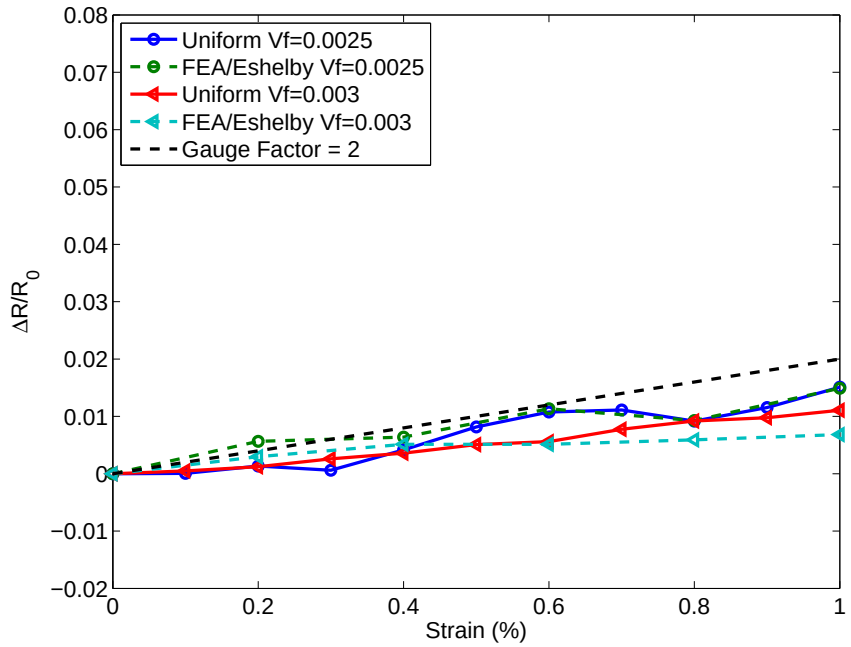

Figure VI.39. Predicted normalized change in resistance for MWCNT/PP with Poisson's ratio of 0.5 using the FEA/Eshelby piezoresistivity model.

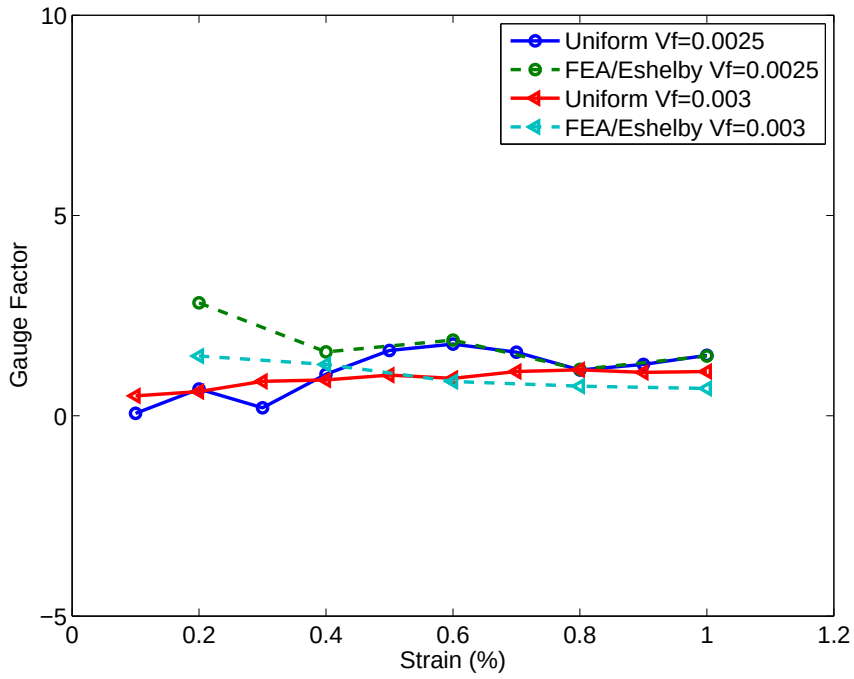

Figure VI.40. Predicted gauge factors for MWCNT/PP with Poisson's ratio of 0.5 using the FEA/Eshelby piezoresistivity model.

VI.E. Discussion of piezoresistivity results

The most interesting result from all of the piezoresistive modeling is that Poisson's ratio has such a large effect on piezoresistive performance. While Poisson's ratio has recently been of interest in understanding modern material behavior [111], this material property is usually either assumed to be 0.3, or it is outright ignored by researchers. However, the work herein indicates that tailoring the effective Poisson's ratio of piezoresistive nanocomposites could increase sensing performance drastically. Additionally, experimental studies by Loh et al. [69] have shown that CNT/polymer strain sensors exhibit a decay in sensitivity when subjected to cyclic loading. The effect was attributed to various thermal effects changing the contact resistance between CNTs. However, the decay could actually be caused by the material's strong dependence on Poisson's ratio, which is actually highly viscoelastic. For example, Tscharnuter et al. [110] showed experimentally that the viscoelastic Poisson's ratio for polypropylene varied from 0.3-0.5. If the Poisson's ratio of the material increases during cyclic loading, then, based on the predictions herein, it is reasonable to assume that the material piezoresistance would also decrease during cyclic loading. More experimental work would be needed to verify this hypothesis.

As mentioned previously, the FEA/Eshelby model is much more computationally expensive to use than the uniform strain model. The predictions using this model did provide some insights into the material behavior when compared to the uniform strain predictions. However, in order for the FEA/Eshelby model to fully realize its potential, the model needs further enhancements and efficiency refinements. It could then be used more effectively to explore local mechanisms responsible for CNT/poly-

mer piezoresistance. One possible strategy could be to use the uniform strain model first to get a general idea of a material's piezoresistive performance, and then use the FEA/Eshelby model to further refine the predictions for specific cases. Additionally, both the FEA/Eshelby and uniform strain models would be more accurate if hard-core nanotubes were modeled. Not allowing CNTs to interpenetrate could possibly cause the tunneling resistance between CNTs to affect the piezoresistive response more.

The effect of Poisson's ratio could also have interesting implications for nanocomposites with aligned or partially aligned CNTs, such as the specimens fabricated by Oliva-Aviles. [61] Recall that the dependence of piezoresistivity on Poisson's ratio was explained by clusters of CNTs coming into electron tunneling range of each other, which decreases the resistivity of the network. Nanotubes aligned in the loading direction might negate the effects of Poisson contraction on piezoresistive response because a much greater contraction would be needed to bring the parallel CNTs within tunneling range of each other. However, the effect might still be strong in nanocomposites with higher volume fractions since the CNTs would be much closer together to start with.

One unanswered question from the literature is whether the piezoresistive behavior of these types of materials is dominated by the change in tunneling distances between nanotubes or the piezoresistance of the nanotubes themselves. Yin et al. [60] fabricated a material similar to the MWCNT/PP system modeled herein and measured a linear response.The authors claimed that this must have been due to stretching of the CNTs. However, the predictions presented in this chapter indicated that

a linear response is possible even if the nanotubes do not stretch. It is also quite possible that the dominant mechanism depends on the specific combination of nanotube type and polymer matrix used in a material system and/or the level of strain applied. More experimental and computational investigations are needed to fully understand the dominant mechanisms.

VI.F. Summary

The uniform strain and FEA/Eshelby piezoresistivity models were both used to predict the piezoresistive performance of the MWCNT/epoxy and MWCNT/PP material systems. The two models yielded similar predictions, but the FEA/Eshelby model was much more computationally expensive to use. The predictions from the uniform strain model compared qualitatively well to experimental values from the literature, but it was unclear why the predictions for piezoresistance were lower than experiment. The FEA/Eshelby model seemed to generally predict slightly higher piezoresistance which was attributed to the model accounting for local elastic interactions between CNTs.

All of the piezoresistive results indicated that Poisson's ratio has a large effect on piezoresistive performance. Moreover, the effect of Poisson's ratio in CNT/polymer nanocomposites appeared to be larger and opposite of the Poisson effect seen in metal strain gauges. This was explained by realizing that relative resistance change is a function of material resistivity change and the change in geometry. It was shown that for higher Poisson's ratios, the resistivity decreases with increasing strain.

The effect of contact resistance on piezoresistive performance was investigated.

It was found that the contact resistance did not seem to affect the material piezoresistance much. This was surprising considering the large effect contact resistance was shown to have on electrical conductivity of the nanocomposite. In addition, it was found that the length and diameter of the two types of MWCNTs modeled did not have much effect on the nanocomposite piezoresistance. The dominant factors affecting piezoresistive performance were found to be CNT volume fraction and the Poisson's ratio of the nanocomposite.

CHAPTER VII

CONCLUSIONS

This research aimed to advance the understanding of electrically conducting carbon nanotube/polymer nanocomposites. This is an important class of materials with diverse applications in flexible microelectronics, electromagnetic shielding, and strain sensing. Computational models were developed and used to analyze 2D and 3D CNT networks using a random resistor network approach, and properties such as electrical conductivity and piezoresistance were predicted and compared to results from the literature. Furthermore, dominant mechanisms impacting electrical and piezoresistive performance were identified. The following sections discuss important conclusions from each of the studies performed. Ideas for enhancing the models in future work are then discussed.

VII.A. Effective conductivity of 2D SWCNT thin films

The 2D nanotube network model was used to investigate the electrical properties of SWCNT thin films. Networks consisting of highly exfoliated SWCNTs and partially exfoliated SWCNT bundles were considered, and predictions were compared to experimental results from White et al. [20]. The effects of nanotube chirality were also considered. Parametric studies investigating the effects of RVE size, nanotube resistivity, and contact resistances between the SWCNTs of various chiralities were investigated. For the partially exfoliated networks, it was found that the model could be made to match experimental results if the contact resistance between nan-

otubes was calibrated to experiment. However, the highly exfoliated network model predicted a percolation curve with a slightly different shape than the experimental results. It was concluded that it might be necessary to include the effects of electron tunneling between nanotubes in the model or develop a different method for modeling Schottky barriers between metallic-semiconducting junctions. Additionally, it was found that the contact resistance between individual CNTs and bundles of CNTs greatly affects the conductivity of the film.

VII.B. Effective conductivity of 3D MWCNT/polymer nanocomposites

The electrical conductivities of the MWCNT/epoxy and MWCNT/polypropylene (PP) systems were predicted using the 3D random resistor network model. The conductivities of the nanocomposites were calculated at various volume fractions and compared to experimental results from the literature. Parametric studies were performed to investigate the effects of RVE size, number of RVEs, CNT length, CNT resistance, and contact resistance between CNTs. The parametric studies were used to determine the number and size of RVEs needed to predict electrical properties that were representative of the bulk material. It was observed that for smaller volume fractions, only a very small percentage of the CNTs in a given network were actually connected to the network backbone, and only a small number of CNTs in the backbone carried any substantial electrical current. As the volume fraction increased, a much larger percentage of nanotubes contributed to the current-carrying capacity of the network, which was found to increase composite conductivity.

It was found that the MWCNT/epoxy predictions matched experimental values

well assuming a contact resistance of 2.0×10^5 Ω, which was measured experimentally in the literature. The CNT length of 5.0 μm reported in the literature also seemed to provide the best predictions. The MWCNT/PP predictions did not initially compare well to experimental conductivity measurements reported in the literature. However, it was found that adjusting the assumed contact resistance and CNT length was sufficient to calibrate the model to experimental results. The contact resistance was increased by four orders of magnitude to 5.0×10^9 Ω, but the CNT length was only decreased slightly to 2.5 μm. It was hypothesized that the much higher contact resistance needed to calibrate the model indicated that the MWCNTs were better encapsulated in the polypropylene, which caused higher contact resistance values between CNTs. The difference in CNT length was attributed to the large distribution of lengths found in the MWCNTs used in the experimental specimens, as well as uncertainty in measuring the lengths.

VII.C. Piezoresistivity of 3D MWCNT/polymer nanocomposites

The uniform strain and FEA/Eshelby piezoresistivity models were both used to predict the piezoresistive performance of the MWCNT/epoxy and MWCNT/PP material systems. The two models yielded similar predictions, but the FEA/Eshelby model was much more computationally expensive to use. The predictions from the uniform strain model compared qualitatively well to experimental values from the literature, but it was unclear why the predictions for piezoresistance were lower than experiment. The FEA/Eshelby model seemed to generally predict slightly higher piezoresistance which was attributed to the model accounting for local elastic inter-

actions between CNTs.

All of the piezoresistive results using both models indicated that Poisson's ratio has a large effect on piezoresistive performance. Moreover, the effect of Poisson's ratio in CNT/polymer nanocomposites appeared to be larger and opposite of the Poisson effect seen in metal strain gauges. This was explained by realizing that relative resistance change is a function of material resistivity change and the change in geometry. It was shown that for higher Poisson's ratios, the resistivity decreases with increasing strain, which limits the total change in resistance.

The effect of contact resistance on piezoresistive performance was investigated. It was found that the contact resistance did not seem to affect the material piezoresistance much. This was surprising considering the large effect contact resistance was shown to have on electrical conductivity of the nanocomposite. In addition, it was found that the length and diameter of the two types of MWCNTs modeled did not have much effect on the nanocomposite piezoresistance. The dominant factors affecting piezoresistive performance were found to be CNT volume fraction and the Poisson's ratio of the nanocomposite.

VII.D. Future work

There are many model features that were not able to be implemented for this work, but they might prove useful or necessary for different types of analyses in the future. Many of the features have been implemented and investigated by other researchers while others are unique to the models described in this work. There are many illuminating studies that could be performed if these features were added to

the models.

One feature that has been implemented much in the literature is the ability to model curved nanotubes. An inspection of microscopy images of many CNT/polymer nanocomposites reveals that most of the CNTs are curved structures, and it would seem rational to want to model the CNTs as closely to their physical likeness as possible. However, as many researchers have found, the computational requirements for curved CNTs in three dimensions are much higher than straight CNTs, and the effect of curviness has not been shown to be necessary for accurate predictions. In addition to the curved nature of CNTs, it is frequently observed in the literature that CNTs form bundles or agglomerations when dispersed in certain types of polymers. While the MWCNT/epoxy and MWCNT/polypropylene material systems investigated in this work have been shown experimentally to have very little agglomerates, there are many other material systems that do not exhibit such good dispersion. It would be useful if the model could probe how the degree of dispersion affects the dominant mechanisms responsible for conductivity and piezoresistivity.

As shown in Chapter V, the characterization of CNT morphology is quite important to being able to accurately predict electrical conductivity. The CNTs used to prepare many nanocomposite specimens are frequently made up of a large variety of nanotube lengths. Thus, being able to incorporate distributions of properties into the model would probably result in more accurate predictions, especially when less is known about the morphology of the CNTs in question. However, the distributions of properties would probably result in more unique realizations needed to obtain an effective response. The two material systems studied using the 3D network models

both consisted of MWCNTs dispersed in a polymer. Compared to SWCNTs, the MWCNTs have smaller aspect ratios which result in reduced computational time. However, there is much interest in the literature in using SWCNTs, so using the models to investigate SWCNT material systems would provide useful insight for another widely used class of material.

It was already pointed out that one drawback of the piezoresistivity models used in this work is the assumption of soft-core CNTs that can interpenetrate. While this assumption can provide valuable insight into structure-property relationships, it is probably necessary to implement hard-core CNTs to obtain better accuracy. The FEA/Eshelby piezoresistivity model would definitely be more accurate using hard-core CNTs. Additionally, the piezoresistivity studies in this work focused on a very narrow type of piezoresistive response. Specifically, the piezoresistance was only measured for materials in uniaxial tension. An obvious extension of this work would involve investigating the piezoresistive performance of various materials in compressive and shear loading states. Furthermore, the degree of CNT alignment could be controlled such that materials could be optimized for strain sensing in specific loading states.

Another possible future use for the computational models in this work is their combination with optimization methods to optimize conducting polymers or piezoresistive sensors. There are many readily available optimization algorithms that could be used to search for combinations of CNT and network properties that result in desired material behavior. Additionally, when calibrating the model to experimental results, optimization algorithms could be used to find combinations of network

parameters that match experimental values.

The hybrid FEA/Eshelby piezoresistivity model was used to predict piezoresistive material response in this work. However, the rigorous development of this framework in Chapter II could be extended further to investigate other micromechanics problems of interest. The current piezoresistivity model uses the interior and exterior point Eshelby solution for an infinite cylinder. Additionally, the solution for a sphere are given in Chapter II. The Eshelby solution for various other ellipsoidal shapes could be derived and used to investigate materials with inclusions other than nanotubes. In addition to the piezoresistive response, mechanical properties such as volume averaged elastic moduli could be predicted. Moreover, the framework could easily be used to study nanocomposites with multiple types of inclusions.

REFERENCES

[1] Iijima, S., "Helical microtubules of graphitic carbon," *Nature*, Vol. 354, 1991, pp. 56–58.

[2] Ounaies, Z., Park, C., Wise, K., Siochi, E., and Harrison, J., "Electrical properties of single wall carbon nanotube reinforced polyimide composites," *Composites Science and Technology*, Vol. 63, No. 11, 2003, pp. 1637–1646.

[3] Pötschke, P., Dudkin, S. M., and Alig, I., "Dielectric spectroscopy on melt processed polycarbonate-multiwalled carbon nanotube composites," *Polymer*, Vol. 44, No. 17, Aug. 2003, pp. 5023–5030.

[4] Sandler, J., Kirk, J., Kinloch, I., Shaffer, M., and Windle, A., "Ultra-low electrical percolation threshold in carbon-nanotube-epoxy composites," *Polymer*, Vol. 44, No. 19, Sept. 2003, pp. 5893–5899.

[5] Skákalová, V., Dettlaff-Weglikowska, U., and Roth, S., "Electrical and mechanical properties of nanocomposites of single wall carbon nanotubes with PMMA," *Synthetic Metals*, Vol. 152, No. 1-3, Sept. 2005, pp. 349–352.

[6] Smith, C., "Piezoresistance effect in germanium and silicon," *Physical Review*, Vol. 94, No. 1, 1954, pp. 42–49.

[7] Barlian, A., Park, W., Mallon, J., Rastegar, A., and Pruitt, B., "Review: Semiconductor piezoresistance for microsystems," *Proceedings of the IEEE Inst Electr Electron Eng*, Vol. 97, No. 3, 2009, pp. 513–552.

[8] Li, C., Thostenson, E. T., and Chou, T.-W., "Sensors and actuators based on carbon nanotubes and their composites: a review," *Composites Science and Technology*, Vol. 68, No. 6, May 2008, pp. 1227–1249.

[9] Gibson, R. F., "A review of recent research on mechanics of multifunctional composite materials and structures," *Composite Structures*, Vol. 92, No. 12, Nov. 2010, pp. 2793–2810.

[10] Ghoniem, N., Busso, E., Kioussis, N., and Huang, H., "Multiscale modelling of nanomechanics and micromechanics: an overview," *Philosophical Magazine*, Vol. 83, No. 31, 2003, pp. 3475–3528.

[11] Wernik, J. M. and Meguid, S. A., "Coupling atomistics and continuum in solids: status, prospects, and challenges," *International Journal of Mechanics and Materials in Design*, Vol. 5, No. 1, Sept. 2009, pp. 79–110.

[12] Bauhofer, W. and Kovacs, J. Z., "A review and analysis of electrical percolation in carbon nanotube polymer composites," *Composites Science and Technology*, Vol. 69, No. 10, Aug. 2009, pp. 1486–1498.

[13] Hu, N., Masuda, Z., Yan, C., Yamamoto, G., Fukunaga, H., and Hashida, T., "The electrical properties of polymer nanocomposites with carbon nanotube fillers." *Nanotechnology*, Vol. 19, No. 21, May 2008, pp. 215701.

[14] Stauffer, D. and Aharony, A., *Introduction to Percolation Theory*, Taylor and Francis Inc, Philadelphia, PA, 2nd ed., 1994.

[15] Stauffer, D., "Classical Percolation," *Quantum and Semi-classical Percolation and Breakdown in Disordered Solids*, edited by B. K. Chakrabarti, K. K. Bardhan, and A. K. Sen, Vol. 762 of *Lecture Notes in Physics*, Springer Berlin Heidelberg, Berlin, Heidelberg, 2009, pp. 1–19.

[16] Snow, E. S., Novak, J. P., Campbell, P. M., and Park, D., "Random networks of carbon nanotubes as an electronic material," *Applied Physics Letters*, Vol. 82, No. 13, 2003, pp. 2145–2147.

[17] Topinka, M., Rowell, M. W., Goldhaber-Gordon, D., McGehee, M. D., Hecht, D. S., and Gruner, G., "Charge transport in interpenetrating networks of semiconducting and metallic carbon nanotubes." *Nano Letters*, Vol. 9, No. 5, May 2009, pp. 1866–1871.

[18] Simien, D., Fagan, J., Luo, W., Douglas, J. F., Migler, K., and Obrzut, J., "Influence of nanotube length on the optical and conductivity properties of thin single-wall carbon nanotube networks." *ACS Nano*, Vol. 2, No. 9, Sept. 2008, pp. 1879–1884.

[19] McLachlan, D., "Equation for the conductivity of metal-insulator mixtures," *Journal of Physics C: Solid State Physics*, Vol. 18, 1985, pp. 1891–1897.

[20] White, K. L., Shuai, M., Zhang, X., Sue, H.-J., and Nishimura, R., "Electrical conductivity of well-exfoliated single-walled carbon nanotubes," *Carbon*, Vol. 49, No. 15, Dec. 2011, pp. 5124–5131.

[21] Kumar, S., Pimparkar, N., Murthy, J. Y., and Alam, M., "Theory of transfer characteristics of nanotube network transistors," *Applied Physics Letters*, Vol. 88, No. 12, 2006, pp. 123505.

[22] Ishida, M. and Nihey, F., "Estimating the yield and characteristics of random network carbon nanotube transistors," *Applied Physics Letters*, Vol. 92, No. 16, 2008, pp. 163507.

[23] Li, J., Zhang, Z.-B., and Zhang, S.-L., "Percolation in random networks of heterogeneous nanotubes," *Applied Physics Letters*, Vol. 91, No. 25, 2007, pp. 253127.

[24] Kocabas, C., Pimparkar, N., Yesilyurt, O., Kang, S. J., Alam, M., and Rogers, J., "Experimental and theoretical studies of transport through large scale, partially aligned arrays of single-walled carbon nanotubes in thin film type transistors." *Nano Letters*, Vol. 7, No. 5, May 2007, pp. 1195–1202.

[25] Wang, Y., Di, C.-a., Liu, Y., Kajiura, H., Ye, S., Cao, L., Wei, D., Zhang, H., Li, Y., and Noda, K., "Optimizing single-walled carbon nanotube films for applications in electroluminescent devices," *Advanced Materials*, Vol. 20, No. 23, Dec. 2008, pp. 4442–4449.

[26] Hu, L., Hecht, D. S., and Grüner, G., "Percolation in transparent and conducting carbon nanotube networks," *Nano Letters*, Vol. 4, No. 12, Dec. 2004, pp. 2513–2517.

[27] Scardaci, V., Coull, R., and Coleman, J. N., "Very thin transparent, conductive carbon nanotube films on flexible substrates," *Applied Physics Letters*, Vol. 97, No. 2, 2010, pp. 023114.

[28] Balberg, I., Anderson, C., Alexander, S., and Wagner, N., "Excluded volume and its relation to the onset of percolation," *Physical Review B*, Vol. 30, No. 7, 1984, pp. 3933–3943.

[29] Pötschke, P., Bhattacharyya, A. R., and Janke, A., "Carbon nanotube-filled polycarbonate composites produced by melt mixing and their use in blends with polyethylene," *Carbon*, Vol. 42, No. 5-6, Jan. 2004, pp. 965–969.

[30] Ramasubramaniam, R., Chen, J., and Liu, H., "Homogeneous carbon nanotube/polymer composites for electrical applications," *Applied Physics Letters*, Vol. 83, No. 14, 2003, pp. 2928–2930.

[31] Gojny, F. H., Wichmann, M. H., Fiedler, B., Kinloch, I., Bauhofer, W., Windle, A. H., and Schulte, K., "Evaluation and identification of electrical and thermal conduction mechanisms in carbon nanotube/epoxy composites," *Polymer*, Vol. 47, No. 6, March 2006, pp. 2036–2045.

[32] Hu, N., Masuda, Z., Yamamoto, G., Fukunaga, H., Hashida, T., and Qiu, J., "Effect of fabrication process on electrical properties of polymer/multi-wall carbon nanotube nanocomposites," *Composites Part A: Applied Science and Manufacturing*, Vol. 39, No. 5, May 2008, pp. 893–903.

[33] Via, M. D., King, J. A., Keith, J. M., and Bogucki, G. R., "Electrical conductivity modeling of carbon black/polycarbonate, carbon nanotube/polycarbonate, and exfoliated graphite nanoplatelet/polycarbonate composites," *Journal of Applied Polymer Science*, Vol. 124, 2012, pp. 182–189.

[34] McLachlan, D., "A new interpretation of percolation conductivity results with large critical regimes," *Solid State Communications*, Vol. 60, No. 10, 1986, pp. 821–825.

[35] Balberg, I., "Tunneling and nonuniversal conductivity in composite materials," *Physical Review Letters*, Vol. 59, No. 12, 1987, pp. 1305–1308.

[36] Balberg, I. and Binenbaum, N., "Cluster structure and conductivity of three-dimensional continuum systems," *Physical Review A*, Vol. 31, No. 2, 1985, pp. 1222–1225.

[37] Balberg, I., "Recent developments in continuum percolation," *Philosophical Magazine Part B*, Vol. 56, No. 6, Dec. 1987, pp. 991–1003.

[38] Balberg, I., "Limits on the continuum-percolation transport exponents," *Physical Review B*, Vol. 57, No. 21, June 1998, pp. 13351–13354.

[39] McLachlan, D. S., Chiteme, C., Park, C., Wise, K. E., Lowther, S. E., Lillehei, P. T., Siochi, E. J., and Harrison, J. S., "AC and DC percolative conductivity of single wall carbon nanotube polymer composites," *Journal of Polymer Science Part B: Polymer Physics*, Vol. 43, No. 22, Nov. 2005, pp. 3273–3287.

[40] Rubin, Z., Sunshine, S., Heaney, M., Bloom, I., and Balberg, I., "Critical behavior of the electrical transport properties in a tunneling-percolation system," *Physical Review B*, Vol. 59, No. 19, May 1999, pp. 12196–12199.

[41] Toker, D., Azulay, D., Shimoni, N., Balberg, I., and Millo, O., "Tunneling and percolation in metal-insulator composite materials," *Physical Review B*, Vol. 68, 2003, pp. 041403.

[42] Pike, G. and Seager, C., "Percolation and conductivity: a computer study," *Physical Review B*, Vol. 10, No. 4, 1974, pp. 1421–1434.

[43] Balberg, I. and Binenbaum, N., "Computer study of the percolation threshold in a two-dimensional anisotropic system of conducting sticks," *Physical Review B*, Vol. 28, No. 7, 1983, pp. 3799–3812.

[44] Balberg, I., "Universal percolation-threshold limits in the continuum," *Physical Review B*, Vol. 31, No. 6, 1985, pp. 4053–4055.

[45] Balberg, I., Binenbaum, N., and Wagner, N., "Percolation thresholds in the three-dimensional sticks system," *Physical Review Letters*, Vol. 52, No. 17, 1984, pp. 1465–1468.

[46] Kirkpatrick, S., "Percolation and conduction," *Reviews of Modern Physics*, Vol. 45, No. 4, 1973, pp. 574–588.

[47] Ward, B., *A Numerical Resistor Network Model for the Determination of Electrical Properties of Nanocomposites*, Master's thesis, Rice University, Houston, TX, 2012.

[48] Spanos, P. and Elsbernd, P., "Estimation of the physical properties of nanocomposites by finite-element discretization and Monte Carlo simulation," *Philosophical Transactions of the Royal Society A*, Vol. 371, No. 1993, 2013, pp. 20120494.

[49] Spanos, P. and Kontsos, A., "A multiscale Monte Carlo finite element method for determining mechanical properties of polymer nanocomposites," *Probabilistic Engineering Mechanics*, Vol. 23, No. 4, Oct. 2008, pp. 456–470.

[50] Seidel, G. D. and Lagoudas, D. C., "A micromechanics model for the electrical conductivity of nanotube-polymer nanocomposites," *Journal of Composite Materials*, Vol. 43, No. 9, April 2009, pp. 917–941.

[51] Rahatekar, S. S., Shaffer, M. S., and Elliott, J. A., "Modelling percolation in fibre and sphere mixtures: routes to more efficient network formation," *Composites Science and Technology*, Vol. 70, No. 2, Feb. 2010, pp. 356–362.

[52] Wichmann, M. H. G., Buschhorn, S. T., Gehrmann, J., and Schulte, K., "Piezoresistive response of epoxy composites with carbon nanoparticles under tensile load," *Physical Review B*, Vol. 80, No. 24, Dec. 2009, pp. 1–8.

[53] Rizvi, R., Cochrane, B., Biddiss, E., and Naguib, H., "Piezoresistance characterization of poly(dimethyl-siloxane) and poly(ethylene) carbon nanotube composites," *Smart Materials and Structures*, Vol. 20, No. 9, Sept. 2011, pp. 094003.

[54] Kang, J., Park, C., and Scholl, J., "Piezoresistive characteristics of single wall carbon nanotube/polyimide nanocomposites," *Journal of Polymer Science: Part B: Polymer Physics*, Vol. 47, No. 10, 2009, pp. 994–1003.

[55] Park, M., Kim, H., and Youngblood, J. P., "Strain-dependent electrical resistance of multi-walled carbon nanotube/polymer composite films," *Nanotechnology*, Vol. 19, No. 5, Feb. 2008, pp. 055705.

[56] Hu, N., Karube, Y., Yan, C., Masuda, Z., and Fukunaga, H., "Tunneling effect in a polymer/carbon nanotube nanocomposite strain sensor," *Acta Materialia*, Vol. 56, No. 13, Aug. 2008, pp. 2929–2936.

[57] Hu, N., Karube, Y., Arai, M., Watanabe, T., Yan, C., Li, Y., Liu, Y., and Fukunaga, H., "Investigation on sensitivity of a polymer/carbon nanotube composite strain sensor," *Carbon*, Vol. 48, No. 3, March 2010, pp. 680–687.

[58] Simmons, J. G., "Generalized formula for the electric tunnel effect between similar electrodes separated by a thin insulating film," *Journal of Applied Physics*, Vol. 34, No. 6, 1963, pp. 1793–1803.

[59] Taya, M., Kim, W., and Ono, K., "Piezoresistivity of a short fiber/elastomer matrix composite," *Mechanics of Materials*, Vol. 28, 1998, pp. 53–59.

[60] Yin, G., Hu, N., Karube, Y., Liu, Y., Li, Y., and Fukunaga, H., "A carbon nanotube/polymer strain sensor with linear and anti-symmetric piezoresistivity," *Journal of Composite Materials*, Vol. 45, No. 12, April 2011, pp. 1315–1323.

[61] Oliva-Avilés, A., Avilés, F., and Sosa, V., "Electrical and piezoresistive properties of multi-walled carbon nanotube/polymer composite films aligned by an electric field," *Carbon*, Vol. 49, No. 9, Aug. 2011, pp. 2989–2997.

[62] Kang, I., Khaleque, M. A., Yoo, Y., Yoon, P. J., Kim, S.-Y., and Lim, K. T., "Preparation and properties of ethylene propylene diene rubber/multi walled carbon nanotube composites for strain sensitive materials," *Composites Part A: Applied Science and Manufacturing*, Vol. 42, No. 6, June 2011, pp. 623–630.

[63] Srivastava, R. K., Vemuru, V. S. M., Zeng, Y., Vajtai, R., Nagarajaiah, S., Ajayan, P. M., and Srivastava, A., "The strain sensing and thermalmechanical behavior of flexible multi-walled carbon nanotube/polystyrene composite films," *Carbon*, Vol. 49, No. 12, Oct. 2011, pp. 3928–3936.

[64] Theodosiou, T. and Saravanos, D., "Numerical investigation of mechanisms affecting the piezoresistive properties of CNT-doped polymers using multiscale models," *Composites Science and Technology*, Vol. 70, No. 9, Sept. 2010, pp. 1312–1320.

[65] Lu, J., Lu, M., Bermak, A., and Lee, Y., "Study of piezoresistance effect of carbon nanotube-PDMS composite materials for nanosensors," *Proceedings of the 7th IEEE International Conference on Nanotechnology*, Hong Kong, 2007, pp. 1240–1243.

[66] Dang, Z.-M., Jiang, M.-J., Xie, D., Yao, S.-H., Zhang, L.-Q., and Bai, J., "Supersensitive linear piezoresistive property in carbon nanotubes-silicone rub-

ber nanocomposites," *Journal of Applied Physics*, Vol. 104, No. 2, 2008, pp. 024114.

[67] Thostenson, E. and Chou, T.-W., "Carbon nanotube networks: sensing of distributed strain and damage for life prediction and self healing," *Advanced Materials*, Vol. 18, No. 21, Nov. 2006, pp. 2837–2841.

[68] Gao, L., Chou, T.-W., Thostenson, E. T., Zhang, Z., and Coulaud, M., "In situ sensing of impact damage in epoxy/glass fiber composites using percolating carbon nanotube networks," *Carbon*, Vol. 49, No. 10, Aug. 2011, pp. 3382–3385.

[69] Loh, K., Lynch, J., Shim, B., and Kotov, N., "Tailoring piezoresistive sensitivity of multilayer carbon nanotube composite strain sensors," *Journal of Intelligent Material Systems and Structures*, Vol. 19, No. 7, Oct. 2007, pp. 747–764.

[70] Pham, G., Park, Y., Liang, Z., Zhang, C., and Wang, B., "Processing and modeling of conductive thermoplastic/carbon nanotube films for strain sensing," *Composites Part B: Engineering*, Vol. 39, No. 1, Jan. 2008, pp. 209–216.

[71] Stampfer, C., Jungen, A., Linderman, R., Obergfell, D., Roth, S., and Hierold, C., "Nano-electromechanical displacement sensing based on single-walled carbon nanotubes." *Nano Letters*, Vol. 6, No. 7, July 2006, pp. 1449–1453.

[72] Stampfer, C., Helbling, T., Obergfell, D., Schöberle, B., Tripp, M. K., Jungen, A., Roth, S., Bright, V. M., and Hierold, C., "Fabrication of single-walled

carbon-nanotube-based pressure sensors." *Nano Letters*, Vol. 6, No. 2, Feb. 2006, pp. 233–237.

[73] Stampfer, C., Helbling, T., Jungen, A., and Hierold, C., "Piezoresistance of single-walled carbon nanotubes," *Transducers and Eurosensors: The 14th International Conference on Solid-State Sensors, Actuators, and Microsystems*, Lyon, France, 2007, pp. 1565–1568.

[74] Hierold, C., Jungen, A., Stampfer, C., and Helbling, T., "Nano electromechanical sensors based on carbon nanotubes," *Sensors and Actuators A: Physical*, Vol. 136, No. 1, May 2007, pp. 51–61.

[75] Grow, R. J., Wang, Q., Cao, J., Wang, D., and Dai, H., "Piezoresistance of carbon nanotubes on deformable thin-film membranes," *Applied Physics Letters*, Vol. 86, No. 9, 2005, pp. 093104.

[76] Cao, J., Wang, Q., and Dai, H., "Electromechanical properties of metallic, quasimetallic, and semiconducting carbon nanotubes under stretching," *Physical Review Letters*, Vol. 90, No. 15, April 2003, pp. 18–21.

[77] Matsumoto, M. and Nishimura, T., "Mersenne twister: a 623-dimensionally equidistributed uniform pseudo-random number generator," *ACM Transactions on Modeling and Computer Simulation*, Vol. 8, No. 1, Jan. 1998, pp. 3–30.

[78] Reddy, J. N., *An Introduction to the Finite Element Method*, McGraw Hill, New York, NY, 3rd ed., 2006.

[79] Knudsen, H. and Fazekas, S., "Robust algorithm for random resistor networks using hierarchical domain structure," *Journal of Computational Physics*, Vol. 211, No. 2, Jan. 2006, pp. 700–718.

[80] OpenMP Architecture Review Board, "OpenMP," `http://openmp.org/wp/openmp-specifications/`, 2012, [Online; accessed June 2013].

[81] Hobara, R., Yoshimoto, S., Ikuno, T., Katayama, M., Yamauchi, N., Wongwiriyapan, W., Honda, S.-I., Matsuda, I., Hasegawa, S., and Oura, K., "Electronic transport in multiwalled carbon nanotubes contacted with patterned electrodes," *Japanese Journal of Applied Physics*, Vol. 43, No. 8B, July 2004, pp. L1081–L1084.

[82] Kaneto, K., Tsuruta, M., Sakai, G., Cho, W., and Ando, Y., "Electrical conductivities of multi-wall carbon nano tubes," *Synthetic Metals*, Vol. 103, 1999, pp. 2543–2546.

[83] Fuhrer, M., Nygard, J., Shih, L., Forero, M., Yoon, Y., Mazzoni, M., Choi, H., Ihm, J., Louie, S., Zettl, A., and McEuen, P., "Crossed nanotube junctions," *Science*, Vol. 288, No. 5465, April 2000, pp. 494–497.

[84] Marsaglia, G., "Choosing a point from the surface of a sphere," *The Annals of Mathematical Statistics*, Vol. 43, No. 2, 1972, pp. 645–646.

[85] Neubert, H., *Strain Gauges: Kinds and Uses*, Macmillan, London, England, 1967.

[86] Dobie, W. and Isaac, P., *Electric Resistance Strain Gauges*, English Universities Press, London, England, 1948.

[87] Yarnell, J., *Resistance Strain Gauges: Their construction and use*, Electronic Engineering, London, England, 1951.

[88] Eshelby, J., "The determination of the elastic field of an ellipsoidal inclusion, and related problems," *Proceedings of the Royal Society of London. Series A, Mathematical and Physical Sciences*, Vol. 241, No. 1226, 1957, pp. 376–396.

[89] Benveniste, Y., "A new approach to the application of Mori-Tanaka's theory in composite materials," *Mechanics of Materials*, Vol. 6, 1987, pp. 147–157.

[90] Duan, H., Wang, J., Huang, Z., and Karihaloo, B., "Eshelby formalism for nano-inhomogeneities," *Proceedings of the Royal Society A: Mathematical, Physical and Engineering Sciences*, Vol. 461, No. 2062, Oct. 2005, pp. 3335–3353.

[91] Eshelby, J., "The elastic field outside an ellipsoidal inclusion," *Proceedings of the Royal Society of London. Series A, Mathematical and Physical Sciences*, Vol. 252, No. 1271, 1959, pp. 561–569.

[92] Mura, T., *Micromechanics of Defects in Solids*, Kluwer Academic Publishers, Dordrecht, The Netherlands, 2nd ed., 1987.

[93] Ju, J. and Sun, L., "A novel formulation for the exterior-point Eshelby's tensor of an ellipsoidal inclusion," *Journal of Applied Mechanics*, Vol. 66, 1999, pp. 570–574.

[94] Jin, X., Keer, L. M., and Wang, Q., "A closed-form solution for the Eshelby tensor and the elastic field outside an elliptic cylindrical inclusion," *Journal of Applied Mechanics*, Vol. 78, No. 3, 2011, pp. 031009.

[95] Kim, B. R. and Lee, H. K., "Closed form solution of the exterior-point eshelby tensor for an elliptic cylindrical inclusion," *Journal of Applied Mechanics*, Vol. 77, No. 2, 2010, pp. 024503.

[96] Ju, J. and Chen, T., "Micromechanics and effective elastoplastic behavior of two-phase metal matrix composites," *Journal of Engineering Materials and Technology*, Vol. 116, 1994.

[97] Meng, C., Heltsley, W., and Pollard, D. D., "Evaluation of the Eshelby solution for the ellipsoidal inclusion and heterogeneity," *Computers & Geosciences*, Vol. 40, March 2012, pp. 40–48.

[98] Ferrers, N., "On the potentials of ellipsoids, ellipsoidal shells, elliptic laminae and elliptic rings of variable densities," *Quart. J. Pure Appl. Math*, 1877.

[99] Dyson, F., "The potentials of ellipsoids of variable densities," *Quart. J. Pure Appl. Math*, 1891, pp. 259–288.

[100] Lubarda, V., Blume, J., and Needleman, A., "An analysis of equilibrium dislocation distributions," *Acta Metallurgica et Materialia*, Vol. 41, No. 2, Feb. 1993, pp. 625–642.

[101] Giessen, E. and Needleman, A., "Discrete dislocation plasticity: a simple planar model," *Modelling and Simulation in Materials Science and Engineering*, Vol. 3, 1995, pp. 689–735.

[102] Cleveringa, H., Van der Giessen, E., and Needleman, A., "Comparison of discrete dislocation and continuum plasticity predictions for a composite material," *Acta Materialia*, Vol. 45, No. 8, 1997, pp. 3163–3179.

[103] Cleveringa, H., Van der Giessen, E., and Needleman, a., "Discrete dislocation simulations and size dependent hardening in single slip," *Le Journal de Physique IV*, Vol. 08, No. PR4, June 1998, pp. Pr4–83–Pr4–92.

[104] Ju, J. W. and Yanase, K., "Micromechanics and effective elastic moduli of particle-reinforced composites with near-field particle interactions," *Acta Mechanica*, Vol. 215, No. 1-4, May 2010, pp. 135–153.

[105] Sunday, D., "Geometry Algorithms," `http://www.geomalgorithms.com`, [Online; accessed June 2013].

[106] Bentley, J. L., "Multidimensional binary search trees used for associative searching," *Communications of the ACM*, Vol. 18, No. 9, Sept. 1975, pp. 509–517.

[107] Tagliasacchi, A., "KD-Tree for Matlab," `http://www.mathworks.com/matlabcentral/fileexchange/21512-kd-tree-for-matlab`, 2008, [Online; accessed June 2013].

[108] Chu, C.-C., White, K. L., Liu, P., Zhang, X., and Sue, H.-J., "Electrical conductivity and thermal stability of polypropylene containing well-dispersed multi-walled carbon nanotubes disentangled with exfoliated nanoplatelets," *Carbon*, Vol. 50, No. 12, Oct. 2012, pp. 4711–4721.

[109] Mott, P. and Roland, C., "Limits to Poissons ratio in isotropic materials," *Physical Review B*, Vol. 80, No. 13, Oct. 2009, pp. 132104.

[110] Tscharnuter, D., Jerabek, M., Major, Z., and Lang, R. W., "Time-dependent poissons ratio of polypropylene compounds for various strain histories," *Mechanics of Time-Dependent Materials*, Vol. 15, No. 1, Sept. 2011, pp. 15–28.

[111] Greaves, G., Greer, A., Lakes, R., and Rouxel, T., "Poisson's ratio and modern materials," *Nature Materials*, Vol. 10, 2011, pp. 823–838.

APPENDIX A

FEA/ESHELBY MICROMECHANICS FRAMEWORK

The purpose of this appendix is to show some of the capabilities of the hybrid FEA/Eshelby micromechanics framework that was developed in Section II.C.2. Several benchmark models were solved using both conventional FEA and the hybrid framework, and comparisons between the solutions are presented herein.

A.1. Four sphere model

The first model considered is a cubic RVE with four spheres embedded in it, as shown in Figure A.1. The spheres have a Young's modulus of 1.0 TPa and Poisson's ratio of 0.3. The matrix has a Young's modulus of 3.0 GPa and Poisson's ratio of 0.3. The very stiff modulus was chosen for the spheres to make sure the framework is able to handle the high elastic mismatch between carbon nanotubes and polymers such as epoxy. The boundary conditions for the model are such that the

The finite element mesh used for the FEA model is shown in Figure A.2. The mesh consists of 345,000 quadratic tetrahedral elements with approximately 1.4 million degrees of freedom. The mesh is shown with one quarter of the elements removed so that 3 of the 4 spheres can be easily seen.

The finite element mesh used for the hybrid framework model is shown in Figure A.3. The mesh consists of 64,000 quadratic hexahedral elements. The material properties for each element of the mesh are the same as the properties for the matrix. Note that there are no material boundaries anywhere in the mesh. This mesh shall

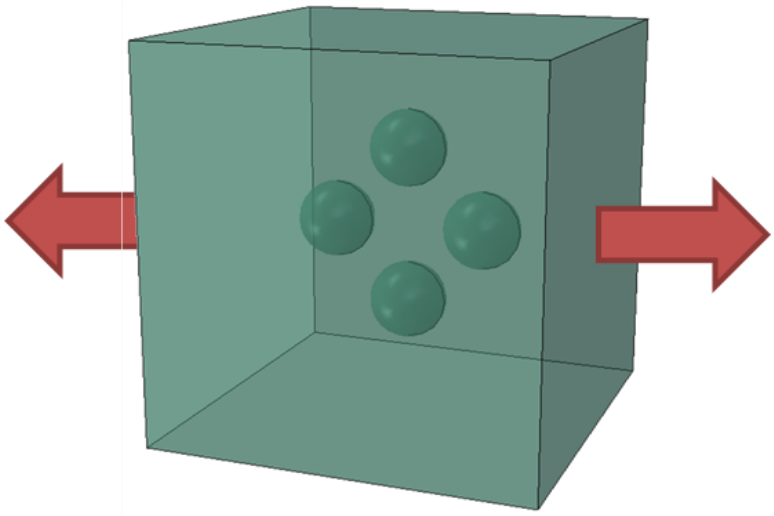

Figure A.1. Configuration for the 4 sphere benchmark model.

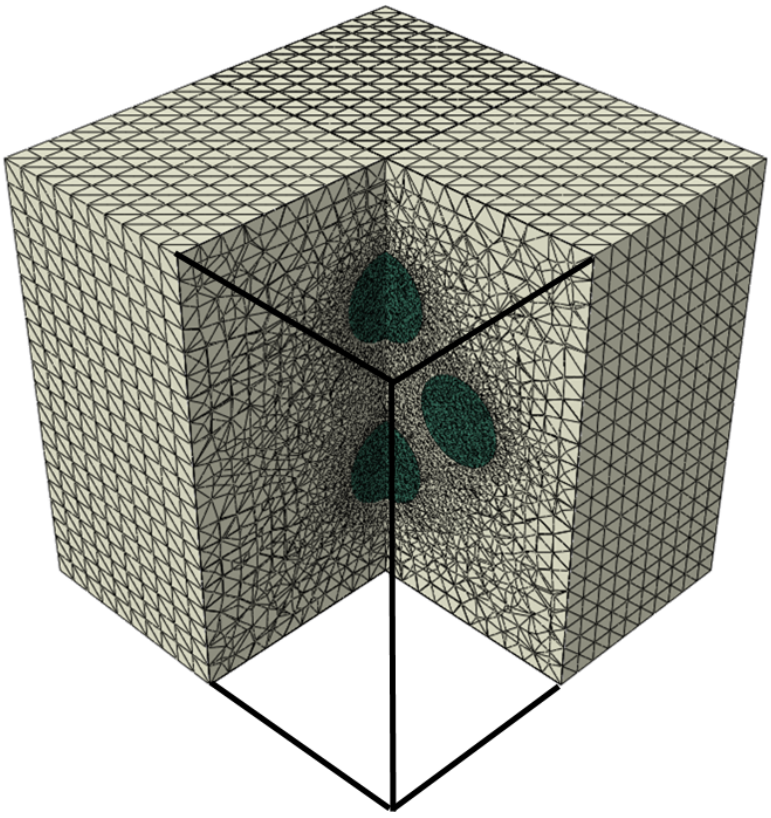

Figure A.2. Finite element mesh used for the 4 sphere benchmark model.

be referred to as the block mesh herein, it will be used for all of the benchmark problems in this section. This highlights one of the useful features of the framework. The mesh used is not required to be complex, and the same mesh can be used for an infinite number of configurations.

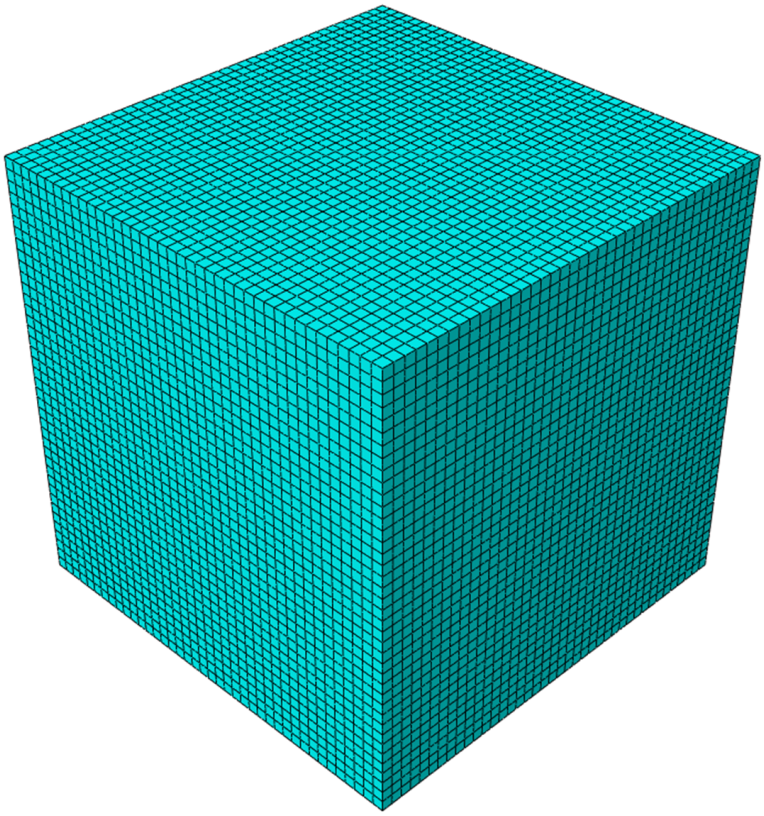

Figure A.3. Finite element mesh used for the hybrid framework model.

The contours for the strain component ε_{11} are shown for the FEA and hybrid Eshelby models in Figure A.4. Note that one quarter of the elements are again removed to show the contours in and around the spheres. It is clear from the contour data that the strains for the two models are qualitatively similar. Note that since

there are no material boundaries in the hybrid FEA/Eshelby mesh, the strain contours look jagged where the material boundaries should be. This is simply an artifact of the simple block mesh that was used and the finite element interpolation used to visualize the results. Because the Eshelby solution is sampled at each node of the mesh, visualizing elements that cross material boundaries requires interpolating between the Eshelby solution sampled inside and outside the equivalent inclusion. This results in the jagged contours seen in the figure. If a mesh were constructed such that individual elements could not cross material boundaries, the jagged contours would not be present. However, such a mesh would be difficult to generate for the types of problems that the hybrid model was designed for.

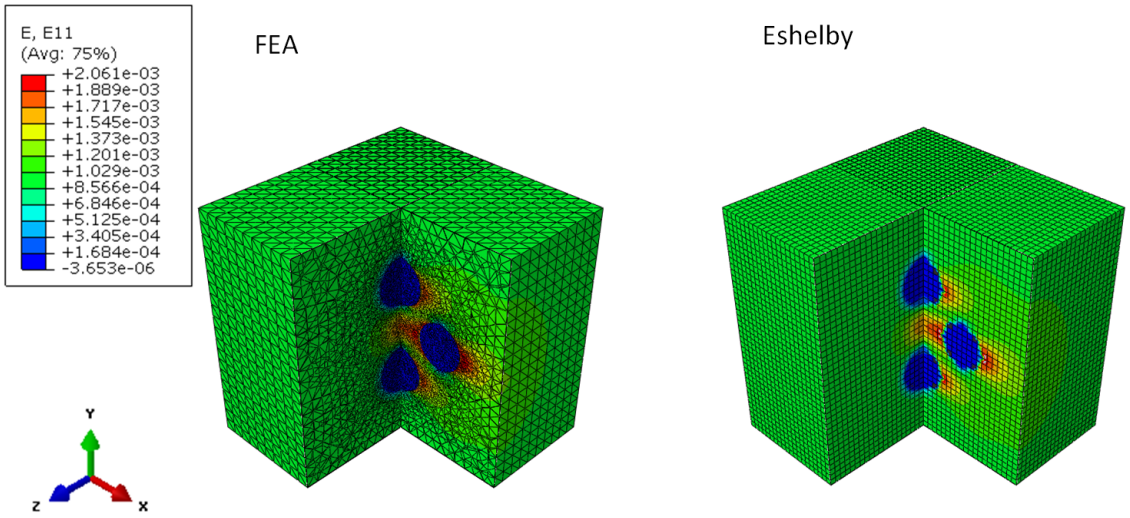

Figure A.4. Strain contours for the strain component ε_{11} for the 4 sphere benchmark model.

The contours for the strain components ε_{22} and ε_{33} are shown in Figure A.5 and Figure A.6, respectively. The element boundaries have been removed for clarity.

Like the ε_{11} component, ε_{22} and ε_{33} both show good qualitative agreement between the FEA and hybrid Eshelby models. Looking closely at the contour plots for the FEA models, the strain fields between the spherical inhomogeneities indicate that the inhomogeneities are indeed interacting with each other. The contour plots for the hybrid models indicate that this model also captures some of the interaction effects between the spheres.

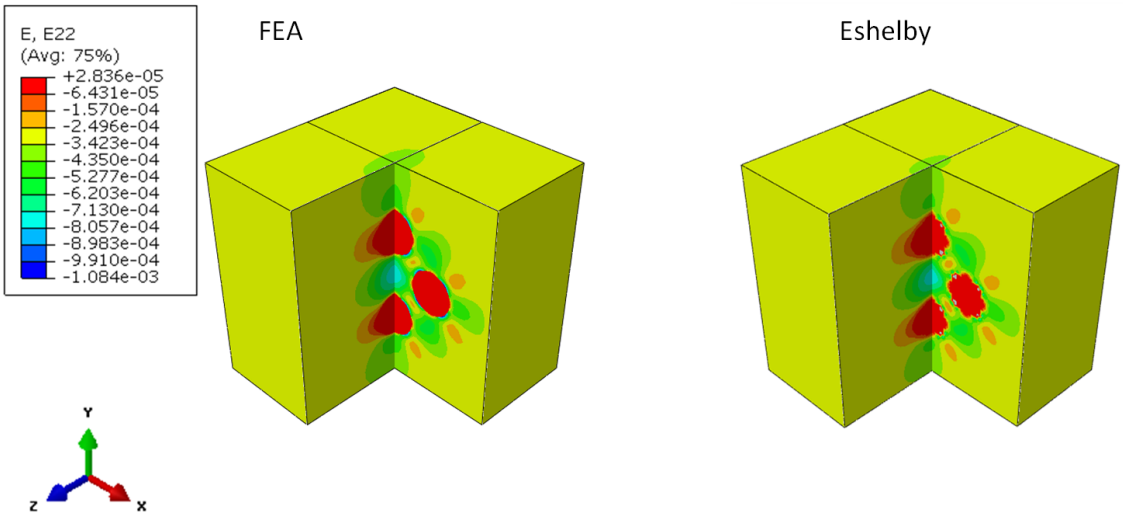

Figure A.5. Strain contours for the strain component ε_{22} for the 4 sphere benchmark model.

A.2. Ten sphere model

The second model considered is a cubic RVE with ten spheres embedded in it, as shown in Figure A.7. The spheres again have a Young's modulus of 1.0 TPa and Poisson's ratio of 0.3. The matrix has a Young's modulus of 3.0 GPa and Poisson's ratio of 0.3.

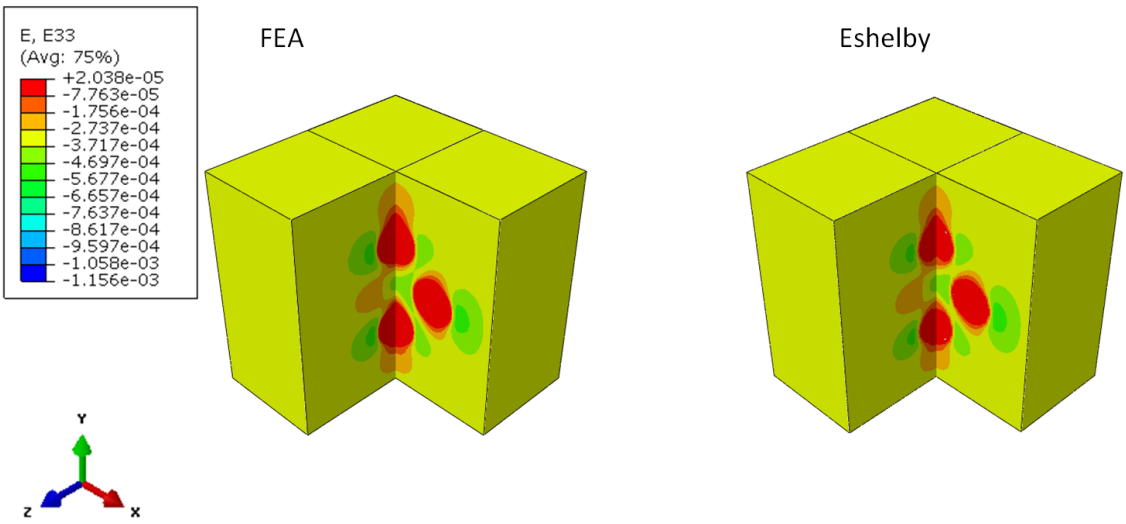

Figure A.6. Strain contours for the strain component ε_{33} for the 4 sphere benchmark model.

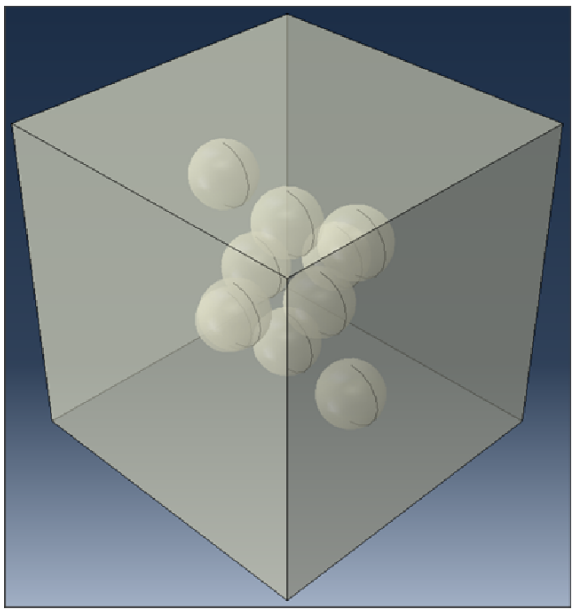

Figure A.7. Configuration for the 10 sphere benchmark model.

The finite element mesh used for the FEA model is shown in Figure A.8. The mesh consists of 699,252 quadratic tetrahedral elements with more than 2.8 million degrees of freedom. The mesh is shown with half of the elements removed so that 8 of the 10 spheres can be easily seen. It is clear from the figure that the spheres are relatively close to each other and a large amount of element refinement is needed in the regions around the spheres. The red line in Figure A.8 represents a path along which certain results are plotted.

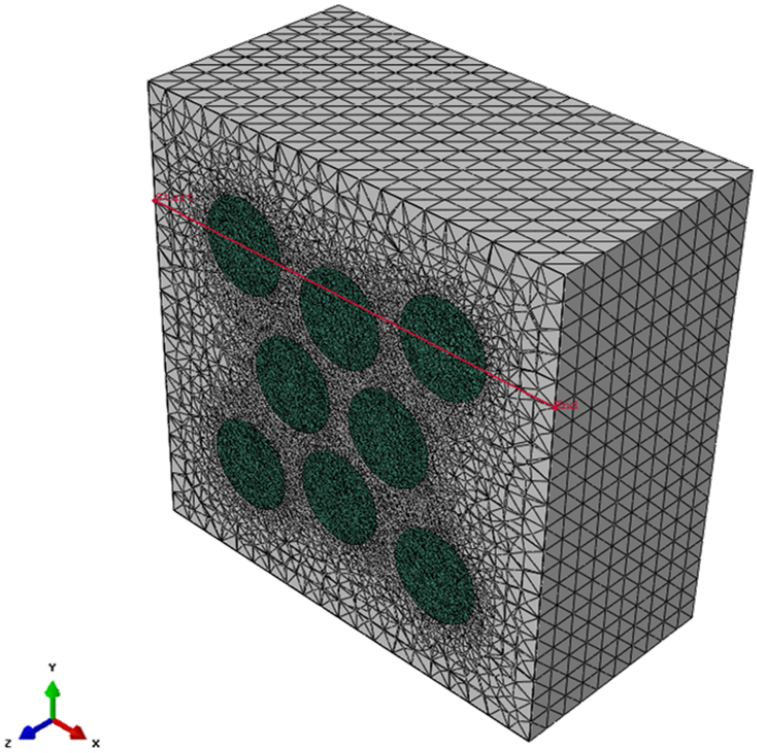

Figure A.8. Finite element mesh used for the 10 sphere benchmark model.

Because the original objective for the hybrid FEA/Eshelby framework was to calculate displacements between inhomogeneities (carbon nanotubes), it is important

to investigate the accuracy of the displacements calculated using the framework. Contour plots of the displacement u_1 are given in Figure A.9 for the FEA and hybrid models. Half of the elements in each mesh are again removed so that the interior of the meshes can be seen. The element edges are also removed for clarity. It is clear from the displacement contours that the displacement field inside the RVE is not uniform, and the contours for the hybrid model compare qualitatively well with the FEA contours. Again note that the contours are jagged around material boundaries for the reasons mentioned previously with the four sphere RVE results.

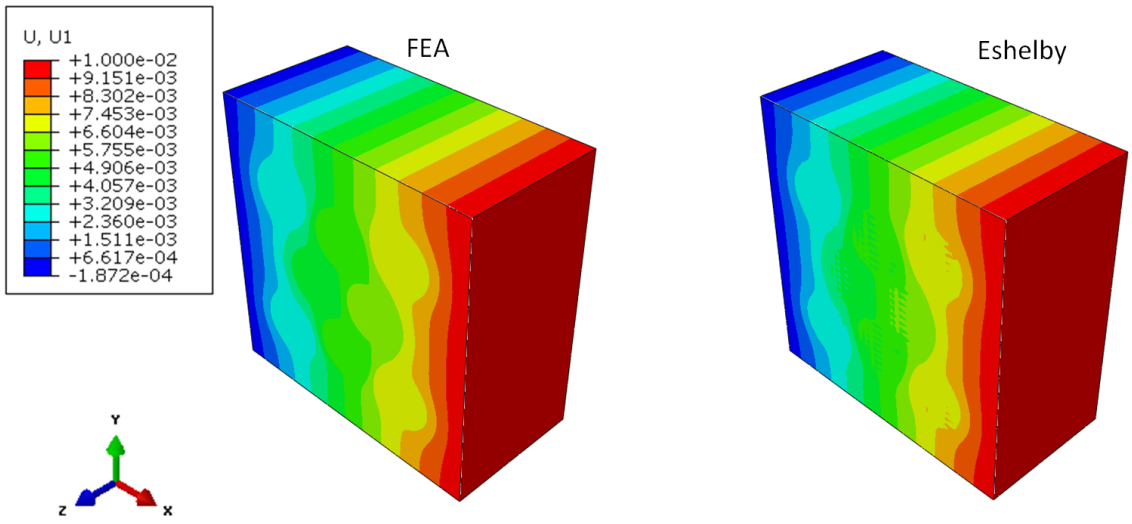

Figure A.9. Displacement contours for the component u_1 for the 10 sphere benchmark model.

While the contour plots shown above are good for qualitatively comparing the solutions between the FEA and hybrid models, the solutions must also be compared quantitatively. Thus, the displacement u_1 is plotted along a path through the FEA and hybrid models in Figure A.10. The path is given as the red line in Figure A.8, and

it passes through three of the spheres. The portions of the path that are inside the spheres are visible in Figure A.10 as the three flat regions of the FEA displacement curve. The displacements calculated for the hybrid model compare very well to the FEA displacements outside of the spheres, and the error increases inside the spheres. However, the maximum error between the hybrid and FEA displacement curves is approximately 7%. The difference in displacement between the FEA and hybrid models is most likely due to the assumptions made when calculating the interacting eigenstrains as outlined in Chapter II.C.2.c. Specifically, the equivalent eigenstrains for each inhomogeneity are assumed to be constant and are only calculated at the center of each sphere. This is why the Eshelby results match the FEA displacement so well at the centers of the spheres. It should also be noted that the intended use for the hybrid micromechanics model is to calculate the relative displacements between the center axes of carbon nanotubes, which appears to be where the model is most accurate.

The stress component σ_{11} is plotted in Figure A.11 for the FEA and hybrid models. The magnitudes of σ_{11} are visibly different between the two models, but the contours have very similar shapes. The maximum error between the FEA and hybrid stresses is approximately 30%. It is clear from these results that the hybrid model does better calculating displacements than stresses and strains. Again, the current use for the hybrid framework calculating displacements between inhomogeneities (carbon nanotubes). However, the framework does show some promise with calculating stresses and strains. If the framework were modified to include nonuniform interacting eigenstrains, the results would most likely improve. The framework

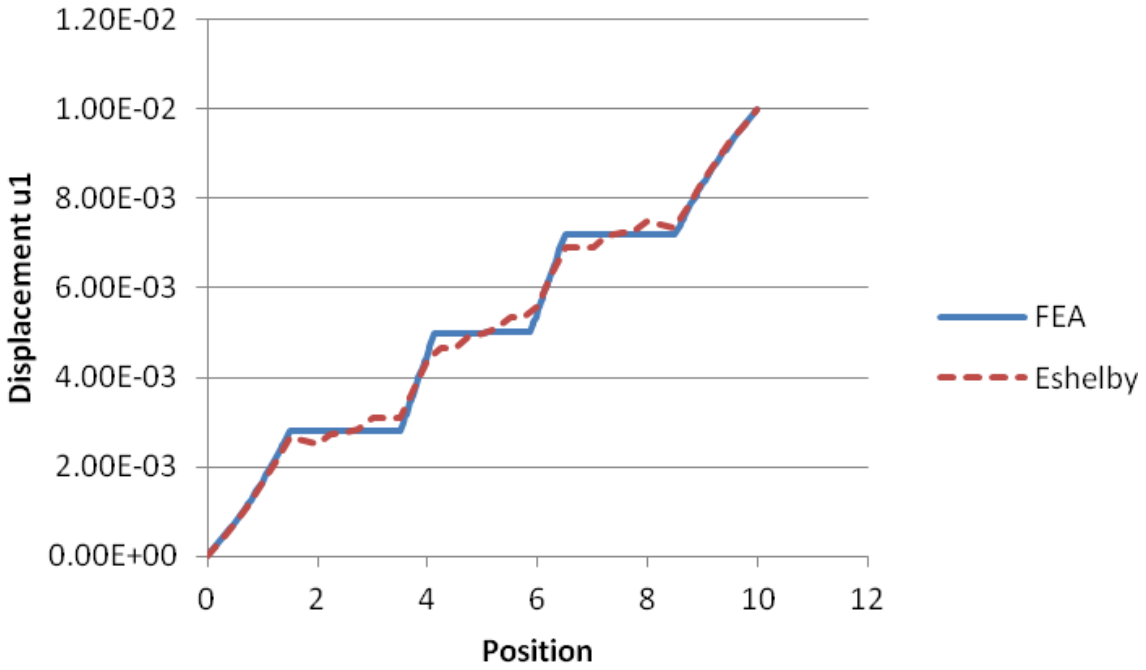

Figure A.10. Displacement component u_1 plotted along path given in Figure A.8 for the 10 sphere benchmark model. Results are shown for the FEA and FEA/Eshelby models.

could then be used to solve other micromechanics problems like calculating volume averaged effective properties.

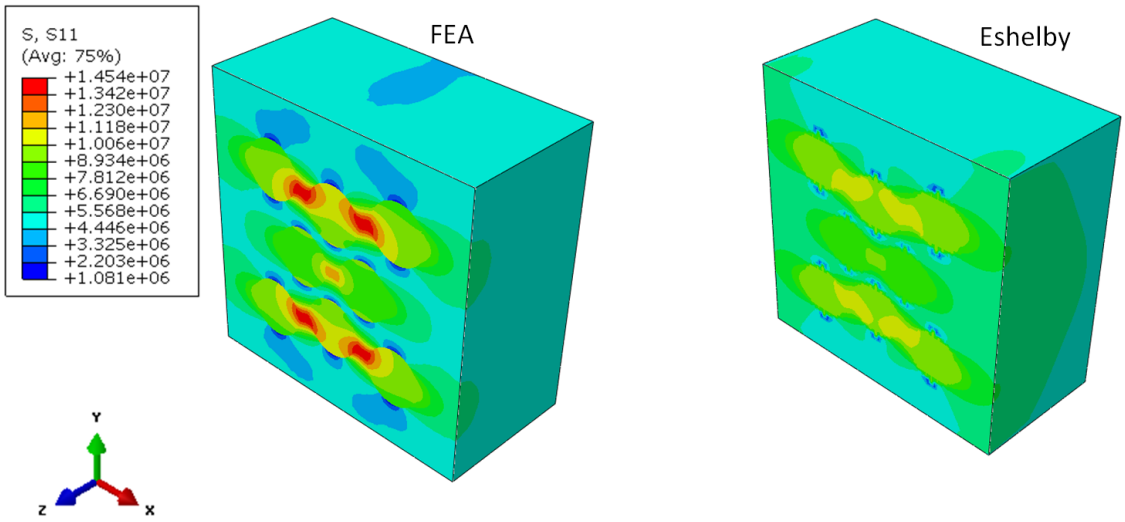

Figure A.11. Stress contours for the stress component σ_{11} for the 10 sphere benchmark model.